ANALYSIS OF NONLOCAL EFFECTS IN TURBULENCE CLOSURES WITH APPLICATION TO WALL-BOUNDED FLOWS

By
Jessie Liu and Ali Mani

Prepared with support from
The Boeing Company,
the Office of Naval Research,
the Lawrence Livermore National Laboratory, and
the Stanford Graduate Fellowship Program

Report No. TF-194

Flow Physics and Computational Engineering Group
Department of Mechanical Engineering
Stanford University
Stanford, CA 94305

March 2024

Analysis of Nonlocal Effects in Turbulence Closures with Application To Wall-Bounded Flows

By

Jessie Liu and Ali Mani

Prepared with support from
The Boeing Company,
the Office of Naval Research,
the Lawrence Livermore National Laboratory, and
the Stanford Graduate Fellowship Program

Report No. TF-194

Flow Physics and Computational Engineering Group
Department of Mechanical Engineering
Stanford University
Stanford, CA 94305

March 2024

Abstract

Turbulence modeling of wall-bounded flows is important to a wide variety of applications, including in engineering, e.g., aircraft and ships, and in geophysics, e.g., atmospheric boundary layers. In turbulent flows, direct numerical simulation (DNS) of the governing equations is often intractable due to the wide range of scales that must be resolved. Instead, turbulence modeling approaches, such as Reynolds-averaged Navier-Stokes (RANS) models, are widely-used in engineering applications. RANS models compute averaged quantities, such as the mean velocities needed for the prediction of drag or lift on an aircraft, that are sufficient for many engineering applications.

Widely-used RANS models rely on a local and isotropic eddy viscosity approximation that is inadequate for complex flows. This work begins by revisiting an existing framework for incorporating nonlocal and anisotropic effects, namely Reynolds stress transport models. While we include recent experimental/DNS data from literature with the goal of improving model accuracy and develop an analytical near-wall model for capturing the leading-order behavior of all components of the Reynolds stresses near the wall, we encounter substantial challenges in making model improvements, particularly due to the distinct model requirements for both near-wall, low turbulent intensity regions, and away-from-wall, high turbulent intensity regions. This motivates both the development of an alternative modeling approach and a physical investigation of nonlocal and anisotropic effects in turbulent wall-bounded flows, which are the focuses of the rest of this work.

The macroscopic forcing method (MFM) of Mani and Park (2021) allows computation of the exact nonlocal and anisotropic eddy viscosity. However, to compute the exact eddy viscosity, a brute force application of MFM requires as many DNSs as degrees of freedom in the averaged space. We develop a systematic and cost-effective approach for quantifying and modeling the nonlocal eddy viscosity that needs only information about a few of the low-order eddy viscosity moments, which can be computed efficiently using only one simulation per moment. The resulting model form, using what we call *matched moment inverse* operators, closely approximates the shape of the true nonlocal eddy viscosity kernel and is in the form of a partial differential equation rather than a difficult to solve integro-partial differential equation.

We then focus on a physical investigation of the exact nonlocal and anisotropic eddy viscosity in turbulent wall-bounded flows. To alleviate the computational cost of a brute force MFM approach,

we develop an adjoint-based macroscopic forcing method (adjoint MFM) for targeted computation of the nonlocal eddy viscosity, which relates the Reynolds stresses at a given location to the mean velocity gradient at all points in space, using only one simulation per desired location. While prior works have examined the wall-normal nonlocal eddy viscosity in turbulent channel flow, we use adjoint MFM to examine the streamwise and wall-normal nonlocal eddy viscosity in turbulent channel flow at select near-wall locations.

Acknowledgments

This work was supported by The Boeing Company and the Office of Naval Research. Additional support was provided by the Burt and Deedee McMurtry Stanford Graduate Fellowship and the Department of Energy (Lawrence Livermore National Laboratory).

THIS PAGE DELIBERATELY LEFT BLANK

Contents

List of Tables

List of Figures

Chapter 1

Introduction

1.1 Background and motivation

Turbulent wall-bounded flows are important in a wide variety of applications such as in engineering, e.g., in aerodynamics (Lacy and Clark (2020)) and naval hydrodynamics (Liefvendahl and Fureby (2017)), and in geophysics, e.g., atmospheric boundary layers (Gibson and Launder (1978)). Direct numerical simulation (DNS) of the governing equations is often intractable due to the wide range of scales that must be resolved in turbulent flow simulations, the smallest being on the order of the dissipation scale, e.g., $\mathcal{O}(1\,\mu m)$ for an aircraft, to the largest being on the order of the geometry, e.g., $\mathcal{O}(10\,m)$ for an aircraft. Instead of DNS, turbulence modeling approaches are used. In large eddy simulation (LES), only the large scales are resolved and the small unresolved scales are modeled. In Reynolds-averaged Navier–Stokes (RANS) models, only the averaged quantities, such as the mean velocities needed for prediction of drag or lift on an aircraft, rather than the instantaneous quantities are computed.

Regardless of the modeling approach, the presence of walls introduces additional challenges. These challenges are elaborated on in Pope (2000), a summary of which is provided here:

- Near the wall, viscous effects dominate and the Reynolds number is very low. Whereas far away from the wall, viscous effects are negligible. Models for wall-bounded flows should correctly transition between both regimes.
- Very near the wall, due to the no-slip and no-penetration boundary conditions and the continuity equation, the velocity fluctuations in the wall-normal direction are much smaller than those in the streamwise and spanwise directions, leading to a two-component turbulence limit.
- In wall-bounded flows, the mean shear is often highest at the wall.

- There is a "wall-blocking" effect due to the no-penetration boundary condition at the wall which acts through the pressure field (Hunt and Graham (1978)).

Additional complex phenomena such as flow separation due to adverse pressure gradients make wall-bounded turbulence modeling even more challenging. In this thesis, we focus on the RANS modeling approach, which generally has lower computational cost than LES and is widely used in engineering applications.

1.2 Reynolds-averaged Navier–Stokes models

For a Newtonian incompressible flow, the Navier–Stokes equations can be written as:

$$\frac{\partial u_i}{\partial t} + u_j \frac{\partial u_i}{\partial x_j} = -\frac{1}{\rho}\frac{\partial p}{\partial x_i} + \nu \frac{\partial^2 u_i}{\partial x_j \partial x_j} \tag{1.1a}$$

$$\frac{\partial u_i}{\partial x_i} = 0 \tag{1.1b}$$

where $u_i(\mathbf{x}, t)$ is the velocity field, $p(\mathbf{x}, t)$ is the pressure field, ρ is the density of the fluid, and ν is the kinematic viscosity of the fluid.

RANS models predict averaged quantities, and the definition of averaging is problem-dependent. For example, the average can be defined as an ensemble average if the flow is ergodic, a time average if the flow is statistically stationary, and/or a spatial average if the flow is homogeneous over spatial directions. In general, the mean quantity is not the same as the instantaneous quantity, and a Reynolds decomposition (Reynolds (1895)) is applied:

$$u_i = U_i + u_i', \tag{1.2a}$$

$$p = P + p', \tag{1.2b}$$

where the uppercase variable denotes the mean and the prime denotes the fluctuations about the mean. Substitution of the Reynolds decomposition in (1.2a) and (1.2b) into the Navier–Stokes equations in (1.1a) and (1.1b) and averaging leads to the RANS equations:

$$\frac{\partial U_i}{\partial t} + U_j \frac{\partial U_i}{\partial x_j} = -\frac{1}{\rho}\frac{\partial P}{\partial x_i} + \nu \frac{\partial^2 U_i}{\partial x_j \partial x_j} - \frac{\partial}{\partial x_j}\overline{u_j' u_i'} \tag{1.3a}$$

$$\frac{\partial U_i}{\partial x_i} = 0 \tag{1.3b}$$

where the bar denotes averaging. The Reynolds stress tensor, $\overline{u_j' u_i'}$, is unclosed in the sense that attempts to analytically derive equations governing the Reynolds stress tensor, as shown later, result in more unclosed terms. Hence, RANS closure models are used instead for the Reynolds stresses.

One- or two-equation RANS models such as the widely-used Spalart-Allmaras (SA) model (Spalart

and Allmaras (1992)), Menter shear stress transport (SST) model (Menter (1994)), and Wilcox k-ω model (Wilcox (1998)) use the Boussinesq approximation (Boussinesq (1877)). The Boussinesq approximation has two underlying assumptions: 1) The length and time scales of the underlying velocity fluctuations are much smaller than that of the mean velocity fields, and hence the mixing by the turbulent fluctuations is assumed to be local. 2) The mixing by the underlying fluctuations is assumed to be isotropic; hence, the Reynolds stress tensor and mean strain rate tensor are aligned. Under the Boussinesq approximation an analogy is drawn to Brownian motion, for which random molecular mixing is modeled using a diffusive flux, and the Reynolds stress tensor is modeled in terms of the eddy viscosity and the mean velocity gradient:

$$-\overline{u_i' u_j'} = 2\nu_\mathrm{T} S_{ij} - \frac{2}{3} k \delta_{ij}, \tag{1.4}$$

where ν_T is the eddy viscosity, $k \equiv \overline{u_i' u_i'}/2$ is the turbulent kinetic energy, δ_{ij} is the Kronecker delta, and S_{ij} is the mean strain rate tensor:

$$S_{ij} = \frac{1}{2}\left(\frac{\partial U_i}{\partial x_j} + \frac{\partial U_j}{\partial x_i}\right). \tag{1.5}$$

The mean strain rate tensor is used to respect the symmetry of the Reynolds stress tensor. The turbulent kinetic energy is added such that the trace of (1.4) is consistent but is often omitted from models where k is not readily available. While this term is still unclosed, it is often left without modeling since it can be absorbed by the mean pressure term, which is also an isotropic tensor.

One equation models, e.g., SA (Spalart and Allmaras (1992)), develop a transport equation for the eddy viscosity, ν_T. Two-equation models, e.g., Menter's SST (Menter (1994)) or Wilcox's k-ω (Wilcox (1998)) model, form ν_T from other quantities, such as k and ω, representing a turbulent kinetic energy scale and turbulent eddy inverse time scale, respectively, and then develop transport equations for each of these quantities.

For the near-wall region, models, e.g., SA (Spalart and Allmaras (1992)), add near-wall terms based on the distance from the wall and empirical functions. Other models, e.g., Menter's SST model (Menter (1994)), use $\phi = \alpha\phi_w + (1-\alpha)\phi_h$ to blend between the coefficients for the near-wall model, ϕ_w, and the coefficients for the away-from-wall model, ϕ_h, where α is a blending parameter based on empirical functions.

For turbulent flows, the underlying isotropy and locality assumptions of the Boussinesq approximation are often invalid (Corrsin (1975)). Kraichnan (1987) derived an exact nonlocal and anisotropic expression for the Reynolds stress tensor using a Green's function. Hamba (2005) modified the expression to be feasible for numerical implementation to be able to computationally measure

the eddy viscosity for a given flow. The generalized eddy viscosity is:

$$-\overline{u_i' u_j'}(\mathbf{x}, t) = \int_{\mathbf{y},\tau} D_{ijkl}(\mathbf{x}, \mathbf{y}, t, \tau) \frac{\partial U_l}{\partial x_k}\bigg|_{\mathbf{y},\tau} \mathrm{d}\mathbf{y}\mathrm{d}\tau, \tag{1.6}$$

where $D_{ijkl}(\mathbf{x}, \mathbf{y}, t, \tau)$ is the nonlocal and anisotropic eddy viscosity kernel. The eddy viscosity is 1) spatiotemporally nonlocal in that the Reynolds stress tensor depends on the mean velocity gradient at all points in space and in its time history as captured via a nonlocal integral and 2) anisotropic in that the Reynolds stress tensor and velocity gradient tensor are not necessarily aligned as captured via a fourth-order tensor. While for a given flow, the closure in (1.6) is exact, and the eddy viscosity kernel, $D_{ijkl}(\mathbf{x}, \mathbf{y}, t, \tau)$, can be computed using the Green's function approach of Hamba (1995, 2005) or the macroscopic forcing method (Mani and Park (2021)), in general, the closure in (1.6) presents additional challenges:

- The eddy viscosity kernel, $D_{ijkl}(\mathbf{x}, \mathbf{y}, t, \tau)$, is cost-prohibitive to compute: A brute-force approach would require as many DNSs as degrees of freedom in the averaged space.
- The nonlocal integral in (1.6) is cost-prohibitive to implement in a computational fluid dynamics solver: A spatially nonlocal eddy viscosity would raise the computational cost from $\mathcal{O}(N)$ to $\mathcal{O}(N^2)$; a temporally nonlocal eddy viscosity would require keeping the history of the mean flow stored in memory.

We discuss these challenges in detail in Section 1.3.

Some RANS models include anisotropic effects by adding functions of the strain rate tensor and rotation rate tensor in the Reynolds stress closure. For example, SA with Quadratic Constitutive Relation (SA-QCR) (Spalart (2000)) uses

$$-\overline{u_i' u_j'} = \tau_{ij} - c_1(O_{ik}\tau_{jk} + O_{jk}\tau_{ik}), \tag{1.7}$$

where τ_{ij} is the Reynolds stresses given by the Boussinesq eddy viscosity model in (1.4), c_1 is a dimensionless coefficient, and O_{ij} is the normalized rotation rate tensor:

$$O_{ik} = \frac{2W_{ik}}{\sqrt{\frac{\partial U_m}{\partial x_n}\frac{\partial U_m}{\partial x_n}}},\ W_{ik} = \frac{1}{2}\left(\frac{\partial U_i}{\partial x_k} - \frac{\partial U_k}{\partial x_i}\right). \tag{1.8}$$

Further modifications for SA-QCR are provided by Mani et al. (2013) and Rumsey et al. (2020). The explicit algebraic k-ω model (Hellsten (2005); Wallin and Johansson (2000)), or more generally, explicit algebraic Reynolds stress models, use

$$-\overline{u_i' u_j'} = 2\nu_\mathrm{T} S_{ij} - \frac{2}{3}k\delta_{ij} - a_{ij}^{(\mathrm{ex})}k, \tag{1.9}$$

where

$$a_{ij}^{(\mathrm{ex})} = f\left(S_{ij}, S_{ik}W_{kj} - W_{ik}S_{kj}, S_{ik}S_{kj} - \frac{1}{3}S_{mn}S_{mn}\delta_{ij}, \dots\right) \tag{1.10}$$

is a function of tensors from an integrity basis derived by Pope (1975) such that any symmetric deviatoric second-order tensor formed by S_{ij} and W_{ij} can be expressed as a combination of these tensors.

A simple nonlocal model for including a history effect along Lagrangian trajectories is (Durbin and Reif (2011)):

$$T\frac{D}{Dt}\overline{u_i'u_j'} = -2\nu_{\mathrm{T}}S_{ij} - \overline{u_i'u_j'}, \tag{1.11}$$

where $D/Dt \equiv \partial/\partial t + U_m\partial/\partial x_m$ is the mean material derivative, T is a relaxation timescale associated with the history effect, and we have omitted the $2/3k\delta_{ij}$ term. At steady state or under quasi-steady conditions when the flow evolves much slower than this relaxation timescale, the time derivative in (1.11) can be neglected, resulting in the equilibrium Reynolds stresses given by the Boussinesq eddy viscosity model in Equation (1.4).

More generally, Reynolds stress models can include nonlocal and anisotropic effects by solving a transport equation for each component of the Reynolds stress tensor. Reynolds stress models such as the Launder, Reece, and Rodi (LRR) model (Launder et al. (1975)) or the Speziale, Sarkar, and Gatski (SSG) model (Speziale et al. (1991)) offer closure to the unclosed terms in the exact Reynolds stress transport equation (Pope (2000)):

$$\frac{D}{Dt}\overline{u_i'u_j'} + \frac{\partial}{\partial x_k}T_{kij} = \mathcal{P}_{ij} + \mathcal{R}_{ij} - \varepsilon_{ij}, \tag{1.12}$$

where the Reynolds stress flux T_{kij} is

$$T_{kij} = T_{kij}^{(u)} + T_{kij}^{(p)} + T_{kij}^{(\nu)}, \tag{1.13a}$$

$$T_{kij}^{(u)} = \overline{u_i'u_j'u_k'}, \tag{1.13b}$$

$$T_{kij}^{(p)} = \frac{1}{\rho}\overline{u_i'p'}\delta_{jk} + \frac{1}{\rho}\overline{u_j'p'}\delta_{ik}, \tag{1.13c}$$

$$T_{kij}^{(\nu)} = -\nu\frac{\partial\overline{u_i'u_j'}}{\partial x_k}, \tag{1.13d}$$

the production $\mathcal{P}_{ij}$ is

$$\mathcal{P}_{ij} = -\overline{u_i'u_k'}\frac{\partial U_j}{\partial x_k} - \overline{u_j'u_k'}\frac{\partial U_i}{\partial x_k}, \tag{1.14}$$

the pressure–rate-of-strain tensor $\mathcal{R}_{ij}$ is

$$\mathcal{R}_{ij} = \overline{\frac{p'}{\rho}\left(\frac{\partial u_i'}{\partial x_j} + \frac{\partial u_j'}{\partial x_i}\right)}, \tag{1.15}$$

and the dissipation ε_{ij} is

$$\varepsilon_{ij} = 2\nu \overline{\frac{\partial u_i}{\partial x_k} \frac{\partial u_j}{\partial x_k}}. \tag{1.16}$$

The exact Reynolds stress transport equation is derived by multiplying the Navier–Stokes equation for u_i in (1.1a) by u_j and adding the same equation formulated for u_j and multiplied by u_i. Substituting the Reynolds decomposition in (1.2a) and (1.2b) into the equation for $u_i u_j$ and averaging leads to the Reynolds stress transport equation in (1.12) after some additional algebraic manipulation. In the Reynolds stress transport equation in (1.12), the mean material derivative D/Dt, the viscous term in (1.13d), and the production term in (1.14) are closed, while the remaining terms need closure. Moreover, for dimensional considerations, an auxiliary scalar equation is needed, and a common choice is the isotropic dissipation, ε (Launder et al. (1975); Speziale et al. (1991)).

Some models, e.g., the LRR model (Launder et al. (1975)) and JHh-v2 model (Jakirlić and Hanjalić (2002); Cécora et al. (2015)), handle the presence of walls by adding wall-reflection terms (Gibson and Launder (1978)) that are a function of the distance from the wall and modify the closure for the pressure–rate-of-strain in the near-wall region. The SSG model (Speziale et al. (1991)) is only intended for regions away from walls; however, the SSG/LRR-ω model (Cécora et al. (2015); Eisfeld et al. (2016); Eisfeld and Rumsey (2020)) blends the behavior of an away-from-wall SSG model with a near-wall LRR model using Menter's baseline (BSL)-ω equation (Menter (1994)), which uses an effective ε equation away from the wall and Wilcox's ω equation (Wilcox (1988)) near the wall.

To approximate the nonlocal effect of the wall on the Reynolds stresses, other models such as the elliptic relaxation model of Durbin (1993) and elliptic blending model of Manceau and Hanjalić (2002) solve additional elliptic equations (in addition to a Reynolds stress transport model). The elliptic relaxation model of Durbin (1993) solves a tensorial elliptic equation, which is then used in the closure model for the pressure–rate-of-strain tensor. The elliptic blending model (Manceau and Hanjalić (2002)) simplifies this approach to an elliptic equation for a scalar variable that blends between near-wall and away-from-wall model behavior. Alternatively, the $v2-f$ model (Durbin (1991)) is a simplified version of the elliptic relaxation model (Durbin (1993)) and focuses only on modeling the wall-normal component of the Reynolds stress tensor, $\overline{v^2}$. Rather than a Reynolds stress transport model, the $v2-f$ model is a three-equation model with a Boussinesq eddy viscosity based on $\overline{v^2}$, a turbulent kinetic energy scale k, and a dissipation scale ε, with an additional elliptic equation for a variable f (four equations total).

1.3 The macroscopic forcing method

The macroscopic forcing method (MFM) of Mani and Park (2021) is a numerical tool for probing closure operators, such as the exact nonlocal and anisotropic eddy viscosity in Equation (1.6) for RANS closure, using forced DNSs. While the closure operators are naturally flow-dependent, data from MFM measurements can be used to inform RANS models of deficiencies in their modeling

approximations and regions of sensitivity to the mean velocity gradient.

While MFM can be used to compute the entire nonlocal and anisotropic eddy viscosity kernel, $D_{ijkl}(\mathbf{x}, \mathbf{y}, t, \tau)$, as shown in Equation (1.6), a brute-force approach, similar to the Green's function approach of Hamba (2005) requires probing the eddy viscosity at each $(\mathbf{y}, \tau)$ using separate forced DNSs. Thus, computing the entire nonlocal and anisotropic eddy viscosity kernel using a brute-force approach requires as many DNSs as degrees of freedom in the averaged space, which for many flows is computationally intractable.

As an alternative to the brute-force approach, MFM can also be used to compute moments of the eddy viscosity, requiring only one forced DNS per moment (per velocity gradient direction), which we show in more detail in Chapter 3. The moments are related to the generalized eddy viscosity in Equation (1.6) via a Taylor series expansion locally about $\mathbf{y} = \mathbf{x}$ and $\tau = t$ (also known as a Kramers–Moyal expansion (Van Kampen (1992)):

$$-\overline{u_i' u_j'}(\mathbf{x}, t) = \left[D^0_{ijkl}(\mathbf{x}, t) + D^{1_s}_{ijklm}(\mathbf{x}, t) \frac{\partial}{\partial x_m} + \cdots + D^{1_t}_{ijkl}(\mathbf{x}, t) \frac{\partial}{\partial t} + \cdots \right] \frac{\partial U_l}{\partial x_k} \tag{1.17}$$

where D^0_{ijkl} is the zeroth-order spatial and temporal moment:

$$D^0_{ijkl}(\mathbf{x}, t) = \int \int D_{ijkl}(\mathbf{x}, \mathbf{y}, t, \tau) \mathrm{d}\mathbf{y} \mathrm{d}\tau, \tag{1.18}$$

$D^{1_s}_{ijklm}$ is the first-order spatial moment (superscript s for spatial):

$$D^{1_s}_{ijklm}(\mathbf{x}, t) = \int \int (y_m - x_m) D_{ijkl}(\mathbf{x}, \mathbf{y}, t, \tau) \mathrm{d}y_m \mathrm{d}\tau, \tag{1.19}$$

$D^{1_t}_{ijkl}$ is the first-order temporal moment (superscript t for temporal):

$$D^{1_t}_{ijkl}(\mathbf{x}, t) = \int \int (\tau - t) D_{ijkl}(\mathbf{x}, \mathbf{y}, t, \tau) \mathrm{d}\mathbf{y} \mathrm{d}\tau. \tag{1.20}$$

MFM has been used to investigate the nonlocal and anisotropic eddy viscosity in turbulent channel flow (Park and Mani (2023a)), a two-dimensional (2D) canonical separated boundary layer (Park et al. (2022a)), a canonical separated boundary layer with sweep (Park and Mani (2023b)), and the eddy diffusivity for scalar transport in Rayleigh-Taylor instability (Lavacot et al. (2023)).

Of particular relevance to this work, Park et al. (2022a) used MFM to compute the anisotropic and local eddy viscosity, D^0_{ijkl}, corresponding to the leading-order term in Equation (1.17) for a 2D canonical separated boundary layer in which the flat-plate turbulent boundary layer separation is induced by a blowing and suction boundary condition (Spalart and Coleman (1997); Na and Moin (1998); Abe (2017); Wu et al. (2020)). In addition to showing large differences in the eddy viscosity used by the SA model and the MFM-measured eddy viscosity, Park et al. (2022a) also used the

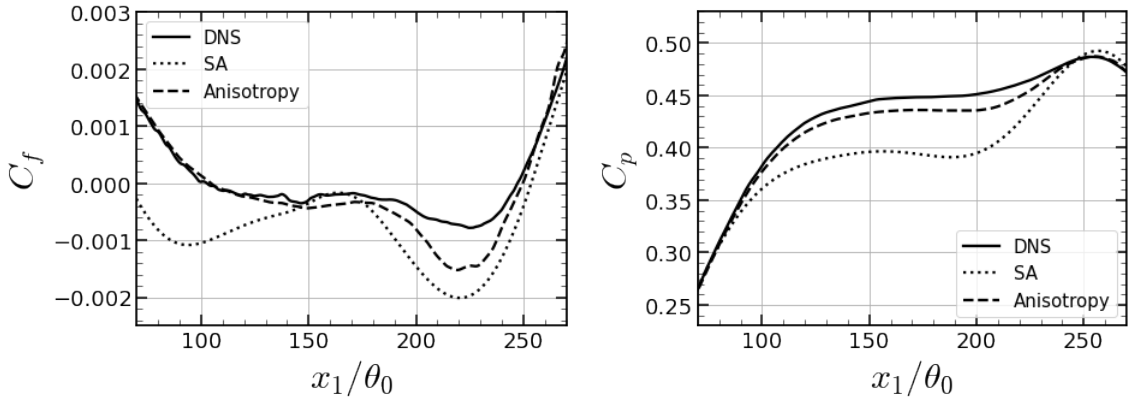

(a) (b)

Figure 1.1: Figure reproduced from Park et al. (2022b) which is based on Park et al. (2022a). Comparison of using the MFM-measured anisotropic but local eddy viscosity in Equation (1.21) against the mean of DNS and an isotropic and local model (SA model (Spalart and Allmaras (1992)) for a canonical separated boundary layer. The MFM-measured anisotropic but local eddy viscosity improves the prediction of the (a) friction coefficient and (b) pressure coefficient, especially around flow separation at $x_1/\theta_0 = 103$, but there is still some remaining error, particularly before flow reattachment at $x_1/\theta_0 = 246$ due to nonlocal effects.

MFM-measured leading-order eddy viscosity in a model of the form:

$$-\overline{u_i' u_j'}(x_1, x_2) = D^0_{ijkl}(x_1, x_2)\frac{\partial U_l}{\partial x_k}, \tag{1.21}$$

which is based on the leading term of the expansion in (1.17) for the 2D separated boundary layer (averaged in time and in the homogeneous spanwise direction, x_3). They showed that while the MFM-measured anisotropic but local eddy viscosity greatly improved prediction of the friction coefficient and pressure coefficient, as reproduced in Figure 1.1, there is some remaining error, particularly near the region of reattachment, around $x_1/\theta_0 = 246$. This indicates that while modeling approaches that include anisotropy but not nonlocality such as SA-QCR in (1.7) or explicit algebraic Reynolds stress models in (1.9) can partially improve prediction of complex flows, nonlocal effects also need to be captured, which is one of the motivations for the work in this thesis.

1.4 Present work

The objective of this thesis is to investigate nonlocal effects in RANS models particularly for wall-bounded applications in which the presence of walls introduces many additional challenges. As discussed in Section 1.3, for a given flow, MFM can be used to compute the nonlocal and anisotropic

eddy viscosity kernel in Equation (1.6). However, MFM requires many forced DNSs which is computationally intractable for many flows. Moreover, for modeling purposes, the nonlocal integral in (1.6) is costly and difficult to implement into computational fluid dynamics solvers. We address these issues in this thesis by:

- Proposing a systematic and cost-effective approach for quantifying and modeling a nonlocal eddy viscosity using MFM-measured moments of the eddy viscosity, which can be computed using one forced DNS per eddy viscosity moment. The resulting reduced-order model is in the form of a partial differential equation rather than a difficult to implement integro-partial differential equation as shown in Chapter 4.

- For flows in which the nonlocal and anisotropic eddy viscosity is needed only in targeted regions, e.g., at locations where there is a lack of understanding of RANS model requirements, we propose an adjoint-based MFM which uses one simulation per desired eddy viscosity location.

The outline for this thesis is:

In Chapter 2, we attempt to incorporate and modify nonlocal and anisotropic effects by revisiting an analytical Reynolds stress modeling approach. The main contributions of this chapter are: 1) a collection of experimental and DNS data for determining model coefficients including new data that has not been previously used in this context; 2) a demonstration of using this data to determine the coefficients of a Reynolds stress model; and 3) progress towards development of a near-wall model that preserves the expected analytical Reynolds stress scalings near the wall. While we are unable to adequately capture the Reynolds stress behavior in turbulent channel flow, this chapter motivates: 1) developing an alternative modeling approach using information about the nonlocal and anisotropic eddy viscosity from MFM as shown in Chapter 4, and 2) a more fundamental examination of the eddy viscosity in wall-bounded flows as shown in Chapter 6.

In Chapter 3, we introduce MFM in more detail for both passive scalar and momentum transport. We introduce both the brute-force approach and the method used for directly computing moments of the eddy diffusivity or eddy viscosity.

In Chapter 4, we develop what we call *matched moment inverse* operators for modeling nonlocal eddy diffusivities for passive scalar transport. The main contribution of this chapter is a systematic approach for modeling a nonlocal eddy diffusivity that only needs information about the eddy diffusivity moments, which can be computed efficiently using MFM. The additional advantages of the proposed model form are that it closely approximates the shape of the true nonlocal eddy diffusivity kernel and is in the form of a partial differential equation rather than an integro-partial differential equation. We demonstrate the approach for modeling nonlocal eddy diffusivities in homogeneous and inhomogeneous flows. We then generalize the approach for modeling nonlocal eddy viscosities for momentum transport and show an example for turbulent channel flow.

In Chapter 5, we develop adjoint MFM for targeted computation of nonlocal closure operators.

The main contribution of this chapter is a method for efficiently computing the nonlocal closure operator using one DNS simulation per desired location, rather than a brute-force approach which requires as many DNSs as the number of degrees of freedom in the averaged space. We show validation of adjoint MFM for computing the nonlocal eddy viscosity at a specific wall-normal location, which describes the dependence of the Reynolds stresses at a given location on mean the velocity gradient at all wall-normal locations, in turbulent channel flow at a Reynolds number of $\mathrm{Re}_\tau = 180$.

In Chapter 6, we extend adjoint MFM to two-dimensions to measure the streamwise and wall-normal nonlocal eddy viscosity at select near-wall locations in turbulent channel flow at $\mathrm{Re}_\tau = 180$. The main findings of this chapter are: 1) The streamwise nonlocality lengthscale is much longer than the wall-normal nonlocality lengthscale and increases with distance from the wall. While this is qualitatively expected due to the increase in mean streamwise velocity with distance from the wall, we quantify this effect. 2) The mean velocity gradient at a given point influences the shear component of the Reynolds stress farther downstream than the shear component of the Reynolds stress at the same point is influenced by the mean velocity gradient upstream. 3) We examine the anisotropy of the eddy viscosity by comparing various components of the eddy viscosity kernel. The D_{2111} component of the eddy viscosity is larger in magnitude than D_{2121}, indicating larger sensitivity of the shear component of the Reynolds stress to the streamwise gradient, $\partial U_1/\partial x_1$, than the wall-normal gradient, $\partial U_1/\partial x_2$. We hypothesize that the larger sensitivity to $\partial U_1/\partial x_1$ remains in wall-bounded flows where $\partial U_1/\partial x_1$ is active, e.g., in spatially-developing boundary layers or separated flows. 4) We also examine the anisotropy by comparing the eddy viscosity kernel for various components of the Reynolds stress tensor. The normal components of the Reynolds stresses have much longer streamwise nonlocality lengthscales than the shear component of the Reynolds stresses. We discuss the implications of these findings for modeling.

In Chapter 7, we conclude and discuss concurrent and future work.

Chapter 2

Analytical Reynolds stress model development

In this chapter, we adopt a modeling framework based on the Reynolds stress transport equation. As discussed in Chapter 1, Reynolds stress transport models provide closures for the unclosed terms in the Reynolds stress transport equation and can include nonlocal and anisotropic effects. We particularly adopt this framework because we are motivated by the results of Park et al. (2022a), which showed that while an anisotropic but local eddy viscosity can improve the prediction of the skin friction coefficient for a canonical separated boundary layer as shown in Figure 1.1, there is some remaining error especially in the region near flow reattachment due to nonlocal effects. Moreover, even in the absence of nonlocal effects, analytical equations for an anisotropic but local eddy viscosity would involve 81 coefficients corresponding to each direction of the fourth-order anisotropic eddy viscosity tensor. Whereas, a Reynolds stress transport model involves six equations corresponding to each direction of the Reynolds stress tensor and naturally allows incorporation of anisotropic and nonlocal effects.

Before we detail an attempt at model development in Section 2.2, we first document simple canonical flows that can be used for determining model coefficients in Section 2.1. These flows can be used for a variety of RANS models, not just Reynolds stress transport models, and are chosen to build in complexity. For example, we begin with decaying homogeneous isotropic turbulence, in which only the dissipation term is active, and build up to turbulent channel flow, in which near-wall terms are active. We present recent updates from the literature for all flows and show new flows, e.g., forced homogeneous turbulence, that have not been previously used in this context.

Reference	Type	Re_λ	n
Batchelor and Proudman (1956)	Theoretical, $\sim k_s^4$	High	10/7
Saffman (1967)	Theoretical, $\sim k_s^2$	High	6/5
Comte-Bellot and Corrsin (1971)	Experiment, passive grid	$60-70$	1.25
Mohamed and La Rue (1990)	Experiment, passive grid	$28-44$	1.3
Mydlarski and Warhaft (1996)	Experiment, active grid	$50-473$	1.21
Krogstad and Davidson (2011)	Experiment, passive grid	$70-90$	$1.1-1.27$
Thormann and Meneveau (2014)	Experiment, active grid	$200-300$	$1-1.3$
Sinhuber et al. (2015)	Experiment, passive grid	$\mathrm{Re_M} \approx 10^4-10^6$	1.18 ± 0.02

Table 2.1: Literature review of decaying HIT data and the power law of decay, n. Re_λ is a Taylor microscale Reynolds number and Re_M is a grid mesh Reynolds number.

2.1 Canonical flows for determining coefficients

2.1.1 Decaying homogeneous isotropic turbulence

In decaying homogeneous isotropic turbulence (HIT), the turbulence is generated via a grid and advected downstream with a uniform velocity. Because there are no mean velocity gradients (and no production), the turbulence decays, and only the dissipation term is active.

In a frame moving with the uniform velocity, the turbulent kinetic energy, $k \equiv \overline{u_i' u_i'}/2$, decays according to a power law:

$$k(t) = k_0 \left(\frac{t}{t_0} \right)^{-n}, \tag{2.1}$$

where t_0 is a reference time and k_0 is the turbulent kinetic energy at that time. Theoretical results for the power law exponent, n, are based on the low wavenumber asymptote of the energy spectrum. Batchelor and Proudman (1956) postulated that this asymptote was of the form $E(k_s) = Ak_s^m$, where k_s is the wavenumber and the subscript s is added to distinguish it from the turbulent kinetic energy k, and $m = 4$, which leads to $n = 10/7$. Saffman (1967) postulated that $m = 2$, which leads to $n = 6/5$.

Table 2.1 shows a literature review of data for decaying HIT. Reanalysis of older experimental data (Skrbek and Stalp (2000)) and recent high Reynolds number experiments (Sinhuber et al. (2015)) suggest closer agreement with the $n = 6/5$ of Saffman (1967).

2.1.2 Forced homogeneous turbulence

In forced homogeneous turbulence (HT), a linear forcing is added to sustain the turbulence but there are no mean velocity gradients. The forcing may be anisotropic, and hence, in forced HT only the return to isotropy and dissipation terms are active. Following Lundgren (2003) and Rosales and

Meneveau (2005), we consider the incompressible Navier–Stokes equations:

$$\frac{\partial u_i}{\partial t} + u_j \frac{\partial u_i}{\partial x_j} = -\frac{1}{\rho}\frac{\partial p}{\partial x_i} + \nu \frac{\partial^2 u_i}{\partial x_j \partial x_j}. \tag{2.2}$$

Substitution of the Reynolds decomposition, $u_i = U_i + u_i'$, into (2.2) and subtracting the RANS equation for the mean velocity field (Equation (1.3a)) leads to

$$\frac{\partial u_i'}{\partial t} + (U_j + u_j')\frac{\partial u_i'}{\partial x_j} = -\frac{1}{\rho}\frac{\partial p'}{\partial x_i} + \nu \frac{\partial^2 u_i'}{\partial x_j \partial x_j} + \frac{\partial}{\partial x_j}\overline{u_j' u_i'} - u_j' \frac{\partial U_i}{\partial x_j}. \tag{2.3}$$

The last term in (2.3) is related to production of turbulent kinetic energy in the Reynolds stress transport equation and suggests a linear forcing to mimic the effect of mean shear on the turbulent flow:

$$\frac{\partial u_i'}{\partial t} + u_j' \frac{\partial u_i'}{\partial x_j} = -\frac{1}{\rho}\frac{\partial p'}{\partial x_i} + \nu \frac{\partial^2 u_i'}{\partial x_j \partial x_j} + A_{ji} u_j'. \tag{2.4}$$

Lundgren (2003) and Rosales and Meneveau (2005) used an isotropic forcing

$$A_{ji} = \begin{bmatrix} A & 0 & 0 \\ 0 & A & 0 \\ 0 & 0 & A \end{bmatrix} \tag{2.5}$$

for forced homogeneous isotropic turbulence, where A is an arbitrary constant and related to the turbulent Reynolds number of the simulation (Carroll and Blanquart (2013)).

Dhandapani et al. (2019) and Rah et al. (2018) used anisotropic forcing to mimic the presence of the mean velocity gradient in homogeneous shear flow and at the centerline of an axisymmetric jet, respectively. Dhandapani et al. (2019) considered a forcing of the form:

$$A_{ji} = \begin{bmatrix} 0 & B_{\mathrm{NHST}} & 0 \\ 0 & 0 & 0 \\ 0 & 0 & 0 \end{bmatrix}, \tag{2.6}$$

where B_{NHST} is a constant for simulations of nearly homogeneous shear turbulence (NHST). Rah et al. (2018) considered forcing of the form:

$$A_{ji} = \begin{bmatrix} B_{\mathrm{RJ}} & 0 & 0 \\ 0 & \frac{1}{2}B_{\mathrm{RJ}} & 0 \\ 0 & 0 & \frac{1}{2}B_{\mathrm{RJ}} \end{bmatrix}, \tag{2.7}$$

where B_{RJ} is a constant related to the centerline velocity of a round jet (RJ).

Previous models (Sarkar and Speziale (1990)) have used experimental data (Choi and Lumley

Reference	Re_λ	B	τ_{11}/k	τ_{22}/k	τ_{33}/k	τ_{21}/k
Dhandapani et al. (2019)	128	37.1	1.02	0.57	0.41	0.39
Rah et al. (2018)	255	1.22	0.98	0.51	0.51	0

Table 2.2: Forced HT simulation data from Dhandapani et al. (2019) and Rah et al. (2018), where $\tau_{ij} \equiv \overline{u_i' u_j'}$ is normalized by the turbulent kinetic energy, k.

(2001); Le Penven et al. (1985)) for decaying anisotropic turbulence for determining coefficients of the return to isotropy and dissipation terms, but forced HT has not been used in this context previously. For model comparison, the analytically known forcing is also added to the model equations. To derive the form of the added forcing, similar to derivation of the Reynolds stress transport equation, consider (2.4) multiplied by u_j' and summation of the same equation written for u_j' multiplied by u_i':

$$u_j' \frac{\partial u_i'}{\partial t} + u_i' \frac{\partial u_j'}{\partial t} + \cdots = \cdots + A_{ki} u_k' u_j' + A_{kj} u_k' u_i'. \tag{2.8}$$

Averaging leads to

$$\frac{\partial \overline{u_i' u_j'}}{\partial t} + \cdots = \cdots + A_{ki} \overline{u_k' u_j'} + A_{kj} \overline{u_k' u_i'} \tag{2.9}$$

and shows the forcing term, $A_{ki}\overline{u_k' u_j'} + A_{kj}\overline{u_k' u_i'}$, that should be added to the Reynolds stress model for comparison with forced HT data. At steady state, the forcing balances the return to isotropy and dissipation terms. We show the highest Reynolds number data from Dhandapani et al. (2019) and Rah et al. (2018) in Table 2.2, and Section 2.3.2 shows usage of this data for determining dissipation and return to isotropy coefficients.

2.1.3 Homogeneous shear flow

In homogeneous shear flow, the imposed mean velocity gradient is constant. In a model, the terms involving the mean velocity gradient, return to isotropy, and dissipation are active, but because the flow is homogeneous, the turbulent diffusion terms are inactive. Homogeneous shear flow can be created in wind tunnel experiments in which the mean velocity gradient is imposed as $\mathcal{S} = \mathrm{d}U_1/\mathrm{d}x_2$, and there is no mean flow in the x_2 and x_3 directions. The Reynolds stresses grow exponentially with downstream distance (or equivalently, in time in a frame moving with mean velocity U_c). However, the flow reaches a self-similar state such that the Reynolds stresses normalized by the kinetic energy are approximately constant (Champagne et al. (1970)). Similarly, the turbulence timescale, $\tau \equiv k/\varepsilon$, and the ratio of turbulent production to dissipation, $\mathcal{P}/\varepsilon$, is also approximately constant. The equation for the turbulent kinetic energy is:

$$\frac{\mathrm{d}k}{\mathrm{d}t} = \mathcal{P} - \varepsilon, \tag{2.10}$$

Reference	Type	$\mathrm{Re}_{\lambda_{11}}$	τ_{11}/k	τ_{22}/k	τ_{33}/k	τ_{21}/k	$\mathcal{S}\tau$	$\mathcal{P}/\varepsilon$
Champagne et al. (1970)	Experiment	180	0.96	0.50	0.56	-0.35	6.1	1.7
Harris et al. (1977)	Experiment	300	1.00	0.40	0.60	-0.30	5.5	-
Tavoularis and Corrsin (1981)	Experiment	205	1.05	0.37	0.58	-0.28	6.5	1.8
Tavoularis and Corrsin (1981)	Experiment	238	1.07	0.37	0.56	-0.28	6.1	1.7
Rogallo (1981)	DNS	76	1.02	0.37	0.61	-0.30	-	-
Rogallo (1981)	DNS	104	0.97	0.42	0.61	-0.31	-	-
Rogers and Moin (1987)	DNS	72.6	1.06	0.32	0.62	-0.33	4.3	1.4
De Souza et al. (1995)	Experiment	1120	1.09	0.41	0.51	-0.24	5.9	1.4
Isaza and Collins (2009)	DNS	-	0.97	0.39	0.63	-0.33	5.2	1.6

Table 2.3: Literature review of homogeneous shear flow. The Reynolds stresses, $\tau_{ij} \equiv \overline{u_i' u_j'}$, normalized by the turbulent kinetic energy, k, are approximately constant for homogeneous shear flow.

which can be rewritten as:

$$\frac{\mathrm{d}k}{\mathrm{d}t} = \frac{k}{\tau}\left(\frac{\mathcal{P}}{\varepsilon} - 1\right), \tag{2.11}$$

which shows that the turbulent kinetic energy grows exponentially as:

$$k(t) = k_0 \exp\left[\frac{t}{\tau}\left(\frac{\mathcal{P}}{\varepsilon} - 1\right)\right]. \tag{2.12}$$

Table 2.3 shows a literature review of homogeneous shear flow data.

2.1.4 Channel flow

In turbulent channel flow, a mean pressure gradient drives flow between two parallel walls. The mean streamwise velocity U_1 is nonzero and varies only in the wall-normal direction, x_2, such that $\mathrm{d}U_1/\mathrm{d}x_2$ is the only component of the mean velocity gradient that is active. All terms in the Reynolds stress transport equation, including terms with the molecular viscosity are active.

In fully developed turbulent channel flow, there is an inner layer near the wall in which viscous stresses dominate and an outer layer in which the viscosity is negligible. In the inner layer, the characteristic velocity scale is the friction velocity, $u_\tau \equiv \sqrt{\tau_\mathrm{w}/\rho}$, where τ_w is the wall shear stress given by $\tau_\mathrm{w} \equiv \rho\nu \mathrm{d}U_1/\mathrm{d}x_2|_{x_2=0}$. The characteristic lengthscale is the viscous lengthscale, $\delta_\nu \equiv \nu/u_\tau$. The distance from the wall is characterized by wall units, $y^+ = x_2/\delta_\nu$. The friction Reynolds number is defined as $\mathrm{Re}_\tau \equiv u_\tau \delta/\nu = \delta/\delta_\nu$, where δ is the channel half-height.

Log layer

At high Reynolds number, in the inner layer ($y/\delta \ll 1$) but far away from the wall ($y^+ \gg 1$) such that viscous effects are negligible, the mean velocity profile is known to follow the log law (von Kármán (1930)):

$$U^+ = \frac{1}{\kappa}\ln y^+ + B, \tag{2.13}$$

Reference	Type	Re_τ	κ
Mckeon et al. (2004)	Experiment, Pipe	$310 \times 10^3 \leq \mathrm{Re_D} \leq 13.6 \times 10^6$	0.421 ± 0.002
Marusic et al. (2013)	Analysis of experiments	$2 \times 10^4 < \mathrm{Re}_\tau < 6 \times 10^5$	0.39 ± 0.02
Lee and Moser (2015)	DNS, Channel	5186	0.384 ± 0.004
Abe and Antonia (2016)	Analysis of DNS	Extrapolation to high Re_τ	0.394
Luchini (2017)	Analysis of DNS	Extrapolation to high Re_τ	0.392
Spalart and Abe (2021)	Analysis of DNS	Extrapolation to large Re_τ	0.395 ± 0.001

Table 2.4: Literature review of the von Kàrmàn constant, κ, for the log law in Equation (2.13).

where κ is the von Kàrmàn constant, B is a constant, and $U^+ = U_1/u_\tau$.

Textbooks (Pope (2000)) have generally quoted values of $\kappa = 0.41$ and $B = 5.2$. However, more recent analysis and high Reynolds number data suggests that κ is between 0.39 and 0.40 (Spalart and Abe (2021)). Table 2.4 shows a sampling of recent log layer data and analyses.

Models generally assume a constant Reynolds stress region in the log layer. However, this assumption is not supported by the data, particularly for $\overline{u_1'^+ u_1'^+}$ and $\overline{u_3'^+ u_3'^+}$, where $\overline{u_i'^+ u_j'^+} \equiv \overline{u_i' u_j'}/u_\tau^2$, as shown by Figure 2.1.

At high Reynolds number, the shear component of the Reynolds stress, $-\overline{u_1'^+ u_2'^+}$, theoretically plateaus to 1 (Townsend (1976); Pope (2000)), which is confirmed by analysis of data (Spalart and Abe (2021)). The wall-normal component of the Reynolds stress, $\overline{u_2'^+ u_2'^+}$, also appears to plateau, which Spalart and Abe (2021) and Chen et al. (2018) extrapolated out to 1.33 and 1.35, respectively, in the high Reynolds number limit. However, the other Reynolds stresses, $\overline{u_1'^+ u_1'^+}$ and $\overline{u_3'^+ u_3'^+}$, do not appear to plateau as shown in Figure 2.1. Theories exist for the high Reynolds number behavior of $\overline{u_1'^+ u_1'^+}$ and $\overline{u_3'^+ u_3'^+}$, for example Townsend's attached eddy hypothesis (Townsend (1976)) which predicts:

$$\overline{u_1'^+ u_1'^+} = A_1 - B_1 \log(y/\delta), \tag{2.14a}$$

$$\overline{u_2'^+ u_2'^+} = A_2, \tag{2.14b}$$

$$\overline{u_3'^+ u_3'^+} = A_3 - B_3 \log(y/\delta), \tag{2.14c}$$

and more recent asymptotic analysis by Monkewitz (2022) and Chen et al. (2018); however, the behavior of $\overline{u_1'^+ u_1'^+}$ and $\overline{u_3'^+ u_3'^+}$ is still inconclusive. Regardless, current RANS models predict plateaus for all Reynolds stress components in the log layer (Spalart and Abe (2021)), which is not supported by the data.

Reynolds stress scaling in the near-wall region

Due to the no-slip and no-penetration boundary conditions at the wall, the Reynolds stresses have analytically expected scalings (Pope (2000); Manceau and Hanjalić (2002)), which we now rederive.

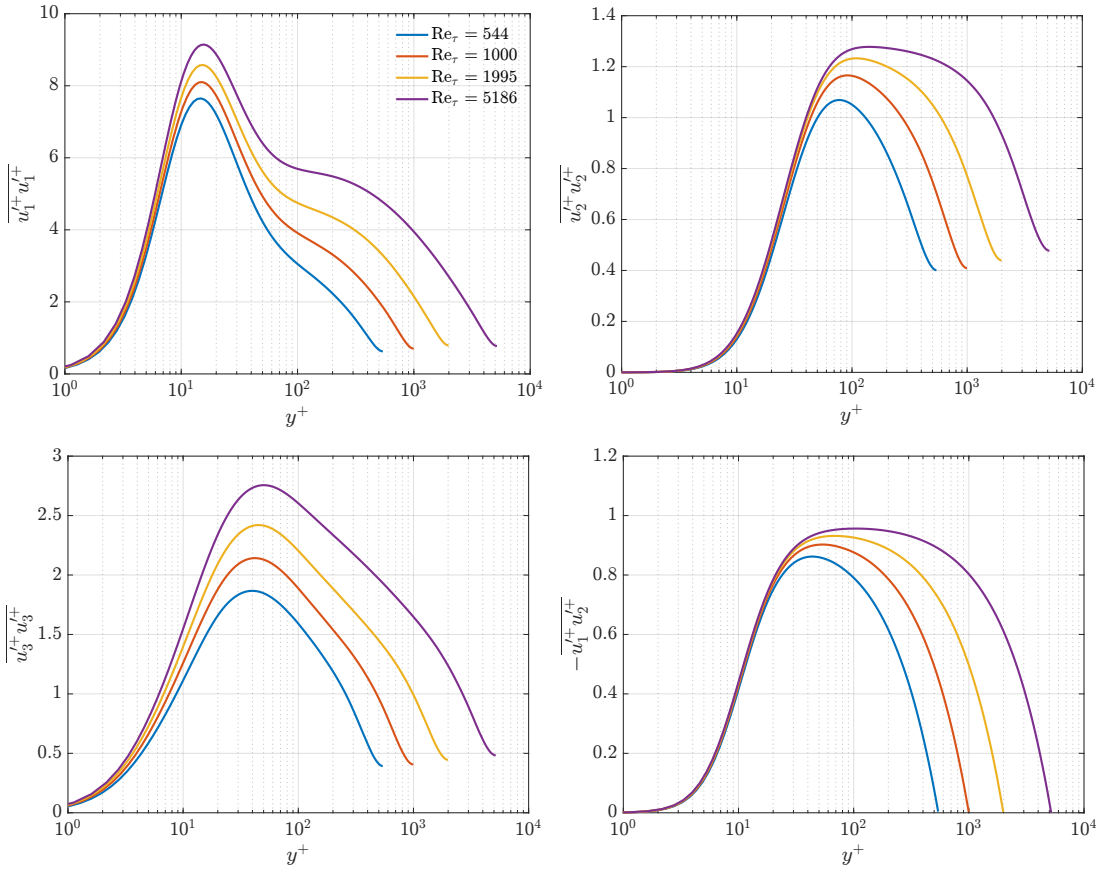

Figure 2.1: Reynolds stresses for turbulent channel flow up to $\mathrm{Re}_\tau = 5186$ using the DNS data of Lee and Moser (2015).

For a fixed x_1, x_3, and t, and small wall-distance y, the fluctuating velocity components can be Taylor series expanded:

$$u_1' = a_1 + b_1 y + c_1 y^2 + \dots \tag{2.15a}$$
$$u_2' = a_2 + b_2 y + c_2 y^2 + \dots \tag{2.15b}$$
$$u_3' = a_3 + b_3 y + c_3 y^2 + \dots \tag{2.15c}$$

Due to the no-slip and no-penetration boundary conditions, $u_1'(y=0) = u_2'(y=0) = u_3'(y=0)$, and thus $a_1 = a_2 = a_3 = 0$. Moreover, due to the continuity equation and no variation of the velocity fluctuations in the x_1 and x_3 directions at the wall, $\mathrm{d}u_2'/\mathrm{d}x_2(y=0) = 0$, and thus $b_2 = 0$:

$$u_1' = b_1 y + \dots \tag{2.16a}$$
$$u_2' = c_2 y^2 + \dots \tag{2.16b}$$
$$u_3' = b_3 y + \dots \tag{2.16c}$$

The leading-order scaling for various components of the Reynolds stress tensor can be formed by multiplying the expansions in (2.16) with each other and averaging:

$$\overline{u_1' u_1'} = \overline{b_1^2} y^2 + \dots \tag{2.17a}$$
$$\overline{u_2' u_2'} = \overline{c_2^2} y^4 + \dots \tag{2.17b}$$
$$\overline{u_3' u_3'} = \overline{b_3^2} y^2 + \dots \tag{2.17c}$$
$$\overline{u_1' u_2'} = \overline{b_1 c_2} y^3 + \dots \tag{2.17d}$$

Recent high Reynolds number DNS data from Lee and Moser (2015) confirms that these expected analytical scalings hold as shown in Figure 2.2. However, the coefficients $\overline{b_1^2}$, $\overline{c_2^2}$, etc. are Reynolds number dependent (Smits et al. (2021)).

Reynolds stress models do not currently obey these analytical scalings in the near-wall region. For example, the LRR model (Launder et al. (1975)) uses near-wall reflection terms to improve the near-wall behavior but misses the expected scaling for $\overline{u_2' u_2'}$ and $\overline{u_1' u_2'}$. More complex models, such as the elliptic relaxation model (Durbin (1993)), are able to capture the expected scaling for $\overline{u_2' u_2'}$ but miss the scaling for $\overline{u_1' u_2'}$. While the elliptic blending model (Manceau and Hanjalić (2002)), can capture the expected scaling for all components, they report that enforcing $\overline{u_1' u_2'} \sim y^4$ in the model performs better than enforcing the analytically expected $\overline{u_1' u_2'} \sim y^3$. While there is debate about whether a model needs to satisfy these analytically-expected scalings, as noted by Durbin and Reif (2011): "The solution to a Reynolds stress model should in principle be consistent with these [scalings]. However, in practice, it may be sufficient to ensure that $-\overline{u_1' u_2'}$ and $\overline{u_2' u_2'}$ are small compared to $\overline{u_1' u_1'}$ when $y^+ << 1$," we use them as a guide for model development in Section 2.4.

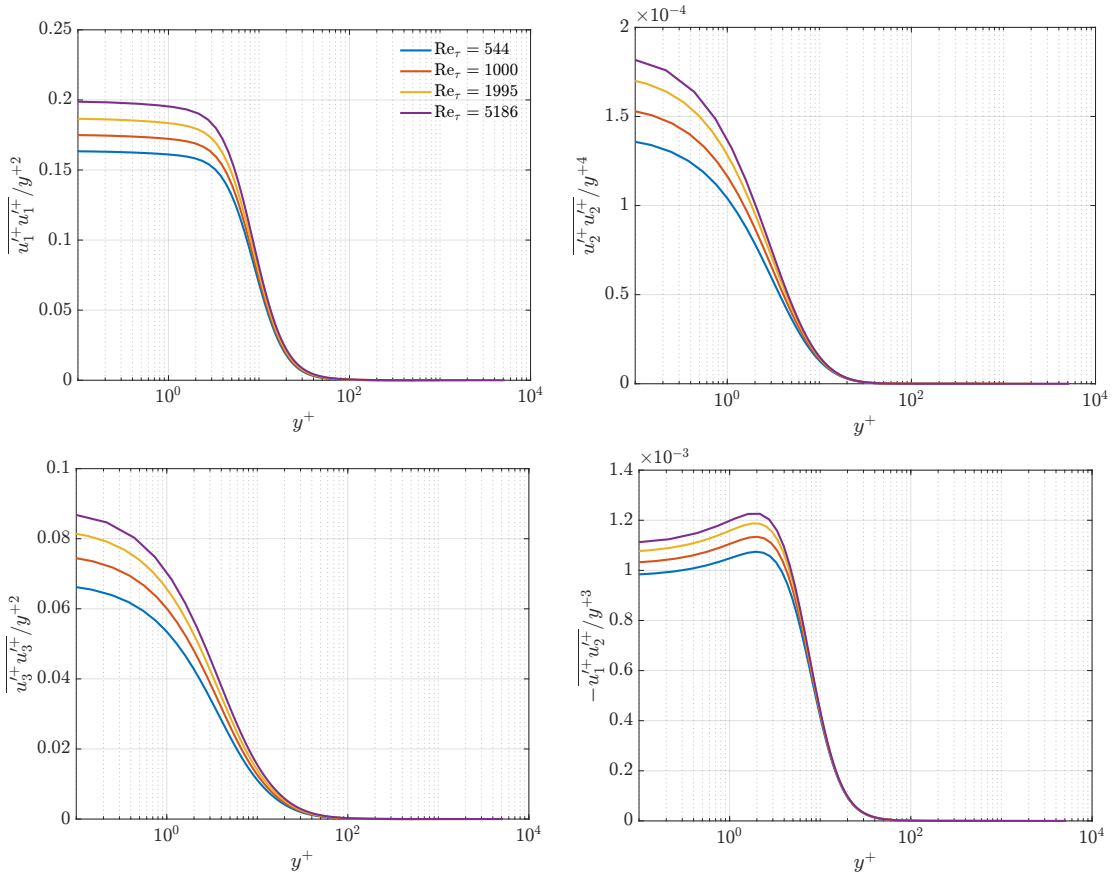

Figure 2.2: Near-wall scaling of Reynolds stress tensor components using the DNS data of Lee and Moser (2015).

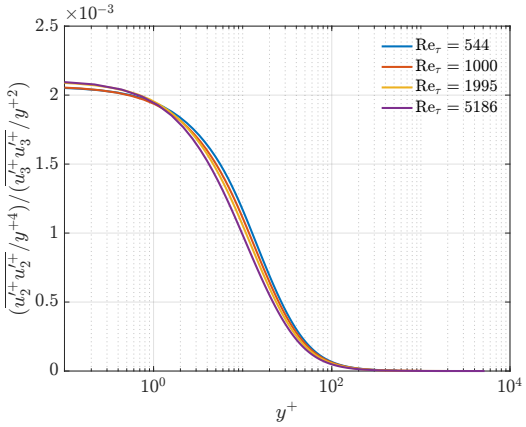

Figure 2.3: The ratio of $(\overline{u_2'^+ u_2'^+}/y^{+4})/(\overline{u_3'^+ u_3'^+}/y^{+2})$ is approximately constant near the wall. Plotted using the DNS data of Lee and Moser (2015).

We observe that while the coefficients for $\overline{u_2'u_2'}$ and $\overline{u_3'u_3'}$, $\overline{c_2^2}$ and $\overline{b_3^2}$ are Reynolds number dependent, their ratio is constant, $(\overline{u_2'^+ u_2'^+}/y^{+4})/(\overline{u_3'^+ u_3'^+}/y^{+2}) = 2.1 \times 10^{-3}$, as shown in Figure 2.3, which we will use for near-wall model development in Section 2.4.

2.2 Model framework

In general, a Reynolds stress model for $\tau_{ij} = \overline{u_i'u_j'}$ is of the form:

$$\frac{D}{Dt}\tau_{ij} = f\left(\tau_{kl}, \frac{\partial U_n}{\partial x_m}, \nu, (\varepsilon, \omega, \nu_T, L, \dots)\right) \tag{2.18a}$$

$$\frac{D}{Dt}(\varepsilon, \omega, \nu_T, L, \dots) = \text{RHS} \tag{2.18b}$$

where the right hand side of the model in (2.18a) may include the Reynolds stress tensor itself, mean velocity gradient tensor, molecular viscosity, and an auxiliary scale variable, e.g., $\varepsilon, \omega, \nu_T, L, \dots$, is needed for dimensional considerations. Correspondingly, this auxiliary variable has its own general transport equation in (2.18b).

Many models (Launder et al. (1975); Speziale et al. (1991)) use the dissipation scale ε as the auxiliary variable. In this work, we show an example model with a characteristic turbulence lengthscale L as the auxiliary variable because:

- L has a natural boundary condition on the wall ($L = 0$). Whereas, dissipation is finite on the wall and other variables, e.g., an inverse timescale ω, may be infinite on the wall.
- L is expected to smoothly diminish as the turbulence lengthscale decreases approaching the wall whereas the magnitude of dissipation increases near the wall.

- L also has a natural boundary condition on the wall for rough surfaces, e.g., $L = l$ on the wall for some finite roughness lengthscale, l.

However, due to the choice of L, care should be taken regarding the influence of L in laminar regions. As an example, consider a scenario in which a turbulent flow has relaminarized. The lengthscale in such regions is not necessarily zero. For example, in decaying HIT, the turbulence lengthscale grows as the turbulence decays because the small-scale features are dissipated more quickly than the large-scale features. After a long time, this lengthscale is nonzero. However, the value of the lengthscale in a laminar region should not influence the turbulent region, a criterion which we call the "laminar constraint."

One way to obey the laminar constraint is to formulate Equation (2.18b) for $k^\alpha L^\beta$ rather than L, where α and β are arbitrary powers. In laminar regions, $k = 0$, and thus the value of L has no influence. We show an example of starting from an equation for the simplest choice of $\alpha = \beta = 1$, i.e., kL, and deriving an equivalent equation for L. We show an example only with a diffusion term as the other model terms do not involve spatial derivatives of k or L and are thus more straightforward:

$$\frac{D\tau_{ij}}{Dt} = \cdots + \frac{\partial}{\partial x_m}\left(c_D D \frac{\partial \tau_{ij}}{\partial x_m}\right), \tag{2.19a}$$

$$\frac{DkL}{Dt} = \cdots + \frac{\partial}{\partial x_m}\left(c_D D \frac{\partial kL}{\partial x_m}\right), \tag{2.19b}$$

where c_D is a dimensionless coefficient and D is the viscosity, e.g., modeled by $D = \sqrt{k}L$. Manipulating the derivatives in (2.19b),

$$k\frac{DL}{Dt} + L\frac{Dk}{Dt} = \cdots + k\frac{\partial}{\partial x_m}\left(c_D D \frac{\partial L}{\partial x_m}\right) + 2c_D D \frac{\partial k}{\partial x_m}\frac{\partial L}{\partial x_m} + L\frac{\partial}{\partial x_m}\left(c_D D \frac{\partial k}{\partial x_m}\right). \tag{2.20}$$

An equation for k can be derived by taking the trace of Equation (2.19a) and using the definition $\tau_{kk} = 2k$. Subtraction of the k equation multiplied by L from Equation (2.20) leads to an equation for L:

$$\frac{DL}{Dt} = \cdots + \frac{\partial}{\partial x_m}\left(c_D D \frac{\partial L}{\partial x_m}\right) + 2c_D D \frac{1}{k}\frac{\partial k}{\partial x_m}\frac{\partial L}{\partial x_m}, \tag{2.21}$$

where the cross-diffusion term appears because the diffusion term is originally formulated for kL.

2.2.1 Baseline model form

We now show a model form (without the near-wall model, which will be discussed in Section 2.4), which we will use to demonstrate the procedure for determining coefficients in Section 2.3. This

model form is based on kL with the equivalent equation shown for L:

$$\frac{D\tau_{ij}}{Dt} = c_{fp}\left(\tau_{kj}\frac{\partial U_i}{\partial x_k} + \tau_{ki}\frac{\partial U_j}{\partial x_k}\right) - c_{fB}\tau_{kk}S_{ij} - c_{fT}\tau_{mn}\frac{\partial U_n}{\partial x_m}\delta_{ij} + c_{fW}\left(\tau_{ki}\frac{\partial U_k}{\partial x_j} + \tau_{kj}\frac{\partial U_k}{\partial x_i}\right) \tag{2.22a}$$

$$-\frac{c_{fR}}{T_h}\left(\tau_{ij} - \frac{1}{3}\tau_{kk}\delta_{ij}\right) - \frac{c_{f\varepsilon} - c_{sg}}{T_h}\tau_{ij} + \frac{\partial}{\partial x_m}\left(c_D D\frac{\partial \tau_{ij}}{\partial x_m}\right)$$

$$\frac{DL}{Dt} = \frac{c_{sp}}{2}L\frac{\tau_{mn}}{\tau_{kk}}\frac{\partial U_n}{\partial x_m} + \frac{c_{sg}}{2}\sqrt{k} + \frac{\partial}{\partial x_m}\left(c_D D\frac{\partial L}{\partial x_m}\right) + 2c_D D\frac{1}{k}\frac{\partial k}{\partial x_m}\frac{\partial L}{\partial x_m} \tag{2.22b}$$

where $S_{ij} = \frac{1}{2}\left(\frac{\partial U_i}{\partial x_j} + \frac{\partial U_j}{\partial x_i}\right)$, $D = \sqrt{k}L$, and $T_h = L/\sqrt{k}$. The terms in the τ_{ij} equation in (2.22a) are similar to those of the LRR model (Launder et al. (1975)). Modifications to the baseline model form are discussed in 2.5.

In comparison with the exact Reynolds stress transport equation, in the model in (2.22a), the first four terms (c_{fp}, c_{fB}, c_{fT}, and c_{fW} terms) represent the combination of closed production term and terms modeling the rapid pressure–strain (Launder et al. (1975)). The next term (c_{fR} term) is a linear return to isotropy term (Rotta (1951)) modeling the slow pressure–strain. The next to last term ($c_{f\varepsilon}$ term) is an anisotropic decay term modeling dissipation. The last term (c_D term) is a diffusion term modeling turbulent transport.

In the L equation in (2.22b), the first term (c_{sp} term) is a production-like term. The second term (c_{sg} term) is a growth term, such that in decaying HIT and in the absence of all other terms in the L equation, the turbulence lengthscale grows. The third term and fourth terms (c_D terms) are diffusion and cross-diffusion terms stemming from a diffusion term for kL.

Additional modifications, such as nonlinear return to isotropy terms (Sarkar and Speziale (1990)), etc., are discussed in the following sections and in Appendix A. In Appendix A.1, we also consider a model form that splits τ_{ij} into $\tau_{ij} = F_{ij}L^2$: Through specification of boundary conditions on F_{ij} and a model form that ensures linear growth of $L \sim y$ from the wall, we satisfy the analytical scalings for the Reynolds stresses in the near-wall region shown in Section 2.1.4 for all components except τ_{22}. For example, consider the Taylor series expansion:

$$F_{ij} = a_{ij} + b_{ij}y + c_{ij}y^2 + \ldots \tag{2.23}$$

Specifying a Dirichlet boundary condition, for example $F_{21}(y = 0) = 0$, leads to $F_{21} = b_{21}y$, and when combined with $L \sim y$, leads to the desired scaling $\tau_{21} = F_{21}L^2 \sim y^3$. Specifying a Neumann boundary condition, for example $\partial F_{11}/\partial y(y = 0) = 0$, leads to $F_{11} = a_{11}$, and the desired scaling $\tau_{11} = F_{11}L^2 \sim y^2$. The $F_{ij}L^2$ model form has implications away from the wall as well, especially for the diffusion term, which is discussed in Appendix A.1. Ultimately, the challenge of requiring $L \sim y$ throughout both the viscous sublayer and log layer leads to complications in capturing the log layer

behavior in the mean streamwise velocity as shown in Appendix A.1.

2.3 Determining model coefficients

In this section, we demonstrate a procedure for determining model coefficients using the experimental and DNS data from Section 2.1. We use the baseline kL Reynolds stress model form shown in Equations (2.22a) and (2.22b) as an example. We begin with the simplest canonical flow, decaying HIT, and build in complexity.

2.3.1 Decaying homogeneous isotropic turbulence

In decaying HIT, in which there are no mean velocity gradients and no diffusion, the model equations are:

$$\frac{\mathrm{d}k}{\mathrm{d}t} = -(c_{f\varepsilon} - c_{sg})\frac{k^{3/2}}{L}, \tag{2.24a}$$

$$\frac{\mathrm{d}L}{\mathrm{d}t} = \frac{c_{sg}}{2}k^{1/2}, \tag{2.24b}$$

where the equation for the turbulent kinetic energy k comes from taking the trace of Equation (2.22a). Because the flow is isotropic, $\tau_{12} = \tau_{23} = \tau_{13} = 0$ and $\tau_{11} = \tau_{22} = \tau_{33} = 2k/3$. For the turbulent kinetic energy to decay, $c_{f\varepsilon} - c_{sg} > 0$, and for the turbulence lengthscale to grow, $c_{sg} > 0$.

Substitution of the power law for k in Equation (2.1) into (2.24b) and integrating with respect to time leads to

$$L = \frac{c_{sg}}{2}k_0^{1/2}t_0^{n/2}\left(\frac{2}{2-n}t^{-n/2+1}\right) + L_0. \tag{2.25}$$

Substitution of this expression for L (ignoring the arbitrary initial condition, L_0) and the power law for k into Equation (2.24a) leads to a constraint on the coefficients:

$$-c_{sg}\frac{n}{2-n} + c_{f\varepsilon} - c_{sg} = 0. \tag{2.26}$$

As discussed in Section 2.1.1, we use $n = 6/5$ based on Saffman's theoretical analysis (Saffman (1967)) and recent high Reynolds number experiments (Sinhuber et al. (2015)).

2.3.2 Forced homogeneous turbulence

In forced HT, there is an assumption that the added linear forcing activates only the slow pressure–strain part of the model, i.e., return to isotropy terms, and that the rapid pressure–strain part of the model, which depends on the mean velocity gradient, is inactive. The model equation is:

$$\frac{\mathrm{d}\tau_{ij}}{\mathrm{d}t} = -\frac{c_{fR}}{T_h}\left(\tau_{ij} - \frac{1}{3}\tau_{kk}\delta_{ij}\right) - \frac{c_{f\varepsilon} - c_{sg}}{T_h}\tau_{ij} + A_{ki}\tau_{kj} + A_{kj}\tau_{ki}, \tag{2.27}$$

where $T_h = L/\sqrt{k}$. In simulations, the turbulence lengthscale is bounded by the computational domain size, and thus rather than examine the equation for L, L (and correspondingly T_h) will be treated as a free parameter in our process for determining coefficients. The coefficients c_{fR}, $c_{f\varepsilon}$, and c_{sg} are to be determined in conjunction with the constraint from decaying HIT in Equation (2.26).

Isotropic forcing

With isotropic forcing, $A_{ji} = A\delta_{ji}$. The model equation is:

$$\frac{\mathrm{d}k}{\mathrm{d}t} = -\frac{c_{f\varepsilon} - c_{sg}}{T_h}k + 2Ak. \tag{2.28}$$

The true kinetic energy balance is (Rosales and Meneveau (2005); Carroll and Blanquart (2013)):

$$\frac{\mathrm{d}k}{\mathrm{d}t} = -\varepsilon + 2Ak, \tag{2.29}$$

and at steady state, the dissipation balances the added forcing. The homogeneous time scale T_h is a free parameter. If we choose to define $L \equiv c_L k^{3/2}/\varepsilon$ with $c_L = 1$, and thus $T_h = L/\sqrt{k} = k/\varepsilon$, then at steady state:

$$T_h = \frac{k}{\varepsilon} = \frac{1}{2A}. \tag{2.30}$$

Substitution of (2.30) into Equation (2.28) at steady state leads to

$$c_{f\varepsilon} - c_{sg} = 1, \tag{2.31}$$

and in combination with the decaying HIT constraint on the coefficients in (2.26),

$$c_{sg} = \frac{2-n}{n}, \tag{2.32a}$$

$$c_{f\varepsilon} = \frac{2-n}{n} + 1. \tag{2.32b}$$

Based on Saffman's $n = 6/5$ (Saffman (1967)),

$$c_{sg} = 2/3, \tag{2.33a}$$

$$c_{f\varepsilon} = 5/3. \tag{2.33b}$$

Anisotropic forcing

For the nearly homogeneous shear turbulence forcing used by Dhandapani et al. (2019) and shown in Equation (2.6), the steady-state model equations are:

$$0 = -\frac{c_{fR}}{T_h}\left(\tau_{11} - \frac{1}{3}\tau_{kk}\right) - \frac{c_{f\varepsilon} - c_{sg}}{T_h}\tau_{11} + 2B_{\mathrm{NHST}}\tau_{21}, \tag{2.34a}$$

$$0 = -\frac{c_{fR}}{T_h}\left(\tau_{22} - \frac{1}{3}\tau_{kk}\right) - \frac{c_{f\varepsilon} - c_{sg}}{T_h}\tau_{22}, \tag{2.34b}$$

$$0 = -\frac{c_{fR}}{T_h}\left(\tau_{33} - \frac{1}{3}\tau_{kk}\right) - \frac{c_{f\varepsilon} - c_{sg}}{T_h}\tau_{33}, \tag{2.34c}$$

$$0 = -\frac{c_{fR}}{T_h}\tau_{21} - \frac{c_{f\varepsilon} - c_{sg}}{T_h}\tau_{21} + B\tau_{22}. \tag{2.34d}$$

The return to isotropy coefficient, c_{fR}, is to be determined and T_h is a free parameter dependent on the simulation domain size.

In this case, there are more equations than unknown coefficients, and we use both an *a priori* and *a posteriori* procedure for choosing c_{fR}. In the *a priori* procedure, the data for τ_{ij}/k is specified from literature, and we solve for the coefficient. If the values for the coefficient are relatively close regardless of the equation(s) being used, then that indicates a good choice of model form. In the *a posteriori* procedure, the coefficient is specified and we compare the model output, τ_{ij}/k, with the data from the literature. We then vary the coefficient and examine the model output to study the sensitivity of the model to the coefficient. Because there is some uncertainty in the data, and hence some uncertainty in the coefficient, we want to ensure that the model form is not overly sensitive to the coefficient. The *a priori* procedure is used for examining the model form and getting an estimate of the value of the coefficient. The *a posteriori* procedure is used for examining the error in the model output and the sensitivity to the coefficient. We demonstrate the *a priori* and *a posteriori* procedure with a linear return isotropy term.

The *a priori* analysis for the linear return to isotropy term is shown in Table 2.5. For example, using only the τ_{22} equation in (2.34b), and specifying τ_{22}/k using the data from Table 2.2 to solve for c_{fR} leads to:

$$c_{fR} = -\frac{(c_{f\varepsilon} - c_{sg})\frac{\tau_{22}}{k}}{\frac{\tau_{22}}{k} - \frac{2}{3}}, \tag{2.35}$$

where $c_{f\varepsilon} - c_{sg} = 1$ from Equation (2.31). Table 2.5 shows the result of using other equations. Some equations, e.g., for τ_{22} or τ_{33}, result in c_{fR} directly, and an additional equation, e.g., for τ_{11} or τ_{21}, can be used to solve for T_h, which we do not show. We also show inclusion of an equation for the turbulent kinetic energy, k, formed by taking the sum of Equations (2.34a)-(2.34c):

$$0 = -\frac{(c_{f\varepsilon} - c_{sg})}{T_h}2k + 2B_{\mathrm{NHST}}\tau_{21}. \tag{2.36}$$

Equation(s) ((2.34a)-(2.34d), (2.36))	c_{fR}	T_h
τ_{22}	6.7	-
τ_{33}	1.8	-
τ_{11}, τ_{21}	2.8	0.9
k, τ_{11}	3.1	0.95
k, τ_{21}	3.0	0.95

Table 2.5: Example of *a priori* analysis for determining the return to isotropy coefficient c_{fR} using the anisotropic forced HT data of Dhandapani et al. (2019). Some equations, e.g., for τ_{22} or τ_{33}, result in c_{fR} directly, and an additional equation, e.g., for τ_{11} or τ_{21}, can be used to solve for T_h, which we do not show.

Table 2.5 shows a wide range in the coefficient c_{fR} depending on which equation is used. For example, to achieve zero error in τ_{22}/k would require a coefficient of $c_{fR} = 6.7$; whereas, to achieve zero error in τ_{33}/k would require a coefficient of $c_{fR} = 1.8$. This gap indicates a poor model form as drawbacks of the linear return to isotropy model are widely known in literature (Pope (2000)). A value of $c_{fR} = 3$ is reasonable as it lies in between the extremes in c_{fR} and is based on a combination of equations through the equation for k and τ_{21} as shown in Table 2.5.

For the round jet forcing used by Rah et al. (2018) and shown in Equation 2.7, the steady-state model equations are:

$$0 = -\frac{c_{fR}}{T_h}\left(\tau_{11} - \frac{1}{3}\tau_{kk}\right) - \frac{(c_{f\varepsilon} - c_{sg})}{T_h}\tau_{11} + 2B_{\mathrm{RJ}}\tau_{11}, \tag{2.37a}$$

$$0 = -\frac{c_{fR}}{T_h}\left(\tau_{22} - \frac{1}{3}\tau_{kk}\right) - \frac{(c_{f\varepsilon} - c_{sg})}{T_h}\tau_{22} + B_{\mathrm{RJ}}\tau_{22}, \tag{2.37b}$$

where the τ_{33} equation is identical to the τ_{22} equation and the τ_{21} equation gives $\tau_{21} = 0$. Solving for the unknowns, c_{fR} and T_h, using the data in Table 2.2 leads to $c_{fR} = 1.1$ and $T_h = 0.55$.

Because of the discrepancy in c_{fR} in the *a priori* analysis, which indicates issues with the model form, in Appendix A.2 we consider a quadratic return to isotropy term of the form:

$$-\frac{c_{fNR}}{T_h k}\tau_{ik}\tau_{kj}, \tag{2.38}$$

and a traceless quadratic term:

$$-\frac{c'_{fNR}}{\sqrt{k}L}\left(\tau_{ik}\tau_{kj} - \frac{1}{3}\tau_{mn}\tau_{mn}\delta_{ij}\right). \tag{2.39}$$

With some rearrangement, the traceless quadratic return to isotropy term is identical to the return to isotropy form proposed by Sarkar and Speziale (1990). While the additional quadratic term can reduce the model errors when compared with the anisotropic forced HT data from Dhandapani et al. (2019) and Rah et al. (2018), after imposing a numerical robustness constraint on the coefficients for the baseline model form, the improvement in model errors is small as shown in Appendix A.2.

τ_{ij}/k	Model	Dhandapani et al. (2019)	Error
τ_{11}/k	1.0	0.99	1%
τ_{22}/k	0.50	0.58	14%
τ_{33}/k	0.50	0.43	16%
τ_{21}/k	0.35	0.38	7%

Table 2.6: Example of *a posteriori* analysis for the return to isotropy coefficient $c_{fR} = 3$ and comparison with the anisotropic forced HT data of Dhandapani et al. (2019).

τ_{ij}/k	Model	Rah et al. (2018)	Error
τ_{11}/k	0.78	0.98	20%
τ_{22}/k	0.61	0.51	20%

Table 2.7: Example of *a posteriori* analysis for the return to isotropy coefficient $c_{fR} = 3$ and comparison with the anisotropic forced HT data of Rah et al. (2018).

Thus, we proceed with the simpler linear return to isotropy term.

In the *a posteriori* analysis, the coefficient c_{fR} of the linear return to isotropy term is specified and the unknowns are τ_{ij}/k and T_h. There is an additional constraint based on the definition of the turbulent kinetic energy, $\tau_{kk} = 2k$. Table 2.6 shows the *a posteriori* analysis with $c_{fR} = 3$ as an example and comparison with the data of Dhandapani et al. (2019). Table 2.7 shows the comparison with the data of Rah et al. (2018). Table 2.8 shows *a posteriori* analysis varying c_{fR} in order to examine the sensitivity to c_{fR} and errors in comparison with Dhandapani et al. (2019). Similarly, Table 2.9 shows errors in comparison with Rah et al. (2018).

In comparison with the data from Dhandapani et al. (2019), the model error in τ_{11}/k is lowest around $c_{fR} = 3$. Increasing c_{fR}, decreases the error in τ_{22}/k but increases the errors in all other components. Decreasing c_{fR}, decreases the error in τ_{33}/k and τ_{21}/k but increases the error in the other components. However, the model is not very sensitive and choices of $c_{fR} = 2.5 \sim 3$ keep the errors reasonably within 20%. In comparison with the data from Rah et al. (2018), decreasing c_{fR}, decreases the error in all components until $c_{fR} = 1.1$ where the model error is zero. However, this choice of c_{fR} leads to large modeling errors in comparison with the Dhandapani et al. (2019) data.

The difficulty in finding a coefficient that performs well in both cases is due to model form error. The linear return to isotropy term is known to be insufficient for many flows (Pope (2000)), and we

c_{fR}	1.5	2	2.5	3	3.5	4	4.5	5
τ_{11}/k	0.21	0.12	0.05	0.01	0.03	0.06	0.08	0.10
τ_{22}/k	0.31	0.23	0.18	0.14	0.11	0.08	0.06	0.04
τ_{33}/k	0.07	0.03	0.11	0.16	0.21	0.24	0.27	0.29
τ_{21}/k	0.05	0.01	0.03	0.07	0.11	0.14	0.17	0.20

Table 2.8: Example of *a posteriori* analysis for the return to isotropy coefficient and varying the coefficient to examine the sensitivity. The table shows normalized errors in comparison with the anisotropic forced HT data of Dhandapani et al. (2019).

c_{fR}	1.5	2	2.5	3	3.5	4	4.5	5
τ_{11}/k	0.09	0.14	0.18	0.20	0.22	0.23	0.24	0.25
τ_{22}/k	0.08	0.14	0.17	0.20	0.21	0.22	0.23	0.24

Table 2.9: Example of *a posteriori* analysis for the return to isotropy coefficient and varying the coefficient to examine the sensitivity. The table shows normalized errors in comparison with the anisotropic forced HT data of Rah et al. (2018).

discuss nonlinear return to isotropy terms in Appendix A.2. Homan et al. (2023) used forced HT simulations and sampled a wider range of possible anisotropic forcing. They then discussed fitting coefficients for linear and nonlinear return to isotropy model forms using regression techniques.

2.3.3 Homogeneous shear flow

In homogeneous shear flow, an imposed mean velocity gradient $\mathcal{S} = \mathrm{d}U_1/\mathrm{d}x_2$ causes the turbulent kinetic energy to grow exponentially in time as shown in Equation (2.12). However, the flow reaches a regime in which the normalized Reynolds stresses, τ_{ij}/k, the nondimensionalized shear, $\mathcal{S}\tau$ (where $\tau \equiv k/\varepsilon$ is a turbulence timescale based on the kinetic energy and dissipation), and the ratio of production to dissipation, $\mathcal{P}/\varepsilon$, are constant. Correspondingly, in the model we have considered, the turbulence time scale, $T_h = L/\sqrt{k}$, should be a constant. Hence, if k grows exponentially as $k = k_0 \exp(2\beta t)$, then L should grow exponentially as $L = L_0 \exp(\beta t)$, where β is a function of τ and $\mathcal{P}/\varepsilon$ as shown in Equation (2.12). The model time scale, T_h, is related to the turbulence time scale, τ, with some constant c_{hL} that is unknown since L is not directly measurable, i.e., $L = c_{hL}k^{3/2}/\varepsilon$.

Using the above assumptions, the model equations are:

$$0 = \left(2c_{fp} - c_{fT} - \frac{c_{sp}}{2}\frac{\tau_{11}}{k}\right)\left(\frac{\tau_{21}}{k}\right)(c_{hL}S\tau) - c_{fR}\left(\frac{\tau_{11}}{k} - \frac{2}{3}\right) - c_{f\varepsilon}\left(\frac{\tau_{11}}{k}\right), \tag{2.40a}$$

$$0 = \left(-c_{fT} + 2c_{fW} - \frac{c_{sp}}{2}\frac{\tau_{22}}{k}\right)\left(\frac{\tau_{21}}{k}\right)(c_{hL}S\tau) - c_{fR}\left(\frac{\tau_{22}}{k} - \frac{2}{3}\right) - c_{f\varepsilon}\left(\frac{\tau_{22}}{k}\right), \tag{2.40b}$$

$$0 = \left(-c_{fT} - \frac{c_{sp}}{2}\frac{\tau_{33}}{k}\right)\left(\frac{\tau_{21}}{k}\right)(c_{hL}S\tau) - c_{fR}\left(\frac{\tau_{33}}{k} - \frac{2}{3}\right) - c_{f\varepsilon}\left(\frac{\tau_{33}}{k}\right), \tag{2.40c}$$

$$0 = \left[c_{fp}\left(\frac{\tau_{22}}{k}\right) - c_{fB} + c_{fW}\left(\frac{\tau_{11}}{k}\right) - \frac{c_{sp}}{2}\left(\frac{\tau_{21}}{k}\right)^2\right](c_{hL}S\tau) - (c_{fR} + c_{f\varepsilon})\left(\frac{\tau_{21}}{k}\right), \tag{2.40d}$$

$$0 = \left[\frac{1}{S\tau}\left(\frac{P}{\varepsilon} - 1\right) - \frac{c_{sp}}{2}\frac{\tau_{21}}{k}\right](c_{hL}S\tau) - c_{sg}, \tag{2.40e}$$

where the coefficients to be determined are c_{fp}, c_{fB}, c_{fT}, c_{fW}, c_{sp}, and c_{hL}.

For an *a priori* analysis of the coefficients, the values of the normalized Reynolds stresses are specified to be the average of the data shown in Table 2.3:

$$\frac{\tau_{11}}{k} = 1.02, \frac{\tau_{11}}{k} = 0.39, \frac{\tau_{33}}{k} = 0.59, \frac{\tau_{21}}{k} = -0.30, \frac{\mathcal{S}}{\tau} = 5.2, \frac{\mathcal{P}}{\varepsilon} = 1.6. \tag{2.41}$$

There are more unknown coefficients than equations, and so we write all coefficients in terms of the free parameter, c_{hL}. Equation (2.40e) can be rearranged to solve for c_{sp} in terms of c_{hL}:

$$c_{sp}c_{hL} = 0.85 - 0.77c_{hL}. \tag{2.42}$$

The other coefficients in terms of $c_{sp}c_{hL}$ are:

$$c_{fP}c_{hL} = 0.11c_{sp}c_{hL} - 0.64, \tag{2.43a}$$
$$c_{fB}c_{hL} = -0.054c_{sp}c_{hL} + 0.32, \tag{2.43b}$$
$$c_{fT}c_{hL} = -0.30c_{sp}c_{hL} + 0.48, \tag{2.43c}$$
$$c_{fW}c_{hL} = -0.050c_{sp}c_{hL} + 0.30. \tag{2.43d}$$

Specifying $c_{hL} = 1$, such that $L = k^{3/2}/\varepsilon$, leads to:

$$c_{sp} = 0.086, c_{fP} = -0.63, c_{fB} = 0.32, c_{fT} = 0.46, c_{fW} = 0.29. \tag{2.44}$$

As a note, we intentionally do not enforce a constraint on these coefficients such that the terms involving the mean velocity gradient offer closure only to the pressure–rate-of-strain. In other words, noting that the exact equation for the turbulent kinetic energy is a balance between production and dissipation (ignoring diffusion):

$$\frac{Dk}{Dt} = -\tau_{ij}\frac{\partial U_i}{\partial x_j} - \varepsilon, \tag{2.45}$$

the trace of the pressure–rate-of-strain exactly vanishes. To arrive at the modeled turbulent kinetic energy equation, we take the trace of the τ_{ij} equation in (2.22a):

$$\frac{Dk}{Dt} = \frac{1}{2}(2c_{fP} - 3c_{fT} + 2c_{fW})\tau_{ij}\frac{\partial U_i}{\partial x_j} - \frac{c_{f\varepsilon} - c_{sg}}{T_h}k, \tag{2.46}$$

where $T_h = L/\sqrt{k}$. Most models enforce a constraint such that the terms modeling the pressure–rate-of-strain tensor also have no trace. This would be equivalent to enforcing

$$\frac{1}{2}(2c_{fP} - 3c_{fT} + 2c_{fW}) = -1, \tag{2.47}$$

such that only the exact production term involves the mean velocity gradient, and dissipation is modeled by the last term in (2.46) involving $k^{3/2}/L$ after substitution of T_h. Not enforcing the constraint in (2.47) implies that the model for dissipation may involve terms with the mean velocity gradient. Using the coefficients in (2.44), $(2c_{fP} - 3c_{fT} + 2c_{fW})/2 \approx -1.03$, which is close to the constraint in (2.47) even though we did not specifically enforce it.

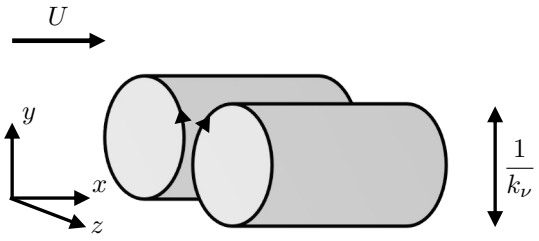

Figure 2.4: Modeling approximation of near-wall streamwise rolls.

2.4 Near-wall model

In this section, we detail progress towards development of a near-wall model that satisfies the analytically expected scalings shown in Section 2.1.4.

We consider the observed streamwise roll structures in the near-wall region (Jiménez (2013)) to be approximated by sinusoidal counter-rotating vortices that are infinitely long in the streamwise coordinate x as shown Figure 2.4. The fluctuations are modeled as:

$$v'(y) = v(y)\sin(k_\nu z), \tag{2.48a}$$

$$w'(y) = w(y)\cos(k_\nu z), \tag{2.48b}$$

$$p' = p(y)\sin(k_\nu z), \tag{2.48c}$$

where k_ν is a wavenumber that is related to the height of the near-wall structures, y is the wall-normal coordinate, and z is the spanwise coordinate. We first derive a model form for v' and w' before modeling u' and k_ν.

In the near-wall region, viscous effects dominate over inertial effects, and the governing Stokes flow equations for the velocity fluctuations are:

$$\frac{\partial v'}{\partial t} = \nu\frac{\partial^2 v'}{\partial y^2} + \nu\frac{\partial^2 v'}{\partial z^2} - \frac{\partial p'}{\partial y}, \tag{2.49a}$$

$$\frac{\partial w'}{\partial t} = \nu\frac{\partial^2 w'}{\partial y^2} + \nu\frac{\partial^2 w'}{\partial z^2} - \frac{\partial p'}{\partial z}, \tag{2.49b}$$

$$0 = \frac{\partial v'}{\partial y} + \frac{\partial w'}{\partial z}, \tag{2.49c}$$

where $\nu = 1/\mathrm{Re}$ is the molecular viscosity in the nondimensionalized Navier–Stokes equations.

Substitution of the expressions in (2.48) into the governing equations in (2.49) leads to

$$\frac{\partial v}{\partial t} = \nu\frac{\partial^2 v}{\partial y^2} - \nu v k_\nu^2 - \frac{\partial p}{\partial y}, \tag{2.50a}$$

$$\frac{\partial w}{\partial t} = \nu\frac{\partial^2 w}{\partial y^2} - \nu w k_\nu^2 - k_\nu p, \tag{2.50b}$$

$$0 = \frac{\partial v}{\partial y} - w k_\nu. \tag{2.50c}$$

Multiplying the v equation in (2.50a) by v and the w equation in (2.50b) by w and averaging leads to

$$\frac{1}{2}\frac{\partial \overline{v^2}}{\partial t} = \frac{1}{2}\nu\frac{\partial^2 \overline{v^2}}{\partial y^2} - \nu\overline{\frac{\partial v}{\partial y}\frac{\partial v}{\partial y}} - \nu\overline{v^2}k_\nu^2 - \overline{v\frac{\partial p}{\partial y}}, \tag{2.51a}$$

$$\frac{1}{2}\frac{\partial \overline{w^2}}{\partial t} = \frac{1}{2}\nu\frac{\partial^2 \overline{w^2}}{\partial y^2} - \nu\overline{\frac{\partial w}{\partial y}\frac{\partial w}{\partial y}} - \nu\overline{w^2}k_\nu^2 - k_\nu\overline{wp}, \tag{2.51b}$$

where the dissipation term (second term) and pressure term (fourth term) on the right hand side in Equations (2.51a) and (2.51b) need closure. Consider a Taylor series expansion of w, similar to Equation (2.16c), and p:

$$w = b_3 y + c_3 y^2 + \ldots, \tag{2.52a}$$

$$p = a_4 + b_4 y + c_4 y^2 + \ldots. \tag{2.52b}$$

Substitution of this expansion into the simplified equations in (2.50a)-(2.50c) leads to

$$v = \frac{1}{2}a k_\nu y^2 + \frac{1}{3}b k_\nu^2 y^3 + \ldots, \tag{2.53a}$$

$$w = a y + b k_\nu y^2 + \ldots, \tag{2.53b}$$

$$p = 2\nu b + \nu a k_\nu y + \nu b k_\nu^2 y^2 + \ldots, \tag{2.53c}$$

where the expansion for v is related to the expansion for w via the continuity equation in (2.50c), and equating parameters of similar order in y in the simplified governing equations in (2.50a)-(2.50c) leads to constraints on the coefficients, where $b_3 = a$ and $c_3 = b k_\nu$. We form expansions for $\overline{v^2}$ and $\overline{w^2}$ by multiplying these expansions with themselves and averaging:

$$\overline{v^2} = \frac{1}{4}a^2 k_\nu^2 y^4 + \frac{1}{3}a b k_\nu^3 y^5 + \ldots, \tag{2.54a}$$

$$\overline{w^2} = a^2 y^2 + 2 a b k_\nu y^3 + \ldots. \tag{2.54b}$$

These scalings suggest that for the dissipation term to be on the same order as the viscous diffusion terms in Equations (2.51a) and (2.51b), the closure should be of the form $\nu\overline{v^2}/y^2$ and

$\nu\overline{w^2}/y^2$, respectively, with some prefactor, similar to the dissipation term of Manceau and Hanjalić (2002). This term can also be thought of as the anisotropic dissipation term in the baseline model equation in (2.22a) but with a molecular timescale $T_m = y^2/\nu$ rather than $T_h = L/\sqrt{k}$.

The pressure term in the $\overline{v^2}$ equation in (2.51a) is leading order, $\mathcal{O}(y^2)$, and should couple with $\overline{w^2}$, and a simple closure term is $\nu k_\nu^2 \overline{w^2}$. The pressure term in the $\overline{w^2}$ equation in (2.51b) is higher order, $\mathcal{O}(y)$, and thus we neglect this term since the viscous diffusion term and dissipation term are $\mathcal{O}(1)$. Similarly, $\nu k_\nu^2 \overline{v^2}$ and $\nu k_\nu^2 \overline{w^2}$ are of higher order in Equations (2.51a) and (2.51b), respectively, and neglected. Inclusion of the closures for the dissipation and pressure terms and neglecting higher-order terms leads to the model form:

$$\frac{\partial \overline{v^2}}{\partial t} = \nu \left(\frac{\partial^2 \overline{v^2}}{\partial y^2} - c_{m\beta} \frac{\overline{v^2}}{y^2} + c_{m\gamma} k_\nu^2 \overline{w^2} \right), \tag{2.55a}$$

$$\frac{\partial \overline{w^2}}{\partial t} = \nu \left(\frac{\partial^2 \overline{w^2}}{\partial y^2} - c_{m\alpha} \frac{\overline{w^2}}{y^2} \right). \tag{2.55b}$$

The model form for $\overline{v^2}$ and $\overline{w^2}$ is the same as the model form for τ_{22} and τ_{33}, since multiplying the expressions for the fluctuations in (2.48a) and (2.48b) with themselves and averaging leads to $\tau_{22} = \overline{v'v'} = \overline{v^2}/2$ and similarly $\tau_{33} = \overline{w^2}/2$.

To determine the coefficients, substitution of the scalings in (2.54a) and (2.54b) into the model in (2.55a) and (2.55b) leads to the leading-order constraints:

$$c_{m\alpha} = 2, \tag{2.56a}$$

$$c_{m\beta} = 12 + 4c_{m\gamma}. \tag{2.56b}$$

Appendix A.3 shows that the analytical solution to the model equations in (2.55a) and (2.55b) follows the expected $\overline{v^2} \sim y^4$ and $\overline{w^2} \sim y^2$ scaling. Additionally, for positive values of τ_{22}, $c_{m\beta} \geq 12$ and $c_{m\gamma} \geq 0$ is needed as shown in Appendix A.3. Moreover, for stability of the coupled system in (2.55a) and (2.55b), the eigenvalues of the matrix:

$$\mathbf{A} = \begin{bmatrix} -\frac{c_{m\beta}}{y^2} & c_{m\gamma} k_\nu^2 \\ 0 & -\frac{c_{m\alpha}}{y^2} \end{bmatrix} \tag{2.57}$$

should be negative, which necessitates:

$$c_{m\alpha} c_{m\beta} > 0,\ c_{m\alpha} + c_{m\beta} > 0, \tag{2.58}$$

from examining the determinant and trace of $\mathbf{A}$, respectively. These conditions are automatically satisfied with $c_{m\alpha} = 2$, $c_{m\beta} = 12 + 4c_{m\gamma}$, and $c_{m\gamma} \geq 0$.

The inverse lengthscale k_ν is defined based on the wall shear stress as:

$$k_\nu \equiv k_0 \sqrt{\frac{1}{\nu}\frac{\partial U}{\partial y}\bigg|_{\text{wall}}}, \tag{2.59}$$

where the dimensionless coefficient k_0 will be chosen based on the value of $(\overline{u_2'^+ u_2'^+}/y^{+4})/(\overline{u_3'^+ u_3'^+}/y^{+2}) = 2.1 \times 10^{-3}$ at the wall from the DNS data of Lee and Moser (2015) as shown in Figure 2.3. Using the leading-order scalings for $\overline{v^2}$ and $\overline{w^2}$ in Equations (2.54a) and (2.54b), respectively:

$$\frac{\overline{v^2}/y^4}{\overline{w^2}/y^2} = \frac{1}{4}k_\nu^2. \tag{2.60}$$

Converting to viscous units leads to

$$\frac{\overline{u_2'^+ u_2'^+}/y^{+4}}{\overline{u_3'^+ u_3'^+}/y^{+2}} = \frac{1}{4}k_\nu^{+2} = 2.1 \times 10^{-3}, \tag{2.61}$$

and $k_\nu^+ = 0.092$. In viscous units, Equation (2.59) becomes $k_\nu^+ = k_0$, and thus we use:

$$k_0 = 0.092. \tag{2.62}$$

We note that while the coupled model form in (2.55a) and (2.55b) is designed to capture the analytically expected scaling and constant $(\overline{u_2'^+ u_2'^+}/y^{+4})/(\overline{u_3'^+ u_3'^+}/y^{+2})$, addition of the coupling term in Equation (2.55a) tends to push τ_{22} in the wrong direction. In other words, near the wall, τ_{22} is physically expected to be much smaller than the other components. However, the addition of the coupling term in Equation (2.55a) works towards increasing $\overline{v^2}$ rather than decreasing it. We discuss this issue in more detail in the context of channel flow in Section 2.4.1.

To derive model equations for τ_{11} and τ_{21}, we consider the streamwise fluctuations to be transported like a passive scalar by the sinusoidal counter-rotating vortices such that

$$u'(y) = u(y)\sin(k_\nu z). \tag{2.63}$$

Similar to the process for developing equations for $\overline{v^2}$ and $\overline{w^2}$, substitution of u' into the governing equations, developing expansions for u, etc. leads to the model form:

$$\frac{\partial \overline{u^2}}{\partial t} = \nu\frac{\partial^2 \overline{u^2}}{\partial y^2} - \nu c_{m\phi}\frac{\overline{u^2}}{y^2}, \tag{2.64a}$$

$$\frac{\partial \overline{uv}}{\partial t} = \nu\frac{\partial^2 \overline{uv}}{\partial y^2} - \nu c_{m\psi}\frac{\overline{uv}}{y^2}, \tag{2.64b}$$

where higher-order terms are neglected and details of the derivation are shown in Appendix A.4.

Substitution of the leading-order expansions for $\overline{u^2}$ and $\overline{uv}$ leads to:

$$c_{m\phi} = 2, \tag{2.65a}$$

$$c_{m\psi} = 6. \tag{2.65b}$$

2.4.1 Channel flow

For channel flow, the baseline kL model equations with the near-wall model of Section 2.4 included are:

$$\frac{\partial \tau_{11}}{\partial t} = (2c_{fp} - c_{fT})\tau_{21}\frac{\partial U_1}{\partial x_2} - \frac{c_{fR}}{T_h}\left(\tau_{11} - \frac{1}{3}\tau_{kk}\right) - \left(\frac{c_{f\epsilon} - c_{sg}}{T_h}\right)\tau_{11} + \frac{\partial}{\partial x_2}\left(c_D D\frac{\partial \tau_{11}}{\partial x_2}\right) + \nu\left(\frac{\partial^2 \tau_{11}}{\partial x_2^2} - c_{m\phi}\frac{\tau_{11}}{d^2}\right) \tag{2.66a}$$

$$\frac{\partial \tau_{22}}{\partial t} = (-c_{fT} + 2c_{fW})\tau_{21}\frac{\partial U_1}{\partial x_2} - \frac{c_{fR}}{T_h}\left(\tau_{22} - \frac{1}{3}\tau_{kk}\right) - \left(\frac{c_{f\epsilon} - c_{sg}}{T_h}\right)\tau_{22} + \frac{\partial}{\partial x_2}\left(c_D D\frac{\partial \tau_{22}}{\partial x_2}\right) + \nu\left(\frac{\partial^2 \tau_{22}}{\partial x_2^2} + c_{m\gamma}k_\nu^2\tau_{33} - c_{m\beta}\frac{\tau_{22}}{d^2}\right) \tag{2.66b}$$

$$\frac{\partial \tau_{33}}{\partial t} = -c_{fT}\tau_{21}\frac{\partial U_1}{\partial x_2} - \frac{c_{fR}}{T_h}\left(\tau_{33} - \frac{1}{3}\tau_{kk}\right) - \left(\frac{c_{f\epsilon} - c_{sg}}{T_h}\right)\tau_{33} + \frac{\partial}{\partial x_2}\left(c_D D\frac{\partial \tau_{33}}{\partial x_2}\right) + \nu\left(\frac{\partial^2 \tau_{33}}{\partial x_2^2} - c_{m\alpha}\frac{\tau_{33}}{d^2}\right) \tag{2.66c}$$

$$\frac{\partial \tau_{21}}{\partial t} = \left(c_{fp}\tau_{22} - \frac{1}{2}c_{fB}\tau_{kk} + c_{fW}\tau_{11}\right)\frac{\partial U_1}{\partial x_2} - \left(\frac{c_{fR} + c_{f\epsilon} - c_{sg}}{T_h}\right)\tau_{21} + \frac{\partial}{\partial x_2}\left(c_D D\frac{\partial \tau_{21}}{\partial x_2}\right) + \nu\left(\frac{\partial^2 \tau_{21}}{\partial x_2^2} - c_{m\psi}\frac{\tau_{21}}{d^2}\right) \tag{2.66d}$$

$$\frac{\partial L}{\partial t} = \frac{c_{sp}}{2}L\frac{\tau_{21}}{\tau_{kk}}\frac{\partial U_1}{\partial x_2} + \frac{c_{sg}}{2}\sqrt{k} - \frac{c_{sginner}}{2}\sqrt{k}\frac{L}{d} + \frac{\partial}{\partial x_2}\left((c_D D + \nu)\frac{\partial L}{\partial x_2}\right) + 2c_D\frac{D}{k}\frac{\partial k}{\partial x_2}\frac{\partial L}{\partial x_2} \tag{2.66e}$$

where $T_h = L/\sqrt{k}$, $D = \sqrt{k}L$, and d is the wall-distance. The third term in the L equation in (2.66e) is added as a growth-inhibiting term ($c_{sginner} > 0$) that is active when the wall-distance d is of similar magnitude with L. Without it, L grows unbounded in the inner region due to the second term ($c_{sg} > 0$) in Equation (2.66e) which causes growth of L. Far away from the wall, $d >> L$ and the growth-inhibiting term is small.

To be determined are the coefficient of the growth inhibiting term, $c_{sginner}$, the diffusion coefficient, c_D, and the molecular coupling term in the τ_{22} equation, $c_{m\gamma}$. To determine the coefficients, we first used the model equations for the log layer in Appendix A.5 to give an estimate of c_D based

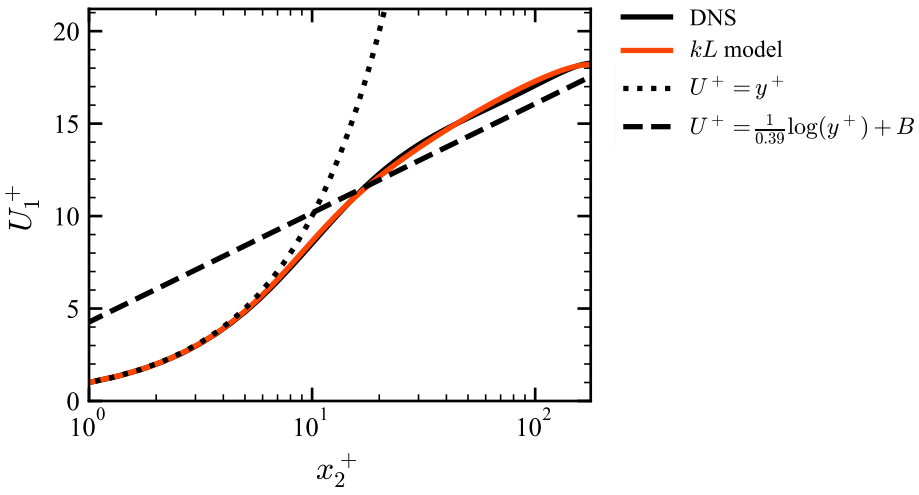

Figure 2.5: Mean velocity comparison of the baseline kL model with the DNS of Lee and Moser (2015) at $\mathrm{Re}_\tau = 180$. The dotted line shows the expected viscous sublayer behavior and the dashed line shows the log layer scaling with $\kappa = 0.39$.

on various choices of $c_{sginner}$. The log layer analysis in Appendix A.5 only gives an estimate of the model behavior as the near-wall $c_{m\gamma}$ term is actually active away from the wall due to the dependence of k_ν^2 on $1/\nu$. The $c_{m\gamma}$ term is still needed for coupling of τ_{22} and τ_{33} as discussed in Section 2.4, and thus we chose small $c_{m\gamma} = 0.1$. Larger choices of $c_{m\gamma}$ increase the centerline value of τ_{22}, and decrease the centerline value of U_1 which causes early departure of U_1 from the log law.

We then use the numerical solution of the turbulent channel flow equations in (2.66a)-(2.66e) to decide the optimal $c_{sginner}$. The coefficients $c_{sginner} = 0.27$ and $c_D = 0.0021$ (from the log layer estimate) are chosen to set the slope of the mean velocity in the log layer. However, the centerline mean velocity is underpredicted, and we adjust c_{fW} from $c_{fW} = 0.29$ as was determined based on homogeneous shear flow to $c_{fW} = 0.34$.

In this manner, the example model form can satisfactorily capture the mean velocity for $\mathrm{Re}_\tau = 180$ as shown in Figure 2.5 and correspondingly τ_{21} as shown in Figure 2.6a. Moreover, L grows linearly throughout the near-wall region and log layer as shown in Figure 2.6b, whereas the $F_{ij}L^2$ model form (briefly introduced in Section 2.2.1 and detailed in Appendix A.1) showed linear growth but with distinct viscous sublayer and log layer regions.

However, this model form mispredicts the normal Reynolds stress components as shown in Figure 2.6a. There are several known issues in joining the near-wall model developed in Section 2.4 and the baseline kL model form: 1) The addition of the $c_{m\gamma}$ term in the near-wall model is problematic. As discussed in Section 2.4, nonzero $c_{m\gamma}$ is needed in the near-wall model to couple the τ_{22} and τ_{33} scaling. However, it is a source term that pushes τ_{22} to be larger, when τ_{22} should actually be much smaller than the other Reynolds stress components near the wall. Moreover, due to the dependence

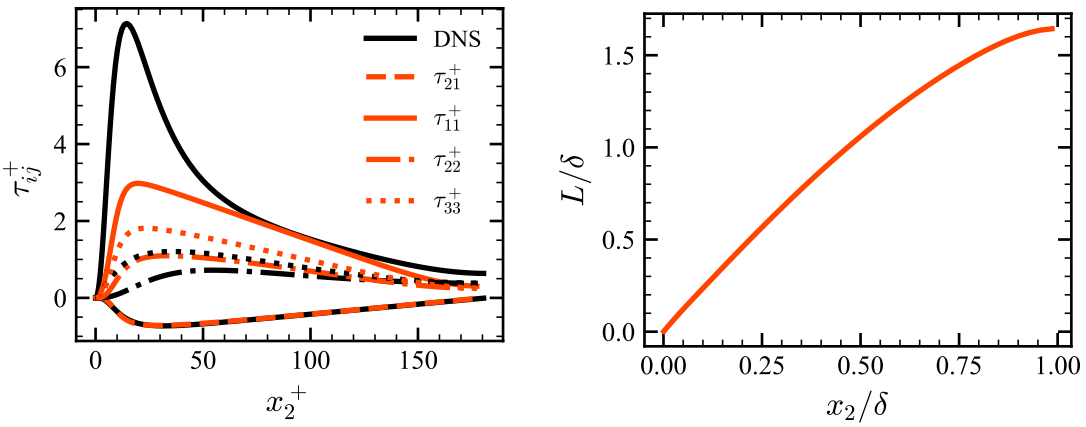

(a) (b)

Figure 2.6: (a) Reynolds stress tensor comparison of the baseline kL model with the DNS of Lee and Moser (2015) at $\mathrm{Re}_\tau = 180$. (b) The corresponding L of the baseline kL model.

of k_ν^2 on $1/\nu$, this term is also active away from the wall and influences the centerline behavior. 2) The return to isotropy term in the baseline kL model interferes with the near-wall model in the τ_{22} equation in (2.66b). Near the wall, all terms in the near-wall model are $\mathcal{O}(y^2)$, and the return to isotropy term is also $\mathcal{O}(y^2)$ due to $1/T_h = \sqrt{k}/L \sim$ constant and $\tau_{kk} \sim y^2$. 3) Adjustment of the c_{fW} coefficient helped to compensate for underprediction of the mean velocity; however, this ad hoc adjustment also pushed τ_{21} to have very small positive values instead of negative values for the first few mesh points at the wall.

2.5 Other model forms

This section documents considered changes to the baseline model form as an attempt to address some of the issues above. The results of some of these modifications are documented in the appendices as noted. Other modifications, for which we do not present results for, introduced new coefficients with ambiguity on how to determine these coefficients, and while initial attempts did not lead to immediate improvements, a deeper investigation of these modifications may be necessary:

- Instead of developing a transport equation for τ_{ij}, we express $\tau_{ij} = F_{ij}L^2$ and attempt to develop a transport equation for F_{ij}, where the boundary conditions on F_{ij} are used to set the near-wall scalings for various components of τ_{ij}. This model form was briefly introduced in Section 2.2.1 and is further explored in Appendix A.1.

- Inclusion of a nonlinear return to isotropy term, e.g., similar to Sarkar and Speziale (1990), as discussed in Appendix A.2.

- Using different values of the diffusion coefficient for τ_{ij} and L equations, e.g., c_{D1} for diffusion of τ_{ij} and c_{D2} for diffusion of L.

- Using the tensorial diffusion term of Daly and Harlow (1970):

$$\frac{D\tau_{ij}}{Dt} = \cdots + c'_D \frac{\partial}{\partial x_m}\left(\frac{L}{\sqrt{k}}\tau_{mn}\frac{\partial \tau_{ij}}{\partial x_n}\right). \tag{2.67}$$

- Changing the wall boundary conditions for L from $L = 0$ to $L \sim 1/k_\nu$.

- Inclusion of a higher-order closure for the pressure term in the near-wall model for $\overline{w^2}$ (Equation (2.55b)):

$$\frac{\partial \overline{w^2}}{\partial t} = \cdots + \nu \frac{c_{m\zeta}}{k_\nu^2}\frac{\overline{v^2}}{d^4} \tag{2.68}$$

  and because k_ν may be zero in regions of zero wall shear stress, modification of k_ν to

$$k_\nu \sim \sqrt{\frac{\sqrt{\overline{u^2} + \overline{v^2} + \overline{w^2}}}{d\nu}}. \tag{2.69}$$

- Modification of the return to isotropy timescale using

$$\frac{1}{T_h} = \frac{\sqrt{k}}{L + \frac{c_T}{k_\nu}} \tag{2.70}$$

  such that near the wall $1/T_h \sim y$ and the return to isotropy term remains higher-order ($\mathcal{O}(y^3)$) than the near-wall model ($\mathcal{O}(y^2)$) in the τ_{22} equation in (2.66b).

- Addition of terms based on L/d that modify the return to isotropy term near the wall similar to the wall-reflection terms used in the LRR model (Launder et al. (1975)) and the $c_{sginner}$ term that inhibits the growth of L in Equation (2.66e) in our model.

2.6 Contributions and lessons learned

In this chapter, we began by documenting a collection of canonical flows that can be used for determining model coefficients. They range from simple flows that are designed to activate only a few model coefficients to more complex flows that activate all model coefficients, including the near-wall model. These canonical flows were: decaying homogeneous isotropic turbulence, forced homogeneous turbulence, homogeneous shear flow, and channel flow. We showed a literature review of recent experimental and DNS data for each flow. Anisotropic forced homogeneous turbulence is a novel flow that has not been previously used for determining model coefficients.

We then showed how to use this canonical flow data in a framework for determining model coefficients. In this chapter, we adopted a Reynolds stress modeling framework as an existing approach for incorporating both anisotropic and nonlocal effects, which are both needed for prediction of complex flows as shown by Park et al. (2022a). We showed both an *a priori* procedure in which the data is specified from literature and the model coefficient is unknown and an *a posteriori* procedure in which the model coefficient is specified and the resulting data is compared with literature. The *a priori* procedure reveals deficiencies in the model form, and the *a posteriori* procedure shows the sensitivity to the model coefficients.

We then showed progress towards development of a near-wall model that is designed to preserve the expected analytical Reynolds stress scalings near the wall. While we were able to capture the mean streamwise velocity in turbulent channel flow, there were some model form issues in joining the near-wall model with the rest of the model that resulted in inadequate behavior for the normal components of the Reynolds stresses. We listed some of the other model form modifications considered, some of which were attempts to address these issues. However, one of the major challenges with analytical RANS model development is the selection of the model form from a large number of possible combinations with each of the model terms.

In this chapter, we focused on analytical Reynolds stress model development using experimental and DNS data for determining the model coefficients. The lessons from this chapter motivate a more fundamental understanding of spatiotemporal nonlocal effects in Reynolds stress models. With this motivation in mind, in the next chapters, we use the macroscopic forcing method (MFM) of Mani and Park (2021) as a numerical tool for measuring the nonlocal and anisotropic eddy viscosity. We develop a method for systematically and cost-effectively incorporating MFM data into a model (Chapter 4) and develop new MFM techniques (Chapter 5) to investigate nonlocal and anisotropic effects in turbulent channel flow (Chapter 6).

Chapter 3

Introduction to the macroscopic forcing method

Sections of this chapter are based on the article published in *Physical Review Fluids* (Liu et al. (2023)) and are reproduced here with some modifications. The full citation is: Jessie Liu, Hannah H. Williams, and Ali Mani. Systematic approach for modeling a nonlocal eddy diffusivity. *Phys. Rev. Fluids*, 8(12):124501, 2023.

3.1 Background and motivation

While in the previous chapter we attempted to incorporate nonlocal and anisotropic effects using a Reynolds stress transport model, in the following chapters we focus on using and building upon the macroscopic forcing method (MFM) of Mani and Park (2021) to obtain information about the exact nonlocal and anisotropic closure operator. In this section, we introduce MFM as it will be needed for the following chapters. For simplicity, we will begin by discussing passive scalar transport and the nonlocal eddy diffusivity, before generalizing to momentum transport and, analogously, the nonlocal eddy viscosity.

MFM of Mani and Park (2021) uses forced DNSs to compute exact closure operators. These closure operators can further be written in terms of generalized eddy diffusivities that are nonlocal in space and time and anisotropic. The eddy diffusivities are exact in that the substitution of these operators back into the mean equations results in exact mean quantities. The practical issue, however, is that for a given flow the nonlocal eddy diffusivity may be very computationally expensive to obtain. One method, introduced by Kraichnan (1987) and later modified by Hamba (1995, 2004) for directly computing the nonlocal eddy diffusivity, is to use the Green's function solution to a passive scalar equation. The nonlocal eddy diffusivity, representing the projection of the scalar

flux into the mean space, is then formulated exactly in terms of the Green's function and velocity fluctuation. Another method, which we use in this work, is MFM of Mani and Park (2021), a linear-algebra-based method for numerically obtaining closure operators. In MFM, one probes the closure operator by applying an appropriate forcing (not necessarily a Dirac delta function) to the governing equations and measures the averaged response. Through this input-output analysis, one can determine the exact nonlocal eddy diffusivity corresponding to the unclosed term. However, because the full nonlocal eddy diffusivity captures the dependency of the scalar flux on the mean scalar gradient everywhere in the averaged space, either of the above brute-force approaches would require as many DNSs as degrees of freedom in the averaged space.

Analogously, for momentum transport, Kraichnan (1987) also derived an exact nonlocal and anisotropic expression for the Reynolds stress tensor using a Green's function. Hamba (2005) modified the expression to be feasible for numerical implementation. Hamba (2005) used the Green's function solution to a linearized formulation of the velocity fluctuation equation where the mean velocity gradient is treated as the source, and the velocity fluctuation is treated as the response. The generalized nonlocal and anisotropic eddy viscosity is then formulated using Green's functions and velocity fluctuations.

While MFM can be used to obtain the generalized eddy diffusivity (or eddy viscosity) similar to the approach of Hamba (2004, 2005) as shown in Appendix B.2, MFM can also be used to obtain moments of the eddy diffusivity using one simulation per desired moment. The challenge lies in using this limited information to model the nonlocal eddy diffusivity which we address in Chapter 4. In this chapter, we first introduce the problem formulation for passive scalar transport in Section 3.2 and computing nonlocal and anisotropic eddy diffusivities in Section 3.3 before generalizing to momentum transport in Section 3.4.

3.2 Problem formulation for passive scalar transport

Consider a passive scalar, $c(\mathbf{x}, t)$, being transported by a flow with velocity, $u_j(\mathbf{x}, t)$. The governing equation is

$$\frac{\partial c}{\partial t} + \frac{\partial}{\partial x_j}(u_j c) = D_M \frac{\partial^2 c}{\partial x_j \partial x_j}, \tag{3.1}$$

where D_M is the molecular diffusivity. In many applications, instead of the full solution, c, one may be only interested in the average of the solution, $\bar{c}$. For example, the average may be taken over ensembles, in time if the flow is statistically stationary, or over homogeneous spatial directions, but its definition is system-dependent and varies between problems. One can derive an equation for $\bar{c}$

by applying the Reynolds decomposition (Reynolds (1895)):

$$c = \bar{c} + c' \tag{3.2a}$$

$$u_j = \bar{u}_j + u'_j \tag{3.2b}$$

where $\overline{()}$ denotes a mean quantity and $()'$ denotes fluctuations about the mean quantity. Substituting (3.2a) and (3.2b) into Equation (3.1) and then averaging the resulting equation leads to the mean scalar transport equation:

$$\frac{\partial \bar{c}}{\partial t} + \frac{\partial}{\partial x_j}(\bar{u}_j \bar{c}) = D_M \frac{\partial^2 \bar{c}}{\partial x_j \partial x_j} - \frac{\partial}{\partial x_j}\overline{u'_j c'}. \tag{3.3}$$

The scalar flux, $\overline{u'_j c'}$, is unknown and further attempts to analytically develop governing equations for this term would result in more unknown quantities, i.e., this term is unclosed. A commonly-used closure model, introduced by Boussinesq (1877), approximates $-\overline{u'_j c'}$ as a diffusive flux:

$$-\overline{u'_j c'}(\mathbf{x}) = D \left.\frac{\partial \bar{c}}{\partial x_j}\right|_{\mathbf{x}}, \tag{3.4}$$

where D is commonly referred to as the eddy diffusivity. Equation (3.4) relies on two simplifying approximations. The first approximation is isotropy of the underlying mixing process, resulting in a scalar eddy diffusivity. More critically relevant to our study, the second approximation is that the mean scalar, $\bar{c}$, varies over a time and length scale much larger than that of the fluctuations, c'. In other words, the fluctuations mix very quickly and very locally due to the underlying flow. In this limit, one can draw an analogy to kinetic theory, where molecular mixing happens very quickly and locally due to Brownian motion, but the average motion represented at the continuum scale, which is much larger than the Brownian mean free path, can be approximated via a local diffusive flux. Reliant on a separation of scales, the Boussinesq approximation is a purely local approximation: $-\overline{u'_j c'}$ at a given location, $\mathbf{x}$, is only dependent on the gradient of $\bar{c}$ at the same location, $\mathbf{x}$.

However, such isotropy and idealized separation of scales between mean fields and fluctuations of continuum passive scalar fields often does not exist in turbulent flows (Corrsin (1975)). When the Boussinesq approximation breaks down, a more general form of the eddy diffusivity is introduced by Berkowicz and Prahm (1979):

$$-\overline{u'_j c'}(\mathbf{x}) = \int_{\mathbf{y}} D_{ji}(\mathbf{x}, \mathbf{y}) \left.\frac{\partial \bar{c}}{\partial x_i}\right|_{\mathbf{y}} \mathrm{d}\mathbf{y}, \tag{3.5}$$

where $-\overline{u'_j c'}$ at a given location, $\mathbf{x}$, may now be influenced by the gradient, $\partial \bar{c}/\partial x_i$, at another location, $\mathbf{y}$. The eddy diffusivity is now tensorial and can capture anisotropy of the underlying mixing process by allowing the mean scalar flux to depend on different directions of the mean scalar

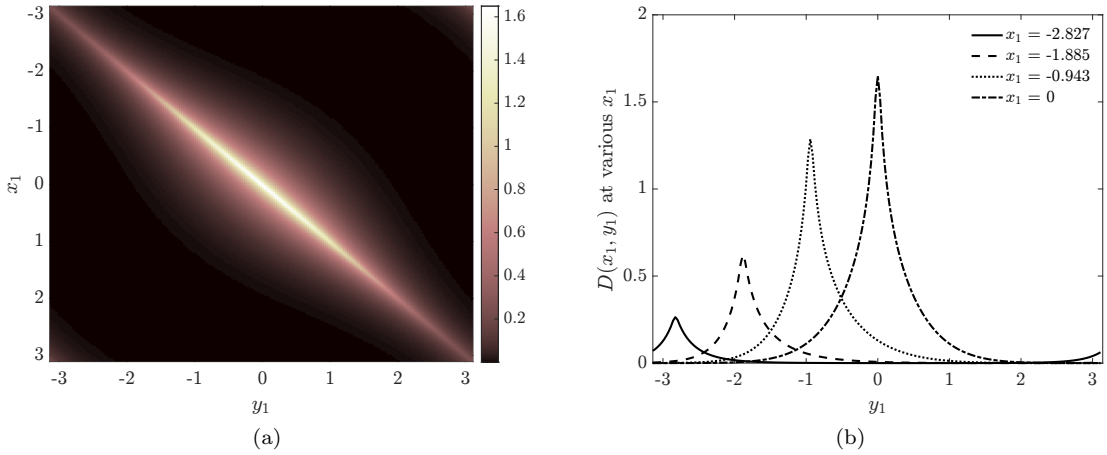

(a) (b)

Figure 3.1: Example of a nonlocal eddy diffusivity. (a) Full nonlocal eddy diffusivity kernel, $D(x_1, y_1)$, and (b) cross sections of $D(x_1, y_1)$ at various x_1 locations.

gradient. Moreover, there is no requirement of length scale separation, and fluctuations are not assumed to mix locally. $D_{ji}(\mathbf{x}, \mathbf{y})$ is a nonlocal eddy diffusivity kernel and captures the dependence of the scalar flux on the mean scalar gradient at other locations. Figure 3.1 shows an example of a nonlocal eddy diffusivity kernel (corresponding to the inhomogeneous model problem with periodic boundary conditions in Section 4.4.1 in which only $D_{11}(x_1, y_1)$ is active). If one considers the eddy diffusivity as a discretized matrix, then for a purely local eddy diffusivity, only the diagonal values would be nonzero. However, the exact nonlocal eddy diffusivity in Figure 3.1a shows some spread around the diagonal, indicating the presence of nonlocality. Figure 3.1b shows cross sections of the nonlocal eddy diffusivity at various x_1 locations.

A nonlocal eddy diffusivity can also include temporal effects (Romanof (1985); Kraichnan (1987); Hamba (1995, 2004)):

$$-\overline{u_j' c'}(\mathbf{x}, t) = \int_{\mathbf{y},\tau} D_{ji}(\mathbf{x}, \mathbf{y}, t, \tau) \frac{\partial \bar{c}}{\partial x_i}\bigg|_{\mathbf{y},\tau} \mathrm{d}\mathbf{y}\mathrm{d}\tau, \tag{3.6}$$

where $-\overline{u_j' c'}$ at a given time, t, may now also depend on the time history, τ, of the gradient of $\bar{c}$.

If the underlying flow is statistically stationary and homogeneous, the nonlocal eddy diffusivity expression in (3.6) has a simplified form (Berkowicz and Prahm (1980)):

$$-\overline{u_j' c'}(\mathbf{x}, t) = \int_{\mathbf{y},\tau} D_{ji}(\mathbf{y} - \mathbf{x}, \tau - t) \frac{\partial \bar{c}}{\partial x_i}\bigg|_{\mathbf{y},\tau} \mathrm{d}\mathbf{y}\mathrm{d}\tau, \tag{3.7}$$

where the nonlocal eddy diffusivity does not depend on the specific point, $(\mathbf{x}, t)$, but rather only on the distance, $(\mathbf{y} - \mathbf{x}, \tau - t)$. We consider nonlocal eddy diffusivities for homogeneous flows in Section 4.3 before considering inhomogeneous flows in Section 4.4.

The moments of the nonlocal eddy diffusivity are related to the full nonlocal eddy diffusivity by

considering the Taylor series expansion of Equation (3.6) locally about $\mathbf{y} = \mathbf{x}$ and $\tau = t$ (also known as a Kramers–Moyal expansion (Van Kampen (1992))) as done by Kraichnan (1987) and Hamba (1995, 2004):

$$-\overline{u_j'c'}(\mathbf{x},t) = \int_{\mathbf{y},\tau} D_{ji}(\mathbf{x},\mathbf{y},t,\tau)\left[1 + (y_k - x_k)\frac{\partial}{\partial x_k} + \cdots + (\tau - t)\frac{\partial}{\partial t} + \ldots\right]\left.\frac{\partial \bar{c}}{\partial x_i}\right|_{\mathbf{x},t} \mathrm{d}\mathbf{y}\mathrm{d}\tau. \quad (3.8)$$

The term involving $\bar{c}$ is now no longer a function of $\mathbf{y}$ and τ and can be taken out of the integral such that

$$-\overline{u_j'c'}(\mathbf{x},t) = \left[D^0_{ji}(\mathbf{x},t) + D^{1_s}_{jik}(\mathbf{x},t)\frac{\partial}{\partial x_k} + \cdots + D^{1_t}_{ji}(\mathbf{x},t)\frac{\partial}{\partial t} + \cdots\right]\frac{\partial \bar{c}}{\partial x_i}, \quad (3.9)$$

where D^0_{ji} is the zeroth-order spatial and temporal moment:

$$D^0_{ji}(\mathbf{x},t) = \int_{\mathbf{y},\tau} D_{ji}(\mathbf{x},\mathbf{y},t,\tau)\mathrm{d}\mathbf{y}\mathrm{d}\tau, \quad (3.10)$$

$D^{1_s}_{jik}$ is the first-order spatial moment (superscript s for spatial):

$$D^{1_s}_{jik}(\mathbf{x},t) = \int_{y_k,\tau} (y_k - x_k) D_{jik}(\mathbf{x},\mathbf{y},t,\tau)\mathrm{d}y_k\mathrm{d}\tau, \quad (3.11)$$

$D^{1_t}_{ji}$ is the first-order temporal moment (superscript t for temporal):

$$D^{1_t}_{ji}(\mathbf{x},t) = \int_{\mathbf{y},\tau} (\tau - t) D_{ji}(\mathbf{x},\mathbf{y},t,\tau)\mathrm{d}\mathbf{y}\mathrm{d}\tau, \quad (3.12)$$

and so forth. The zeroth-order spatial and temporal moment, D^0_{ji}, is the local and anisotropic eddy diffusivity, and higher-order moments characterize the nonlocality of the eddy diffusivity.

3.3 Methods for computing the nonlocal eddy diffusivity and moments of the eddy diffusivity

While the moments of the nonlocal eddy diffusivity may be obtained by computing the full nonlocal eddy diffusivity and then integrating using the definitions in Equations (3.10)-(3.12), Mani and Park (2021) use inverse MFM (IMFM) to compute the moments more directly. We first review methods for obtaining the full nonlocal eddy diffusivity before introducing direct methods for obtaining the eddy diffusivity moments.

The passive scalar transport equation in (3.1) can be written in operator form as

$$\mathcal{L}c = 0, \quad (3.13)$$

where $\mathcal{L}$ is a matrix representing the discretized advection-diffusion operator. The desired equation governing the mean scalar field is

$$\overline{\mathcal{L}}\bar{c} = 0, \tag{3.14}$$

where $\overline{\mathcal{L}}$ is the averaged operator containing both the closed advection-diffusion operator and the closure operator for the scalar flux in Equation (3.3). Let averaging be defined by

$$\bar{c} = Pc, \tag{3.15}$$

where P is the projection operator. Similarly, E is an extension operator such that $E = nP^\top$, where n is the number of points used for averaging. Mani and Park (2021) show that the averaged operator can be found by using

$$\overline{\mathcal{L}} = (P\mathcal{L}^{-1}E)^{-1}. \tag{3.16}$$

The derivation of (3.16) and its connection to the forcing methods introduced later in this section are shown in Appendix B.1.

Once the averaged operator $\overline{\mathcal{L}}$ is obtained, one can subtract out the closed portion of the Reynolds-averaged advection-diffusion operator to find the closure operator, $\overline{\mathcal{L}}'$, using

$$\overline{\mathcal{L}} = \frac{\partial}{\partial t} + \bar{u}_j\frac{\partial}{\partial x_j} - D_M\frac{\partial^2}{\partial x_j \partial x_j} + \overline{\mathcal{L}}'. \tag{3.17}$$

For example, if averages are taken over all directions except x_1 and the unclosed term is simply $\overline{\mathcal{L}}'\bar{c} = \partial/\partial x_1(\overline{u_1'c'})$, after obtaining $\overline{\mathcal{L}}'$ one can then write the closure operator as

$$\overline{\mathcal{L}}' = -\frac{\partial}{\partial x_1}D\frac{\partial}{\partial x_1}. \tag{3.18}$$

By removing the appropriate $\partial/\partial x_1$ matrices, one can recover the eddy diffusivity, D, in discretized form. If D is a purely diagonal matrix, then the eddy diffusivity is purely local. If instead, there are nonzero off-diagonal entries in D, which then multiply a spread of corresponding entries in $\partial\bar{c}/\partial x_1$, then the eddy diffusivity is nonlocal. Matrix multiplication can be expressed as a convolution, and in continuous form, generalizes to the nonlocal eddy diffusivity formulation of Berkowicz and Prahm (1979) in Equation (3.5).

We use this method for obtaining the full nonlocal eddy diffusivities for the simple problems with low degrees of freedom in Chapter 4. However, inversion of $\mathcal{L}$, which is size-dependent on the number of degrees of freedom, can become prohibitively expensive for complex problems. Moreover, for general problems, $\overline{\mathcal{L}}'$ may include multiple unclosed terms from which it may not be possible to extract a nonlocal eddy diffusivity for each term separately using this approach.

Forcing methods, such as MFM of Mani and Park (2021) or use of the Green's function by Hamba (1995, 2004), can take advantage of computational fluid dynamics solvers and probe the nonlocal

eddy diffusivity directly. MFM is a more flexible technique that allows 1) explicit specification of the forcing and post-processing of $\bar{c}$ to arrive at the closure operator, 2) specification of the gradient of $\bar{c}$ as a Dirac delta function and post-processing of the scalar flux to obtain the nonlocal eddy diffusivity, which is consistent with the Green's function approach of Hamba (1995, 2004) as shown in Appendix B.2, or 3) specification of $\bar{c}$ as polynomials and post-processing of scalar fluxes to obtain moments of the nonlocal eddy diffusivity. Moreover, this linear-algebra-based forcing technique does not require the governing (microscopic) equations as analytical partial differential equations but only as operators in discretized form.

Rather than obtaining the full nonlocal eddy diffusivity, we introduce IMFM and its usage for directly obtaining moments of the eddy diffusivity. In IMFM, one adds a forcing in order to maintain a pre-specified mean field and measures the scalar flux response. For example, a forcing, s, is added to the passive scalar transport equation in Equation (3.1):

$$\frac{\partial c}{\partial t} + \frac{\partial}{\partial x_j}(u_j c) - D_M \frac{\partial^2 c}{\partial x_j \partial x_j} = s. \tag{3.19}$$

At each time step, $\bar{c}$ is constrained to its pre-specified value due to s while c is free to evolve. In this procedure, at each time step, one can solve for c without the forcing, and then shift c appropriately (while observing the macroscopic forcing property $s = \bar{s}$) such that the average matches the pre-specified $\bar{c}$.

Specifying the mean field as polynomials leads to moments of the eddy diffusivity. For simplicity, consider a problem in which averaging is taken over all directions except x_1, and there is only one component of the scalar flux, $\overline{u_1' c'}$. Equation (3.9) becomes:

$$-\overline{u_1' c'}(x_1, t) = \left[D^0(x_1, t) + D^{1_s}(x_1, t)\frac{\partial}{\partial x_1} + D^{2_s}(x_1, t)\frac{\partial^2}{\partial x_1^2} + \cdots + D^{1_t}(x_1, t)\frac{\partial}{\partial t} + \ldots \right] \frac{\partial \bar{c}}{\partial x_1}. \tag{3.20}$$

To obtain the zeroth-order spatial and temporal moment of the eddy diffusivity, one can use IMFM to specify $\bar{c} = x_1$ and solve the forced passive scalar transport equation in (3.19). Postprocessing of $-\overline{u_1' c'}$ leads to the zeroth moment:

$$-\overline{u_1' c'}|_{\bar{c}=x_1}(x_1, t) = D^0(x_1, t) \tag{3.21}$$

as shown by substitution of $\bar{c} = x_1$ into (3.20). Specifying $\bar{c}$ as higher-order polynomials leads to higher-order moments of the eddy diffusivity. For the first-order spatial moment, specifying $\bar{c} = x_1^2/2$ leads to

$$-\overline{u_1' c'}|_{\bar{c}=x_1^2/2}(x_1, t) = x_1 D^0(x_1, t) + D^{1_s}(x_1, t) \tag{3.22}$$

as shown by substitution of $\bar{c} = x_1^2/2$ into (3.20). Post-processing the scalar flux and then subtracting out the contribution from the zeroth-order moment leads to D^{1_s}. Similarly, for the second-order

spatial moment, specifying $\bar{c} = x_1^3/6$ leads to

$$-\overline{u_1' c'}|_{\bar{c}=x_1^3/6}(x_1,t) = \frac{x_1^2}{2} D^0(x_1,t) + x_1 D^{1_s}(x_1,t) + D^{2_s}(x_1,t), \tag{3.23}$$

and post-processing the scalar flux and then subtracting out the contribution from the zeroth-order moment and first-order spatial moment leads to D^{2_s}. For the first-order temporal moment, specifying $\bar{c} = x_1 t$ leads to

$$-\overline{u_1' c'}|_{\bar{c}=x_1 t}(x_1,t) = t D^0(x_1,t) + D^{1_t}(x_1,t) \tag{3.24}$$

as shown by substitution of $\bar{c} = x_1 t$ into (3.20). Post-processing the scalar flux and then subtracting out the contribution from the zeroth-moment leads to D^{1_t}.

Generally, calculation of higher-order moments depends on having previously obtained lower-order moments.

3.4 Generalization to momentum transport

For momentum transport, the analogue of the generalized eddy diffusivity in Equation (3.6) is the generalized eddy viscosity (Hamba (2005)):

$$-\overline{u_i' u_j'}(\mathbf{x},t) = \int_{\mathbf{y},\tau} D_{ijkl}(\mathbf{x},\mathbf{y},t,\tau) \frac{\partial U_l}{\partial x_k}\bigg|_{\mathbf{y},\tau} \mathrm{d}\mathbf{y}\mathrm{d}\tau, \tag{3.25}$$

where $D_{ijkl}(\mathbf{x},\mathbf{y},t,\tau)$ is the nonlocal and anisotropic eddy viscosity kernel. In this section, we detail how to compute the eddy viscosity kernel using a brute-force approach as it will become important for Chapter 5 and how to compute moments of the generalized eddy viscosity without computing the entire eddy viscosity kernel as it will become important for Section 4.5.

For the statistically stationary turbulent channel flow considered in the following chapters, averaging is taken in time and over the homogeneous streamwise (x_1) and spanwise (x_3) directions. The simplified eddy viscosity is

$$-\overline{u_i' u_j'}(x_2) = \int D_{ij21}(x_2,y_2) \frac{\partial U_1}{\partial x_2}\bigg|_{y_2} \mathrm{d}y_2, \tag{3.26}$$

where x_2 is the wall-normal direction. Hamba (2005) and Park and Mani (2023a) computed the generalized eddy viscosity, $D_{ij21}(x_2,y_2)$, for turbulent channel flow at $\mathrm{Re}_\tau = 180$. Hamba (2005) used the Green's function solution to a linearized equation for the velocity fluctuations. Park and Mani (2023a) used IMFM, where forcing is added to the governing equations to maintain a prespecified mean velocity gradient. Appendix B.2 shows that the two approaches are equivalent. However, Hamba (2005) further performed averaging of D_{ij21} to enforce symmetry in the Reynolds stress tensor, e.g., $(D_{2121} + D_{1221})/2$, whereas Park and Mani (2023a) did not.

Park and Mani (2023a) simultaneously solve the nondimensionalized incompressible Navier–Stokes equations:

$$\frac{\partial u_i}{\partial t} + \frac{\partial u_j u_i}{\partial x_j} = -\frac{\partial p}{\partial x_i} + \frac{1}{\mathrm{Re}}\frac{\partial^2 u_i}{\partial x_j \partial x_j} + r_i, \tag{3.27a}$$

$$\frac{\partial u_i}{\partial x_i} = 0, \tag{3.27b}$$

where Re is the Reynolds number, p is the fluctuating pressure, and r_i is a body force, which for turbulent channel flow is the nondimensionalized mean pressure gradient, $r_i = (1, 0, 0)$, and the generalized momentum transport (GMT) equations:

$$\frac{\partial v_i}{\partial t} + \frac{\partial u_j v_i}{\partial x_j} = -\frac{\partial q}{\partial x_i} + \frac{1}{\mathrm{Re}}\frac{\partial^2 v_i}{\partial x_j \partial x_j} + s_i, \tag{3.28a}$$

$$\frac{\partial v_i}{\partial x_i} = 0, \tag{3.28b}$$

where u_j is the advection velocity computed from the Navier–Stokes equations in (3.27a) and (3.27b), v_i is a transported vector field, q is a generalized pressure to ensure that v_i is solenoidal, and s_i is the IMFM forcing (and must satisfy $s_i = \overline{s}_i$). In this formulation, the eddy viscosity is

$$-\overline{u_i' v_j'}(x_2) = \int D_{ij21}(x_2, y_2) \frac{\partial V_1}{\partial x_2}\bigg|_{y_2} \mathrm{d}y_2. \tag{3.29}$$

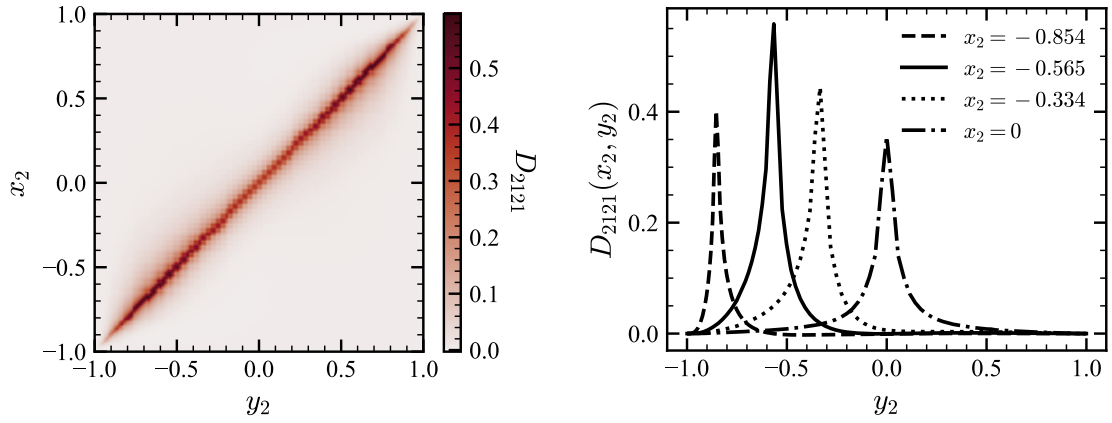

(a) (b)

Figure 3.2: (a) $D_{2121}(x_2, y_2)$ component of the generalized eddy viscosity for a turbulent channel flow at $\mathrm{Re}_\tau = 180$. The rows of D_{2121} represent the dependence of the shear component of the Reynolds stress, $-\overline{u_2' u_1'}(x_2)$, on $\partial U_1/\partial x_2|_{y_2}$. Reproduced from Park and Mani (2023a) with author permission. (b) Rows of D_{2121} for x_2 as labeled. Uses data from Park and Mani (2023a).

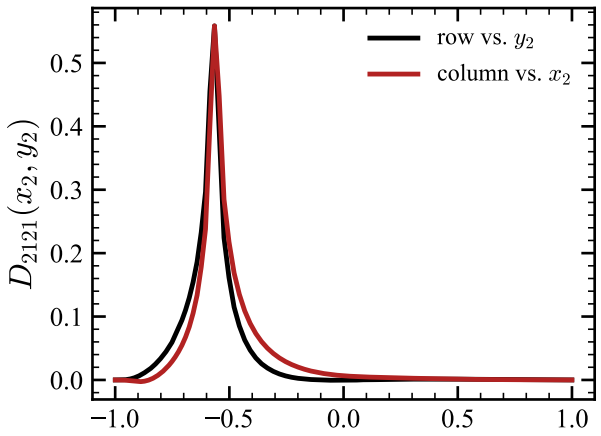

Figure 3.3: A row of D_{2121} at $x_2 = -0.565$, i.e., $D_{2121}(x_2 = -0.565, y_2)$ and the corresponding column, $D_{2121}(x_2, y_2 = -0.565)$, which shows that $D_{2121}(x_2, y_2)$ is not symmetric (data from Park and Mani (2023a) with author permission).

Figure 3.2a shows the D_{2121} component of the eddy viscosity reproduced from Park and Mani (2023a). This component represents the dependence of the shear component of the Reynolds stress, $-\overline{u_2' u_1'}(x_2)$, on the mean velocity gradient at all locations, $\partial U_1/\partial x_2|_{y_2}$. To compute the eddy viscosity, Park and Mani (2023a) use the IMFM forcing to maintain the mean velocity gradient, $\partial V_1/\partial x_2$, as a Dirac delta function. In discretized form, $\mathbf{b} = \mathbf{A}\mathbf{v}$, where $\mathbf{b} = -\overline{u_2' v_1'}$ is a $N \times 1$ vector, $\mathbf{A} = D_{2121}$ is a $N \times N$ matrix, $\mathbf{v} = \partial V_1/\partial x_2$ is a $N \times 1$ vector, and N is the number of degrees of freedom in the averaged space (number of mesh points in x_2). Using IMFM to specify the velocity gradient as $\mathbf{v} = [1\ 0 \ldots 0]^\top$ (a discrete Dirac delta function) and post-processing the resulting $-\overline{u_2' v_1'}$ from a simulation of the Navier–Stokes equations in (3.27a) and (3.27b) and GMT equations in (3.28a) and (3.28b) leads to the first column of $\mathbf{A}$. Specifying $\mathbf{v} = [0\ 1 \ldots 0]^\top$ leads to the second column, and so forth. Thus, obtaining the generalized eddy viscosity using IMFM, or equivalently Hamba's approach (Hamba (2005)) here, requires as many simulations as degrees of freedom in the averaged space. In the case of Park and Mani (2023a), 144 simulations for each of the 144 mesh points in the wall-normal direction were needed to produce the eddy viscosity shown in Figure 3.2a. Each simulation solves both incompressible Navier–Stokes and GMT equations, and hence the total cost is equivalent to 288 DNSs.

Each simulation obtains a column of D_{ijkl}, but the rows of D_{ijkl} are more useful from a physical perspective. The rows give the dependence of the Reynolds stress, $-\overline{u_i' u_j'}$, at a given location, on the mean velocity gradient at all locations. The rows give information about the importance of nonlocality and regions of mean velocity gradient sensitivity. Moreover, the rows of D_{ijkl} are generally not identical to the columns. For example, from Figure 3.2a it may seem that $D_{2121}(x_2, y_2)$ is symmetric and equal to $D_{2121}(y_2, x_2)$. Figure 3.3 shows clear differences between a row of D_{2121}

at $x_2 = -0.565$ and a column at the same location. We address the need for a method for obtaining targeted rows of the generalized eddy viscosity without first performing a brute-force computation of all columns of the eddy viscosity in Chapter 5. Moreover, the method developed in Chapter 5 allows us to perform MFM measurements of streamwise and wall-normal nonlocality at specific near-wall locations in turbulent channel flow in Chapter 6.

To directly compute moments of the eddy viscosity, as detailed for the eddy diffusivity in Section 3.3, consider the Taylor series expansion of the generalized eddy viscosity in Equation (3.29) locally about $y_2 = x_2$:

$$-\overline{u_i' v_j'}(x_2) = \left[D^0_{ij21}(x_2) + D^{1_s}_{ij21}(x_2)\frac{\partial}{\partial x_2} + D^{2_s}_{ij21}(x_2)\frac{\partial^2}{\partial x_2^2} + \cdots \right] \frac{\partial V_1}{\partial x_2}, \tag{3.30}$$

where D^0_{ij21} is the zeroth-order spatial moment:

$$D^0_{ij21}(x_2) = \int D_{ij21}(x_2, y_2)\mathrm{d}y_2, \tag{3.31}$$

$D^{1_s}_{ij21}$ is the first-order spatial moment (superscript s for spatial and where we have dropped the higher-order tensorial notation, e.g., $D^{1_s}_{ijklm}$, since only the x_2 direction is considered):

$$D^{1_s}_{ij21}(x_2) = \int (y_2 - x_2) D_{ij21}(x_2, y_2)\mathrm{d}y_2, \tag{3.32}$$

and similarly, $D^{2_s}_{ij21}$ is the second-order spatial moment:

$$D^{2_s}_{ij21}(x_2) = \int \frac{1}{2}(y_2 - x_2)^2 D_{ij21}(x_2, y_2)\mathrm{d}y_2. \tag{3.33}$$

Using IMFM to specify the mean field as polynomials leads to information about moments of the eddy viscosity. For example, to compute the zeroth-order spatial moment of the eddy viscosity, using IMFM to specify $V_1 = x_2$ and solving the Navier–Stokes equations in (3.27a) and (3.27b) and GMT equations in (3.28a) and (3.28b) leads to the zeroth moment:

$$-\overline{u_i' v_j'}|_{V_1 = x_2}(x_2) = D^0_{ij21}(x_2) \tag{3.34}$$

as shown by substitution of $V_1 = x_2$ into Equation (3.30). Similar to passive scalar transport, specifying V_1 as higher-order polynomials, e.g., $V_1 = x_2^2/2$ and $V_1 = x_2^3/6$, leads to information about higher-order moments of the eddy viscosity. Section 4.5 shows how to systematically use this information about the eddy viscosity moments in a model for turbulent channel flow.

Chapter 4

Systematic approach for modeling a nonlocal eddy diffusivity or eddy viscosity

Sections of this chapter are based on the article published in *Physical Review Fluids* (Liu et al. (2023)) and are reproduced here with some modifications. The full citation is: Jessie Liu, Hannah H. Williams, and Ali Mani. Systematic approach for modeling a nonlocal eddy diffusivity. *Phys. Rev. Fluids*, 8(12):124501, 2023.

4.1 Background and motivation

In this chapter, we will develop *matched moment inverse* operators in the context of passive scalar transport and the nonlocal eddy diffusivity; however, the approach extends naturally to momentum transport using the nonlocal eddy viscosity in Section 3.4, which we demonstrate for turbulent channel flow in Section 4.5.

As discussed in Chapter 3, while a brute-force approach such as MFM (Mani and Park (2021)) or the Green's function approach of Hamba (2004) can be used to compute the nonlocal eddy diffusivity, these approaches are expensive and need as many forced DNSs as degrees of freedom in the averaged space. However, even once obtained, a nonlocal eddy diffusivity may still be expensive to implement in a model due to the resulting integro-differential equation accounting for the effect of the mean scalar gradient everywhere in space (and time). A spatially nonlocal eddy diffusivity would raise the computational cost from $\mathcal{O}(N)$ to $\mathcal{O}(N^2)$; a temporally nonlocal eddy diffusivity would require keeping the history of the mean scalar gradient stored in memory.

Previous works have attempted to address the cost of implementing a nonlocal eddy diffusivity

by suggesting various approaches for modeling a nonlocal eddy diffusivity using a partial differential equation rather than an integro-differential equation. Georgopoulos and Seinfeld (1989) assumed an exponential kernel shape for a temporally nonlocal (but spatially local) eddy diffusivity and arrived at a hyperbolic telegrapher's equation for the mean scalar. Yoshizawa (1985) expanded the nonlocal eddy diffusivity using the two-scale direct interaction approximation and used higher-order terms involving products of the mean scalar gradient and mean velocity gradient as corrections to the local eddy diffusivity. Hamba (1995, 2004) expanded the nonlocal eddy diffusivity using a Taylor series expansion (also known as a Kramers–Moyal expansion (Van Kampen (1992))) and used higher-order terms of the Taylor series as corrections to the local eddy diffusivity. Such an expansion can have convergence issues as we discuss in Section 4.2. Hamba (2004) also suggested another model form based on a partial differential equation for the scalar flux; however, the coefficients of this model require knowledge of the full nonlocal eddy diffusivity. More recently, Hamba (2022) modeled the nonlocal eddy diffusivity for decaying homogeneous isotropic turbulence in Fourier space by using the energy spectrum.

To alleviate the computational cost while keeping the accuracy of the nonlocal eddy diffusivity, we introduce a systematic technique for modeling nonlocal eddy diffusivities using what we call matched moment inverse (MMI) operators. Determining these operators does not require computing the full nonlocal eddy diffusivity—as the name suggests, they require only a few moments of the nonlocal eddy diffusivity, which can be cost-effectively computed using inverse MFM (IMFM) (Mani and Park (2021)).

In Section 4.2, we discuss modeling approaches for nonlocal eddy diffusivities, culminating in the development of MMI. Then, in Section 4.3, we demonstrate the use of MMI for a simple homogeneous problem and illustrate the importance of including nonlocal effects in a model. In Section 4.4, we demonstrate the use of MMI for inhomogeneous flows and address some of the challenges with MMI for inhomogeneous wall-bounded flows.

4.2 Approaches for modeling a nonlocal eddy diffusivity

Given a spatiotemporally nonlocal eddy diffusivity as in Equation (3.6), one may want to model the nonlocal eddy diffusivity in order to express the governing equation for the mean scalar as a partial differential equation rather than an integro-differential equation. For simplicity, consider a problem where averaging is taken over all directions except x_1, and there is only one component of the scalar flux, $\overline{u_1' c'}$. The scalar flux can be expressed exactly as

$$-\overline{u_1' c'}(x_1, t) = \int_{y_1, \tau} D(x_1, y_1, t, \tau) \frac{\partial \overline{c}}{\partial x_1}\bigg|_{y_1, \tau} \mathrm{d}y_1 \mathrm{d}\tau. \tag{4.1}$$

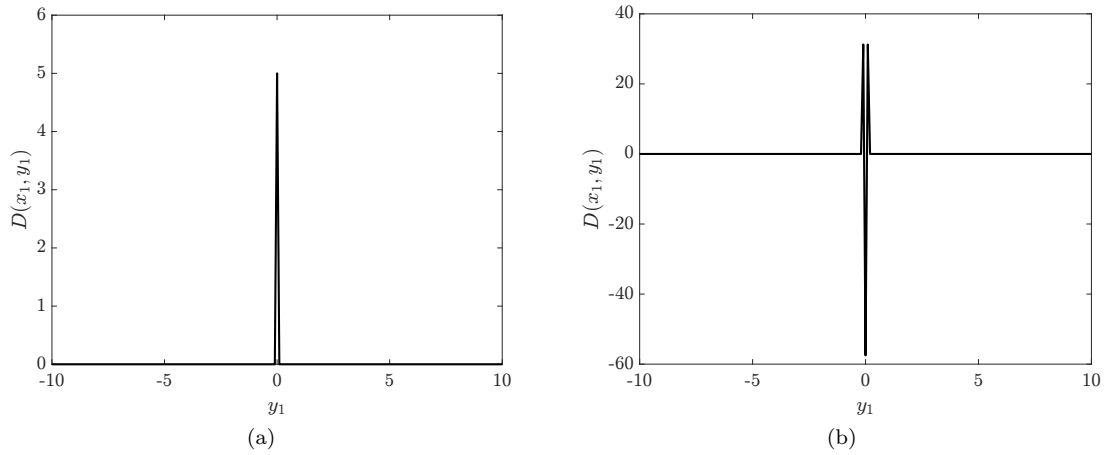

Figure 4.1: (a) Example eddy diffusivity kernel corresponding to the Boussinesq model in Equation (4.2). (b) Example eddy diffusivity kernel corresponding to the explicit model in Equation (4.3) with $D^0 = 1/2$, $D^{1_s} = 0$, and $D^{2_s} = 1/32$ using a second-order central difference scheme and $\Delta y_1 = 0.1$.

4.2.1 Boussinesq model

In the Boussinesq limit, where mixing is purely local, $D(x_1, y_1, t, \tau) = D^0(x_1, t)\delta(y_1 - x_1)\delta(\tau - t)$. The purely local model is given by

$$-\overline{u_1' c'}(x_1, t) = D^0(x_1, t)\frac{\partial \bar{c}}{\partial x_1}, \tag{4.2}$$

where D^0 is the zeroth-order spatial and temporal moment. This is also sometimes called the K-model where the local eddy diffusivity, K, may be generalized to be a tensor to account for anisotropy (Kraichnan (1987); Georgopoulos and Seinfeld (1989); Yoshizawa (1985)). The purely local model is the first term of the Taylor series expansion in Equation (3.9). Figure 4.1a shows an example of the eddy diffusivity kernel shape.

4.2.2 Explicit model

If the Boussinesq locality approximation is not valid, one may consider higher-order terms of the expansion as nonlocal corrections to the local model. For example, including the first- and second-order spatial moments and first-order temporal moment of the nonlocal eddy diffusivity results in

$$-\overline{u_1' c'}(x_1, t) = D^0(x_1, t)\frac{\partial \bar{c}}{\partial x_1} + D^{1_s}(x_1, t)\frac{\partial^2 \bar{c}}{\partial x_1^2} + D^{2_s}(x_1, t)\frac{\partial^3 \bar{c}}{\partial x_1^3} + D^{1_t}(x_1, t)\frac{\partial^2 \bar{c}}{\partial t \partial x_1}. \tag{4.3}$$

This type of model form has been investigated by Hamba (1995, 2004). In general, addition of these higher-order terms may not guarantee improvement of the model as demonstrated in Section 4.3.2 and by Mani and Park (2021). Non-convergence of the Kramers–Moyal expansion has also been

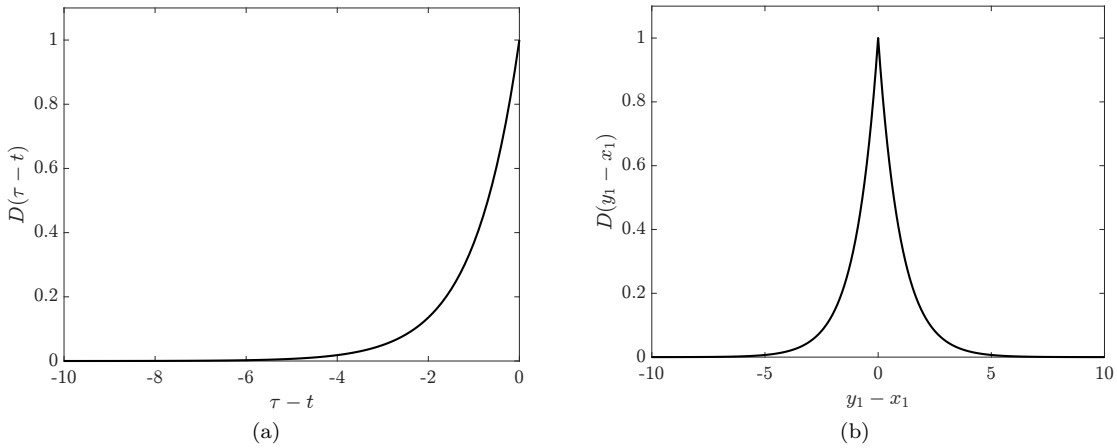

Figure 4.2: (a) Example temporally nonlocal eddy diffusivity kernel in Equation (4.4) with $\alpha = \beta = 1$. (b) Example spatially nonlocal eddy diffusivity kernel in Equation (4.7) with $\alpha = \beta = 1$.

previously shown in the context of molecular dynamics (Pawula (1967)). This lack of convergence may be explained by examining the eddy diffusivity kernel shape as shown in Figure 4.1b. The leading term in Equation (4.3) implies a Dirac delta function as the eddy diffusivity kernel, and adding higher-order corrections is equivalent to adding higher-order derivatives of Dirac delta functions; these corrections are still highly local and may not adequately capture the smooth shape of the nonlocal eddy diffusivity.

4.2.3 A temporally nonlocal model

A simple nonlocal eddy diffusivity kernel that is smooth and can be represented with a partial differential equation is a decaying exponential function. For example, if the flow is statistically stationary and homogeneous, a simple eddy diffusivity that is local in space but nonlocal in time is

$$D(y_1 - x_1, \tau - t) = \delta(y_1 - x_1)\frac{\beta}{\alpha}\exp^{-(t-\tau)/\alpha}, \tag{4.4}$$

where α and β are constants and the history effect of the eddy diffusivity decays exponentially backward in time. Figure 4.2a shows an example of the nonlocal eddy diffusivity kernel. The scalar flux is governed by

$$\left[\alpha\frac{\partial}{\partial t} + 1\right](-\overline{u_1'c'}) = \beta\frac{\partial \bar{c}}{\partial x_1}, \tag{4.5}$$

and as shown by Georgopoulos and Seinfeld (1989), the mean scalar is governed by the hyperbolic telegrapher's equation:

$$\alpha\frac{\partial^2 \bar{c}}{\partial t^2} + \frac{\partial \bar{c}}{\partial t} = \beta\frac{\partial^2 \bar{c}}{\partial x_1^2}, \tag{4.6}$$

which was first derived by Goldstein (1951) for a one-dimensional correlated random walk.

4.2.4 A spatially nonlocal model

Similarly, a simple spatially nonlocal eddy diffusivity kernel that is smooth and can be represented by a partial differential equation is a double-sided exponential function. For example, if the flow is statistically stationary and homogeneous, a simple eddy diffusivity that is nonlocal in space but local in time is

$$D(y_1 - x_1, \tau - t) = \frac{\beta}{\alpha} e^{-|y_1 - x_1|/\alpha} \delta(\tau - t), \tag{4.7}$$

where α and β are constants and the spatial nonlocality of the eddy diffusivity is captured as a double-sided exponential. Figure 4.2b shows an example of the nonlocal eddy diffusivity kernel. As shown by Hamba (2004), the scalar flux is governed by

$$\left[1 - \alpha^2 \frac{\partial^2}{\partial x_1^2}\right] (-\overline{u_1' c'}) = 2\beta \frac{\partial \bar{c}}{\partial x_1}. \tag{4.8}$$

Moreover, the shape of the nonlocal eddy diffusivity kernel as shown in Figure 4.2b often qualitatively resembles the true nonlocal eddy diffusivity kernel, for example, as shown in Figure 3.1b.

4.2.5 Matched moment inverse (MMI) operators

For many flows, the measured nonlocal eddy diffusivity may not be exactly an exponential in time or space (Hamba (2004, 2005); Park and Mani (2023a)). However, it may still be appropriate to model the shape of the nonlocal eddy diffusivity as exponential functions or combinations of exponential functions. For such flows, the key question we seek to address is how to appropriately determine the coefficients. For this purpose, we introduce *matched moment inverse* (MMI) operators which systematically allow determination of the coefficients using, as the name suggests, only measured moments of the nonlocal eddy diffusivity rather than the full measured nonlocal eddy diffusivity. For a statistically stationary and homogeneous flow, consider a model for a spatiotemporally nonlocal eddy diffusivity formed by combining Equation (4.5) and (4.8) (and more generally in which, higher-order terms may be included):

$$\left[a_3 \frac{\partial}{\partial t} + \left(1 + a_1 \frac{\partial}{\partial x_1} + a_2 \frac{\partial^2}{\partial x_1^2}\right)\right] (-\overline{u_1' c'}) = a_0 \frac{\partial \bar{c}}{\partial x_1}. \tag{4.9}$$

The coefficients, a_i, will be determined by matching up to the second spatial moment and first temporal moment of the nonlocal eddy diffusivity. Rearranging,

$$-\overline{u_1' c'} = \left[1 + a_1 \frac{\partial}{\partial x_1} + a_2 \frac{\partial^2}{\partial x_1^2} + a_3 \frac{\partial}{\partial t}\right]^{-1} a_0 \frac{\partial \bar{c}}{\partial x_1}, \tag{4.10}$$

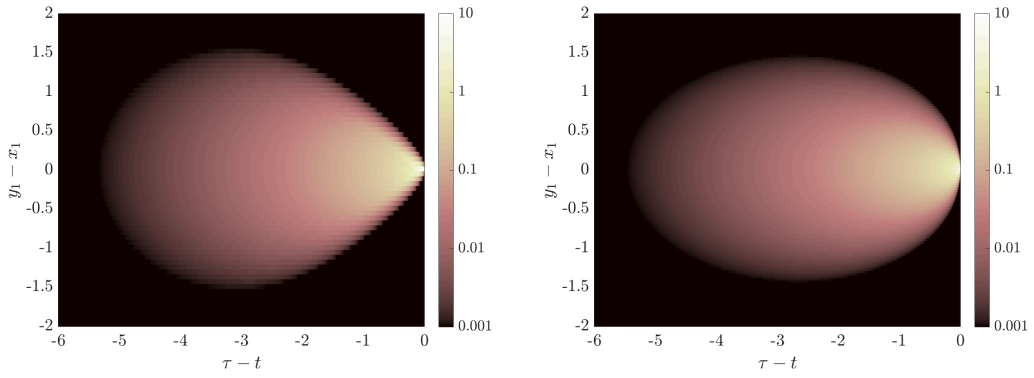

Figure 4.3: (a) The exact spatiotemporally nonlocal eddy diffusivity, $D(y_1 - x_1, \tau - t)$, for the homogeneous model problem in Section 4.3.1. (b) The modeled eddy diffusivity using MMI.

and Taylor series expanding the inverse operator on the right-hand-side leads to

$$-\overline{u_1' c'} = \left[1 - a_1 \frac{\partial}{\partial x_1} - a_2 \frac{\partial^2}{\partial x_1^2} + a_1 \frac{\partial}{\partial x_1}\left(a_1 \frac{\partial}{\partial x_1}\right) + \cdots - a_3 \frac{\partial}{\partial t} + \ldots\right] a_0 \frac{\partial \overline{c}}{\partial x_1}. \tag{4.11}$$

Because the flow is statistically stationary and homogeneous, the coefficients are constants. To match the first few moments of the modeled nonlocal eddy diffusivity with the exact measured moments, compare the expansion in (4.11) with the Taylor series expansion of the nonlocal eddy diffusivity in (3.9) and simplified for a one-dimensional problem in (3.20). This leads to the coefficients: $a_0 = D^0$, $a_1 = -D^{1_s}/D^0$, $a_2 = -D^{2_s}/D^0 + (D^{1_s}/D^0)^2$, and $a_3 = -D^{1_t}/D^0$. After determination of the coefficients, the model form in Equation (4.9) is used for the scalar flux. The bracketed operator on the left-hand-side of (4.9) acting on the scalar flux is the MMI operator and may be generalized to include higher-order derivatives and mixed derivatives.

Note that while the explicit model in Equation (4.3) also matches the low-order measured moments of the eddy diffusivity, the shape of the nonlocal eddy diffusivity is not properly captured and leads to convergence issues. By truncating the Taylor series expansion, each additional term in the explicit model in Equation (4.3) adds a highly local correction and an infinite series is needed for convergence. By keeping an infinite Taylor series in Equation (4.11) that smoothly approximates the nonlocal eddy diffusivity as an exponential function in time and a double-sided exponential function in space, MMI operators better approximate the true shape of the nonlocal eddy diffusivity. For example, Figure 4.3a shows the measured spatiotemporally nonlocal eddy diffusivity for the homogeneous model problem described in Section 4.3, and Figure 4.3b shows the MMI-constructed spatiotemporally nonlocal eddy diffusivity. The two nonlocal eddy diffusivities have the same zeroth-, first-, and second-order spatial and first-order temporal moments.

For inhomogeneous flows, the moments of the eddy diffusivity are functions of space, and correspondingly the coefficients of the MMI model will also be functions of space. In this case, the MMI coefficients cannot analytically be matched with the eddy diffusivity moments since an infinite number of higher-order derivatives of the unknown coefficients appear in the Taylor series expansion of the MMI operator. We present a modified numerical procedure for determining the MMI coefficients in order to match the low-order moments of the eddy diffusivity.

For illustration, consider an inhomogeneous flow in which the eddy diffusivity is spatially nonlocal:

$$-\overline{u_1'c'}(x_1) = \int_{y_1} D(x_1, y_1) \frac{\mathrm{d}\bar{c}}{\mathrm{d}x_1}\bigg|_{y_1} \mathrm{d}y_1. \tag{4.12}$$

The MMI model including up to the second-order spatial moment is

$$\left[1 + a_1(x_1)\frac{\mathrm{d}}{\mathrm{d}x_1} + a_2(x_1)\frac{\mathrm{d}^2}{\mathrm{d}x_1^2}\right](-\overline{u_1'c'}) = a_0(x_1)\frac{\mathrm{d}\bar{c}}{\mathrm{d}x_1}, \tag{4.13}$$

where the coefficients, a_i, are now also functions of x_1 and yet to be determined. The Taylor series expansion of the nonlocal eddy diffusivity is

$$-\overline{u_1'c'}(x_1) = \left[D^0(x_1) + D^{1_s}(x_1)\frac{\mathrm{d}}{\mathrm{d}x_1} + D^{2_s}(x_1)\frac{\mathrm{d}^2}{\mathrm{d}x_1^2} + \dots\right]\frac{\mathrm{d}\bar{c}}{\mathrm{d}x_1}, \tag{4.14}$$

where the moments of the eddy diffusivity are given by

$$D^0 = \int_{y_1} D(x_1, y_1)\mathrm{d}y_1, \tag{4.15a}$$

$$D^{1_s} = \int_{y_1} (y_1 - x_1)D(x_1, y_1)\mathrm{d}y_1, \tag{4.15b}$$

$$D^{2_s} = \int_{y_1} \frac{1}{2}(y_1 - x_1)^2 D(x_1, y_1)\mathrm{d}y_1. \tag{4.15c}$$

To obtain the low-order moments of the eddy diffusivity using IMFM, the forcing is applied such that $\bar{c} = x_1$, $\bar{c} = x_1^2/2$, $\bar{c} = x_1^3/6$, etc. Substituting these $\bar{c}(x_1)$ into Equation (4.14) and post-processing the corresponding $-\overline{u_1'c'}|_{\bar{c}}$ leads to:

$$-\overline{u_1'c'}|_{\bar{c}=x_1} = D^0(x_1), \tag{4.16a}$$

$$-\overline{u_1'c'}|_{\bar{c}=x_1^2/2} = x_1 D^0(x_1) + D^{1_s}(x_1), \tag{4.16b}$$

$$-\overline{u_1'c'}|_{\bar{c}=x_1^3/6} = \frac{x_1^2}{2}D^0(x_1) + x_1 D^{1_s}(x_1) + D^{2_s}(x_1). \tag{4.16c}$$

If $-\overline{u_1'c'}|_{\bar{c}}$ are directly available from IMFM, then one should use them directly. Otherwise, if only the moments are available, one should form $-\overline{u_1'c'}|_{\bar{c}}$ using the expressions above in Equations (4.16a)-(4.16c). $-\overline{u_1'c'}|_{\bar{c}}$ contains exact information about the low-order moments of the true eddy diffusivity

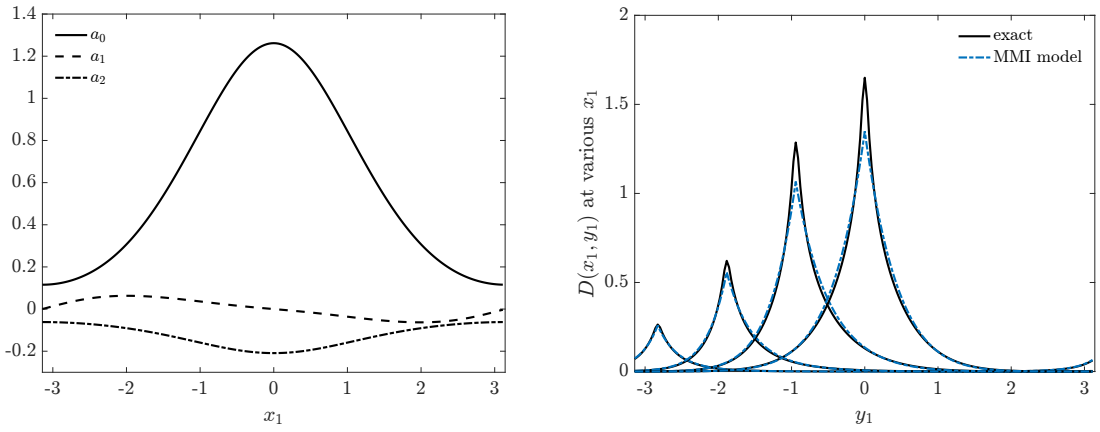

Figure 4.4: For the inhomogeneous model problem with periodic boundaries in Section 4.4.1: (a) MMI coefficients for Equation (4.13). (b) The eddy diffusivity kernel from the MMI model closely approximates the exact eddy diffusivity kernel as shown for various x_1 locations.

that one can now incorporate into the MMI model in Equation (4.13). One can form three equations for $a_0(x_1)$, $a_1(x_1)$, and $a_2(x_1)$ by substituting $\bar{c} = x_1$, $\bar{c} = x_1^2/2$, and $\bar{c} = x_1^3/6$ and the corresponding $-\overline{u_1' c'}|_{\bar{c}}$ from Equations (4.16a)-(4.16c) into Equation (4.13):

$$-\overline{u_1' c'}|_{\bar{c}=x_1} + a_1 \frac{\mathrm{d}}{\mathrm{d}x_1}(-\overline{u_1' c'}|_{\bar{c}=x_1}) + a_2 \frac{\mathrm{d}^2}{\mathrm{d}x_1^2}(-\overline{u_1' c'}|_{\bar{c}=x_1}) = a_0, \tag{4.17a}$$

$$-\overline{u_1' c'}|_{\bar{c}=x_1^2/2} + a_1 \frac{\mathrm{d}}{\mathrm{d}x_1}(-\overline{u_1' c'}|_{\bar{c}=x_1^2/2}) + a_2 \frac{\mathrm{d}^2}{\mathrm{d}x_1^2}(-\overline{u_1' c'}|_{\bar{c}=x_1^2/2}) = a_0 x_1, \tag{4.17b}$$

$$-\overline{u_1' c'}|_{\bar{c}=x_1^3/6} + a_1 \frac{\mathrm{d}}{\mathrm{d}x_1}(-\overline{u_1' c'}|_{\bar{c}=x_1^3/6}) + a_2 \frac{\mathrm{d}^2}{\mathrm{d}x_1^2}(-\overline{u_1' c'}|_{\bar{c}=x_1^3/6}) = a_0 \frac{x_1^2}{2}. \tag{4.17c}$$

This linear system of equations for a_0, a_1, and a_2 is solved point-wise to obtain the MMI coefficients at each x_1 location. For example, Figure 4.4a shows the coefficients of the MMI model for the inhomogeneous model problem with periodic boundaries in Section 4.4.1. Figure 4.4b shows the exact spatially nonlocal eddy diffusivity and the MMI-constructed eddy diffusivity.

The suggested use of MMI is not the only way to mimic the nonlocal behavior of the eddy diffusivity. For example, Hamba (2004) first obtained the exact nonlocal eddy diffusivity and then constructed alternative inverse operators by examining their shape against the exact eddy diffusivity kernel shape. The suggested MMI is an alternative that substantially reduces the number of DNS needed by focusing only on a limited number of moments of the nonlocal eddy diffusivity to characterize the kernel shape, while providing a systematic path for determining the coefficients of the inverse operator.

4.3 Example MMI models for homogeneous flows

4.3.1 Model problem: Dispersion by a parallel flow

As a simple example, consider the dispersion of a passive scalar by a homogeneous, laminar, parallel flow. This problem was first introduced by Taylor (1953) and revisited by Mani and Park (2021) to demonstrate how MFM can be used to obtain the exact nonlocal eddy diffusivity. Moreover, this problem is a simple example in which the scale separation assumption of the Boussinesq approximation does not hold, requiring the consideration of nonlocal effects. Specifically, consider a two-dimensional problem with the governing equation:

$$\frac{\partial c}{\partial t} + \frac{\partial}{\partial x_1}(u_1 c) + \frac{\partial}{\partial x_2}(u_2 c) = D_M \left(\frac{\partial^2 c}{\partial x_1^2} + \frac{\partial^2 c}{\partial x_2^2} \right), \tag{4.18}$$

where $c(x_1, x_2, t)$ is a passive scalar, D_M is the molecular diffusivity, and u_j is the parallel flow velocity:

$$u_1 = U \cos\left(\frac{2\pi}{L_2} x_2 \right), \quad u_2 = 0. \tag{4.19}$$

The domain is $-\infty < x_1 < \infty$ and $0 \leq x_2 < L_2$ with periodic boundary conditions in x_2. Nondimensionalizing x_2 by $L_2/(2\pi)$, x_1 by $UL_2^2/(4\pi^2 D_M)$, and t by $L_2^2/(4\pi^2 D_M)$ leads to the following nondimensionalized equation:

$$\frac{\partial c}{\partial t} + \frac{\partial}{\partial x_1}(\cos(x_2) c) = \epsilon^2 \frac{\partial^2 c}{\partial x_1^2} + \frac{\partial^2 c}{\partial x_2^2}, \tag{4.20}$$

where $\epsilon = 2\pi D_M/(L_2 U)$ is the only nondimensional parameter. As in Mani and Park (2021), for simplification we consider $\epsilon = 0$, corresponding to the limit of large Peclet number, i.e., assume the advective flux is much greater than the diffusive flux in the x_1 direction. The governing equation for the homogeneous example problem is

$$\frac{\partial c}{\partial t} + \frac{\partial}{\partial x_1}(\cos(x_2) c) = \frac{\partial^2 c}{\partial x_2^2}. \tag{4.21}$$

For this problem, averaging is taken over the x_2 direction, i.e.,

$$\bar{c}(x_1, t) = \frac{1}{L_2} \int_0^{L_2} c(x_1, x_2, t) \mathrm{d}x_2. \tag{4.22}$$

Correspondingly, the mean scalar transport equation for this problem is

$$\frac{\partial \bar{c}}{\partial t} + \frac{\partial}{\partial x_1}(\overline{u_1' c'}) = 0, \tag{4.23}$$

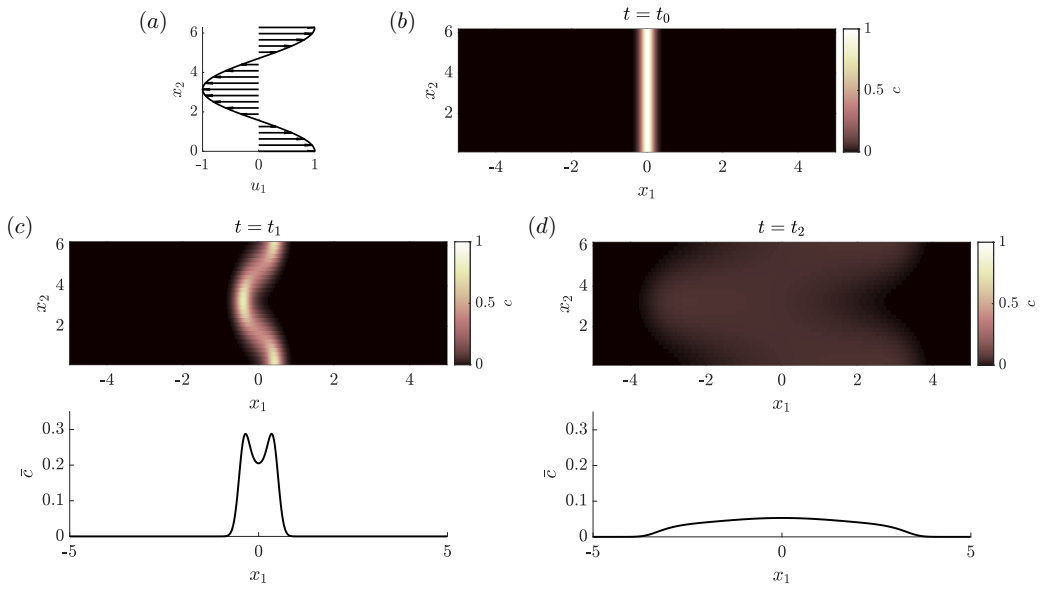

Figure 4.5: (a) The velocity profile for the homogeneous, parallel flow ($u_1 = \cos(x_2)$, $u_2 = 0$). (b) An initial condition corresponding to the release of a narrow band of passive scalar in the center of the domain ($c(t = 0) = \exp(-x_1^2/0.025)$). (c) The dispersed scalar field, $c(x_1, x_2, t)$, and x_2-averaged field, $\bar{c}(x_1, t)$, at time, $t_1 = 0.5$. (d) $c(x_1, x_2, t)$ and $\bar{c}(x_1, t)$ at a later time, $t_2 = 4$.

where $\overline{u_1' c'} = \overline{\cos(x_2) c'}$ is the unclosed scalar flux. The mean advection, $\partial/\partial x_1(\bar{u}_1 \bar{c})$, does not appear in (4.23) since $\bar{u}_1 = \overline{\cos(x_2)} = 0$. The mean diffusion, $\partial^2 \bar{c}/\partial x_2^2$, also drops from (4.23) due to averaging over x_2 and periodic boundary conditions.

Figure 4.5a shows the prescribed velocity profile. Figure 4.5b-d show the initial condition, $c(t = 0) = \exp(-x_1^2/0.025)$, and time snapshots of the dispersed scalar field, $c(x_1, x_2, t)$, and averaged field, $\bar{c}(x_1, t)$ solved using DNS. The goal is to predict the complex behavior of $\bar{c}(x_1, t)$ using a one-dimensional partial differential equation. Mani and Park (2021) also attempted to model this problem by finding the nonlocal eddy diffusivity in Fourier space in both space and time using MFM, analytically fitting the operator in Fourier space, and then transforming it back into physical space. We revisit this problem in order to develop a method that does not need the full nonlocal eddy diffusivity and results in an operator that does not involve the operational square root.

4.3.2 Model comparison

We compare some of the models in Section 4.2 with MMI models for the homogeneous problem. The moments of the nonlocal eddy diffusivity for this problem may be obtained numerically using IMFM or analytically using Taylor's approach for dispersion by a parallel flow (Taylor (1953)) and

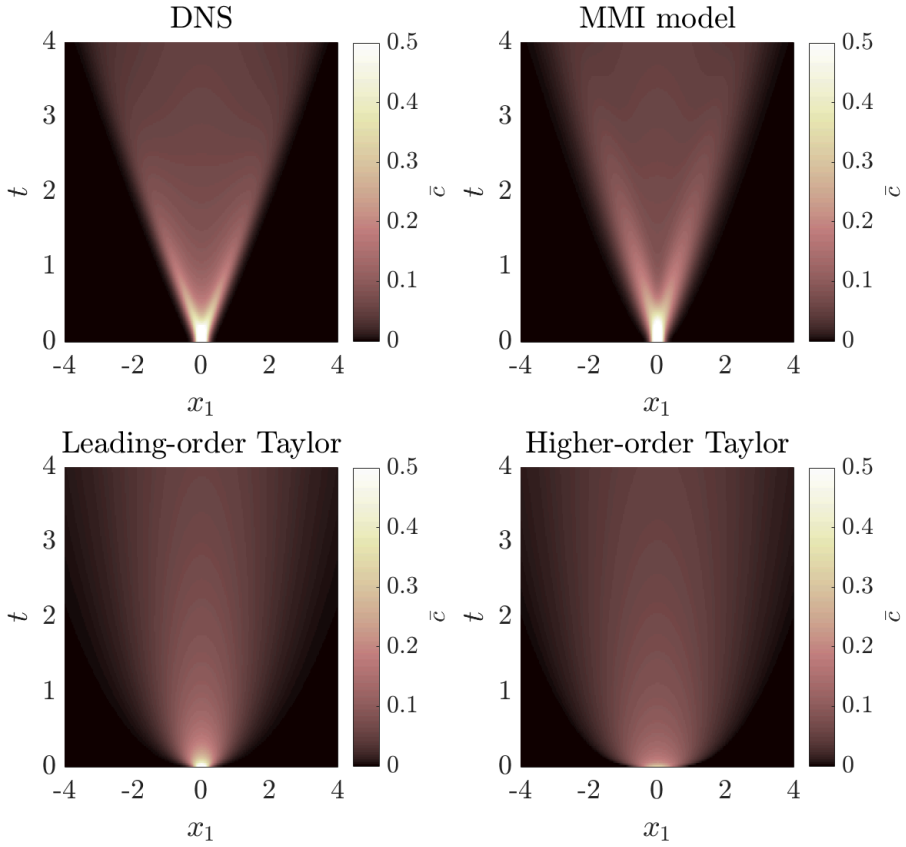

Figure 4.6: Model comparison of the averaged field, $\bar{c}(x_1, t)$, using the initial condition $c(t = 0) = \exp(-x_1^2/0.025)$. The spatiotemporal MMI model in Equation (4.28) closely captures the spread of the averaged field, whereas the leading-order Taylor model and higher-order Taylor model overpredict the spread of the averaged field.

its extension by Aris (1960). Taylor's approach uses the transport equation for the fluctuations, c', and applies the same length/time scale separation assumptions as the Boussinesq approximation to find the leading-order term balance, resulting in the Boussinesq model. Higher-order moments are found by considering perturbative corrections to the leading-order term balance, resulting in models similar to the explicit model in Section 4.2. The first few moments of the nonlocal eddy diffusivity are $D^0 = 1/2$, $D^{1_s} = 0$, $D^{2_s} = 1/32$, and $D^{1_t} = -1/2$.

The Boussinesq model or leading-order Taylor model is

$$-\overline{u_1' c'} = \frac{1}{2} \frac{\partial \bar{c}}{\partial x_1}, \tag{4.24}$$

and the explicit model or higher-order Taylor model is

$$-\overline{u_1' c'} = \frac{1}{2}\frac{\partial \bar{c}}{\partial x_1} + \frac{1}{32}\frac{\partial^3 \bar{c}}{\partial x_1^3} - \frac{1}{2}\frac{\partial^2 \bar{c}}{\partial t \partial x_1}. \tag{4.25}$$

As discussed in Mani and Park (2021), for this problem, the higher-order Taylor model is modified such that the last term in Equation (4.25) does not appear and the signs of the coefficients are consistent with the energy-damping mechanism:

$$-\overline{u_1' c'} = \frac{1}{2}\frac{\partial \bar{c}}{\partial x_1} - \frac{7}{32}\frac{\partial^3 \bar{c}}{\partial x_1^3}. \tag{4.26}$$

The MMI model only incorporating temporal nonlocality and whose coefficients are determined using the procedure in Section 4.2 is

$$\left[\frac{\partial}{\partial t} + 1\right](-\overline{u_1' c'}) = \frac{1}{2}\frac{\partial \bar{c}}{\partial x_1}, \tag{4.27}$$

and similarly the MMI model incorporating spatiotemporal nonlocality is

$$\left[\frac{\partial}{\partial t} + \left(1 - \frac{1}{16}\frac{\partial^2}{\partial x_1^2}\right)\right](-\overline{u_1' c'}) = \frac{1}{2}\frac{\partial \bar{c}}{\partial x_1}. \tag{4.28}$$

Figure 4.3a shows the exact measured nonlocal eddy diffusivity, and Figure 4.3b shows the shape of the nonlocal eddy diffusivity captured by the spatiotemporal MMI model in Equation (4.28). Appendix B.3 details how these spatiotemporal eddy diffusivities are computed.

Figure 4.6 shows the evolution of the averaged field, $\bar{c}(x_1, t)$. Compared with the DNS solution, the spatiotemporal MMI model closely predicts the spread of the averaged field. The leading-order Taylor model causes the mean field to spread out too quickly, indicating the importance of including nonlocality. The higher-order Taylor model performs even worse, which demonstrates that adding a finite number of higher-order corrections from an infinite Taylor series expansion of the eddy diffusivity may not guarantee model improvement. Figure 4.7 shows a comparison between the leading-order Taylor model and higher-order Taylor model at an early time, $t = 0.5$, and a later time, $t = 4$.

Figure 4.8 shows a comparison between the MMI model incorporating temporal nonlocality and the MMI model incorporating spatiotemporal nonlocality. Both models capture the qualitative shape of the DNS solution better than either the leading-order Taylor model or higher-order Taylor model at early times. The spatiotemporal MMI model reasonably matches the DNS solution whereas the temporal MMI model shows some overshoot. The spatiotemporal MMI model excellently captures the late-time solution. All four models are expected to perform well at late times in the limit of slowly-varying mean field, i.e., where the Boussinesq approximation becomes valid. However, in this case, the spatiotemporal MMI model performs well even outside of this limit due to its close

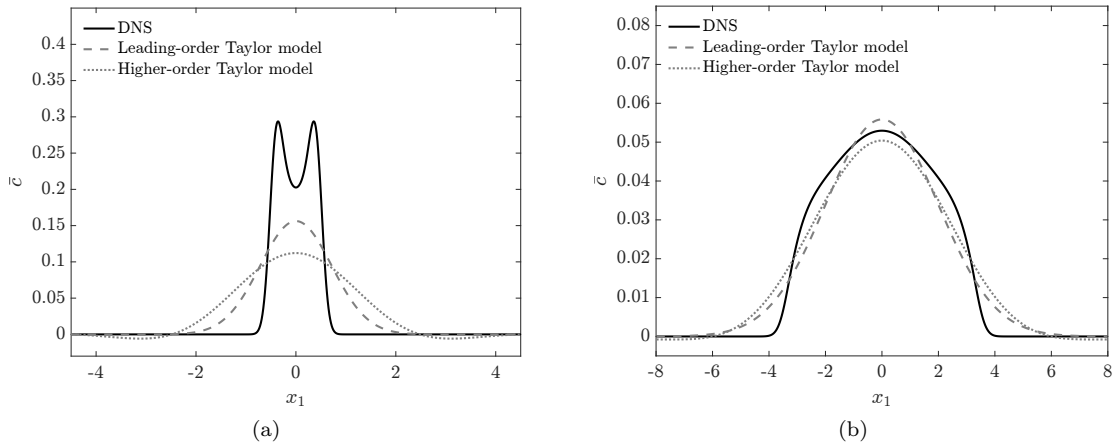

Figure 4.7: Model comparison of leading-order Taylor model and higher-order Taylor model at (a) early time, $t = 0.5$, and (b) late time, $t = 4$.

approximation of the true nonlocal eddy diffusivity as shown in Figure 4.3. A discussion of the error due to the inclusion of only the low-order moments in the spatiotemporal MMI model is included in Appendix B.4. Note also that the higher-order Taylor model actually produces a negative solution, whereas the MMI models do not have this issue.

4.3.3 Comparison with other nonlocal eddy diffusivity models

We now compare the spatiotemporal MMI model in Equation (4.28) with another nonlocal model presented in Mani and Park (2021) for the same homogeneous problem. Mani and Park (2021) approximate the nonlocal eddy diffusivity by fitting an operator to match MFM data in the limits of $k, \omega \to 0$ and $k, \omega \to \infty$, where k is the wavenumber corresponding to the Fourier transform in x_1 direction and ω the frequency corresponding to the Fourier transform in time. Transforming back into physical space, the unclosed scalar flux is modeled as (Mani and Park (2021))

$$-\frac{\partial}{\partial x_1}\overline{u_1' c'}(x_1,t) = \left[-\sqrt{\left(\mathcal{I}+\frac{\partial}{\partial t}\right)^2 - \frac{\partial^2}{\partial x_1^2}} + \left(\mathcal{I}+\frac{\partial}{\partial t}\right)\right]\bar{c}(x_1,t), \tag{4.29}$$

where $\mathcal{I}$ is the identity operator. Note that this MFM-inspired, eddy diffusivity operator does not have the cost-saving advantages of using MMI since any numerical implementation of the model in (4.29) would require nonlocal operations in physical space involving full matrices. We show a comparison of this MFM-inspired model with the MMI model to address a more general modeling question: When adding nonlocal corrections to the local model, is it more appropriate to match the limits of large k and ω or the low-order moments of the nonlocal eddy diffusivity?

To illustrate the effect of matching the limits of large k and ω on the eddy diffusivity, consider

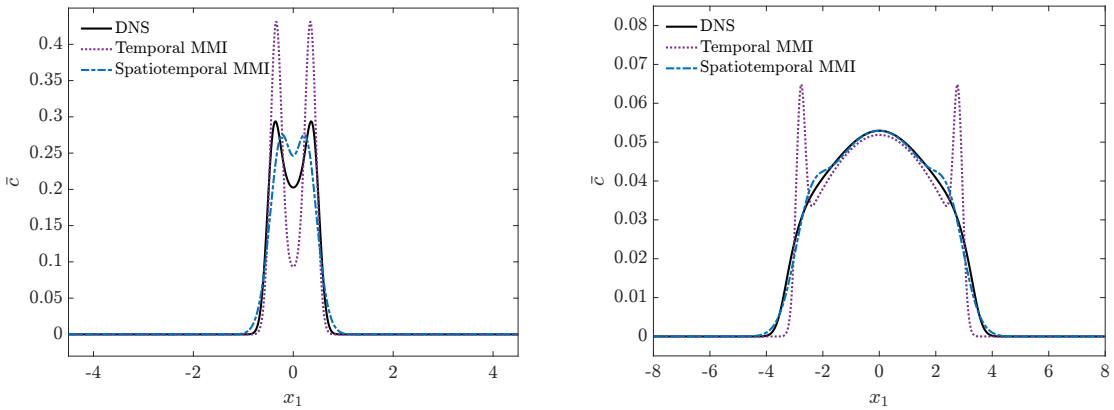

Figure 4.8: Model comparison of the temporal MMI model and spatiotemporal MMI model at (a) early time, $t = 0.5$, and (b) late time, $t = 4$.

the Taylor series expansion in Equation (3.9), simplified for the homogeneous problem in 4.3.1:

$$-\overline{u_1' c'} = \left[D^0 + D^{1_s} \frac{\partial}{\partial x_1} + D^{2_s} \frac{\partial^2}{\partial x_1^2} + \cdots + D^{1_t} \frac{\partial}{\partial t} + \cdots \right] \frac{\partial \bar{c}}{\partial x_1}, \tag{4.30}$$

where the moments of the eddy diffusivity are constants. Taking the Fourier transform leads to:

$$-\widehat{\overline{u_1' c'}} = \left[D^0 + ikD^{1_s} - k^2 D^{2_s} + \cdots + i\omega D^{1_t} + \cdots \right] ik\hat{\bar{c}}. \tag{4.31}$$

This shows that matching the limit of $k, \omega \to 0$ is equivalent to matching the zeroth-order moment of the eddy diffusivity, D^0. Matching the first and second moments of the eddy diffusivity, as done by MMI models, adds corrections in the limit of small k and ω. This prioritizes better capturing smooth and slowly-varying solutions. Whereas, matching large k and ω, as done in Mani and Park (2021), is equivalent to matching high-order moments of the nonlocal eddy diffusivity. This would prioritize capturing sharp and quickly-varying features in the solutions.

For illustration, Figure 4.9a shows a comparison of the exact and modeled spatially nonlocal eddy diffusivities for the homogeneous problem (equivalent to the spatiotemporally nonlocal eddy diffusivities in Figure 4.3a and 4.3b integrated over τ). Figure 4.9b shows the Fourier transform of the spatially nonlocal eddy diffusivities. Because the exact and MMI-modeled spatially nonlocal eddy diffusivities were first obtained in physical space and then Fourier transformed, there is some numerical discretization error due to the use of second-order finite differences; however, the truncated plotting window shown in Fourier space is converged. The eddy diffusivity for the MFM-inspired model is obtained in Fourier space analytically by Fourier transforming Equation (4.29) and

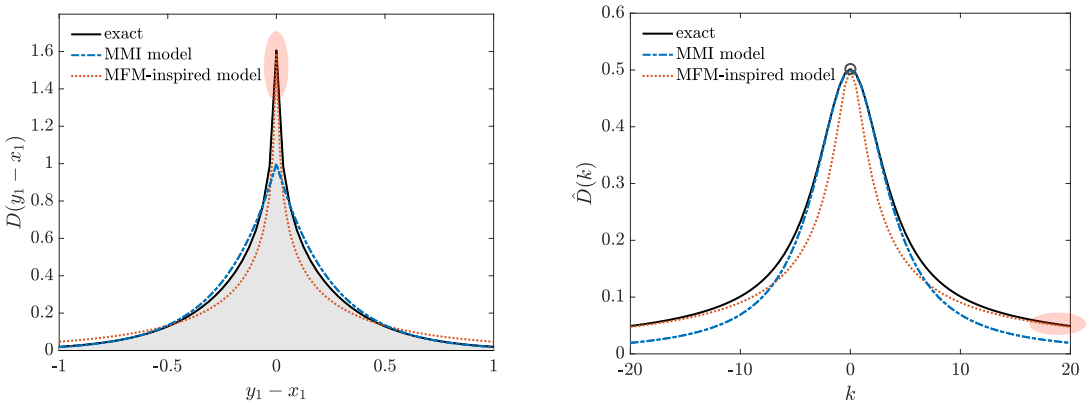

Figure 4.9: Comparison of the spatially nonlocal eddy diffusivities (equivalent to the spatiotemporally nonlocal eddy diffusivities integrated over τ) (a) in physical space and (b) in Fourier space.

evaluating at $\omega = 0$ (equivalent to integration over τ):

$$\hat{D}(k) = \frac{-\sqrt{1+k^2}+1}{-k^2}. \tag{4.32}$$

The eddy diffusivity of the MFM-inspired model in physical space is then obtained by taking the inverse Fourier transform of (4.32).

In Figure 4.9a, the shaded area in gray under the eddy diffusivity, D^0, corresponds to $\hat{D}(0)$ in Fourier space in Figure 4.9b. The first spatial moment of eddy diffusivity, D^{1_s}, is related to the first derivative of the kernel in Fourier space, $\frac{\mathrm{d}}{\mathrm{d}k}\hat{D}(0)$, and so forth. In Fourier space, the MMI model matches the shape of the eddy diffusivity for small k as shown in Figure 4.9b. Whereas, the high wavenumber region, shaded in red in Figure 4.9b, corresponds to the peak in physical space at $D(0)$ which involves a sharp feature in Figure 4.9a. This peak at $D(0)$ is correspondingly captured by the MFM-inspired model. Matching low-order moments better captures the overall shape of the nonlocal eddy diffusivity in physical space, whereas matching large k and ω captures the large wavelength/frequency features of the eddy diffusivity.

Figure 4.10 shows a solution comparison between the MMI model in Equation (4.28) and the MFM-inspired model at early and late time. At early time, when the solution is dominated by a small-scale feature that quickly disperses, the MFM-inspired model performs better. For late time, when the solution features are smooth and both models are expected to perform well, the MMI model performs better than MFM-inspired model. Appendix B.5 shows a comparison with a simple fractional-order closure operator (Mehta et al. (2019); Song and Karniadakis (2018); Di Leoni et al. (2021)), which produces inferior results to both the MMI and MFM-inspired models. This is expected since a simple fractional-order Laplacian cannot capture the limits of large k and ω or low-order corrections to the leading moment of the eddy diffusivity.

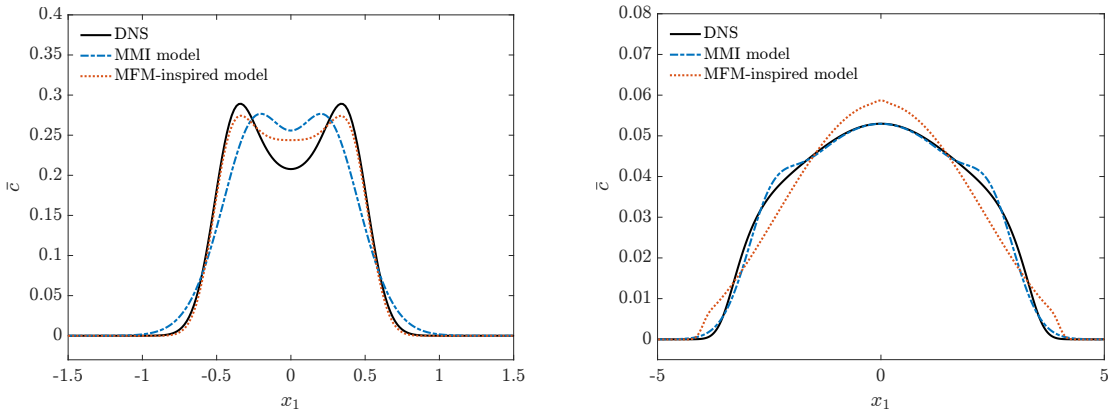

Figure 4.10: MMI model and MFM-inspired model comparison at (a) early time, $t = 0.5$, and (b) late time, $t = 4$.

Whether a model should match the limits of k and ω or the low-order moments of the nonlocal eddy diffusivity depends on the problem of interest. If there is a singularity or very sharp feature in the solution, then a model matching the limits of k and ω may be more appropriate. Otherwise, if the solution is reasonably smooth (as is true for many practical applications), then a model matching the low-order moments is more appropriate.

4.4 Example MMI models for inhomogeneous flows

We begin with an inhomogeneous example with periodic boundary conditions, and then discuss wall-bounded flows and the challenges of determining the MMI coefficients in the near-wall region.

4.4.1 Inhomogeneous problem with periodic boundary conditions

Consider a two-dimensional domain corresponding to the cross-section of a channel with periodic boundary conditions at the left and right walls at $x_1 = \pm\pi$, and a no flux condition, $\partial c/\partial x_2 = 0$, at the top and bottom walls at $x_2 = 0, 2\pi$. The flow consists of two vortices given by the velocity field:

$$u_1 = \frac{1}{2}[2 + \cos(x_1)]\cos(x_2), u_2 = \frac{1}{2}\sin(x_1)\sin(x_2). \tag{4.33}$$

Streamlines of the velocity field are shown in Figure 4.11a. The steady, governing equation is

$$\frac{\partial}{\partial x_1}(u_1 c) + \frac{\partial}{\partial x_2}(u_2 c) = \epsilon^2 \frac{\partial^2 c}{\partial x_1^2} + \frac{\partial^2 c}{\partial x_2^2} + f, \tag{4.34}$$

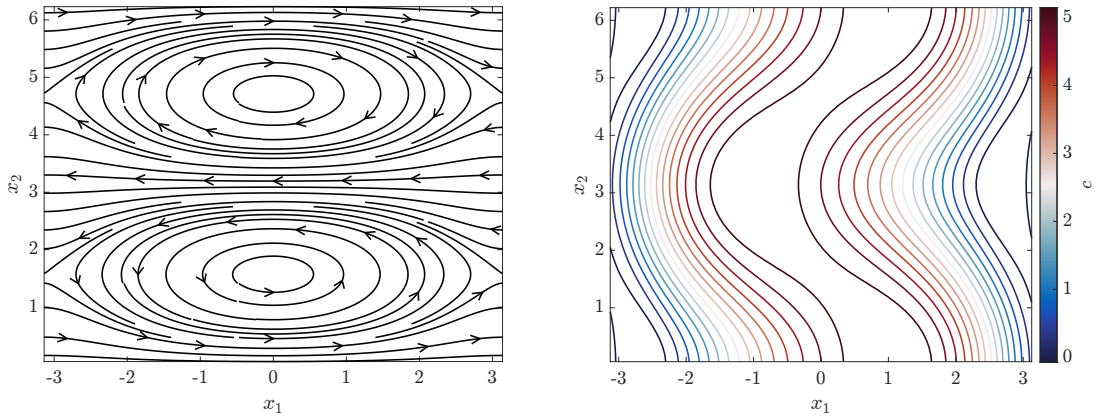

Figure 4.11: (a) Streamlines of the velocity field in Equation (4.33). (b) Contour plot of $c(x_1, x_2)$ from DNS.

where f is an external source function. The parameter, ϵ^2, results from directional nondimensionalization as in Section 4.3.1. For this example problem, we consider $\epsilon^2 = 0.05$ and f to be an oscillatory source function given by $f = \cos(x_1)$.

Figure 4.11b shows contours of $c(x_1, x_2)$ from DNS. The problem is discretized using second-order central difference on a uniform staggered mesh with $N_1 = 200$ grid points in x_1 and $N_2 = 50$ grid points in x_2. Due to the boundary conditions of the problem, $c(x_1, x_2)$ can arbitrarily be shifted by a constant. Hence, there is an additional constraint such that at the first point in x_1, the average of $c(x_1, x_2)$ over x_2 is zero.

As in Section 4.3.1, averaging is defined in the x_2 direction as

$$\bar{c}(x_1) = \frac{1}{L_2} \int_0^{L_2} c(x_1, x_2) \mathrm{d}x_2, \tag{4.35}$$

where $L_2 = 2\pi$. The corresponding mean scalar transport equation for this problem is

$$\frac{\mathrm{d}}{\mathrm{d}x_1} \overline{u_1' c'} = \epsilon^2 \frac{\mathrm{d}^2 \bar{c}}{\mathrm{d}x_1^2} + \bar{f}. \tag{4.36}$$

The MMI model matching up to the second-order spatial moment of the nonlocal eddy diffusivity is:

$$\left[1 + a_1(x_1) \frac{\mathrm{d}}{\mathrm{d}x_1} + a_2(x_1) \frac{\mathrm{d}^2}{\mathrm{d}x_1^2}\right] (-\overline{u_1' c'}) = a_0(x_1) \frac{\mathrm{d}\bar{c}}{\mathrm{d}x_1}, \tag{4.37}$$

where the procedure for determining the coefficients is described in Section 4.2. Figure 4.4a shows the coefficients for the MMI model, and Figure 4.4b shows cross sections of the exact nonlocal eddy diffusivity obtained using MFM and the modeled eddy diffusivity. The MMI model closely captures the double-sided exponential shape of the exact eddy diffusivity including the slight asymmetry at

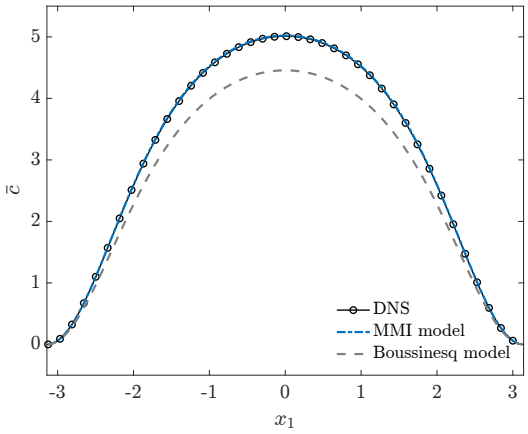

Figure 4.12: Model comparison for the inhomogeneous problem with periodic boundary conditions. The MMI model closely matches the DNS solution.

some x_1 locations. Appendix B.6 provides an appropriate IMFM formulation for obtaining moments of the eddy diffusivity for problems in which the periodic boundary conditions are incompatible with the IMFM required $\bar{c}$. Appendix B.6 also provides details for obtaining the exact eddy diffusivity for periodic problems.

Figure 4.12 shows a comparison between the MMI model and DNS solution for the inhomogeneous problem with periodic boundary conditions. The DNS solution corresponds to averaging the full solution in Figure 4.11b over the x_2 direction. The Boussinesq model given by

$$-\overline{u_1' c'} = D^0(x_1)\frac{\partial \bar{c}}{\partial x_1} \tag{4.38}$$

is also shown for comparison. The Boussinesq model greatly underpredicts the solution while the MMI model solution is almost indistinguishable from the DNS solution.

As shown in Figure 4.4a, the coefficient a_1 is smaller than the other coefficients; however, as discussed in Appendix B.7, the effect of a_1 is non-negligible. Appendix B.7 shows the effect of setting $a_1 = 0$, which leads to improvement over the Boussinesq model in the mean solution but still underprediction of the DNS solution.

4.4.2 Wall-bounded inhomogeneous flows

As an example application of the MMI model to wall-bounded inhomogeneous flows, we consider the model problem of Mani and Park (2021) which uses the same two-dimensional channel geometry as in Section 4.4.1, but replaces the periodic boundary conditions with solid walls and Dirichlet boundary conditions $c(x_1 = \pm\pi) = 0$. To satisfy the no-slip and no-penetration conditions at the

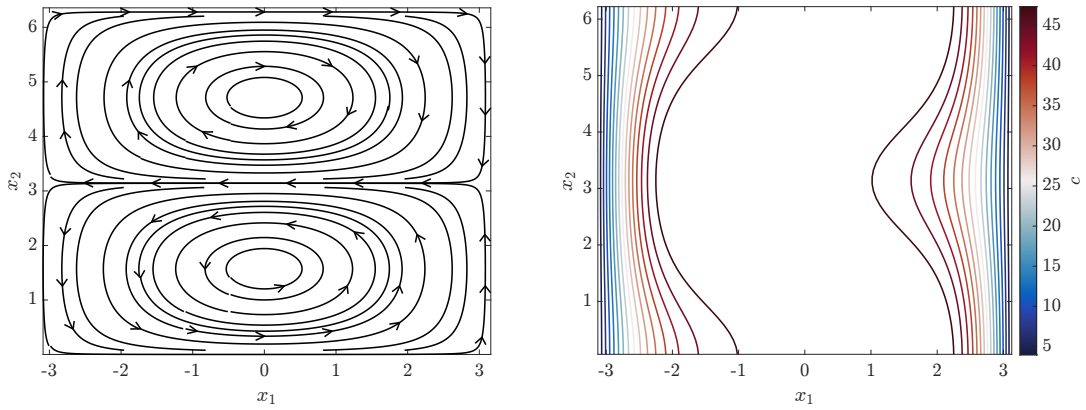

(a) (b)

Figure 4.13: (a) Streamlines of the velocity field in Equation (4.39). (b) Contour plot of $c(x_1, x_2)$ from DNS.

solid wall, the velocity field is modified to be:

$$u_1 = [1 + \cos(x_1)]\cos(x_2), u_2 = \sin(x_1)\sin(x_2). \tag{4.39}$$

Streamlines of the velocity field are shown in Figure 4.13a. The governing equation is given by Equation (4.34) with $\epsilon^2 = 0.05$ as before. The source function, f, is specified to be a constant, $f = 1$. Contours of $c(x_1, x_2)$ from DNS with grid resolution $N_1 = 200$ and $N_2 = 50$ are shown in Figure 4.13b. Averaging is defined over x_2 by Equation (4.35), and the corresponding mean scalar equation is given by Equation (4.36) as before.

The steady MMI model is given in Equation (4.37), and the coefficients are found via the procedure described in Section 4.2. Figure 4.14a shows the MMI coefficients for the wall-bounded inhomogeneous flow. The coefficients are well-behaved in the center of the domain; however, near the wall, there is a sharp spike in the MMI coefficients at $|x_1| \approx 2.5$. The location of the singularity remains fixed under mesh refinement, indicating that the issue is not due to the numerics. Despite the ill-behaved coefficients, the resulting $\bar{c}(x_1)$ from the MMI model is still very accurate, as shown in Figure 4.15, and greatly outperforms the Boussinesq model given in Equation (4.38).

To gain an understanding of why this singularity in the coefficients occurs, Figure 4.14b shows the exact eddy diffusivity obtained using MFM at various x_1 locations approaching the wall. While the modeled eddy diffusivity closely follows the exact eddy diffusivity, both eddy diffusivities deviate from a double-sided exponential shape, gradually becoming smoother and smaller in magnitude near the wall as the flow also diminishes.

The transition in kernel behavior due to the presence of the wall causes the singularity seen in the MMI coefficients. The ill-behaved coefficients are a result of the specific MMI model form in Equation (4.37). In the procedure for determining the coefficients, the determinant of the point-wise

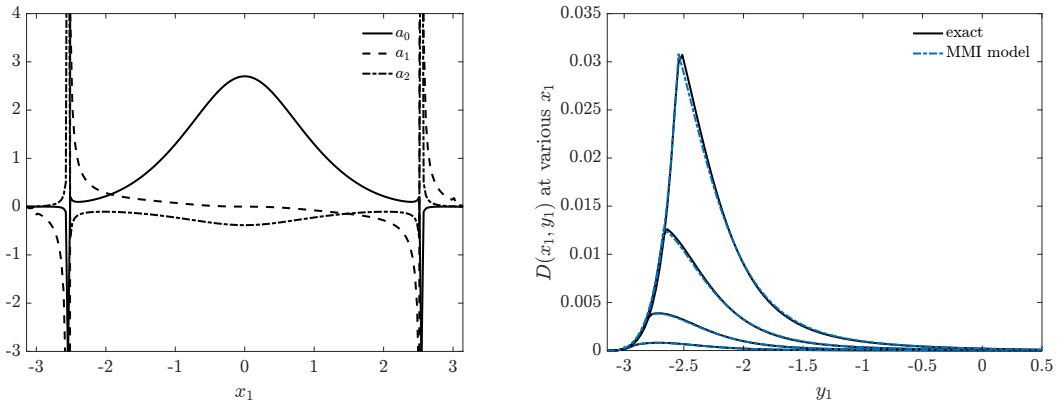

Figure 4.14: (a) MMI coefficients for Equation (4.37) for the wall-bounded inhomogeneous problem. (b) The exact and modeled nonlocal eddy diffusivity shown for various x_1 approaching the wall ($x_1 = -2.922, -2.796, -2.670, -2.545$).

matrix formed by the linear system in Equations (4.17a)-(4.17c) crosses zero at the location of the singularity.

However, near the wall, molecular effects dominate. For example, the molecular diffusivity, ϵ^2, is larger than the leading-order eddy diffusivity, D^0, until $|x_1| \approx 2.35$, which includes the region of singularity at $|x_1| \approx 2.5$. The MMI model form is unimportant near the wall, and the resulting $\bar{c}(x_1)$ is still very accurate as shown in Figure 4.15.

Coefficient regularization

We provide a coefficient regularization technique to remedy the singularity in the MMI coefficients in Figure 4.14a. Because the molecular term dominates near the wall, a portion of the molecular diffusion flux with small parameter σ is added when determining the MMI coefficients:

$$\left[1 + a_1(x_1)\frac{\mathrm{d}}{\mathrm{d}x_1} + a_2(x_1)\frac{\mathrm{d}^2}{\mathrm{d}x_1^2}\right]\left(-\overline{u_1'c'} + \sigma\frac{\mathrm{d}\bar{c}}{\mathrm{d}x_1}\right) = a_0(x_1)\frac{\mathrm{d}\bar{c}}{\mathrm{d}x_1}, \tag{4.40}$$

where σ is a constant smaller than the molecular diffusivity, ϵ^2. With this choice, away from the wall, the added regularization is negligible. Near the wall, the added regularization dominates and prevents the singularity in the coefficients by preventing the effective kernel shape from diminishing. In other words, as $-\overline{u_1'c'}$ goes to zero near the wall, the additional $\sigma\mathrm{d}\bar{c}/\mathrm{d}x_1$ term adds a Dirac delta function to the kernel that keeps it from diminishing.

Once the coefficients are determined using Equation (4.40), the closure model for the scalar flux is:

$$-\overline{u_1'c'} = \left[1 + a_1(x_1)\frac{\mathrm{d}}{\mathrm{d}x_1} + a_2(x_1)\frac{\mathrm{d}^2}{\mathrm{d}x_1^2}\right]^{-1} a_0(x_1)\frac{\mathrm{d}\bar{c}}{\mathrm{d}x_1} - \sigma\frac{\mathrm{d}\bar{c}}{\mathrm{d}x_1}, \tag{4.41}$$

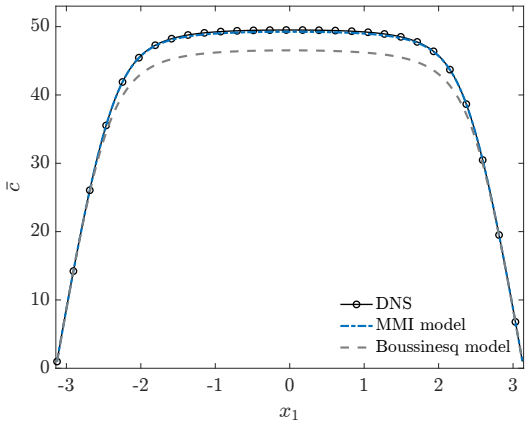

Figure 4.15: Model comparison for the wall-bounded inhomogeneous problem. The MMI model closely matches the DNS solution.

where the portion of the molecular diffusion flux that was added for regularization when determining the coefficients is now subtracted.

However, for model implementation, we found the following closure form to be more robust:

$$\left[1 + a_1(x_1)\frac{\mathrm{d}}{\mathrm{d}x_1} + a_2(x_1)\frac{\mathrm{d}^2}{\mathrm{d}x_1^2}\right](-\overline{u_1'c'}) = (a_0(x_1) - \sigma)\frac{\mathrm{d}\bar{c}}{\mathrm{d}x_1}, \tag{4.42}$$

where the coefficients are still determined using Equation (4.40). With this model implementation, even choices of σ larger than ϵ^2 (up to $\sigma \approx 3\epsilon^2$) still produced very accurate solutions with up to around one percent maximum error. In the procedure for determining the coefficients, due to the presence of the MMI operator acting on the regularization term in Equation (4.40), the added regularization is not purely local. The model form in Equation (4.42) mimics an added nonlocal effect of the regularization term. Equation (4.42) also still ensures that the implemented MMI model matches the zeroth moment, i.e., case when $\bar{c} = x_1$. The presence of σ will affect the higher-order moments of the eddy diffusivity; for example, substituting $\bar{c} = x_1^2/2$ into Equation (4.42) results in an extra $\sigma(x_1 + a_1)$ when compared with Equation (4.17b). However, as long as σ is small, this error in the higher-order moments is also small.

Figure 4.16a shows the MMI coefficients for the wall-bounded inhomogeneous problem with coefficient regularization. The coefficient, σ, is chosen to be $0.1\epsilon^2$ where ϵ^2 is the nondimensionalized molecular diffusivity in the x_1 direction. With regularization, the coefficients are now well-behaved; however, this is not yet systematic with regards to choice of σ.

Figure 4.16b shows a comparison between the MMI model with coefficient regularization in Equation (4.42) and the DNS solution. The MMI model with coefficient regularization performs even slightly better the original MMI model in Equation (4.37) although this depends on the choice of σ. While the coefficient regularization technique performs well for this wall-bounded inhomogeneous

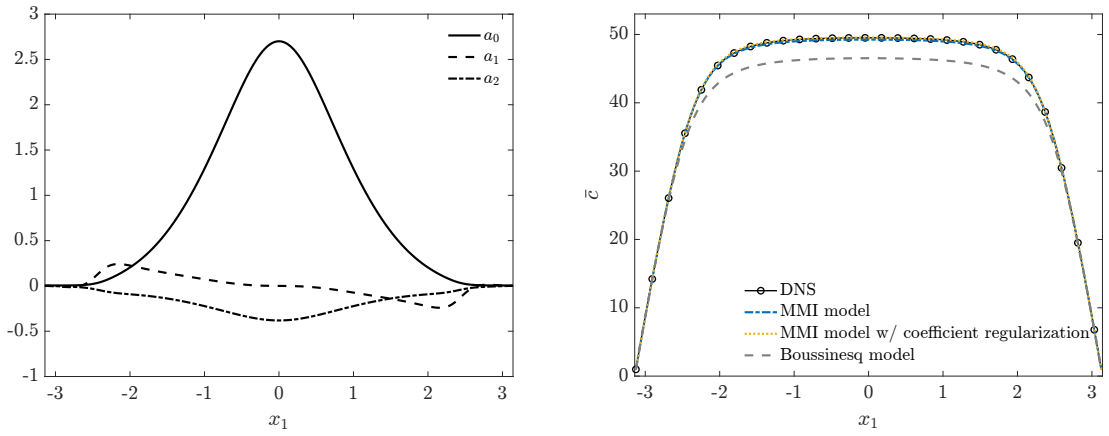

Figure 4.16: (a) MMI coefficients using the regularization in Equation (4.40). (b) Model comparison for the wall-bounded inhomogeneous problem.

problem, this does not address the original issue with the potential model form error. The MMI model form in Equation (4.37) admits a variety of exponential kernel shapes, but there are some shapes it cannot capture, and the model form may need to be modified. Alternative formulations for the MMI model are shown in Appendix B.8, but this is still an area of ongoing investigation.

4.5 Example MMI models for nonlocal eddy viscosities in turbulent channel flow

This section extends the MMI formulation developed for passive scalar transport in Sections 4.1-4.4 to momentum transport. We demonstrate example MMI models for turbulent channel flow at $\mathrm{Re}_\tau = 180$ using the low-order eddy viscosity moments computed by Park and Mani (2023a). Section 3.4 details using IMFM to compute moments of the eddy viscosity. The MMI model forms follow naturally from Section 4.2.5, however there are additional challenges due to the statistical noise present in turbulent flows.

An MMI model that includes up to the second-order spatial moment of the eddy viscosity is

$$\left[1 + a_1(x_2)\frac{\mathrm{d}}{\mathrm{d}x_2} + a_2(x_2)\frac{\mathrm{d}^2}{\mathrm{d}x_2^2}\right](-\overline{u_2'v_1'}) = a_0(x_2)\frac{\mathrm{d}V_1}{\mathrm{d}x_2}, \tag{4.43}$$

where the coefficients $a_0(x_2)$, $a_1(x_2)$, and $a_2(x_2)$ are determined using the procedure described in Section 4.2.5. To compute the zeroth-, first-, and second-order eddy viscosity moments, Park and Mani (2023b) used IMFM to specify $V_1 = x_2$, $V_1 = (1-x_2)^2$, and $V_1 = x_2^3$, respectively. We directly use $\overline{u_2'v_1'}|_{V_1}$ from these simulations (as shown in Figure 4.17) to solve for the MMI coefficients. The

system of linear equations:

$$-\overline{u_2'v_1'}|_{V_1=x_2} + a_1\frac{\mathrm{d}}{\mathrm{d}x_2}\left(-\overline{u_2'v_1'}|_{V_1=x_2}\right) + a_2\frac{\mathrm{d}^2}{\mathrm{d}x_2^2}\left(-\overline{u_2'v_1'}|_{V_1=x_2}\right) = a_0, \tag{4.44a}$$

$$-\overline{u_2'v_1'}|_{V_1=(1-x_2^2)} + a_1\frac{\mathrm{d}}{\mathrm{d}x_2}\left(-\overline{u_2'v_1'}|_{V_1=(1-x_2^2)}\right) + a_2\frac{\mathrm{d}^2}{\mathrm{d}x_2^2}\left(-\overline{u_2'v_1'}|_{V_1=(1-x_2^2)}\right) = a_0(-2x_2), \tag{4.44b}$$

$$-\overline{u_2'v_1'}|_{V_1=x_2^3} + a_1\frac{\mathrm{d}}{\mathrm{d}x_2}\left(-\overline{u_2'v_1'}|_{V_1=x_2^3}\right) + a_2\frac{\mathrm{d}^2}{\mathrm{d}x_2^2}\left(-\overline{u_2'v_1'}|_{V_1=x_2^3}\right) = a_0(3x_2^2), \tag{4.44c}$$

is solved at each x_2 mesh point for a_0, a_1, and a_2.

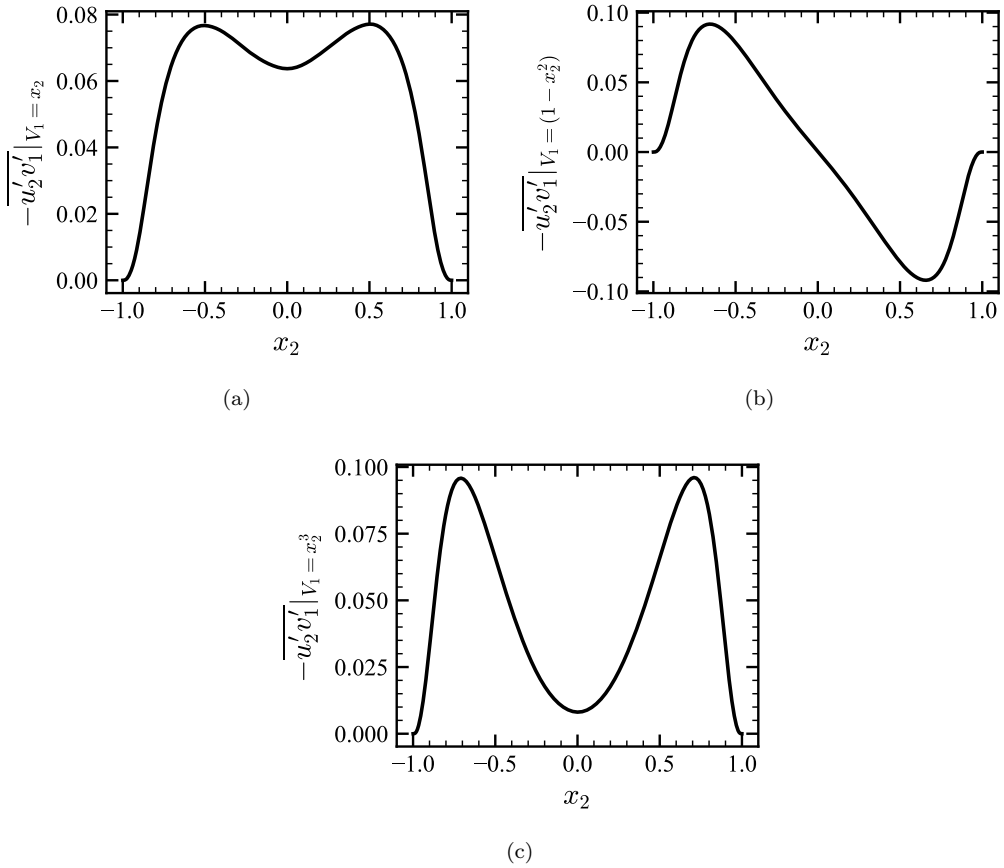

Figure 4.17: $-\overline{u_2'v_1'}|_{V_1}$ from IMFM calculations of Park and Mani (2023b) where (a) $V_1 = x_2$, (b) $V_1 = (1 - x_2)^2$, and (c) $V_1 = x_2^3$.

DNS and MFM simulation details are given in Park and Mani (2023a) and similar to the channel setup and numerical details in Section 5.3. We average over a longer period of 1000 eddy turnover time (δ/u_τ) than Park and Mani (2023a) for better statistical convergence. For testing the MMI

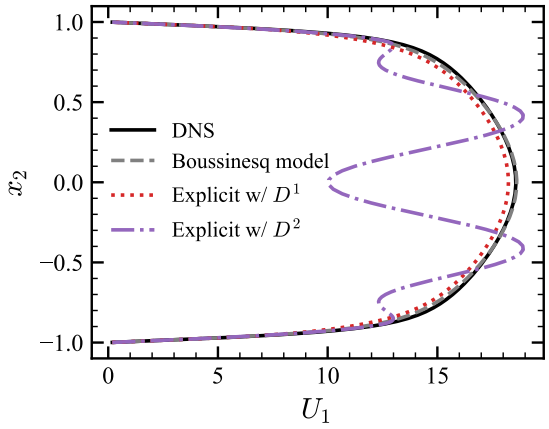

Figure 4.18: Comparison of adding higher-order corrections using the explicit model form in Equation (4.49) with DNS. Results provided by Danah Park.

model, the RANS equation for the mean streamwise velocity is

$$0 = -\frac{\partial P}{\partial x_1} + \frac{1}{Re}\frac{\partial^2 U_1}{\partial x_2^2} - \frac{\partial}{\partial x_2}\overline{u_2' u_1'} \tag{4.45}$$

where the mean pressure gradient is specified to be -1, and the model form for $-\overline{u_2' v_1'}$ is used interchangeably with $-\overline{u_2' u_1'}$. Equation (4.45) is solved using second-order central difference on a staggered mesh with a no-slip boundary condition enforced at the walls using ghost cells.

Due to the difficulties of computing MMI coefficients in the near-wall region as discussed in Section 4.4.2, we use the coefficient regularization technique introduced in Section 4.4.2, where a small constant parameter σ is added when determining the MMI coefficients:

$$\left[1 + a_1(x_2)\frac{\mathrm{d}}{\mathrm{d}x_2} + a_2(x_2)\frac{\mathrm{d}^2}{\mathrm{d}x_2^2}\right]\left(-\overline{u_2' v_1'} + \sigma\frac{\mathrm{d}V_1}{\mathrm{d}x_2}\right) = a_0(x_2)\frac{\mathrm{d}V_1}{\mathrm{d}x_2}. \tag{4.46}$$

For model implementation, we use

$$\left[1 + a_1(x_2)\frac{\mathrm{d}}{\mathrm{d}x_2} + a_2(x_2)\frac{\mathrm{d}^2}{\mathrm{d}x_2^2}\right](-\overline{u_2' v_1'}) = (a_0(x_2) - \sigma)\frac{\mathrm{d}V_1}{\mathrm{d}x_2} \tag{4.47}$$

as discussed in Section 4.4.2. We first investigate a MMI model that includes the zeroth- and first-order spatial moment, e.g., Equation (4.43) with $a_2 = 0$, before investigating inclusion of the second-order spatial moment.

For comparison, we also show the local Boussinesq model:

$$-\overline{u_2' v_1'} = D^0(x_2)\frac{\mathrm{d}V_1}{\mathrm{d}x_2}, \tag{4.48}$$

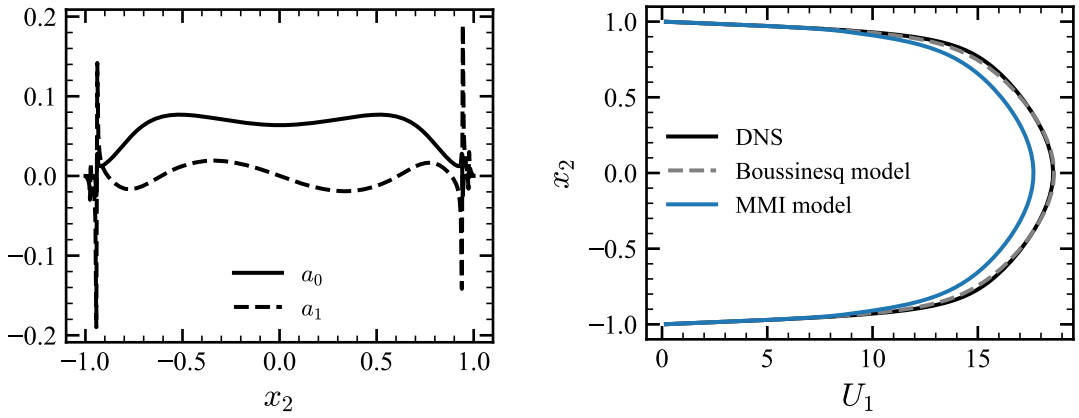

(a) (b)

Figure 4.19: For the MMI model in Equation (4.43) including up to the first-order spatial moment of the eddy viscosity ($a_2 = 0$): (a) Model coefficients. (b) Mean streamwise velocity with the Boussinesq model in Equation (4.48) shown for comparison.

where D^0 is the zeroth-order spatial moment. For this flow, the Boussinesq model already sufficiently captures the mean streamwise velocity. However, we demonstrate that using the MMI model to add higher-order eddy viscosity moments does not harm the solution and improves modeling of the true eddy viscosity. In contrast, an explicit model of the form:

$$-\overline{u_2'v_1'}(x_2) = D^0(x_2)\frac{\partial V_1}{\partial x_2} + D^{1_s}(x_2)\frac{\partial^2 V_1}{\partial x_2^2} + D^{2_s}(x_2)\frac{\partial^3 V_1}{\partial x_2^3}, \tag{4.49}$$

where D^{1_s} and D^{2_s} are the first- and second-order spatial moment of the eddy viscosity, respectively, diverges as shown in Figure 4.18 (results provided by Danah Park). The addition of higher-order corrections based on a truncated Taylor series makes the solution for the mean streamwise velocity progressively worse.

Figure 4.19a shows the coefficients for an MMI model that includes the zeroth- and first-order spatial moment without any coefficient regularization ($\sigma = 0$). The singularities in the coefficients at the walls indicate that a coefficient regularization is needed. Figure 4.19b shows a comparison of the mean streamwise velocity with DNS and the Boussinesq model in Equation (4.48).

Figure 4.20a shows the coefficients for the MMI model with a moderate choice of regularization parameter, $\sigma = 0.005$, which is on the order of the molecular viscosity, $\nu = 1/\mathrm{Re}_\tau = 1/180$, and Figure 4.20b shows the comparison of the mean streamwise velocity with DNS.

Figure 4.21a shows the coefficients for a MMI model that includes up to the second-order spatial moment of the eddy viscosity as in Equation (4.43) and without coefficient regularization. With the addition of the second-order moment, there is more amplification of statistical noise due to inclusion

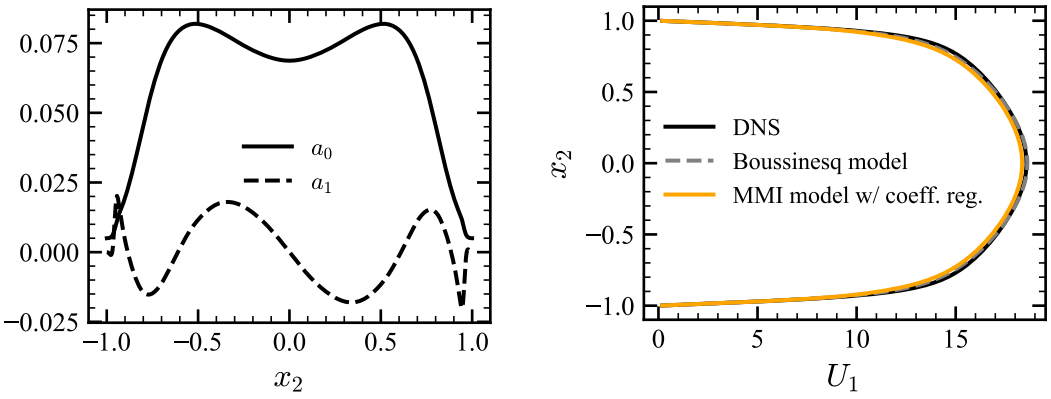

(a) (b)

Figure 4.20: For the MMI model with the coefficient regularization ($\sigma = 0.005$) in Equation (4.47) including up to the first-order spatial moment of the eddy viscosity ($a_2 = 0$): (a) Model coefficients. (b) Mean streamwise velocity.

of the higher-order derivative, $\mathrm{d}^2/\mathrm{d}x_2^2$. We use a Savitzky-Golay filter with a window length of 5 and polynomial order of 2 on the $-\overline{u_2'v_1'}|_{V_1}$ data for noise-reduction when determining the coefficients in Figure 4.21a. Again, the singularities in the coefficients near the wall indicate that coefficient regularization is needed. Figure 4.21b shows a comparison of the mean streamwise velocity and DNS.

Figures 4.22a and 4.22b show the coefficients for the MMI model with a large choice of regularization parameter, $\sigma = 0.5$. With the choice of regularization parameter, the Savitzky-Golay filter is not necessary. Figure 4.22c shows a comparison of the mean streamwise velocity and DNS.

The main additional challenge that arises with MMI models for turbulent wall-bounded flows is in the coefficient-fitting procedure described in Section 4.2.5. In turbulent flows, the statistical convergence of the $-\overline{u_2'v_1'}|_{V_1}$ data from MFM becomes an issue and the derivatives of $-\overline{u_2'v_1'}|_{V_1}$ amplify noise in the data during the coefficient-fitting procedure. This issue can partially be addressed by filtering the $-\overline{u_2'v_1'}|_{V_1}$ data, e.g., with a Savitzky-Golay filter as used above, or partially by the coefficient regularization technique described in Section 4.4.2. However, the model coefficients and mean solution are sensitive to both the filter and coefficient regularization parameters.

In turbulent channel flow, the local approximation, e.g., Boussinesq model in Equation (4.48), adequately captures the mean streamwise velocity. Hence, a comparison of the eddy viscosity is more insightful. A local eddy viscosity has a delta Dirac eddy viscosity kernel. Inclusion of up to the first-order spatial moment of the eddy viscosity leads to a nonlocal eddy viscosity kernel that is an exponential function in shape as shown in Figure 4.23a at $x_2 = -0.456$ without coefficient regularization. The MFM-measured eddy viscosity was computed by Park and Mani (2023a). The

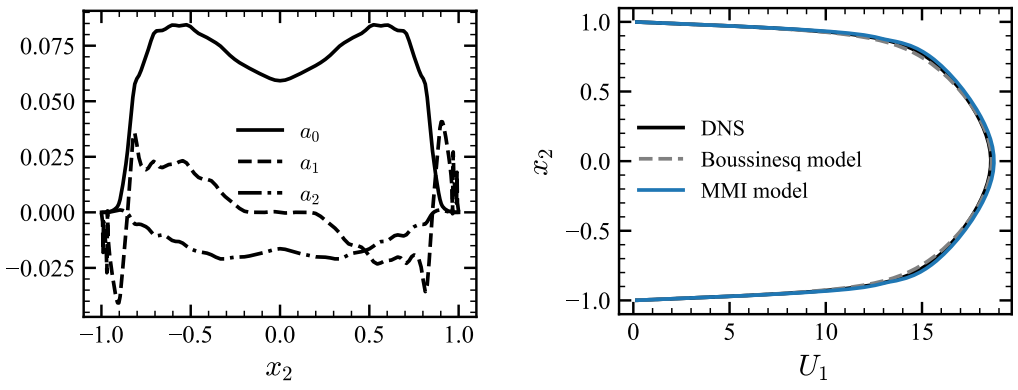

(a) (b)

Figure 4.21: For the MMI model in Equation (4.43) including up to the second-order spatial moment of the eddy viscosity. A Savitzky-Golay filter is used on the $-\overline{u_2'v_1'}|_{V_1}$ data for noise-reduction in the coefficient-fitting procedure: (a) Model coefficients. (b) Mean streamwise velocity.

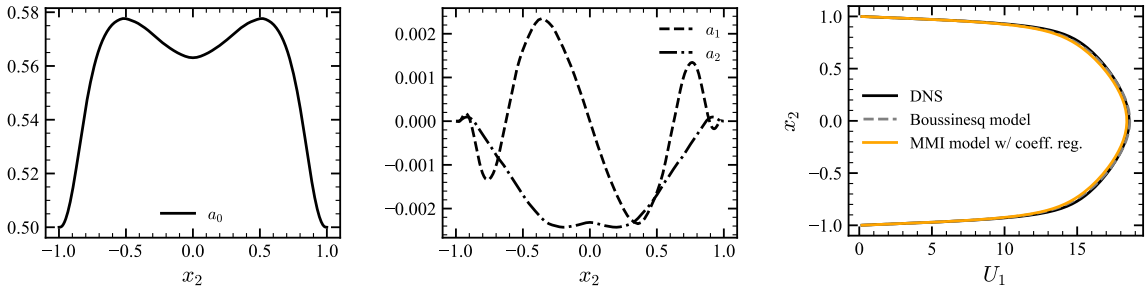

(a) (b) (c)

Figure 4.22: For the MMI model with the coefficient regularization ($\sigma = 0.5$) in Equation (4.47) including up to the second-order spatial moment of the eddy viscosity: (a) Model coefficients. (b) Mean streamwise velocity.

oscillations are due to the use of second-order central difference and can be removed with another choice of numerical scheme, e.g., upwinding.

Inclusion of up to the second-order spatial moment of the eddy viscosity leads to a double-sided exponential kernel that approximates the shape of the true nonlocal eddy viscosity kernel. Figure 4.23b shows the eddy viscosity at $x_2 = -0.456$ with and without coefficient regularization ($\sigma = 0.5$). Without coefficient regularization, the noise in the MFM data leads to singularities in the coefficients and in the eddy viscosity kernel near the wall. The coefficient regularization removes these singularities and tends to pull the eddy viscosity towards a more local solution, which in this case explains why a large choice of coefficient regularization ($\sigma = 0.5$) performs well, although the result is not yet systematic with regards to the choice of coefficient regularization parameter.

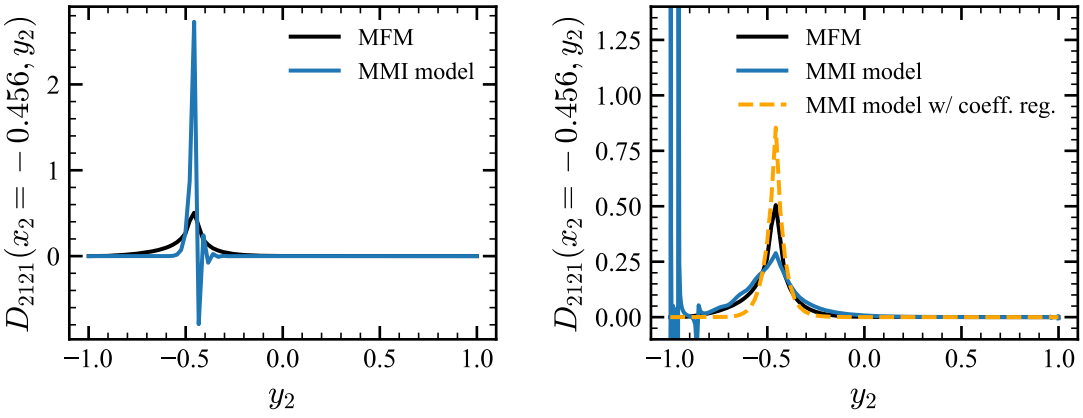

(a) (b)

Figure 4.23: Comparison of the MMI-modeled eddy viscosity kernel with the MFM-measured eddy viscosity of Park and Mani (2023a) at $x_2 = -0.456$ for (a) A MMI model that includes up to the first-order spatial moment without coefficient regularization. (b) A MMI model that includes up to the second-order spatial moment without and with coefficient regularization ($\sigma = 0.5$).

4.6 Conclusions

A nonlocal eddy diffusivity can greatly improve modeling of mean scalar transport when the Boussinesq approximation is invalid. However, both obtaining and implementing full nonlocal eddy diffusivities are too expensive for most practical applications, and thus we developed matched moment inverse (MMI) operators to model the nonlocal eddy diffusivity. These operators offer leading-order corrections to capture nonlocal effects in the eddy diffusivity by systematically matching the low-order moments of the true nonlocal eddy diffusivity, while avoiding the known divergence issues of explicit models that truncate the Kramers–Moyal expansion. By keeping an infinite Taylor series in the expansion rather than truncating the expansion, MMI models better approximate smooth nonlocal eddy diffusivity kernels whereas explicit models that truncate the expansion have highly local kernels. MMI models quantitatively approximate the shape of the nonlocal eddy diffusivity as combinations of exponential functions. These assumptions may break down in near-wall regions where the eddy diffusivity diminishes; however, in these regions the molecular effects dominate, and the model form becomes unimportant.

Moreover, the resulting MMI model is in the form of a differential equation rather than a computationally- or memory- intensive nonlocal integral. These models only require information about the moments of the nonlocal eddy diffusivity, which can be obtained using one simulation per moment, rather than the full nonlocal eddy diffusivity, which would require as many simulations as degrees of freedom in the averaged space. Furthermore, we showed that MMI models are expected to perform well as long as the mean scalar field is reasonably smooth; for fields with sharp features,

one may want to consider other operators that match the large and small wavenumber limits instead.

In this chapter, we demonstrated the application of MMI models to homogeneous and inhomogeneous example problems. We discussed challenges in inhomogeneous wall-bounded flows where the scalar flux goes to zero near the wall, and showed a coefficient regularization technique although this is not yet systematic with regards to the regularization parameter. We then demonstrated MMI models for momentum transport in turbulent channel flow. Additional challenges arose due to statistical convergence and amplification of noise by the higher-order derivatives in the coefficient-fitting procedure. While the local model performed adequately for turbulent channel flow, the addition of higher-order eddy viscosity moments using a MMI model form did not harm the solution for the mean streamwise velocity and improved modeling of the nonlocal eddy viscosity; in contrast, the addition of higher-order eddy viscosity moments using a truncated Taylor series expansion made the solution progressively worse.

Concurrent work in Lavacot et al. (2023) demonstrates the application of MMI to two-dimensional Rayleigh-Taylor instability, where we also show that a MMI model performs better than an explicit model that truncates the Taylor series expansion. Moreover, without the presence of walls, we have fewer of the coefficient singularity issues encountered in the inhomogeneous wall-bounded flows considered in this work.

Chapter 5

Adjoint macroscopic forcing method

The work in this chapter has been submitted to *Physical Review Fluids*. The full list of authors is: Jessie Liu, Florian Schäfer, Spencer H. Bryngelson, Tamer A. Zaki, and Ali Mani.

5.1 Background and motivation

While in Chapter 4, we addressed the cost of MFM by developing a systematic approach to model a nonlocal eddy viscosity using limited information about the eddy viscosity moments, in this chapter we develop a method to cost-effectively compute the exact (rather than modeled) eddy viscosity in targeted regions of the domain. For many applications, the exact eddy viscosity may be desired only within subregions of the domain where RANS models are particularly inaccurate, such as in regions of flow separation (Jespersen et al. (2016); Probst et al. (2010); Park et al. (2022a)). The generalized nonlocal and anisotropic eddy viscosity at such locations can inform RANS models of the sensitivity of the Reynolds stresses at those locations to the mean velocity gradient at all locations. However, computing the generalized eddy viscosity using the aforementioned brute-force approaches in Chapter 3 requires forcing the mean velocity gradient at each location in the averaged space, entailing as many simulations as degrees of freedom in the averaged space.

We develop an adjoint-based method to compute the generalized eddy viscosity at a specific physical location using one simulation rather than via an expensive brute-force approach. Figure 5.1 illustrates obtaining the generalized eddy viscosity for a canonical turbulent channel flow, using both the brute-force and our proposed approach. The mean velocity gradient is specified as an impulse at a specific location (Figure 5.1; blue plane), and a forced DNS is used to examine the Reynolds stress response. One such brute-force simulation characterizes how the mean velocity

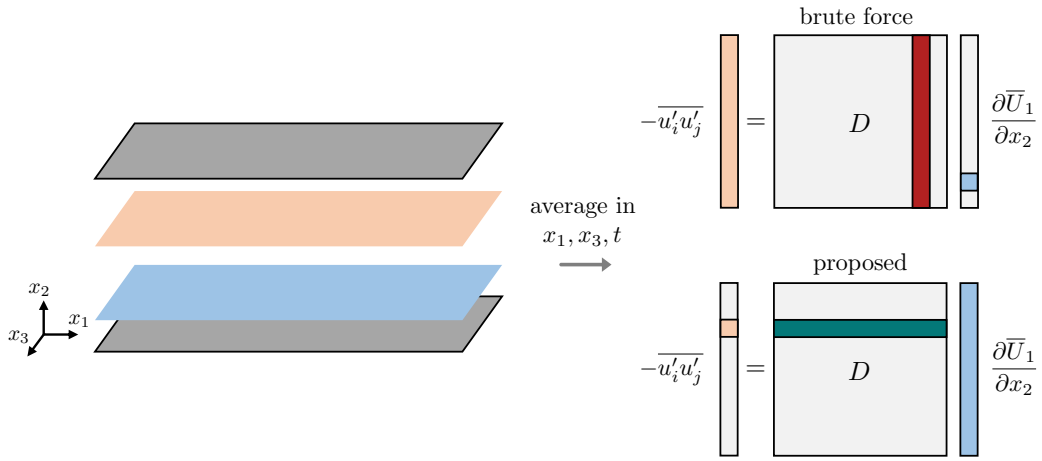

Figure 5.1: MFM illustration for a channel flow. With a brute-force approach, the mean velocity gradient, $\partial U_1/\partial x_2$, is specified as an impulse at a specific location in x_2 (blue plane), which corresponds to activating one element of the mean velocity gradient vector as shown in the top right of the figure. A forced DNS is used to measure the Reynolds stress response, $-\overline{u_i'u_j'}$ at all locations. This recovers one column of the discretized eddy viscosity, D, and must be repeated for all mean velocity gradient locations. The proposed adjoint MFM obtains a more physically relevant row of D, relating the Reynolds stress at one location (orange plane) to the mean velocity gradient at all locations as shown in the bottom right of the figure.

gradient at a specific location influences the Reynolds stress at all locations, forming a column of the discretized eddy viscosity. The proposed adjoint-based approach characterizes how the Reynolds stress at a specific location (Figure 5.1; orange plane) is influenced by the mean velocity gradient at all locations, forming a row of the discretized eddy viscosity and is more physically relevant. While we formulate the adjoint-based approach for Reynolds stress closures in this chapter, this approach can be used to inform closures more generally, e.g., for scalar fluxes as introduced in Chapter 3.

The adjoint-based formulation in this chapter can also aid in efficiently computing the eddy viscosity for the entire domain. Bryngelson et al. (2024) reveal sparsity in the discretized eddy viscosity to establish Fast MFM, substantially reducing the number of simulations required to obtain the generalized eddy viscosity. The adjoint-based method in this chapter enables a straightforward and computationally efficient way of recovering the operator rows (and columns) required for Fast MFM. Through selective forcing, such that the output of each simulation contains information about multiple rows and columns of the discretized eddy viscosity, we developed a method to reconstruct the discretized eddy viscosity for the entire domain using substantially fewer simulations than a brute-force approach.

In Section 5.2, we develop adjoint MFM for obtaining the eddy viscosity for a specific Reynolds stress location. In Section 5.3, we discuss the numerical details of the simulations. In Section 5.4, we

compare MFM and adjoint MFM for obtaining the eddy viscosity at a specified wall-normal location in turbulent channel flow at $\mathrm{Re}_\tau = 180$.

5.2 Adjoint macroscopic forcing method

We develop a method for obtaining a specific row of the generalized eddy viscosity, representing the nonlocal dependence of the Reynolds stress at a specific point on mean velocity gradients at all points in space/time, using an adjoint formulation of the GMT equations.

Discretely, the generalized eddy viscosity is part of a linear operator, $\overline{\mathcal{L}}$, that acts on the mean variables, V, such that the mean equation is

$$\overline{\mathcal{L}}\, V = 0. \tag{5.1}$$

For example, V is a vector of all mean velocity components and pressure, $V = [V_j \; \overline{Q}]^\top$, and $\overline{\mathcal{L}}$ includes closed operators and the Reynolds stress closure operator formed by the eddy viscosity, written discretely in block form as

$$\overline{\mathcal{L}} = \begin{bmatrix} \dfrac{\partial}{\partial t} + U_i \dfrac{\partial}{\partial x_i} - \dfrac{1}{\mathrm{Re}} \dfrac{\partial^2}{\partial x_i \partial x_i} - \dfrac{\partial}{\partial x_i} D_{ijkl} \dfrac{\partial}{\partial x_k} & \dfrac{\partial}{\partial x_j} \\ \dfrac{\partial}{\partial x_j} & 0 \end{bmatrix}. \tag{5.2}$$

Similarly, the governing equations, e.g, the GMT equations in (3.28a) and (3.28b), can be written as

$$\mathcal{L} v = 0. \tag{5.3}$$

Mani and Park (2021) show that

$$\overline{\mathcal{L}} = (P \mathcal{L}^{-1} E)^{-1}, \tag{5.4}$$

where P is a projection operator such that $V = Pv$ and E is an extension operator such that $E = nP^\top$, where n is the number of points used for averaging. The derivation of Equation (5.4) is shown in Appendix B.1. In practice, most problems have a large number of degrees of freedom, and $\mathcal{L}$ is expensive to invert directly, so Park and Mani (2023a) use IMFM as described in Section 3.4 to compute the generalized eddy viscosity. However, we show Equation (5.4) to illustrate the relationship between the generalized eddy viscosity embedded in the averaged operator, $\overline{\mathcal{L}}$, and the governing equations.

The desired rows of the eddy viscosity, D_{ijkl}, are the same as the columns of its transpose, $D^\top_{ijkl}$.

The transpose $D^{\top}_{ijkl}$ is linearly embedded in the transpose of the averaged operator, $\overline{\mathcal{L}}^{\top}$, which can be computed from Equation (5.4) according to:

$$\overline{\mathcal{L}}^{\top} = (E^{\top}\mathcal{L}^{-\top}P^{\top})^{-1} = (P\mathcal{L}^{-\top}E)^{-1}. \tag{5.5}$$

Equation (5.5) is similar to Equation (5.4), and rather than inverting $\mathcal{L}^{\top}$ directly, IMFM can be used on $\mathcal{L}^{\top}$ to compute columns of $D^{\top}_{ijkl}$. This is equivalent to using IMFM on the adjoint of the governing equations. The adjoint of the GMT equations in (3.28a) and (3.28b) is

$$-\frac{\partial v_i^{\dagger}}{\partial t} - \frac{\partial u_j v_i^{\dagger}}{\partial x_j} = \frac{\partial q^{\dagger}}{\partial x_i} + \frac{1}{\mathrm{Re}}\frac{\partial^2 v_i^{\dagger}}{\partial x_j \partial x_j} + s_i, \tag{5.6a}$$

$$\frac{\partial v_i^{\dagger}}{\partial x_i} = 0, \tag{5.6b}$$

where $v_i^{\dagger}$ and $q^{\dagger}$ are the adjoint velocity and pressure, respectively. We define a reverse time $\tau \equiv t_f - t$, where t_f is the final simulation time, so

$$\frac{\partial v_i^{\dagger}}{\partial \tau} - \frac{\partial u_j v_i^{\dagger}}{\partial x_j} = \frac{\partial q^{\dagger}}{\partial x_i} + \frac{1}{\mathrm{Re}}\frac{\partial^2 v_i^{\dagger}}{\partial x_j \partial x_j} + s_i, \tag{5.7a}$$

$$\frac{\partial v_i^{\dagger}}{\partial x_i} = 0. \tag{5.7b}$$

The advective velocity fields, u_j, are first computed using a DNS of the incompressible Navier–Stokes equations in forward time order and then read in reverse time order for solving Equation (5.7a). It is important to remark that the adjoint equations in (5.7a) and (5.7b) are the dual of the GMT system and not of the Navier–Stokes equations. As a result, these equations differ from the adjoint Navier–Stokes operator commonly adopted in nonlinear optimization and data assimilation (e.g., Wang et al. (2019a); Wang and Zaki (2021); Zaki and Wang (2021)). Specifically, the difference arises due to the treatment of the advection term, which is linear in the GMT system and is linearized when deriving the adjoint to the Navier–Stokes equations. In this regard, the adjoint GMT equation in (5.7a) is therefore more akin to the adjoint to the scalar transport equation (Wang et al. (2019b)), but also additionally includes the adjoint pressure $q^{\dagger}$ and is accompanied by the divergence-free condition in Equation (5.7b).

A specific row of D_{ijkl} can now be obtained by using IMFM on the adjoint GMT equations in (5.7a) and (5.7b). In considering the transpose of D_{ijkl}, the tensorial components are also transposed such that $D_{ijkl} \rightarrow D_{klij}$. For example, consider the discretization of the generalized eddy viscosity

of Equation (3.25):

$$\begin{bmatrix} -\overline{u_1'v_1'} \\ -\overline{u_1'v_2'} \\ -\overline{u_1'v_3'} \\ -\overline{u_2'v_1'} \\ \vdots \\ -\overline{u_3'v_3'} \end{bmatrix} = \begin{bmatrix} D_{1111} & D_{1112} & D_{1113} & D_{1121} & \dots & D_{1133} \\ D_{1211} & D_{1212} & D_{1213} & D_{1221} & \dots & D_{1233} \\ D_{1311} & D_{1312} & D_{1313} & D_{1321} & \dots & D_{1333} \\ D_{2111} & D_{2112} & D_{2113} & D_{2121} & \dots & D_{2133} \\ \vdots & \vdots & \vdots & \vdots & \ddots & \vdots \\ D_{3311} & D_{3312} & D_{3313} & D_{3321} & \dots & D_{3333} \end{bmatrix} \begin{bmatrix} \partial V_1/\partial x_1 \\ \partial V_2/\partial x_1 \\ \partial V_3/\partial x_1 \\ \partial V_1/\partial x_2 \\ \vdots \\ \partial V_3/\partial x_3 \end{bmatrix}, \tag{5.8}$$

where for each $i, j, k, l \in \{1, 2, 3\}$, $-\overline{u_i'v_j'}$ is a $N \times 1$ vector, D_{ijkl} is a $N \times N$ block matrix, and $\partial\overline{V_l}/\partial x_k$ is a $N \times 1$ vector where N is the number of degrees of freedom in the averaged space. In IMFM, as used by Park and Mani (2023a), forcing one element of $\partial V_1/\partial x_2$ to be nonzero and post-processing $-\overline{u_i'v_j'}$ leads to one column in each D_{ij21} matrix. Adjoint MFM obtains a row in each D_{21ij} matrix. If, for example, a row of D_{1121} is desired instead, then one should force an element of $\partial V_1^\dagger/\partial x_1$ and post-process $\overline{u_2'v_1^{\dagger\prime}}$.

5.3 Channel setup and numerical details

For DNS of the turbulent channel flow, we use the three-dimensional incompressible Navier–Stokes solver developed by Bose et al. (2010) and modified by Seo et al. (2015). The flow is driven by a nondimensionalized mean pressure gradient, $r_i = (1, 0, 0)$. The Reynolds number, $\mathrm{Re}_\tau = u_\tau\delta/\nu$, is defined based on the channel half-height, $\delta = 1$, and friction velocity, $u_\tau = 1$.

Park and Mani (2023a) modified the solver to include the GMT equations in (3.28a) and (3.28b). We modified the solver for the adjoint GMT equations in (5.7a) and (5.7b). We first conduct a DNS with output fields u_j at each timestep. We then solve Equation (5.7a) by stepping backward in time and reading the u_j fields in reverse order. The solenoidal condition in Equation (5.7b) is enforced using a fractional-step method. The post-processing involves averaged statistics, not instantaneous flow fields, so the differences between continuous and discrete adjoint formulations are unimportant (Wang et al. (2022)).

Periodic boundary conditions are enforced in the streamwise (x_1) and spanwise (x_3) directions, and no-slip and no-penetration boundary conditions are enforced at the walls. All solvers use semi-implicit time advancement (Kim and Moin (1985)); second-order Crank–Nicolson is used for the wall-normal diffusion terms and Adams–Bashforth is used for all other terms. For spatial discretization, the solvers use second-order finite differences on a staggered mesh (Morinishi et al. (1998)) with uniform spacing in x_1 and x_3 and nonuniform spacing in x_2. The domain size is $L_1 \times L_2 \times L_3 = 2\pi \times 2 \times \pi$ with $N = 144$ grid cells in each direction. The pressure Poisson equation is solved using Fourier transforms in the periodic x_1 and x_3 directions and a tridiagonal solver in the x_2 direction.

5.3.1 Obtaining rows of D_{2121}

Park and Mani (2023a) specify the mean streamwise velocity as Heaviside functions, $V_1 = \theta(x_2 - x_2^*)$, at wall-normal locations, x_2^*, which are maintained by the forcing. This specifies the mean velocity gradient as a Dirac delta function, $\partial V_1/\partial x_2 = \delta(x_2 - x_2^*)$. Park and Mani (2023a) then post-processed $-\overline{u_2' v_1'}$ to obtain the column of D_{2121} at x_2^* and repeated the procedure for all x_2^*.

Using the adjoint formulation, the adjoint mean streamwise velocity is specified as a Heaviside function, and post-processing of $-\overline{u_2' v_1^{\dagger\prime}}$ leads to a row of $-D_{2121}$. A negative sign accounts for the transposition of $\partial/\partial x_2$ in the velocity gradient.

5.3.2 Obtaining rows of other components of D_{ij21}

For other components, which require maintaining adjoint mean velocity gradient directions other than $\partial V_1^\dagger/\partial x_2$ as Dirac delta functions, specifying the adjoint mean velocity fields as Heaviside functions may not be mathematically well-posed. For example, obtaining a row of D_{1121} requires specifying $\partial V_1^\dagger/\partial x_1$ as a Dirac delta function, $\partial V_1^\dagger/\partial x_1 = \delta(x_2 - x_2^*)$, and post-processing $\overline{u_2' v_1^{\dagger\prime}}$. An adjoint mean velocity field that satisfies both $\partial V_1^\dagger/\partial x_1 = \delta(x_2 - x_2^*)$ and $\partial V_1^\dagger/\partial x_2 = 0$ does not exist. Thus, we decompose the adjoint velocity field into $v_i^\dagger = V_i^\dagger + v_i^{\dagger\prime}$, specify $\partial V_1^\dagger/\partial x_1$ analytically, and solve the corresponding equation for $v_i^{\dagger\prime}$. In other words, the decomposition is substituted into the adjoint GMT equation in (5.7a):

$$\frac{\partial V_i^\dagger}{\partial \tau} + \frac{\partial v_i^{\dagger\prime}}{\partial \tau} - u_j \frac{\partial V_i^\dagger}{\partial x_j} - u_j \frac{\partial v_i^{\dagger\prime}}{\partial x_j} = \frac{\partial q^\dagger}{\partial x_i} + \frac{1}{\mathrm{Re}} \frac{\partial^2 V_i^\dagger}{\partial x_j \partial x_j} + \frac{1}{\mathrm{Re}} \frac{\partial^2 v_i^{\dagger\prime}}{\partial x_j \partial x_j} + s_i, \tag{5.9}$$

and $\partial V_i^\dagger/\partial x_j$ is analytically specified. The IMFM forcing, s_i, now maintains $\overline{v_i^{\dagger\prime}} = 0$. For further simplification, the mean temporal term and mean diffusion term may be absorbed by the forcing since they adhere to the property $s_i = \overline{s}_i$:

$$\frac{\partial v_i^{\dagger\prime}}{\partial \tau} - u_j \frac{\partial V_i^\dagger}{\partial x_j} - u_j \frac{\partial v_i^{\dagger\prime}}{\partial x_j} = \frac{\partial q^\dagger}{\partial x_i} + \frac{1}{\mathrm{Re}} \frac{\partial^2 v_i^{\dagger\prime}}{\partial x_j \partial x_j} + s_i. \tag{5.10}$$

Continuing the above example for obtaining a row of D_{1121}, substituting $\partial V_1^\dagger/\partial x_1 = \delta(x_2 - x_2^*)$ into Equation (5.10) leads to the following equation for $v_i^{\dagger\prime}$:

$$\frac{\partial v_i^{\dagger\prime}}{\partial \tau} - u_1 \delta(x_2 - x_2^*)\delta_{i1} - \frac{\partial u_j v_i^{\dagger\prime}}{\partial x_j} = \frac{\partial q^\dagger}{\partial x_i} + \frac{1}{\mathrm{Re}} \frac{\partial^2 v_i^{\dagger\prime}}{\partial x_j \partial x_j} + s_i, \tag{5.11}$$

where δ_{i1} is the Kronecker delta and s_i maintains $\overline{v_i^{\dagger\prime}} = 0$. We enforce a solenoidal $v_i^{\dagger\prime}$ as

$$\frac{\partial v_i^{\dagger\prime}}{\partial x_i} = 0. \tag{5.12}$$

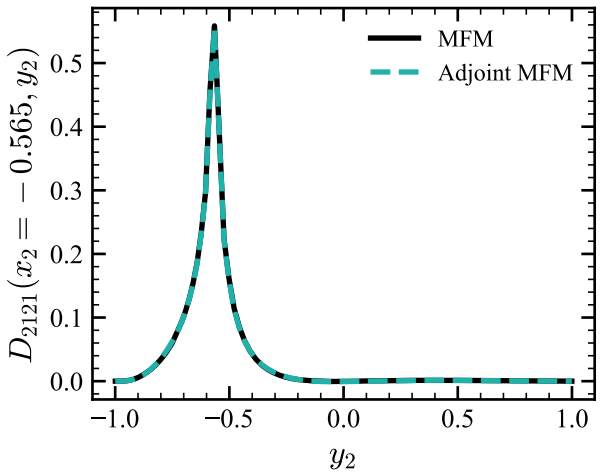

Figure 5.2: Comparison of $D_{2121}(x_2 = -0.565, y_2)$ (corresponding to row 50 of 144) using adjoint MFM and from a brute-force calculation by Park and Mani (2023a) using MFM.

While the solenoidal condition is enforced on $v_i^{\dagger\prime}$, the analytically specified adjoint mean velocity gradient may not be solenoidal, e.g., when $\partial V_1^\dagger/\partial x_1 = \delta(x_2 - x_2^*)$ and all other adjoint mean velocity gradient components are zero. Because the GMT equations in (3.28a) and (3.28b) are linear and ultimately only the superposition of the components of D_{ijkl} is needed for the Reynolds stress tensor, we relax the solenoidal constraint on the adjoint mean velocity gradient to ease computation of the individual components of D_{ijkl} by activating various components of the adjoint mean velocity gradient independently. Alternatively, the adjoint mean velocity gradient can be considered an IMFM forcing to the governing equation for $v_i^\dagger$ that satisfies the requisite property ($s = \overline{s}$).

5.4 Results

5.4.1 Eddy viscosity comparison

As an illustrative example, we compare the eddy viscosity at one location, $x_2 = -0.565$, obtained using the adjoint formulation with that of Park and Mani (2023a) obtained using a brute-force approach. We chose $x_2 = -0.565$, corresponding to row 50 out of 144, due to its significant asymmetry in the row versus column as shown in Figure 3.3, although we expect the results to hold for all locations. Park and Mani (2023a) averaged over 500 eddy turnover time (δ/u_τ) for their modeling purposes, whereas we averaged over 115 eddy turnover time, which we found sufficient for verification purposes.

Figure 5.2 shows the eddy viscosity from the adjoint formulation closely matching that of Park

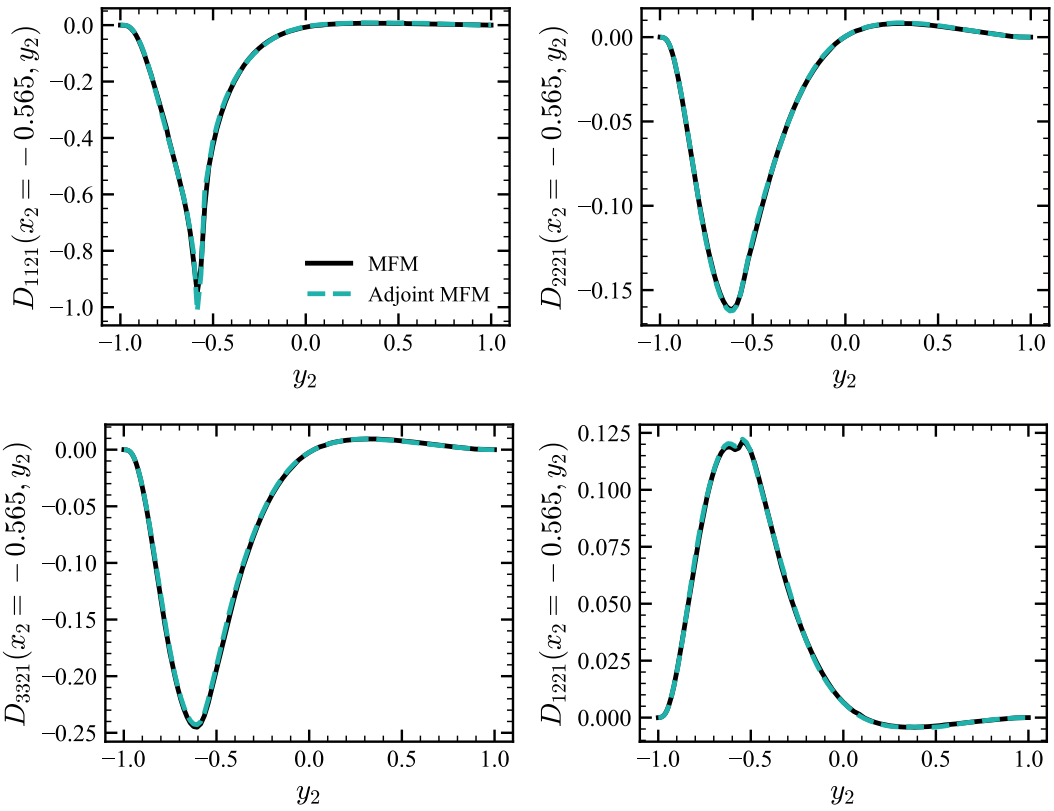

Figure 5.3: Comparison of other components of D_{ij21} at $x_2 = -0.565$ (corresponding to row 50 of 144) using adjoint MFM and from a brute-force calculation by Park and Mani (2023a) using MFM.

and Mani (2023a). The normalized error is less than 1%. We attribute this error to statistical convergence and the shorter averaging times used. For example, the normalized error of a regular MFM calculation averaged over 115 eddy turnover time and compared with the corresponding column is 0.7%, and the normalized error of the adjoint MFM calculation used here is 0.8%. Therefore, the differences in Figure 5.2 are within the uncertainty bounds of the calculation.

Figure 5.3 shows a comparison for the other components of D_{ij21}, which are even more asymmetric with regards to rows versus columns as shown in Appendix C.1. Due to differences in enforcement of the mean velocity gradient as detailed in Section 5.3.2 and the staggered mesh, there is some additional error due to interpolation. However, the eddy viscosity from the adjoint formulation still closely matches that of Park and Mani (2023a). The largest errors are in D_{1121} due to interpolation of a sharp peak with 4% normalized error. The normalized error for all other cases is less than 1.5%.

5.4.2 Cost comparison

A brute-force approach to obtaining the eddy viscosity requires as many simulations as degrees of freedom in the averaged space, which for the turbulent channel flow considered in this chapter is $N = 144$. Each simulation solves both Navier–Stokes and GMT equations for a total of 288 DNSs. The proposed adjoint simulation uses one simulation per desired eddy viscosity location, which includes a forward solve of the Navier–Stokes equations and a backward solve of the GMT equations for a total of 2 DNSs. Additional overhead is associated with reading and writing the velocity fields to disk for the adjoint simulation and more storage is needed.

For problems with many degrees of freedom in the averaged space, obtaining the eddy viscosity using a brute-force approach may be computationally intractable. However, using a single simulation, the adjoint-based formulation enables targeted quantification of the eddy viscosity at a specific location.

5.5 Conclusions

The generalized eddy viscosity at a specific location relates the Reynolds stress at that location to mean velocity gradients at all locations, which can be used to characterize nonlocality and sensitivity to the mean velocity gradient. In this chapter, we developed an adjoint-based MFM to cost-effectively compute the eddy viscosity at a specific location of the Reynolds stress using one simulation. Previous brute-force approaches (Mani and Park (2021); Hamba (2005)) forced the mean velocity gradient at each location in the averaged space and computed the Reynolds stress response, requiring a separate simulation for each mean velocity gradient location. Hence, these approaches needed as many simulations as degrees of freedom in the averaged space.

Adjoint MFM can be used to compute the eddy viscosity in regions of interest in turbulent flows, such as at flow separation or reattachment points, to examine nonlocal effects and inform RANS models of deficiencies in their eddy viscosity approximations. A brute-force approach would characterize the eddy viscosity for the entire domain (including regions where RANS models perform adequately) and require many simulations to do so. On the other hand, adjoint MFM can be used for more targeted computation of the eddy viscosity in only regions of interest and fewer simulations. In Chapter 6, we use adjoint MFM to investigate the streamwise and wall-normal nonlocal eddy viscosity at near-wall locations in turbulent channel flow.

For applications where the generalized eddy viscosity for the entire domain is still desired, adjoint MFM can also aid in substantially reducing the number of simulations by forcing the mean velocity gradient at selective points that leverage hidden sparsity in the discretized eddy viscosity operator (Bryngelson et al. (2024)).

Chapter 6

Investigation of the two-dimensional nonlocal eddy viscosity for turbulent channel flow using the adjoint macroscopic forcing method

The work in this chapter has been submitted to *Physical Review Fluids*. The full list of authors is: Jessie Liu, Florian Schäfer, Spencer H. Bryngelson, Tamer A. Zaki, and Ali Mani.

6.1 Background and motivation

This chapter investigates the streamwise and wall-normal nonlocal eddy viscosity in turbulent channel flow at select near-wall locations using adjoint MFM developed in Chapter 5. Hamba (2004) computed the streamwise and wall-normal nonlocal eddy diffusivity for passive scalar transport in turbulent channel flow at $\mathrm{Re}_\tau = 180$ using a brute force approach. In this chapter, we investigate momentum transport. Park et al. (2022b) computed the first-order temporal moment of the eddy viscosity for turbulent channel flow at $\mathrm{Re}_\tau = 180$ and used the result to estimate the streamwise nonlocality lengthscale based on the temporal moment and the local mean streamwise velocity. In this chapter, we compute the streamwise and wall-normal nonlocal eddy viscosity kernel at several near-wall locations in turbulent channel flow at $\mathrm{Re}_\tau = 180$. We compute a nonlocality lengthscale based on the first-order streamwise moment of the eddy viscosity and compare it with the estimate

from Park et al. (2022b).

In Section 6.2, we define the two-dimensional (2D) streamwise and wall-normal nonlocal eddy viscosity and give numerical details. In Section 6.3.1, we show the 2D nonlocal eddy viscosity kernel for the shear component of the Reynolds stress at several near-wall locations. As qualitatively expected, the streamwise extent of the nonlocal eddy viscosity kernel is longer than the wall-normal extent and increases in both streamwise extent and magnitude with distance from the wall. The measured 2D eddy viscosity kernels quantify this effect. In Section 6.3.2, we compare the 2D eddy viscosity kernel, which captures the influence of the mean velocity gradient upstream on the Reynolds stress at a given location, with the influence of the mean velocity gradient at the same location on the Reynolds stress downstream. This corresponds to the row and column, respectively, of the discretized 2D eddy viscosity. We show that the rows and columns are not identical for the 2D nonlocal eddy viscosity, which necessitated the use of adjoint MFM for efficiently computing the more physically-relevant rows of the 2D eddy viscosity. In Section 6.3.3, we then quantify the streamwise nonlocality lengthscale based on the first-order streamwise moment of the eddy viscosity. In Section 6.3.4, we compare this with the estimate for the streamwise nonlocality lengthscale of Park et al. (2022b) formed by the first-order temporal moment of the eddy viscosity and the local mean velocity and discuss the modeling implications of differences in these lengthscales. Lastly, in Section 6.3.5, we examine the anisotropy in the 2D nonlocal eddy viscosity kernel by comparing other components of the mean velocity gradient tensor and Reynolds stress tensor.

6.2 Problem formulation and numerical details

The streamwise and wall-normal nonlocal eddy viscosity for statistically stationary turbulent channel flow is:

$$-\overline{u_i' v_j'}(x_1, x_2) = \int_{y_1, y_2} D_{ij21}(x_1, x_2, y_1, y_2) \frac{\partial V_1}{\partial x_2}\bigg|_{y_1, y_2} \mathrm{d}y_1 \mathrm{d}y_2, \tag{6.1}$$

where averaging is taken in time and the homogeneous spanwise (x_3) direction. We use adjoint MFM as detailed in Chapter 5 to compute the nonlocal eddy viscosity for select wall-normal (x_2) locations:

$$\overline{u_k' v_l^{\dagger\prime}}(y_1, y_2) = \int_{x_1, x_2} D_{ijkl}(x_1, x_2, y_1, y_2) \frac{\partial V_j^\dagger}{\partial x_i}\bigg|_{x_1, x_2} \mathrm{d}x_1 \mathrm{d}x_2, \tag{6.2}$$

where the daggers denote adjoint variables. For example, the nonlocal eddy viscosity component, D_{2121}, corresponding to the influence of the velocity gradient, $\partial V_1/\partial x_2$, on the shear component of the Reynolds stress, $-\overline{u_2' v_1'}$, using adjoint MFM is

$$\overline{u_2' v_1^{\dagger\prime}}(y_1, y_2) = \int_{x_1, x_2} D_{2121}(x_1, x_2, y_1, y_2) \frac{\partial V_1^\dagger}{\partial x_2}\bigg|_{x_1, x_2} \mathrm{d}x_1 \mathrm{d}x_2. \tag{6.3}$$

where we specify $\partial V_1^\dagger/\partial x_2 = \delta(x_1 - x_1^*)\delta(x_2 - x_2^*)$ and zero for all other velocity gradient components, and post-process $\overline{u_2' v_1^{\dagger\prime}}(y_1, y_2)$ to obtain $D_{2121}(x_1^*, x_2^*, y_1, y_2)$. Because the flow is homogeneous in the x_1 direction, x_1^* can be chosen to be any streamwise location, and the eddy viscosity is a function of the distance, $y_1 - x_1$. Instead of reporting the 2D eddy viscosity kernel as $D_{ijkl}(x_1, x_2, y_1, y_2)$, we will omit the first input and report $D_{ijkl}(x_2, y_1 - x_1, y_2)$.

Similar to Section 5.3.2, specifying the adjoint mean velocity field as a Heaviside function in order to enforce the mean velocity gradient as a Dirac delta function is not mathematically well-posed. For example, an adjoint mean velocity field that satisfies $\partial V_1^\dagger/\partial x_2 = \delta(x_1 - x_1^*)\delta(x_2 - x_2^*)$ and $\partial V_1^\dagger/\partial x_1 = 0$ does not exist. Thus, similar to Section 5.3.2, we decompose the adjoint velocity field into $v_i^\dagger = V_i^\dagger + v_i^{\dagger\prime}$ and specify $\partial V_1^\dagger/\partial x_2$ analytically in the equation for $v_i^{\dagger\prime}$. This allows us to probe each component of D_{ijkl} independently and in the end does not violate any mathematical constraints when a consistent superposition of the various components of the mean velocity gradient appears in the RANS equation. Computing other components of the nonlocal eddy viscosity is similar to Section 5.3.2, where adjoint MFM transposes the components of D_{ijkl}.

The turbulent channel setup and numerical details are similar to Section 5.3. Due to the long streamwise extent of the eddy viscosity kernel, we doubled the domain size in the x_1 direction to $L_1 = 4\pi$. The resolution and remaining directions are unchanged from Section 5.3. The results are averaged over 400 eddy turnover time (δ/u_τ).

6.3 Results

6.3.1 Two-dimensional nonlocal eddy viscosity for D_{2121}

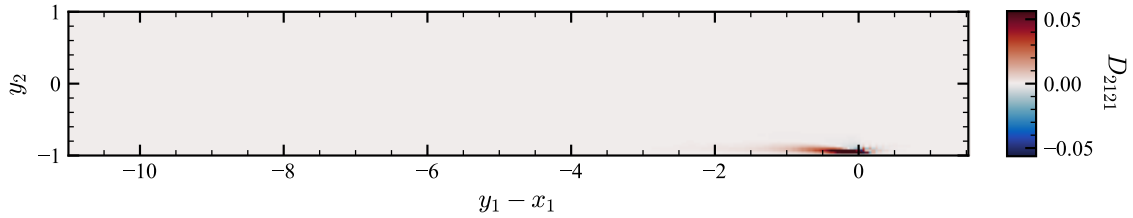

Figure 6.1: Streamwise and wall-normal eddy viscosity kernel, $D_{2121}(x_2 = -0.946, y_1 - x_1, y_2)$, corresponding to the influence of the velocity gradient, $\partial V_1/\partial x_2$, on the shear component of the Reynolds stress, $-\overline{u_2' v_1'}$. The colorbar is truncated at 10% of maximum absolute value to better highlight the region of upstream influence on the Reynolds stress.

Figure 6.1 shows the D_{2121} component of the streamwise and wall-normal nonlocal eddy viscosity, corresponding to the influence of the velocity gradient, $\partial V_1/\partial x_2$, on the shear component of the Reynolds stress, $-\overline{u_2' v_1'}$, at $x_2 = -0.946$. This location corresponds to $x_2^+ \approx 10$ when measured from the bottom wall in viscous units, i.e., $x_2^+ = (1 + x_2)/\delta_\nu$, which is in the buffer layer and near

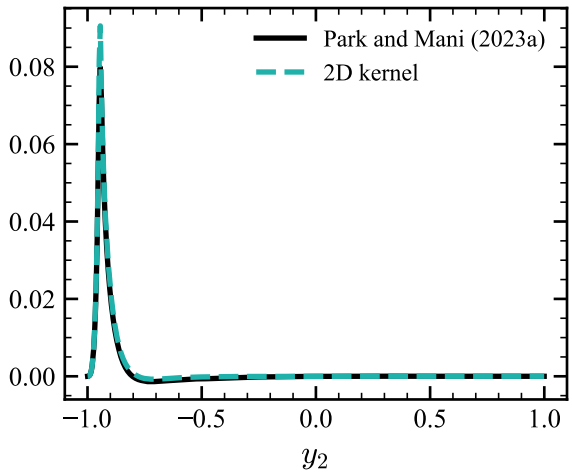

Figure 6.2: Comparison of the 2D eddy viscosity kernel, $D_{2121}(x_2 = -0.946, y_1 - x_1, y_2)$, integrated over the streamwise direction and the 1D wall-normal eddy viscosity kernel of Park and Mani (2023a). There is a small amount of error due to interpolation.

the location of maximum streamwise fluctuation and peak production, $x_2^+ \approx 12$ (Kim et al. (1987)). The colorbar is truncated at 10% of the maximum absolute value to better highlight the region of upstream influence on the Reynolds stress.

Figure 6.1 shows oscillations near the forcing location due to the spatially singular nature of the forcing function. The thin region that needs to be resolved to avoid these oscillations is proportional to ν/U_1 where $\nu = 1/\mathrm{Re} = 1/180$ and $U_1 = 8.35$ at $x_2 = -0.946$. Resolving this region would require around 65 times finer mesh resolution than the current resolution, $\Delta x_1^+ = 7.85$. Appendix D.1 shows the effect of mesh refinement and an upwind scheme rather than a central difference scheme.

To further establish confidence in the quantified eddy viscosity kernels, in Figure 6.2 we show a comparison with the wall-normal nonlocal eddy viscosity computed by Park and Mani (2023a). For comparison purposes, the 2D kernel in Figure 6.1 is integrated over the streamwise direction, resulting in an eddy viscosity that is local in the streamwise direction and nonlocal in the wall-normal direction, similar to Park and Mani (2023a). The error in Figure 6.2, hardly visible in the plot, is due to interpolation and differences in Dirac delta function location on a staggered mesh.

Figure 6.1 shows that the streamwise extent of the eddy viscosity kernel is much longer than the wall-normal extent. Qualitatively, this is expected due to the larger mean streamwise flow. With farther upstream distance from the peak (more negative $y_1 - x_1$), the kernel diminishes and spreads farther away from the wall. At the wall, the kernel diminishes to zero as expected due to diminishing transport from the wall-normal velocity fluctuations u_2' and the wall boundary conditions.

Figure 6.3 shows the D_{2121} component of the eddy viscosity kernel for several wall-normal locations (from top to bottom): $x_2 = -0.978$ ($x_2^+ \approx 4$, viscous sublayer), $x_2 = -0.946$ ($x_2^+ \approx 10$, buffer

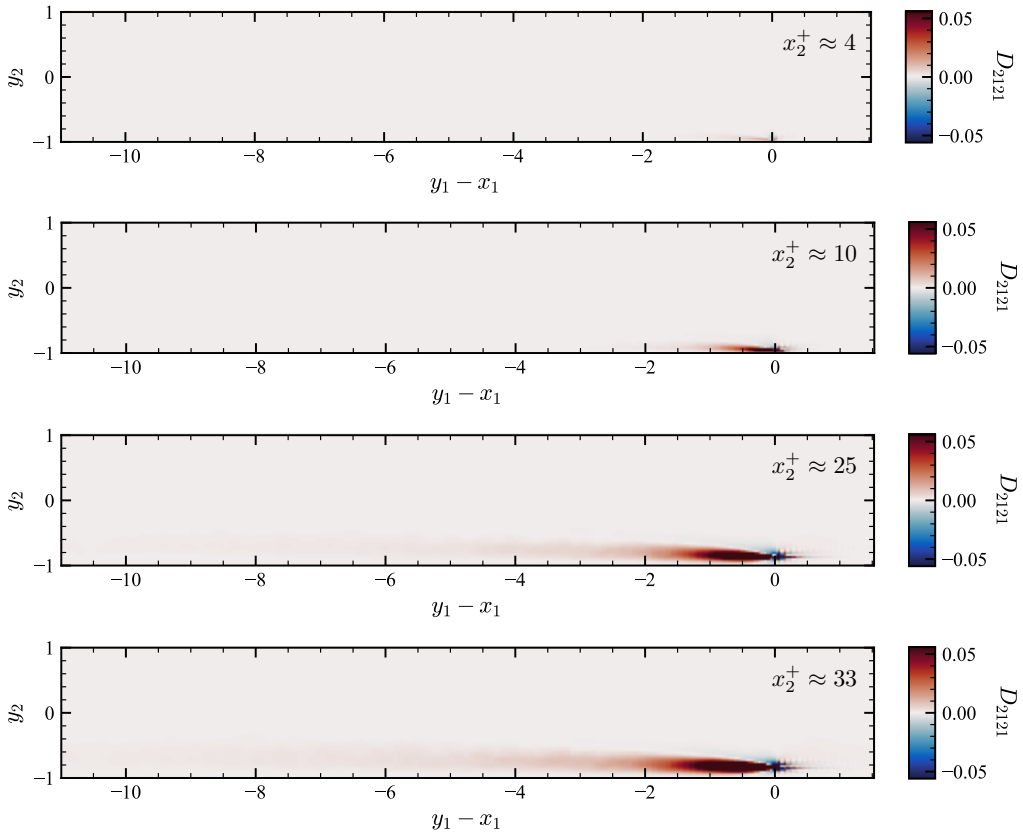

Figure 6.3: $D_{2121}(x_2, y_1 - x_1, y_2)$ for several wall-normal locations (from top to bottom): $x_2 = -0.978$ ($x_2^+ \approx 4$, viscous sublayer), $x_2 = -0.946$ ($x_2^+ \approx 10$, buffer layer), $x_2 = -0.859$ ($x_2^+ \approx 25$, buffer layer), $x_2 = -0.819$ ($x_2^+ \approx 33$, beginning of the log layer).

layer), $x_2 = -0.859$ ($x_2^+ \approx 25$, buffer layer), $x_2 = -0.819$ ($x_2^+ \approx 33$, beginning of the log layer). The streamwise influence of the mean velocity gradient on the shear component of the Reynolds stress both grows in magnitude and length with increasing distance from the wall. In Section 6.3.3, we quantify this streamwise nonlocality lengthscale. The maximum of the colorbar is truncated at ± 0.056, corresponding to 10% of the maximum absolute value of the 2D eddy viscosity kernel for $x_2 = -0.946$.

6.3.2 Comparison of streamwise row and streamwise column

We next compare $D_{2121}(x_2 = x_2^*, y_1 - x_1, y_2)$, e.g., as shown in Figure 6.3, with $D_{2121}(x_2, y_1 - x_1, y_2 = x_2^*)$. As discussed in Chapter 5 for a 1D eddy viscosity that is nonlocal in the wall-normal direction, $D_{2121}(x_2 = x_2^*, y_1 - x_1, y_2)$ is a "row" of the discretized eddy viscosity matrix (now in a 2D sense) showing the dependence of the shear component of the Reynolds stress at x_2^* on the mean velocity

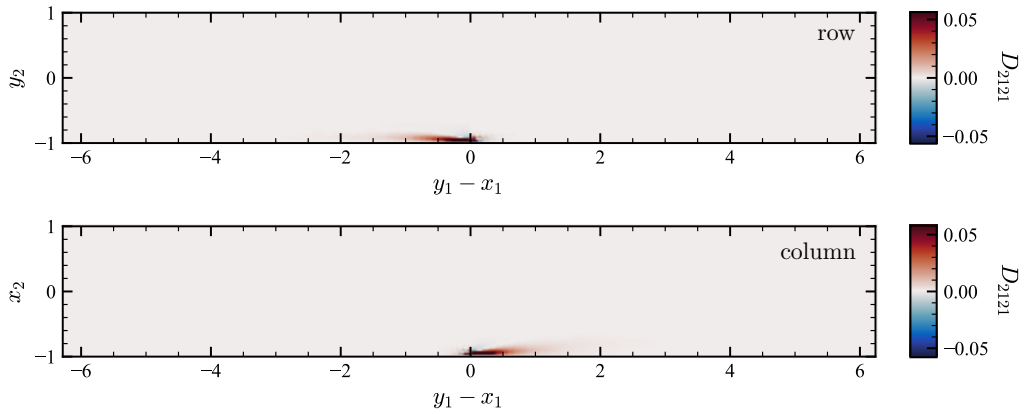

Figure 6.4: Comparison of $D_{2121}(x_2 = -0.946, y_1 - x_1, y_2)$ (row) and $D_{2121}(x_2, y_1 - x_1, y_2 = -0.946)$ (column). The location $x_2^* = -0.946$ corresponds to $x_2^+ \approx 10$ (buffer layer).

gradient at all points in space. For comparison, $D_{2121}(x_2, y_1 - x_1, y_2 = x_2^*)$ is a "column" of the discretized eddy viscosity matrix showing the influence of the mean velocity gradient at x_2^* on the Reynolds stresses everywhere in the domain. Chapter 5 showed that for a 1D eddy viscosity that is nonlocal in the wall-normal direction, the rows and columns of the discretized eddy viscosity are not identical for turbulent channel flow, necessitating the use of adjoint MFM for efficiently computing rows of the eddy viscosity. In this section, we investigate the 2D eddy viscosity and focus on nonlocality in the streamwise direction.

Figure 6.4 and Figure 6.5 show a comparison of $D_{2121}(x_2 = x_2^*, y_1 - x_1, y_2)$ and $D_{2121}(x_2, y_1 - x_1, y_2 = x_2^*)$ at $x_2^* = -0.946$ ($x_2^+ \approx 10$) and $x_2^* = -0.859$ ($x_2^+ \approx 25$), respectively. The column, $D_{2121}(x_2, y_1 - x_1, y_2 = x_2^*)$, is computed by using inverse MFM to specify $\partial V_1/\partial x_2 = \delta(x_1 - x_1^*)\delta(x_2 - x_2^*)$ and zero for all other velocity gradient components and post-processing $-\overline{u_2' v_1'}$. In both figures, the colorbars are truncated at 10% of their respective maximum absolute values. $D_{2121}(x_2, y_1 - x_1, y_2 = x_2^*)$ (column) has a slightly longer streamwise nonlocality lengthscale than $D_{2121}(x_2 = x_2^*, y_1 - x_1, y_2)$ (row), which becomes more apparent for kernels that are farther away from the wall, e.g., at $x_2^+ \approx 25$ as shown in Figure 6.5. This difference is seen more clearly in Figure 6.6, which shows the kernels integrated over the wall-normal direction. Even though the flow is homogeneous in the x_1 direction, the streamwise row, found by integrating the 2D nonlocal eddy viscosity kernel in the wall-normal direction, is not simply the reverse of the streamwise column as shown in Figure 6.6.

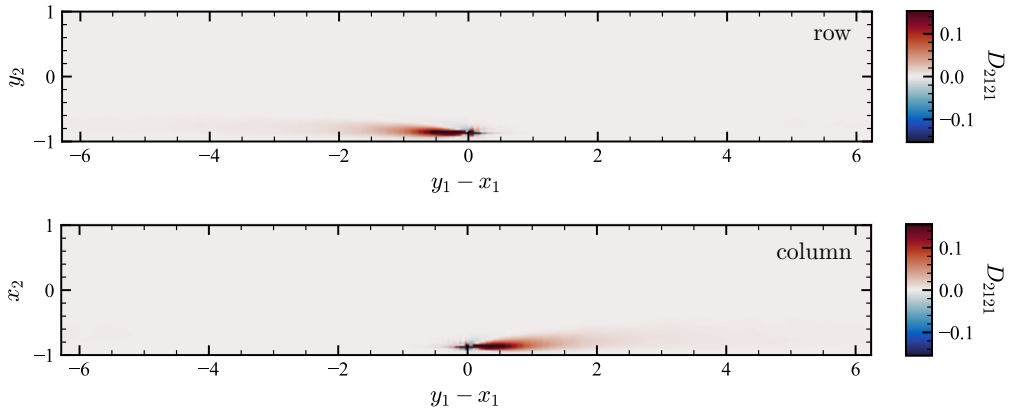

Figure 6.5: Comparison of $D_{2121}(x_2 = -0.859, y_1 - x_1, y_2)$ (row) and $D_{2121}(x_2, y_1 - x_1, y_2 = -0.859)$ (column). The location $x_2^* = -0.859$ corresponds to $x_2^+ \approx 25$ (buffer layer). The maximum values are similar, while $D_{2121}(x_2, y_1 - x_1, y_2 = -0.859)$ (column) shows a slightly longer streamwise nonlocality lengthscale than $D_{2121}(x_2 = -0.859, y_1 - x_1, y_2)$ (row).

6.3.3 Streamwise nonlocality lengthscale

We now characterize the streamwise nonlocality based on the first-order streamwise moment of the eddy viscosity defined by:

$$D^{1_s}_{2121}(x_2) = \int\int (y_1 - x_1) D_{2121}(x_2, y_1 - x_1, y_2) \mathrm{d}y_1 \mathrm{d}y_2. \tag{6.4}$$

The first-order streamwise moment characterizes the centroid of the eddy viscosity in the streamwise direction, given by a streamwise nonlocality lengthscale, $l_{2121} = -D^{1_s}_{2121}/D^0_{2121}$, where D^0_{2121} is the zeroth-order moment of the eddy viscosity:

$$D^0_{2121}(x_2) = \int\int D_{2121}(x_2, y_1 - x_1, y_2) \mathrm{d}y_1 \mathrm{d}y_2. \tag{6.5}$$

The streamwise nonlocality lengthscale, l_{2121}, is computed for various wall-normal locations.

For example, Figure 6.7a shows the streamwise eddy viscosity kernel after integration over the wall-normal direction at $x_2 = -0.946$:

$$\tilde{D}_{2121}(x_2, y_1 - x_1) = \int D_{2121}(x_2, y_1 - x_1, y_2) \mathrm{d}y_2. \tag{6.6}$$

The streamwise eddy viscosity is periodically repeated to illustrate simulation domain effects. Ideally, $D^{1_s}_{2121}$ is calculated for an infinite domain in the x_1 direction. However, due to a finite domain and periodic box effects in the simulations, the streamwise eddy viscosity does not go exactly to zero (e.g., the mean value between $-10 \leq y_1 - x_1 \leq -5$ is about 1×10^{-5} in Figure 6.7a). These nonzero

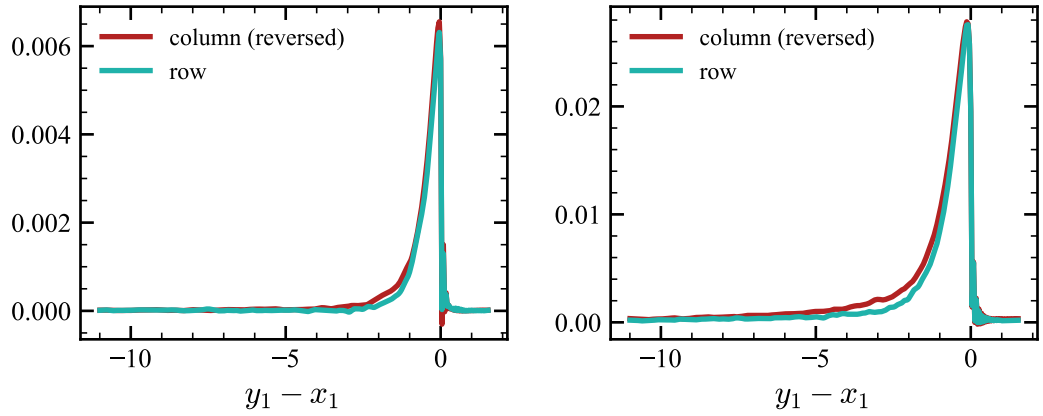

(a) (b)

Figure 6.6: (a) Comparison of the streamwise row at $x_2 = -0.946$ and streamwise column at $y_2 = -0.946$, and (b) comparison of the streamwise row at $x_2 = -0.859$ and streamwise column at $y_2 = -0.859$, computed by integrating the 2D kernels in Figure 6.4 and Figure 6.5, respectively, over the wall-normal direction. The streamwise column is reversed for comparison purposes to highlight that it is not identical to the streamwise row.

values away from the peak of the eddy viscosity kernels are weighted by $y_1 - x_1$ in the calculation of $D^{1_s}_{2121}$ and thus have a larger effect on $D^{1_s}_{2121}$ than on D^0_{2121}. The integration limits become important for calculating $D^{1_s}_{2121}$. With asymmetric integration limits, e.g., $-10 \leq y_1 - x_1 \leq 3$, the nonzero values skew the centroid to the left. Hence, we integrate symmetrically from $\eta = -h$ to $\eta = h$, where $\eta \equiv y_1 - x_1$, and plot $l_{2121} = -D^{1_s}_{2121}/D^0_{2121}$, as a function of the integration limits, $\pm h$, where:

$$D^{1_s}_{2121}(x_2) = \int_{-1}^{1} \int_{\eta=-h}^{\eta=h} \eta D_{2121}(x_2, \eta, y_2) \mathrm{d}\eta \mathrm{d}y_2, \tag{6.7a}$$

$$D^0_{2121}(x_2) = \int_{-1}^{1} \int_{\eta=-h}^{\eta=h} D_{2121}(x_2, \eta, y_2) \mathrm{d}\eta \mathrm{d}y_2. \tag{6.7b}$$

Figure 6.7b shows a flat region in l_{2121} versus h where the integration limits have little effect on l_{2121}. We use the average in this region, $3 \leq h \leq 9$ as the estimate of the streamwise nonlocality lengthscale, l_{2121}. For $x_2 = -0.946$, the streamwise nonlocality lengthscale is $l_{2121} = 0.42$.

6.3.4 Assessment of spatial nonlocality as a history effect in a Lagrangian framework

One way to interpret the long streamwise extent of the 2D nonlocal eddy viscosity kernel and the corresponding l_{2121} is by considering a temporal history effect along the trajectory of a fluid parcel that moves with the mean flow. This history effect can be characterized by an eddy viscosity kernel

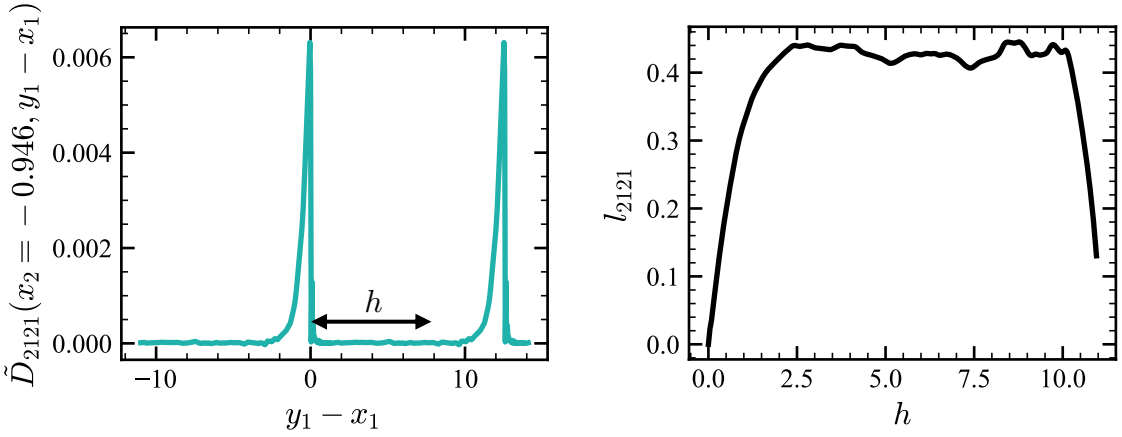

(a) (b)

Figure 6.7: (a) Streamwise dependence of the wall-normal integrated eddy viscosity kernel at $x_2 = -0.946$. (b) $l_{2121} = -D^{1_s}_{2121}/D^0_{2121}$ at $x_2 = -0.946$ as a function of the the integration limits, $\eta = -h$ to $\eta = h$, where $\eta = y_1 - x_1$. The lengthscale is computed based on the flat region where the integration limits have little effect on l_{2121}.

that is nonlocal in time and a corresponding temporal nonlocality timescale, $T_{2121} = -D^{1_t}_{2121}/D^0_{2121}$, where $D^{1_t}_{2121}$ is the first-order temporal moment. In Park et al. (2022b), we used MFM to directly compute $D^{1_t}_{2121}$. Because the velocity is constant along mean streamlines for turbulent channel, under a Lagrangian framework, the streamwise nonlocality lengthscale can be related to the temporal nonlocality lengthscale via $T_{2121}U_1$. Figure 6.8 shows a comparison between the streamwise nonlocality lengthscale calculated using the 2D nonlocal eddy viscosity and the Lagrangian estimate based off of $T_{2121}U_1$ from Park et al. (2022b) at $\mathrm{Re}_\tau = 180$. As seen in Figure 6.8, the two lengthscales are correlated, which is expected given the vivid upstream structure of the eddy viscosity kernel. These lengthscales may be used interchangeably for qualitative estimates of the magnitude of spatial or temporal nonlocality scales. However, as seen in Figure 6.8, $l_{2121} = -D^{1_s}_{2121}/D^0_{2121}$ and $T_{2121}U_1$ are not identical, particularly starting in the buffer layer and into the log layer.

This difference between l_{2121} and $T_{2121}U_1$ has implications for modeling and suggests modifications to the model form starting in the buffer layer. Models often include nonlocal effects by considering a history effect along Lagrangian trajectories using the material derivative and a relaxation timescale, e.g., the simple nonlocal model shown in Equation (1.11) and more generally Reynolds stress transport models:

$$T\frac{D}{Dt}\overline{u_i'u_j'} = -\overline{u_i'u_j'} + \dots. \tag{6.8}$$

This includes an implied streamwise nonlocality lengthscale TU_1 from the advection term. To match

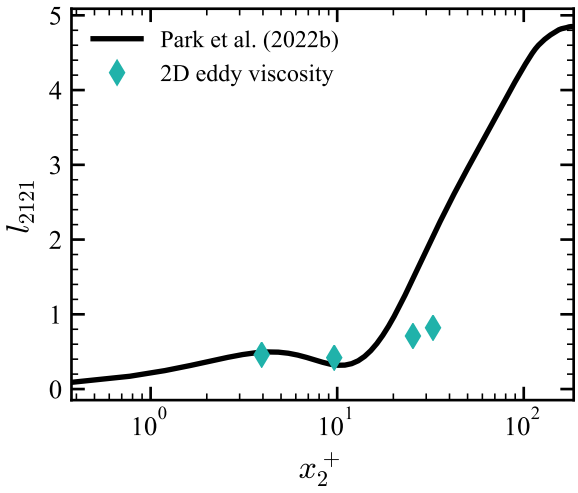

Figure 6.8: Comparison between the streamwise nonlocality lengthscale calculated using the 2D nonlocal eddy viscosity and the estimate of Park et al. (2022b) computed using the temporal moment $T_{2121} = -D^{1_t}_{2121}/D^0_{2121}$ and $T_{2121}U_1$ at $\mathrm{Re}_\tau = 180$.

the measured streamwise nonlocality lengthscale, there should be additional terms with the first-order spatial derivative of the Reynolds stresses, e.g., $a\frac{\partial}{\partial x_1}\overline{u_i'u_j'}$. For example, this could be achieved with a cross-diffusion term or a spatially-varying turbulent viscosity.

6.3.5 Two-dimensional nonlocal eddy viscosity for other components of D_{ijkl}

In this section, we examine the anisotropy of the 2D eddy viscosity by considering other components of D_{ijkl}. We begin by examining the D_{21kl} components of eddy viscosity corresponding to the shear component of the Reynolds stress, $-\overline{u_2'v_1'}$, and other components of the mean velocity gradient tensor, $\partial V_l/\partial x_k$, specifically focusing on $\partial V_1/\partial x_1$. We then examine the D_{ij21} components of the eddy viscosity corresponding the normal components of the Reynolds stress, $-\overline{u_i'v_j'}$, and the wall-normal mean velocity gradient, $\partial V_1/\partial x_2$.

Figure 6.9 shows a comparison of the D_{2121} and D_{2111} component of the eddy viscosity at $x_2 = -0.946$ ($x_2^+ \approx 10$). The D_{2111} component shows the influence of the streamwise gradient of the mean velocity, $\partial V_1/\partial x_1$, on the shear component of the Reynolds stress, $-\overline{u_2'v_1'}$. While $\partial V_1/\partial x_1$ is inactive in channel flow since x_1 is a homogeneous direction, this component would be active in a spatially-developing boundary layer or a separated flow. We use the 2D eddy viscosity kernel from channel flow as a qualitative estimate of the nonlocal effects present in other wall-bounded flows. As shown in Figure 6.9, the D_{2111} component has a much larger magnitude than the D_{2121} component (the colorbars are truncated at 10% of their maximum respective values), indicating that the shear

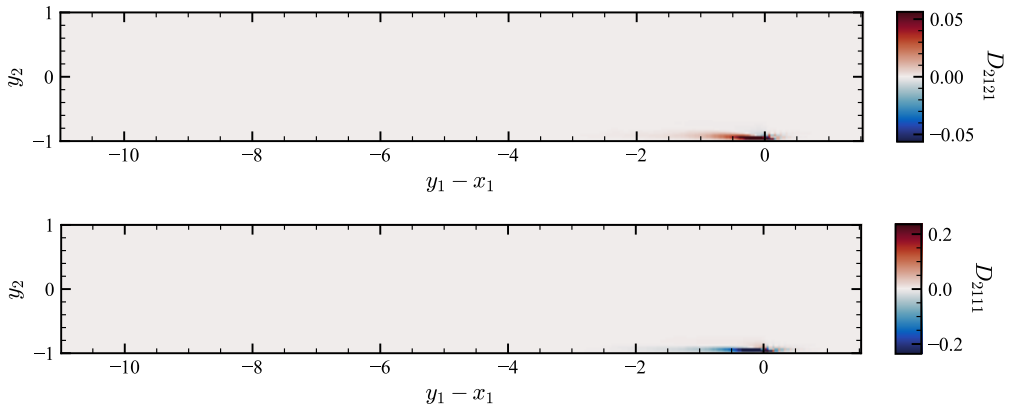

Figure 6.9: Comparison between D_{2121} and D_{2111} at $x_2 = -0.946$ ($x_2^+ \approx 10$). The D_{2111} component shows the influence of streamwise gradient of the mean velocity, $\partial V_1/\partial x_1$, on the shear component of the Reynolds stress, $-\overline{u_2' v_1'}$.

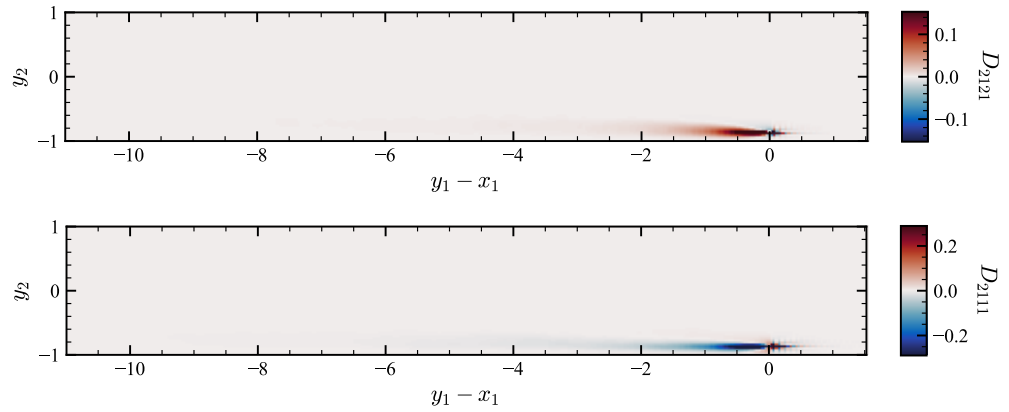

Figure 6.10: Comparison between D_{2121} and D_{2111} at $x_2 = -0.859$ ($x_2^+ \approx 25$).

component of the Reynolds stress has a greater sensitivity to $\partial V_1/\partial x_1$ than $\partial V_1/\partial x_2$. Figure 6.10 shows a similar comparison of the same two components for $x_2 = -0.859$ ($x_2^+ \approx 25$).

The $\overline{u_2' v_1'}$ component of the Reynolds stress tensor describes mixing of the streamwise momentum fluctuations, v_1', by wall-normal fluctuations, u_2'. The Boussinesq approximation would imply this mixing flux is sensitive only to the wall-normal gradient of the mean streamwise velocity. However, we observe a stronger sensitivity to the streamwise gradient (not only is it non-negligible, but actually larger than the sensitivity to the wall-normal gradient).

We additionally examine anisotropy in the eddy viscosity by considering the influence of the wall-normal mean velocity gradient on the normal components of the Reynolds stress tensor. Figure 6.11 shows a comparison between the shear component, D_{2121}, and normal components, D_{1121},

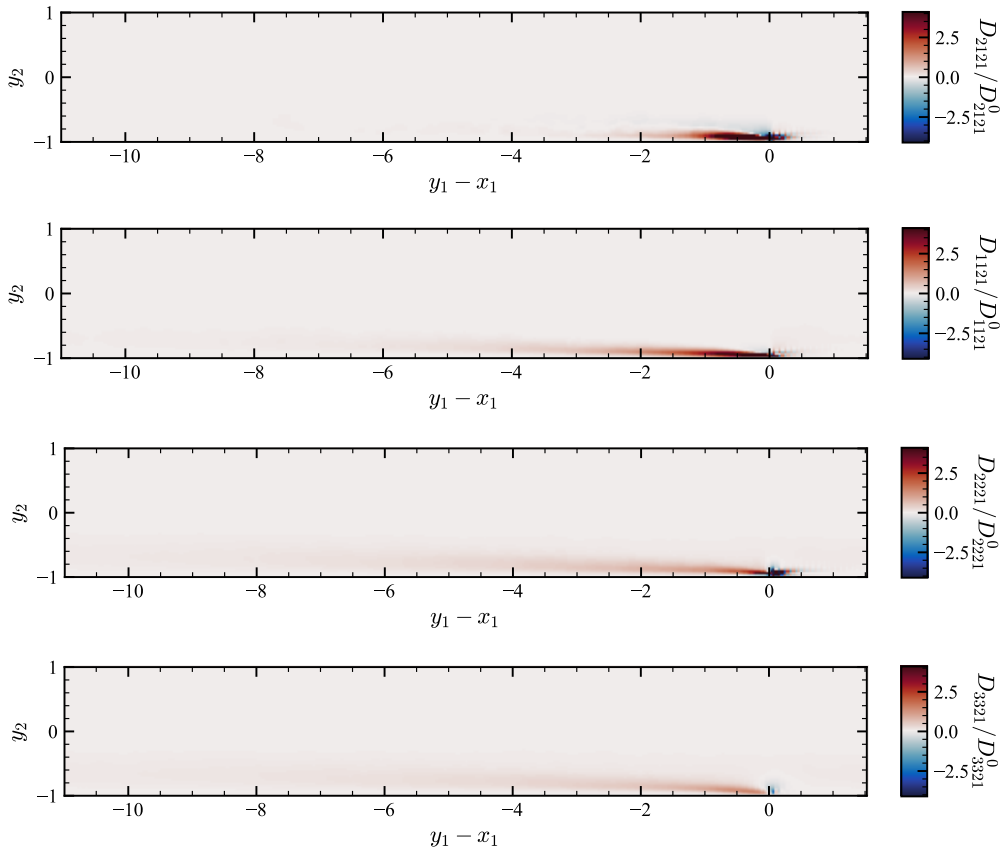

Figure 6.11: Comparison between the shear component, D_{2121}, and the normal components, D_{1121}, D_{2221}, D_{3321}, of the 2D nonlocal eddy viscosity at $x_2 = -0.946$ ($x_2^+ \approx 10$). Each component is normalized by their respective zeroth-order moment, D^0_{ij21}.

D_{2221}, D_{3321}, of the 2D nonlocal eddy viscosity kernel at $x_2 = -0.946$ ($x_2^+ \approx 10$). Each component is normalized by their respective zeroth-order moment, D^0_{ij21}. The colorbar is truncated for easier visual comparison between the components. Due to the long extent of the streamwise nonlocality, D_{3321} is affected by the periodic domain. Appendix D.2 discusses the domain effects on the eddy viscosity in more detail. The shear component D_{2121} has the shortest streamwise nonlocal effect, while the normal components have a much longer streamwise nonlocal effect.

The difference in the streamwise nonlocality lengthscale between the various components of the Reynolds stresses implies an anisotropic lengthscale (or corresponding timescale) for modeling. This is counter to current modeling practice in which most models (Launder et al. (1975); Speziale et al. (1991)) use an isotropic characteristic turbulence timescale, e.g., $T = k/\varepsilon$ for all components of the Reynolds stresses where k is the characteristic turbulent kinetic energy scale and ε is the characteristic dissipation scale.

6.4 Conclusions

In this chapter, we used adjoint MFM, which was developed in Chapter 5, to investigate the streamwise and wall-normal extent of the eddy viscosity kernel in turbulent channel flow at select near-wall locations from the viscous sublayer to the log layer. While in Chapter 5, we showed that the rows and columns of the 1D wall-normal eddy viscosity are not identical in turbulent channel flow, in this chapter we also found that the streamwise row (computed by integrating the 2D eddy viscosity kernel over the wall-normal direction) is not identical to the reverse of the streamwise column even though the x_1 direction is a homogeneous direction. The nonlocal influence of the streamwise column is slightly longer than that of the streamwise row and increases with distance from the wall. Physically, this implies that the mean velocity gradient at a given point influences the Reynolds stress farther downstream than the Reynolds stress at the same point is influenced by the mean velocity gradient upstream.

We also found the nonlocal eddy viscosity kernel is much longer in the streamwise direction than the wall-normal direction, and the nonlocality lengthscale in the streamwise direction increases with distance from the wall. This result is qualitatively expected due to the increase in the mean streamwise velocity with distance from the wall; however, in this work, we quantified this effect. We then characterized the streamwise nonlocality lengthscale using $l_{2121} = -D^{1_s}_{2121}/D^0_{2121}$, where $D^{1_s}_{2121}$ is the first-order streamwise moment of the eddy viscosity and D^0_{2121} is the zeroth-order moment of the eddy viscosity.

For comparison, we also considered a streamwise nonlocality lengthscale based on a history effect along Lagrangian trajectories, $T_{2121}U_1$, where $T_{2121} = -D^{1_t}_{2121}/D^0_{2121}$ and $D^{1_t}_{2121}$ is the first-order temporal moment. While l_{2121} and $T_{2121}U_1$ are correlated, we observed differences, particularly starting in the buffer layer and into the log layer. For modeling, this difference suggests modification of the streamwise nonlocality lengthscale associated with the material derivative, e.g., by including terms of the form $a\frac{\partial}{\partial x_1}\overline{u'_i u'_j}$, which may be cross-diffusion terms or a turbulent diffusion term with a spatially-varying viscosity.

We then examined the anisotropy of the 2D eddy viscosity kernel. We observed that while their streamwise extents are similar, D_{2111} has a larger magnitude than D_{2121}, i.e., the shear component of the Reynolds stress is more sensitive to the streamwise gradient of the mean velocity, $\partial V_1/\partial x_1$, than the wall-normal gradient of the mean velocity, $\partial V_1/\partial x_2$. We also examined the anisotropy in the eddy viscosity kernels by comparing the normal components of the Reynolds stresses with the shear component. We found that the eddy viscosity kernels for the normal components have longer streamwise extent than for the shear component.

These observations can be used to inform models of the needed anisotropy. Under the Boussinesq approximation, the shear component of the Reynolds stresses only depends on the wall-normal mean velocity gradient; whereas, we observe that the influence of streamwise mean velocity gradient is non-negligible. We qualitatively expect this to have an impact in flows where the streamwise mean

velocity gradient is active, such as a spatially-developing boundary layer. Moreover, the anisotropy between the eddy viscosity kernels for various components of the Reynolds stress tensor implies an anisotropic turbulence lengthscale or timescale; whereas, currently most models use an isotropic timescale.

Chapter 7

Conclusions

Incorporating nonlocal effects is critical to RANS modeling of turbulent wall-bounded flows. In this thesis, we investigated and developed methods for incorporating nonlocal effects into RANS models.

We began in Chapter 2 by attempting to incorporate nonlocal effects by using an analytical Reynolds stress modeling approach. We showed progress towards development of a near-wall model that respects the expected near-wall scalings but encountered issues in joining this near-wall model with the rest of the model. We also provided a review of experimental and DNS data for canonical flows that can be used to determine coefficients for RANS models in general, not only Reynolds stress models. These canonical flows build in complexity and include novel flows, such as anisotropic forced homogeneous turbulence, that have not previously been used in the context of modeling. One of the main challenges of analytical RANS model development is in discerning between appropriate model forms.

In the second part of this work, we took an alternative approach using MFM (Mani and Park (2021)), a numerical tool for probing closure operators. While MFM can be used to compute the exact nonlocal and anisotropic eddy viscosity for a given flow, a brute-force approach requires as many forced DNSs as degrees of freedom in the averaged space.

In Chapter 4, we developed a method for systematically modeling a nonlocal eddy viscosity using limited information about the eddy viscosity moments computed using MFM. The cost-saving advantages are that the model only needs information about the eddy viscosity moments, which can be obtained using one simulation per moment, and the proposed model form using matched moment inverse operators is in the form of a partial differential equation rather than an integro-partial differential equation. We demonstrated that for a wide range of flows, the modeled eddy viscosity kernel closely approximates the shape of the true nonlocal eddy viscosity kernel. For some flows, the model form and coefficient-fitting procedure leads to singularities in the coefficients, especially for wall-bounded flows. While we proposed a coefficient regularization technique for the near-wall region, in which viscous effects dominate and the model form becomes unimportant, this technique is not yet

systematic with regards to the regularization parameter. Future work should focus on investigation of other model forms and coefficient-fitting procedures, particularly for noisy turbulence data in which higher-order derivatives can amplify noise in the coefficient-fitting procedure. Concurrent work in Lavacot et al. (2023) shows application of our matched moment inverse operators to two-dimensional Rayleigh-Taylor instability, where without the presence of walls, there are fewer issues with singularities in the coefficients.

In Chapter 5, we developed adjoint MFM to address another aspect of the cost of brute-force MFM. Adjoint MFM can be used for targeted computation of the nonlocal eddy viscosity, i.e., the dependence of the Reynolds stresses at a specific location on the mean velocity gradient at all points in space, using one simulation per desired location. Concurrent work by Bryngelson et al. (2024) uses a combination of MFM and adjoint MFM simulations to significantly reduce the number of simulations needed to compute the eddy viscosity for the entire domain by leveraging hidden sparsity in the discretized eddy viscosity.

Then in Chapter 6 we used adjoint MFM to investigate the streamwise and wall-normal nonlocal eddy viscosity in turbulent channel flow. The main findings of this chapter were: 1) The streamwise nonlocality lengthscale is much longer than the wall-normal nonlocality lengthscale and increases with distance from the wall. We quantified this effect by computing a streamwise nonlocality lengthscale based on the first streamwise moment of the eddy viscosity kernel. For comparison, we also considered a streamwise nonlocality lengthscale based on a history effect along mean Lagrangian trajectories, which would be associated with a model form based on a relaxation timescale and a material derivative. Differences between the computed streamwise nonlocality lengthscale and the Lagrangian-based estimate suggest a modification of the model form using cross-diffusion terms or a turbulent diffusion term with spatially-varying viscosity. 2) The mean velocity gradient at a given point influences the shear component of the Reynolds stress farther downstream than the shear component of the Reynolds stress at the same point is influenced by the mean velocity gradient upstream. 3) We then examined the anisotropy of the eddy viscosity by comparing various components of the eddy viscosity kernel. The D_{2111} component of the eddy viscosity is larger in magnitude than D_{2121}, indicating larger sensitivity of the shear component of the Reynolds stress to $\partial U_1/\partial x_1$ than $\partial U_1/\partial x_2$. Under the Boussinesq eddy viscosity approximation, the shear component of the Reynolds stress would only be sensitive to $\partial U_1/\partial x_2$; however, we found that the sensitivity to $\partial U_1/\partial x_1$ is non-negligible and is actually larger than the sensitivity to $\partial U_1/\partial x_2$, which we hypothesize would have an effect in spatially-developing layers where $\partial U_1/\partial x_1$ is active. 4) The normal components of the Reynolds stress have much longer streamwise nonlocality lengthscales than the shear component of the Reynolds stress. For modeling purposes, this implies an anisotropic turbulence lengthscale or timescale, whereas most models currently use the same timescale for all components of the Reynolds stress tensor. Future work involves investigation of streamwise and wall-normal nonlocality effects for other flows, e.g., channel flow at higher Reynolds number or separated flows, for comparison.

Appendix A

Appendices for Chapter 2

A.1 $F_{ij}L^2$ model form

In this appendix, we show a model form based on $\tau_{ij} = F_{ij}L^2$ and develop transport equations for F_{ij} and L^2 that capture the expected analytical scalings for the Reynolds stresses for all components except τ_{22}. In this model, L needs to be $\sim y$ in both the viscous sublayer and log layer; however, this leads to complications in capturing the log layer behavior of the mean streamwise velocity in channel flow.

The boundary conditions on F_{ij} and the linear growth of $L \sim y$ are used to set the scalings for the Reynolds stresses near the wall. Consider the Taylor series expansion:

$$F_{ij} = a_{ij} + b_{ij}y + c_{ij}y^2 + \dots \tag{A.1}$$

Specifying a Dirichlet boundary condition, for example $F_{21}(y = 0) = 0$, leads to $F_{21} = b_{21}y$, and when combined with $L \sim y$, leads to the desired scaling $\tau_{21} = F_{21}L^2 \sim y^3$. Specifying a Neumann boundary condition, for example $\partial F_{11}/\partial y(y = 0) = 0$, leads to $F_{11} = a_{11}$, and the desired scaling $\tau_{11} = F_{11}L^2 \sim y^2$.

The model equations for F_{ij} and L^2 are derived based on substitution of $\tau_{ij} = F_{ij}L^2$ into a model form similar to the τ_{ij} equation in (2.22a), e.g.:

$$\frac{D\tau_{ij}}{Dt} = c_p \left(\tau_{kj}\frac{\partial U_i}{\partial x_k} + \tau_{ki}\frac{\partial U_j}{\partial x_k} \right) + \dots, \tag{A.2}$$

and substitution of $\tau_{ij} = F_{ij}L^2$:

$$L^2\frac{DF_{ij}}{Dt} + F_{ij}\frac{DL^2}{Dt} = c_p \left(L^2F_{kj}\frac{\partial U_i}{\partial x_k} + L^2F_{ki}\frac{\partial U_j}{\partial x_k} \right) + \dots. \tag{A.3}$$

We then split the terms among the equations for F_{ij} and L^2:

$$L^2\frac{DF_{ij}}{Dt} = \alpha_1 c_p\left(L^2F_{kj}\frac{\partial U_i}{\partial x_k} + L^2F_{ki}\frac{\partial U_j}{\partial x_k}\right) + \dots, \tag{A.4a}$$

$$F_{ij}\frac{DL^2}{Dt} = (1-\alpha_1)c_p\left(L^2F_{kj}\frac{\partial U_i}{\partial x_k} + L^2F_{ki}\frac{\partial U_j}{\partial x_k}\right) + \dots, \tag{A.4b}$$

where we use α_1 and $(1-\alpha_1)$ for illustration purposes since $\alpha_1 c_p$ will be renamed with a new coefficient in the final model. To reduce the tensorial equation for L^2 to a scalar equation, we take the trace of (A.4b). Considering all terms except the near-wall terms, the model equations are:

$$\begin{aligned}\frac{DF_{ij}}{Dt} =& c_{fp}\left(F_{kj}\frac{\partial U_i}{\partial x_k} + F_{ki}\frac{\partial U_j}{\partial x_k}\right) - c_{fB}F_{kk}S_{ij} - c_{fT}F_{mn}\frac{\partial U_n}{\partial x_m}\delta_{ij} + c_{fW}\left(F_{ki}\frac{\partial U_k}{\partial x_j} + F_{kj}\frac{\partial U_k}{\partial x_i}\right)\\ &-\frac{c_{fR}}{T_h}\left(F_{ij} - \frac{1}{3}F_{kk}\delta_{ij}\right) - \frac{c_{f\epsilon}}{T_h}F_{ij} + \frac{\partial}{\partial x_m}\left(c_D D\frac{\partial F_{ij}}{\partial x_m}\right) + \frac{1}{L^2}c_{fD}D\frac{\partial F_{ij}}{\partial x_m}\frac{\partial L^2}{\partial x_m}\end{aligned} \tag{A.5a}$$

$$\frac{DL^2}{Dt} = \frac{1}{F_{kk}}c_{sp}L^2F_{mn}\frac{\partial U_n}{\partial x_m} + \frac{c_{sg}}{T_h}L^2 + \frac{\partial}{\partial x_m}\left(c_D D\frac{\partial L^2}{\partial x_m}\right) + \frac{1}{F_{kk}}c_{sD}D\frac{\partial F_{kk}}{\partial x_m}\frac{\partial L^2}{\partial x_m} \tag{A.5b}$$

where $D = \sqrt{k}L$, $T_h = L/\sqrt{k}$, and $2c_D = c_{fD} + c_{sD}$. This results in a slightly different model form from the baseline model shown in Equation (2.22a) and (2.22b). The effective τ_{ij} equation is found by summing the F_{ij} equation in (A.5a) multiplied by L^2 and the L^2 equation in (A.5b) multiplied by F_{ij}:

$$\begin{aligned}\frac{D\tau_{ij}}{Dt} =& c_{sp}\frac{\tau_{ij}}{\tau_{kk}}\tau_{mn}\frac{\partial U_n}{\partial x_m} + c_{fp}\left(\tau_{kj}\frac{\partial U_i}{\partial x_k} + \tau_{ki}\frac{\partial U_j}{\partial x_k}\right) - c_{fB}\tau_{kk}S_{ij} - c_{fT}\tau_{mn}\frac{\partial U_n}{\partial x_m}\delta_{ij}\\ &+c_{fW}\left(\tau_{ki}\frac{\partial U_k}{\partial x_j} + \tau_{kj}\frac{\partial U_k}{\partial x_i}\right) - \frac{c_{fR}}{T_h}\left(\tau_{ij} - \frac{1}{3}\tau_{kk}\delta_{ij}\right) - \frac{c_{f\varepsilon} - c_{sg}}{T_h}\tau_{ij}\\ &+\frac{\partial}{\partial x_m}\left(c_D D\frac{\partial \tau_{ij}}{\partial x_m}\right) + (c_{fD} - 2c_D)\frac{D}{L^2}\frac{\partial \tau_{ij}}{\partial x_m}\frac{\partial L^2}{\partial x_m} + \frac{\tau_{ij}}{\tau_{kk}}c_{sD}\frac{D}{L^2}\frac{\partial \tau_{kk}}{\partial x_m}\frac{\partial L^2}{\partial x_m}\end{aligned} \tag{A.6a}$$

$$\frac{DL^2}{Dt} = c_{sp}L^2\frac{\tau_{mn}}{\tau_{kk}}\frac{\partial U_n}{\partial x_m} + \frac{c_{sg}}{T_h}L^2 + \frac{\partial}{\partial x_m}\left(c_D D\frac{\partial L^2}{\partial x_m}\right) + c_{sD}\frac{D}{\tau_{kk}}\frac{\partial \tau_{kk}}{\partial x_m}\frac{\partial L^2}{\partial x_m} - c_{sD}\frac{D}{L^2}\frac{\partial L^2}{\partial x_m}\frac{\partial L^2}{\partial x_m} \tag{A.6b}$$

where when compared with the baseline model in Equation (2.22a), the effective τ_{ij} equation has an additional production-like term (first term) and additional cross-diffusion terms (last two terms).

As for the near-wall model, splitting the viscous term for τ_{ij}:

$$\frac{D\tau_{ij}}{Dt} = \dots + \nu\frac{\partial^2\tau_{ij}}{\partial x_m \partial x_m} \tag{A.7}$$

results in

$$\frac{DF_{ij}}{Dt} = \cdots + \nu \frac{\partial^2 F_{ij}}{\partial x_m \partial x_m}, \tag{A.8a}$$

$$\frac{DL^2}{Dt} = \cdots + \nu \frac{\partial^2 L^2}{\partial x_m \partial x_m} + 2\nu \frac{1}{F_{kk}} \frac{\partial F_{kk}}{\partial x_m} \frac{\partial L^2}{\partial x_m}, \tag{A.8b}$$

where the cross-diffusion term appears in the L^2 equation in (A.8b) rather than the F_{ij} equation because a term of the form

$$\nu \frac{1}{L^2} \frac{\partial F_{ij}}{\partial x_m} \frac{\partial L^2}{\partial x_m} \tag{A.9}$$

would be $\mathcal{O}(1/y)$ and dominate in the F_{ij} equation. Moreover, additional terms in the near-wall model for L^2 are needed to ensure that $L \sim y$ near the wall:

$$\frac{DL^2}{Dt} = \cdots + \nu \left(\frac{\partial^2 L^2}{\partial x_m \partial x_m} - c_{mA} \frac{\partial L}{\partial x_m} \frac{\partial L}{\partial x_m} + c_{mB} \right). \tag{A.10}$$

For example, substitution of the solution $L = \alpha y$ into (A.10) leads to

$$c_{mB} = \alpha^2 (c_{mA} - 2) \tag{A.11}$$

and a constraint that $c_{mA} > 2$ for positive L.

To determine the coefficients, we use the process outlined in Section 2.3. The model equations are identical to the baseline model for decaying HIT and forced HT. The addition of the c_{sp} term in (A.6a) affects the model equations and coefficients for homogeneous shear flow. We then use the log layer equations to determine the diffusion coefficients. However, because only the differences $(c_D - c_{fD})$ and $(c_D - c_{sD})$ appear in the log layer equations, an additional flow is needed to discern between c_D, c_{fD}, and c_{sD}. For this purpose, we use the self-similar axisymmetric jet and the experimental data of Hussein et al. (1994).

In channel flow, the remaining coefficients to be determined are the near-wall model coefficients, c_{mA} and c_{mB}. The length scale, L, is intended to grow linearly from the wall; however, a distinct inner and outer region appears in L, which affects the model's ability to correctly capture the log law. For improved behavior of L, we modified the diffusion term to the tensorial diffusion term of Daly and Harlow (1970):

$$\frac{D\tau_{ij}}{Dt} = \cdots + c_D \frac{\partial}{\partial x_k} \left(\frac{L}{\sqrt{k}} \tau_{kl} \frac{\partial \tau_{ij}}{\partial x_l} \right), \tag{A.12}$$

which for channel flow modifies $D = \sqrt{k}L$ to $D = (L/\sqrt{k})\tau_{22}$. However, the distinct inner and outer regions in L remain an issue. Figure A.1a shows an example of the mean streamwise velocity for channel flow at $\mathrm{Re}_\tau = 180$. Figure A.1b shows the corresponding L. In the derivation of the log layer equations, we assumed $L = c_{lL} y$. However, Figure A.1b shows two separate slopes for L in the viscous sublayer and log layer with a nonzero intercept in the log layer. This in turn affects

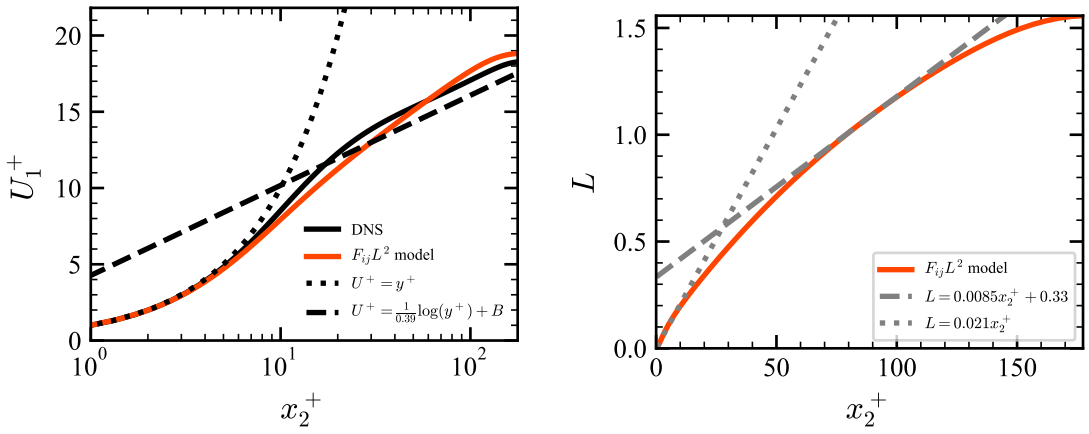

(a) (b)

Figure A.1: (a) Mean velocity comparison of the $F_{ij}L^2$ model with the DNS of Lee and Moser (2015) at $\mathrm{Re}_\tau = 180$. (b) Length scale L with approximate fitted linear slopes for the viscous sublayer and log layer.

the ability of the $F_{ij}L^2$ model to correctly capture the expected log layer behavior of the mean streamwise velocity.

A.2 Nonlinear model forms for return to isotropy

In this appendix, we consider the addition of nonlinear terms to the return to isotropy model. For example, the simplest addition is a term that is quadratic in the Reynolds stress tensor:

$$\frac{D\tau_{ij}}{Dt} = \cdots - \frac{c_{fNR}}{T_h k}\tau_{ik}\tau_{kj}. \tag{A.13}$$

For determining the coefficients, the steady-state forced homogeneous turbulence equations are:

$$0 = -\frac{c_{fR}}{T_h}\left(\tau_{ij} - \frac{1}{3}\tau_{kk}\delta_{ij}\right) - \frac{c_{fNR}}{T_h k}\tau_{ik}\tau_{kj} - \frac{c_{f\varepsilon} - c_{sg}}{T_h}\tau_{ij} + A_{ki}\tau_{kj} + A_{kj}\tau_{ki}, \tag{A.14}$$

where the return to isotropy coefficients, c_{fR} and c_{fNR}, are to be determined, and T_h is a free parameter. With $c_{fR} = 3$ and $c_{fNR} = -3$, Table A.1 and Table A.2 show low model errors when compared with the anisotropic forced HT data of Dhandapani et al. (2019) and Rah et al. (2018), respectively. However, there is an additional constraint for numerical robustness such that the turbulence extracts energy from the mean flow (Park et al. (2022a)):

$$\int_V \overline{u_i' u_j'}\frac{\partial U_i}{\partial x_j}\mathrm{d}V \leq 0, \tag{A.15}$$

τ_{ij}/k	Quadratic model	Dhandapani et al. (2019)	Error
τ_{11}/k	1.03	0.99	4%
τ_{22}/k	0.55	0.58	5%
τ_{33}/k	0.42	0.43	2%
τ_{21}/k	0.36	0.38	5%

Table A.1: *A posteriori* analysis for the nonlinear return to isotropy coefficients $c_{fR} = 3$ and $c_{fNR} = -3$ and comparison with the anisotropic forced HT data from Dhandapani et al. (2019).

τ_{ij}/k	Quadratic model	Rah et al. (2018)	Error
τ_{11}/k	1.0	0.98	2%
τ_{22}/k	0.50	0.51	2%

Table A.2: *A posteriori* analysis for the nonlinear return to isotropy coefficients $c_{fR} = 3$ and $c_{fNR} = -3$ and comparison with the anisotropic forced HT data from Rah et al. (2018).

and $c_{fNR} \geq -3/4$ is needed to satisfy this constraint, which we now show.

We derive this constraint by taking the trace of the model equation in (2.22a) with the additional nonlinear return to isotropy term:

$$\frac{D\tau_{ii}}{Dt} = (2c_{fp} - 3c_{fT} + 2c_{fW})\tau_{ki}\frac{\partial U_i}{\partial x_k} - \frac{c_{fNR}}{T_h k}\tau_{ik}\tau_{ki} - \frac{c_{f\varepsilon} - c_{sg}}{T_h}\tau_{ii} + \frac{\partial}{\partial x_k}\left(c_D D\frac{\partial \tau_{ii}}{\partial x_k}\right). \tag{A.16}$$

Taking the volume integral of both sides and with suitable boundary conditions and initial conditions such that the net advective and diffusive fluxes are zero:

$$0 = \int_V \left[(2c_{fp} - 3c_{fT} + 2c_{fW})\tau_{ki}\frac{\partial U_i}{\partial x_k} - \frac{c_{fNR}}{T_h k}\tau_{ik}\tau_{ki} - \frac{c_{f\varepsilon} - c_{sg}}{T_h}\tau_{ii}\right] \mathrm{d}V. \tag{A.17}$$

Rearrangement and substitution of $T_h = L/\sqrt{k}$ leads to

$$\int_V \tau_{ki}\frac{\partial U_i}{\partial x_k}\mathrm{d}V = \frac{1}{-2c_{fp} + 3c_{fT} - 2c_{fW}}\int_V \left[-2(c_{f\varepsilon} - c_{sg})\frac{k^{3/2}}{L} - \frac{c_{fNR}}{\sqrt{k}L}\tau_{ik}\tau_{ki}\right] \mathrm{d}V \leq 0. \tag{A.18}$$

The bounds of the nonlinear term can be derived based on the invariants of the Lumley triangle (Pope (2000)):

$$6\eta^2 = b_{ij}b_{ji}, \tag{A.19}$$

where $0 \leq \eta \leq 1/3$ and

$$b_{ij} \equiv \frac{\tau_{ij}}{\tau_{kk}} - \frac{1}{3}\delta_{ij}, \tag{A.20}$$

i.e.,

$$\tau_{ik}\tau_{ki} = 4k^2 b_{ik}b_{ki} + \frac{4}{3}k^2 = 24k^2\eta^2 + \frac{4}{3}k^2. \tag{A.21}$$

τ_{ij}/k	Quadratic model	Dhandapani et al. (2019)	Error
τ_{11}/k	1.01	0.99	2%
τ_{22}/k	0.51	0.58	12%
τ_{33}/k	0.48	0.43	12%
τ_{21}/k	0.36	0.38	6%

Table A.3: *A posteriori* analysis for the nonlinear return to isotropy coefficients $c_{fR} = 3$ and $c_{fNR} = -3/4$ and comparison with the anisotropic forced HT data from Dhandapani et al. (2019).

In the $\eta = 0$ limit:

$$\int_V \tau_{ki} \frac{\partial U_i}{\partial x_k} \mathrm{d}V = \frac{-c_{f\varepsilon} + c_{sg} - 2/3 c_{fNR}}{-2c_{fp} + 3c_{fT} - 2c_{fW}} \int_V \frac{k^{3/2}}{L} \mathrm{d}V \leq 0, \tag{A.22}$$

and since the turbulent kinetic energy, k, and length scale, L, are always non-negative:

$$\frac{-c_{f\varepsilon} + c_{sg} - 2/3 c_{fNR}}{-2c_{fp} + 3c_{fT} - 2c_{fW}} \leq 0. \tag{A.23}$$

In the $\eta = 1/3$ limit:

$$\frac{-c_{f\varepsilon} + c_{sg} - 2c_{fNR}}{-2c_{fp} + 3c_{fT} - 2c_{fW}} \leq 0. \tag{A.24}$$

From forced HIT, the addition of the nonlinear term also modifies the constraint on the decay coefficients $c_{f\varepsilon}$ and c_{sg} from Equation (2.31) to

$$-(c_{f\epsilon} - c_{sg}) - 2/3 c_{fNR} = -1. \tag{A.25}$$

Substitution of (A.25) into (A.23) leads to:

$$-2c_{fp} + 3c_{fT} - 2c_{fW} \geq 0, \tag{A.26}$$

and substitution of (A.25) and (A.26) into (A.24) leads to

$$c_{fNR} \geq -3/4. \tag{A.27}$$

Table A.3 and Table A.4 show a comparison with Dhandapani et al. (2019) and Rah et al. (2018) with $c_{fNR} = -3/4$. The numerical robustness constraint on c_{fNR} in (A.27) results in larger errors than with $c_{fNR} = -3$, and generally, increasing c_{fNR} leads to larger model errors. The model errors are now of similar magnitude to the errors with the linear return to isotropy term shown in Table 2.6 and Table 2.7.

τ_{ij}/k	Quadratic model	Rah et al. (2018)	Error
τ_{11}/k	0.8	0.98	18%
τ_{22}/k	0.6	0.51	17%

Table A.4: *A posteriori* analysis for the nonlinear return to isotropy coefficients $c_{fR} = 3$ and $c_{fNR} = -3/4$ and comparison with the anisotropic forced HT data from Rah et al. (2018).

τ_{ij}/k	Traceless quadratic model	Dhandapani et al. (2019)	Error
τ_{11}/k	1.02	0.99	3%
τ_{22}/k	0.55	0.58	6%
τ_{33}/k	0.44	0.43	1%
τ_{21}/k	0.36	0.38	6%

Table A.5: *A posteriori* analysis for the traceless nonlinear return to isotropy coefficients $c_{fR} = 15$ and $c'_{fNR} = -7.5$ and comparison with the anisotropic forced HT data from Dhandapani et al. (2019).

As an alternative to the quadratic term in Equation (A.13), a quadratic term of the form:

$$\frac{D\tau_{ij}}{Dt} = \cdots - \frac{c'_{fNR}}{\sqrt{k}L}\left(\tau_{ik}\tau_{kj} - \frac{1}{3}\tau_{mn}\tau_{mn}\delta_{ij}\right) \tag{A.28}$$

has no trace and thus would not be affected by the numerical robustness constraint. While the addition of this term can lower the model error in the comparison with Dhandapani et al. (2019) as in Table A.5 for $c_{fR} = 15$ and $c'_{fNR} = -7.5$, the model errors tend to be larger than the linear return to isotropy model for the comparison with Rah et al. (2018) as shown in Table A.6. Moreover, with some choices of coefficients there are multiple solutions or no solutions for this model form.

Because the model errors from an additional quadratic return to isotropy term under an additional numerical robustness constraint are on the order of those of the linear return to isotropy term, we use the simpler linear return to isotropy term in the baseline model. We do not consider higher-order nonlinear terms as these are known to cause oscillations (Speziale et al. (1994)).

τ_{ij}/k	Traceless quadratic model	Rah et al. (2018)	Error
τ_{11}/k	0.74	0.98	25%
τ_{22}/k	0.63	0.51	24%

Table A.6: *A posteriori* analysis for the traceless nonlinear return to isotropy coefficients $c_{fR} = 15$ and $c'_{fNR} = -7.5$ and comparison with the anisotropic forced HT data from Rah et al. (2018).

A.3 Analytical solutions to the near-wall model for $\overline{v^2}$ and $\overline{w^2}$

In this appendix, we show analytical solutions for the near-wall model for $\overline{v^2}$ and $\overline{w^2}$ in Equations (2.55a) and (2.55b), respectively, rewritten here at steady-state:

$$0 = \nu\frac{\partial^2\overline{v^2}}{\partial y^2} - c_{m\beta}\nu\frac{\overline{v^2}}{y^2} + c_{m\gamma}\nu k_\nu^2\overline{w^2}, \tag{A.29a}$$

$$0 = \nu\frac{\partial^2\overline{w^2}}{\partial y^2} - c_{m\alpha}\nu\frac{\overline{w^2}}{y^2}. \tag{A.29b}$$

With $c_{m\alpha} = 2$, the solution to (A.29b) is

$$\overline{w^2} = c_1 y^2 + \frac{c_2}{y}, \tag{A.30}$$

and with the no-slip boundary condition $\overline{w^2}(y = 0) = 0$, $c_2 = 0$, and $\overline{w^2} \sim y^2$ as expected. We rename $c_1 = a^2$ to be consistent with the notation for the $\overline{w^2}$ scaling in Equation (2.54b) and substitution of $\overline{w^2} = a^2y^2$ into the $\overline{v^2}$ equation in (A.29a) and solving leads to

$$\overline{v^2} = \frac{c_{m\gamma}a^2k_\nu^2}{c_{m\beta} - 12}y^4 + c_3 y^{1/2\left(\sqrt{4c_{m\beta}+1}+1\right)} + c_4 y^{1/2\left(-\sqrt{4c_{m\beta}+1}+1\right)}. \tag{A.31}$$

With $c_{m\gamma} \neq 0$, $c_{m\beta} > 12$ is needed for the desired $\overline{v^2} \sim y^4$ scaling to come from the first term, which dominates in the limit of small y. Moreover, $c_{m\gamma} > 0$ is needed for realizable $\overline{v^2} > 0$. The no-penetration boundary condition $\overline{v^2}(y = 0) = 0$ leads to $c_4 = 0$. The coefficient coupling constraint in Equation (2.56b), $c_{m\beta} = 12 + 4c_{m\gamma}$, leads to

$$\overline{v^2} = \frac{1}{4}a^2k_\nu^2y^4 + c_3 y^{1/2\left(\sqrt{4c_{m\beta}+1}+1\right)}, \tag{A.32}$$

and the desired leading-order scaling relationship between $\overline{v^2}$ and $\overline{w^2}$ in Equations (2.54a) and (2.54b) comes from the first term, and the second term (with c_3 coefficient) is higher order.

As a note, the scaling $\overline{v^2} \sim y^4$ is achievable without the coupling term ($c_{m\gamma} = 0$) and $c_{m\beta} = 12$, in which case the second term (with c_3 coefficient) leads to the desired scaling. However, then $\overline{v^2}$ and $\overline{w^2}$ are independent of each other.

A.4 Derivation of near-wall model for $\overline{u^2}$ and $\overline{uv}$

In this appendix, we detail the derivation of the near-wall model for $\overline{u^2}$ and $\overline{uv}$. The streamwise fluctuations u' are modeled as a passive scalar (i.e., no pressure coupling with v' and w') transported

by the sinusoidal counter-rotating vortices in Figure 2.4:

$$u'(y) = u(y)\sin(k_\nu z). \tag{A.33}$$

The governing Stokes flow equation for u' is

$$\frac{\partial u'}{\partial t} + v'\frac{\partial U}{\partial y} = \nu\frac{\partial^2 u'}{\partial y^2} + \nu\frac{\partial^2 u'}{\partial z^2}. \tag{A.34}$$

Substitution of the sinusoidal approximation in (A.33) into (A.34) leads to

$$\frac{\partial u}{\partial t} + v\frac{\partial U}{\partial y} = \nu\frac{\partial^2 u}{\partial y^2} - \nu k_\nu^2 u. \tag{A.35}$$

Multiplication of the u equation in (A.35) by u and averaging leads to

$$\frac{1}{2}\frac{\partial \overline{u^2}}{\partial t} = -\overline{uv}\frac{\partial U}{\partial y} + \frac{1}{2}\nu\frac{\partial^2 \overline{u^2}}{\partial y^2} - \nu\overline{\frac{\partial u}{\partial y}\frac{\partial u}{\partial y}} - \nu k_\nu^2\overline{u^2}, \tag{A.36}$$

where the dissipation term (third term) on the right hand side needs closure. Consider the Taylor series expansion for u:

$$u = b_1 y + c_1 y^2 + \ldots, \tag{A.37}$$

and the corresponding expansion for $\overline{u^2}$ formed by squaring (A.37) and averaging:

$$\overline{u^2} = b_1^2 y^2 + 2b_1 c_1 y^3 + \ldots. \tag{A.38}$$

Similarly, the expansion for $\overline{uv}$ is formed by multiplying the expansion for u in (A.37) with the expansion for v and averaging:

$$\overline{uv} = \frac{1}{2}ab_1 k_\nu y^3 + \ldots. \tag{A.39}$$

Substituting the above expansions into the governing equation for $\overline{u^2}$ in Equation (A.36) shows that the viscous diffusion term (second term) and dissipation term (third term) on the right hand side are $\mathcal{O}(1)$, while the production term (first term) and last term on the right hand side are higher order and neglected. Similar to the model for $\overline{v^2}$ and $\overline{w^2}$, we close the dissipation term using $\nu\overline{u^2}/y^2$:

$$\frac{\partial \overline{u^2}}{\partial t} = \nu\frac{\partial^2 \overline{u^2}}{\partial y^2} - \nu c_{m\phi}\frac{\overline{u^2}}{y^2}, \tag{A.40}$$

and the coefficient $c_{m\phi} = 2$ is needed for $\overline{u^2} \sim y^2$.

Similarly, the governing equation for $\overline{uv}$ is formed by adding the u equation in (A.35) multiplied

by v and the v equation in (2.50a) multiplied by u and averaging:

$$\frac{\partial \overline{uv}}{\partial t} = -\overline{v^2}\frac{\partial \overline{U}}{\partial y} + \nu\frac{\partial^2 \overline{uv}}{\partial y^2} - 2\nu\overline{\frac{\partial u}{\partial y}\frac{\partial v}{\partial y}} - 2\nu k_\nu^2 \overline{uv} - \overline{u\frac{\partial p}{\partial y}} \tag{A.41}$$

Substitution of the expansions into (A.41) shows that the viscous diffusion term (second term), dissipation term (third term), and pressure term (last term) on the right hand side are $\mathcal{O}(y)$, while the production term (first term) and fourth term on the right hand side are higher order and neglected. Similar to the model for the other Reynolds stress components, we close the dissipation term using $\nu\overline{uv}/y^2$. The pressure term also has a similar leading-order scaling to $\nu\overline{uv}/y^2$:

$$\overline{u\frac{\partial p}{\partial y}} = (b_1 y + c_1 y^2 + \dots)(\nu a k_\nu + 2\nu b k_\nu^2 y + \dots) = \nu a b_1 k_\nu y + \dots \tag{A.42}$$

and thus we use $\nu\overline{uv}/y^2$ as well for its closure. The model form for $\overline{uv}$ is:

$$\frac{\partial \overline{uv}}{\partial t} = \nu\frac{\partial^2 \overline{uv}}{\partial y^2} - \nu c_{m\psi}\frac{\overline{uv}}{y^2}, \tag{A.43}$$

where the coefficient $c_{m\psi} = 6$ is needed for $\overline{uv} \sim y^3$.

A.5 Log layer equations for the baseline model form

In the log layer, terms with the molecular viscosity are negligible. We assume the length scale is linear in the log layer, $L = c_{lL}y$, where the coefficient c_{lL} is unknown. Moreover, as with other RANS models, we assume $\tau_{ij}^+ \equiv \tau_{ij}/u_\tau^2$ is constant in the log layer, where u_τ is the friction velocity. Section 2.1.4 discusses that this assumption is valid for τ_{21}^+ and τ_{22}^+, but likely invalid for τ_{11}^+ and τ_{33}^+. Substitution of $L = c_{lL}y$, $\tau_{ij} = \tau_{ij}^+ u_\tau^2$, and $\mathrm{d}U_1/\mathrm{d}x_2 = u_\tau/(\kappa y)$ leads to the model equations:

$$0 = \left(-c_{sp}\frac{\tau_{11}^+}{\tau_{kk}^+} + 2c_{fp} - c_{fT}\right)\frac{\tau_{21}^+}{\kappa} - c_{fR}\frac{\sqrt{k^+}}{c_{lL}}\left(\tau_{11}^+ - \frac{1}{3}\tau_{kk}^+\right) - c_{f\varepsilon}\frac{\sqrt{k^+}}{c_{lL}}\tau_{11}^+ \\ - 2c_D\sqrt{k^+}c_{lL}\tau_{11}^+ + c_{sginner}\sqrt{k^+}\tau_{11}^+, \tag{A.44a}$$

$$0 = \left(-c_{sp}\frac{\tau_{22}^+}{\tau_{kk}^+} - c_{fT} + 2c_{fW}\right)\frac{\tau_{21}^+}{\kappa} - c_{fR}\frac{\sqrt{k^+}}{c_{lL}}\left(\tau_{22}^+ - \frac{1}{3}\tau_{kk}^+\right) - c_{f\varepsilon}\frac{\sqrt{k^+}}{c_{lL}}\tau_{22}^+ \\ - 2c_D\sqrt{k^+}c_{lL}\tau_{22}^+ + c_{sginner}\sqrt{k^+}\tau_{22}^+, \tag{A.44b}$$

$$0 = \left(-c_{sp}\frac{\tau_{33}^+}{\tau_{kk}^+} - c_{fT}\right)\frac{\tau_{21}^+}{\kappa} - c_{fR}\frac{\sqrt{k^+}}{c_{lL}}\left(\tau_{33}^+ - \frac{1}{3}\tau_{kk}^+\right) - c_{f\varepsilon}\frac{\sqrt{k^+}}{c_{lL}}\tau_{33}^+ \\ - 2c_D\sqrt{k^+}c_{lL}\tau_{33}^+ + c_{sginner}\sqrt{k^+}\tau_{33}^+, \tag{A.44c}$$

$$0 = \left(-c_{sp}\frac{\tau_{21}^+}{\tau_{kk}^+}\tau_{21}^+ + c_{fp}\tau_{22}^+ - c_{fB}k^+ + c_{fW}\tau_{11}^+\right)\frac{1}{\kappa} - (c_{fR} + c_{f\epsilon})\frac{\sqrt{k^+}}{c_{lL}}\tau_{21}^+ \\ - 2c_D\sqrt{k^+}c_{lL}\tau_{21}^+ + c_{sginner}\sqrt{k^+}\tau_{21}^+, \tag{A.44d}$$

$$0 = c_{sp}\frac{\tau_{21}^+}{\tau_{kk}^+}\frac{1}{\kappa} + c_{sg}\frac{\sqrt{k^+}}{c_{lL}} - c_{sginner}\sqrt{k^+} + 2c_D\frac{c_{lL}}{\sqrt{k^+}}\tau_{22}^+. \tag{A.44e}$$

The coefficients $c_{sginner}$, c_D, and c_{lL} are unknown. The shear component of the Reynolds stress tensor is set to its theoretical high Reynolds number limit, $\tau_{21}^+ = -1$. The von Kàrmàn constant is set to $\kappa = 0.39$, based on the review of recent literature shown in Table 2.4. Due to the uncertainty in the high Reynolds number behavior of the normal components of the Reynolds stress tensor, τ_{11}^+, τ_{22}^+, and τ_{33}^+ are treated as unknowns. Additionally, τ_{kk}^+ is unknown, and we enforce $\tau_{kk}^+ = \tau_{11}^+ + \tau_{22}^+ + \tau_{33}^+$. With these choices, there are 7 unknowns ($c_{sginner}$, c_D, c_{lL}, τ_{11}^+, τ_{22}^+, τ_{33}^+, τ_{kk}^+), and 6 equations (Equations (A.44a) - (A.44e) and $\tau_{kk}^+ = \tau_{11}^+ + \tau_{22}^+ + \tau_{33}^+$). We sweep values of $c_{sginner}$ and solve for the corresponding c_D, c_{lL}, τ_{11}^+, τ_{22}^+, τ_{33}^+, and τ_{kk}^+. For various values of $c_{sginner}$, we find that only the value of c_D changes, and c_{lL}, τ_{11}^+, τ_{22}^+, and τ_{33}^+ are unchanged. These values are: $c_{lL} = 2.40$, $\tau_{11}^+ = 3.15$, $\tau_{22}^+ = 1.61$, $\tau_{33}^+ = 2.10$. As discussed in Section 2.4.1, we then use the numerical solution of turbulent channel flow in Section 2.4.1 to decide the optimal $c_{sginner}$ ($c_{sginner} = 0.27$, and from the

log layer analysis, $c_D = 0.0021$). Also as discussed in Section 2.4.1, this log layer analysis provides only an estimate of the model behavior as the near-wall model actually influences this behavior.

Appendix B

Appendices for Chapters 3 and 4

B.1 Derivation of the relationship between $\overline{\mathcal{L}}$ and $\mathcal{L}$

For completeness, the derivation of the relationship in (3.16) between the averaged operator, $\overline{\mathcal{L}}$, and the governing operator, $\mathcal{L}$, is reproduced from Mani and Park (2021) below. This appendix also shows the relationship between these operators and the forcing methods detailed in Section 3.3.

The forced governing equation in (3.19) can be written in operator form as

$$\mathcal{L}c = s, \tag{B.1}$$

where $\mathcal{L}$ is a matrix representing the discretized advection-diffusion operator, c is a vector representing the discretized scalar field, and s is vector representing the MFM forcing. Similarly, the forced averaged equation can be written as

$$\overline{\mathcal{L}}\bar{c} = \bar{s}, \tag{B.2}$$

where $\overline{\mathcal{L}}$ is a linear operator and includes the nonlocal eddy diffusivity, $\bar{c}$ is the discretized mean scalar field, and $\bar{s}$ is the MFM forcing. The averaged operator, $\overline{\mathcal{L}}$, is unknown, and a relation between $\overline{\mathcal{L}}$ and $\mathcal{L}$ is desired. Let averaging be defined by a projection operator, P, such that

$$\bar{c} = Pc. \tag{B.3}$$

While the MFM forcing satisfies the property, $s = \bar{s}$, s and $\bar{s}$ may discretely have different dimensions; thus, let E be an extension operator such that

$$s = E\bar{s}. \tag{B.4}$$

Rearranging (B.1) to solve for c and substituting the result into (B.3) leads to

$$\bar{c} = P\mathcal{L}^{-1}s = P\mathcal{L}^{-1}E\bar{s}, \tag{B.5}$$

where the definition of the extension operator in (B.4) is used. Further rearrangement,

$$\left(P\mathcal{L}^{-1}E\right)^{-1}\bar{c} = \bar{s}, \tag{B.6}$$

and comparison with (B.2) leads to the relation for $\overline{\mathcal{L}}$ in (3.16).

In the above approach, the MFM forcing, s, is never explicitly specified, and the entire $\overline{\mathcal{L}}$ operator is obtained at the expense of inverting $\mathcal{L}$. However, as detailed in Mani and Park (2021), one can also use MFM to obtain the averaged operator by explicitly specifying the forcing to obtain columns of $\overline{\mathcal{L}}^{-1}$. For example, one can specify $\bar{s} = [1\,0\,\ldots\,0]^\top$, solve the forced governing equation in (3.19), post-process $\bar{c}$ to obtain the first column of $\overline{\mathcal{L}}^{-1}$ using

$$\bar{c} = \overline{\mathcal{L}}^{-1}\bar{s}, \tag{B.7}$$

and repeat until all columns of $\overline{\mathcal{L}}^{-1}$ are filled. Alternatively, as detailed in Mani and Park (2021) and in Section 3.3, one can also use IMFM to specify $\bar{c}$ for more direct computation of the nonlocal eddy diffusivity or moments of the nonlocal eddy diffusivity.

B.2 Comparison of methods for obtaining the nonlocal eddy diffusivity

This appendix is motivated by the observation of two apparently different derivations for the exact expression of the nonlocal eddy diffusivity. Using a Green's function solution, Hamba (1995, 2004) derived an exact expression for the nonlocal eddy diffusivity, while Mani and Park (2021) presented a derivation based on macroscopic forcing of a linear system. In this appendix, we demonstrate that when IMFM is used to obtain the full nonlocal eddy diffusivity (as opposed to using IMFM to obtain moments as used extensively in this work), its formulation is compatible with the earlier work by Hamba (1995, 2004). In Hamba's approach, the transport equation for the scalar fluctuation, c', is given by

$$\frac{\partial c'}{\partial t} + \frac{\partial}{\partial x_j}(u_j c' - \overline{u_j' c'}) - D_M \frac{\partial^2 c'}{\partial x_j \partial x_j} = -u_j' \frac{\partial \bar{c}}{\partial x_j}. \tag{B.8}$$

The mean scalar gradient on the right-hand-side is considered a source term for c'. Using the Green's function, $g_i'(\mathbf{x}, \mathbf{y}, t, \tau)$, satisfying

$$\frac{\partial g_i'}{\partial t} + \frac{\partial}{\partial x_j}(u_j g_i' - \overline{u_j' g_i'}) - D_M \frac{\partial^2 g_i'}{\partial x_j \partial x_j} = u_i' \delta(\mathbf{x} - \mathbf{y})\delta(t - \tau), \tag{B.9}$$

the solution to Equation (B.8) is

$$c'(\mathbf{x},t) = -\int_{\mathbf{y},\tau} g_i'(\mathbf{x},\mathbf{y},t,\tau)\frac{\partial \bar{c}}{\partial x_i}\bigg|_{\mathbf{y},\tau} \mathrm{d}\mathbf{y}\mathrm{d}\tau. \tag{B.10}$$

Hence, the scalar flux can be written as

$$-\overline{u_j'c'}(\mathbf{x},t) = \int_{\mathbf{y},\tau} \overline{u_j'(\mathbf{x},t)g_i'(\mathbf{x},\mathbf{y},t,\tau)}\frac{\partial \bar{c}}{\partial x_i}\bigg|_{\mathbf{y},\tau} \mathrm{d}\mathbf{y}\mathrm{d}\tau, \tag{B.11}$$

where

$$D_{ji}(\mathbf{x},\mathbf{y},t,\tau) = \overline{u_j'(\mathbf{x},t)g_i'(\mathbf{x},\mathbf{y},t,\tau)} \tag{B.12}$$

is the nonlocal eddy diffusivity, and Equation (B.11) is identical to Equation (3.6).

To compare the approach presented by Mani and Park (2021), which arrived at the same nonlocal eddy diffusivity, consider the forced scalar transport equation:

$$\frac{\partial c}{\partial t} + \frac{\partial}{\partial x_j}(u_j c) - D_M\frac{\partial^2 c}{\partial x_j \partial x_j} = s. \tag{B.13}$$

To obtain the full nonlocal eddy diffusivity, one can specify the macroscopic forcing, $s = \bar{s}$, to maintain the mean scalar gradient as a Dirac delta function, and then post-process $-\overline{u_j'c'}$. To allow further comparison with Hamba's approach, the forced mean scalar transport equation is

$$\frac{\partial \bar{c}}{\partial t} + \frac{\partial}{\partial x_j}(\bar{u}_j\bar{c}) + \frac{\partial}{\partial x_j}(\overline{u_j'c'}) - D_M\frac{\partial^2 \bar{c}}{\partial x_j \partial x_j} = \bar{s}. \tag{B.14}$$

Substituting $\bar{s} = s$ from Equation (B.14) into Equation (B.13) leads to the scalar fluctuation equation:

$$\frac{\partial c'}{\partial t} + \frac{\partial}{\partial x_j}(u_j c') + u_j'\frac{\partial \bar{c}}{\partial x_j} - \frac{\partial}{\partial x_j}(\overline{u_j'c'}) - D_M\frac{\partial^2 c'}{\partial x_j \partial x_j} = 0, \tag{B.15}$$

which is identical to Hamba's equation in (B.8).

Additionally, to compare the MFM forcing with the implied forcing in Hamba's approach, we rearrange (B.14):

$$-\frac{\partial}{\partial x_j}(\overline{u_j'c'}) = \frac{\partial \bar{c}}{\partial t} + \frac{\partial}{\partial x_j}(\bar{u}_j\bar{c}) - D_M\frac{\partial^2 \bar{c}}{\partial x_j \partial x_j} - \bar{s}, \tag{B.16}$$

and observe that the corresponding term in the Green's function equation (Equation (B.9)), $-\partial/\partial x_j(\overline{u_j'g_i'})$, is an implied forcing term that contains the macroscopic forcing. An analogous comparison between Hamba (2005) and Mani and Park (2021) can also be made for momentum transport and Reynolds stress closures.

B.3 Obtaining the spatiotemporal eddy diffusivity for the homogeneous model problem

The spatiotemporal eddy diffusivity shown in Figure 4.3a may be obtained by using the Green's function approach of Hamba (2004) or similarly, IMFM as detailed here. For the homogeneous model problem in Section 4.3.1, the unclosed scalar flux can be written as

$$-\overline{u_1'c'}(x_1,t) = \int_0^t \int_{-\infty}^{\infty} D(y_1 - x_1, \tau - t) \frac{\partial \bar{c}}{\partial x_1}\bigg|_{y_1,\tau} \mathrm{d}y_1 \mathrm{d}\tau, \tag{B.17}$$

where $\bar{()}$ denotes averaging in the x_2-direction, and $D(y_1 - x_1, \tau - t)$ is the spatiotemporal eddy diffusivity. Using IMFM and prescribing $\partial\bar{c}/\partial x_1$ as a Dirac delta function in both space and time:

$$-\overline{u_1'c'}(x_1,t) = \int_0^t \int_{-\infty}^{\infty} D(y_1 - x_1, \tau - t)\delta(y_1,\tau) \mathrm{d}y_1 \mathrm{d}\tau, \tag{B.18}$$

then by the sifting property of the delta function:

$$-\overline{u_1'c'}(x_1,t) = D(-x_1,-t). \tag{B.19}$$

The spatiotemporal eddy diffusivity can be obtained by post-processing $-\overline{u_1'c'}(x_1,t)$ since the flow is homogeneous.

B.4 MMI model error for the homogeneous problem

For the homogeneous model problem in Section 4.3.1, the spatiotemporal MMI model in (4.28) matches up to the second-order spatial moment and first-order temporal moment of the eddy diffusivity. While the MMI model keeps an infinite Taylor series expansion (whereas the leading-order Taylor model and higher-order Taylor model truncate the expansion), the higher-order moments are not enforced to match those of the true eddy diffusivity kernel. The resulting error is discussed in this appendix.

Consider the Taylor series expansion of the nonlocal eddy diffusivity in (3.9) simplified for the homogeneous model problem in Section 4.3.1:

$$-\overline{u_1'c'} = D^0 \frac{\partial \bar{c}}{\partial x_1} + D^{1_s} \frac{\partial^2 \bar{c}}{\partial x_1^2} + D^{2_s} \frac{\partial^3 \bar{c}}{\partial x_1^3} + \cdots + D^{1_t} \frac{\partial^2 \bar{c}}{\partial t \partial x_1} + \ldots \tag{B.20}$$

The order of each term can be estimated by approximating the eddy diffusivity moments using a characteristic velocity, u_{rms}, and mixing length, l, e.g., $D^0 \sim u_{rms} l$, and the mean scalar gradient

using $\Delta\bar{c}/L$, where L is a characteristic length scale of the mean scalar:

$$-\overline{u_1'c'} \sim u_{rms}\Delta\bar{c}\left(\frac{l}{L}\right) + u_{rms}\Delta\bar{c}\left(\frac{l}{L}\right)^2 + u_{rms}\Delta\bar{c}\left(\frac{l}{L}\right)^3 + \dots \tag{B.21}$$

The ratio l/L may be $\mathcal{O}(1)$ for problems with small L, e.g., for the initial condition in the homogeneous problem which consists of a narrow band of $\bar{c}$. In this case, the higher-order terms are not necessarily small. By truncating the Taylor series expansion, the higher-order Taylor model neglects these higher-order terms, which causes the large errors seen at early-time. By keeping an infinite Taylor series expansion, the MMI model can approximate the effects of the higher-order terms depending on how well the shape of the MMI-modeled eddy diffusivity matches that of the true eddy diffusivity.

For problems where $L \gg l$, e.g., in the limit of late time for the homogeneous problem, the error can be estimated. The error in the leading-order Taylor model in (4.24), which only captures the leading term in (B.20), is $\mathcal{O}(1/L^2)$. The error in the spatiotemporal MMI model in (4.28), which captures up to the second-order spatial moment, is $\mathcal{O}(1/L^4)$.

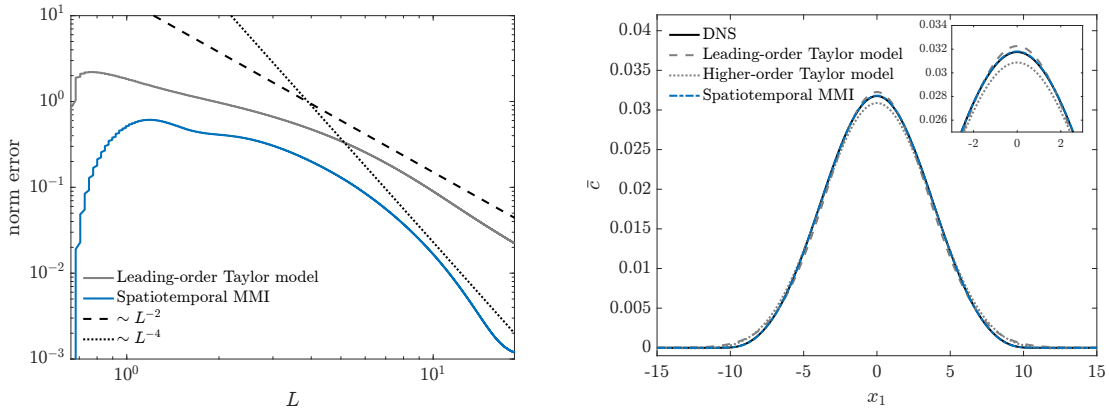

Figure B.1: (a) Error comparison for the leading-order Taylor model and the spatiotemporal MMI model. For large L, the models follow the expected $1/L^2$ and $1/L^4$ scaling, respectively. (b) Model comparison for $t = 12$. In this limit, all models are expected to perform well, however the spatiotemporal MMI model still outperforms both the leading-order Taylor model and the higher-order Taylor model.

Figure B.1a shows the normalized error for the leading-order Taylor model and spatiotemporal MMI model and the expected $1/L^2$ and $1/L^4$ scaling, respectively. The characteristic solution width L is computed at each timestep using the location where $\bar{c}$ drops by 99 percent of its maximum value. At very late time, the error in the spatiotemporal MMI model deviates from the expected scaling as the error in the numerical scheme, which is first-order in time and second-order in space, dominates.

At very late time, all of the models shown are expected to perform well due to the negligible effect of the higher-order terms in the Taylor series expansion. However, the spatiotemporal MMI model still outperforms both the leading-order Taylor model and higher-order Taylor model as shown in Figure B.1b.

B.5 Comparison with a fractional-order operator

Several recent works (Mehta et al. (2019); Song and Karniadakis (2018); Di Leoni et al. (2021)) examine using fractional-order operators for nonlocal models. A simple model with a fractional-order Laplacian for the homogeneous problem in Section 4.3.1 is:

$$\frac{\partial \bar{c}}{\partial t} = \frac{1}{2}\left(\frac{\partial^2}{\partial x_1^2}\right)^{\alpha/2} \bar{c}, \tag{B.22}$$

where $0 < \alpha < 2$, and the coefficient in front of the fractional-order Laplacian is chosen such that when $\alpha = 2$, the model reduces to the leading-order Taylor model (Boussinesq model) in Equation (4.24). Equation (B.22) can be solved by Fourier transforming in x_1:

$$\frac{\partial \bar{\hat{c}}}{\partial t} = \frac{1}{2}\left(-\left(k^2\right)^{\alpha/2}\right)\bar{\hat{c}}, \tag{B.23}$$

where k is the corresponding wavenumber in x_1, and time-advancing in Fourier space.

To obtain the nonlocal eddy diffusivity, recall that the right-hand-side of Equation (B.23) is a model for the derivative of the unclosed scalar flux:

$$ik(-\widehat{\overline{u_1'c'}}) = \frac{1}{2}\left(-\left(k^2\right)^{\alpha/2}\right)\bar{\hat{c}}. \tag{B.24}$$

Rearranging,

$$-\widehat{\overline{u_1'c'}} = \frac{1}{2}\left(k^2\right)^{\alpha/2-1}(ik\bar{\hat{c}}), \tag{B.25}$$

where the gradient of $\bar{c}$ in Fourier space is $ik\bar{\hat{c}}$, and correspondingly the nonlocal eddy diffusivity in Fourier space is:

$$\hat{D}(k) = \frac{1}{2}\left(k^2\right)^{\alpha/2-1}. \tag{B.26}$$

Figure B.2 shows the nonlocal eddy diffusivity in Fourier space for several α in comparison with the exact and MMI-modeled nonlocal eddy diffusivity.

Figure B.3 shows an early time ($t = 0.5$) and late time ($t = 4$) comparison of the spatiotemporal MMI model in Equation (4.28) and the fractional-order model for several choices of α. For early time, the simple fractional-order model with a constant α does not capture the double-peaked feature in the DNS solution of $\bar{c}(x_1)$, whereas the MMI model does. For late time, the fractional-order model overpredicts the spread of $\bar{c}(x_1)$. As shown in Figure B.2, the nonlocal eddy diffusivity of the

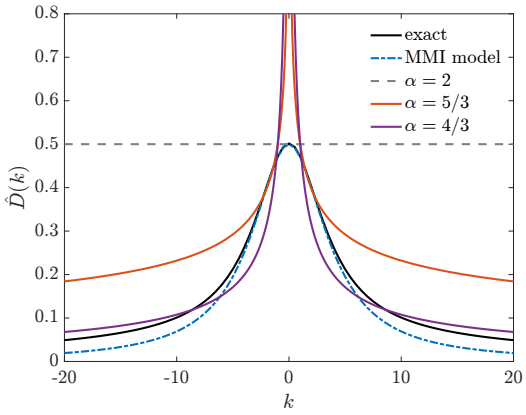

Figure B.2: The nonlocal eddy diffusivity of the simple fractional-order model shown in Fourier space for various choices of α compared with the exact nonlocal eddy diffusivity and the MMI-modeled eddy diffusivity.

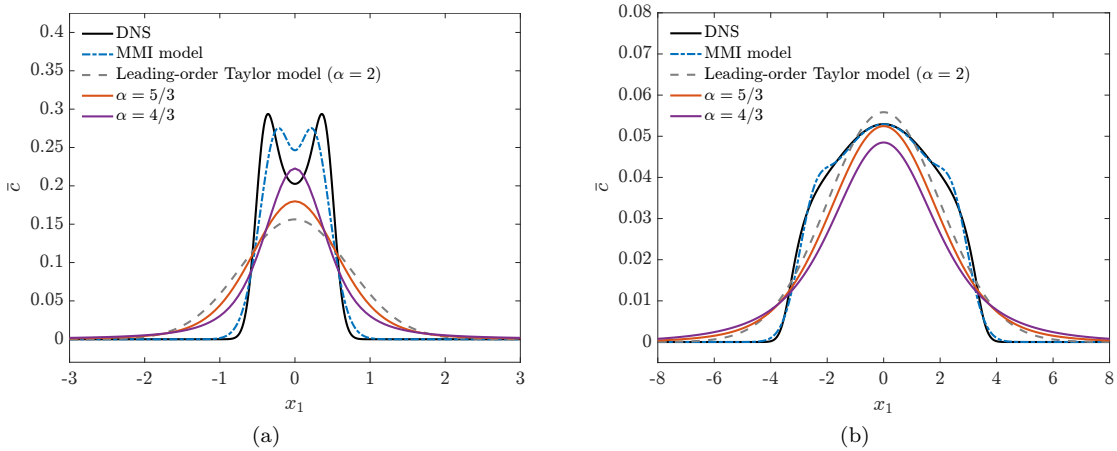

Figure B.3: Fractional-order model comparison for the homogeneous problem in Section 4.3.1 at early time, $t = 0.5$, and late time, $t = 4$.

fractional-order model is larger than the exact nonlocal eddy diffusivity in both of the limits of large k and small k. Thus, the fractional-order model solution disperses too quickly for both early time, where narrow (large wavenumber) features are present, and late time, where very smooth (small wavenumber) features are present.

This result may be remedied by a more sophisticated fractional-order model with a variable α but this is not considered here.

B.6 MFM for periodic problems

B.6.1 Obtaining moments of the nonlocal eddy diffusivity

The $\bar{c}$ required for IMFM, e.g., $\bar{c} = x_1$ for the zeroth moment, may be incompatible with the periodic boundary conditions of the problem as for the inhomogeneous model problem in Section 4.4.1. We decompose $c(x_1, x_2) = \bar{c}(x_1) + c'(x_1, x_2)$ where $\bar{c}(x_1)$ may be nonperiodic but $c'(x_1, x_2)$ is periodic.

Moreover, following a similar line of reasoning as for the input-output relationship between $-\overline{u_1' c'}(x_1)$ and $\bar{c}(x_1)$, $c'(x_1, x_2)$ can be Taylor series expanded as

$$c'(x_1, x_2) = c_0(x_1, x_2)\frac{\partial \bar{c}}{\partial x_1} + c_1(x_1, x_2)\frac{\partial^2 \bar{c}}{\partial x_1^2} + c_2(x_1, x_2)\frac{\partial^3 \bar{c}}{\partial x_1^3} + \ldots, \tag{B.27}$$

where $c_0(x_1, x_2)$, $c_1(x_1, x_2)$, etc. are to be determined. Once determined, to get to the desired moments, multiply Equation (B.27) by $-u_1'(x_1, x_2)$ and average over x_2,

$$-\overline{u_1' c'}(x_1) = -\overline{u_1' c_0}(x_1)\frac{\partial \bar{c}}{\partial x_1} - \overline{u_1' c_1}(x_1)\frac{\partial^2 \bar{c}}{\partial x_1^2} - \overline{u_1' c_2}(x_1)\frac{\partial^3 \bar{c}}{\partial x_1^3} - \ldots, \tag{B.28}$$

which leads to $D^0(x_1) = -\overline{u_1' c_0}(x_1)$, $D^{1_s}(x_1) = -\overline{u_1' c_1}(x_1)$, $D^{2_s}(x_1) = -\overline{u_1' c_2}(x_1)$, etc.

For example, to obtain the zeroth moment of the nonlocal eddy diffusivity for the inhomogeneous model problem in Section 4.4.1, substitute $\bar{c} = x_1$ into Equation (B.27) to get $c'(x_1, x_2) = c_0(x_1, x_2)$, and substitute $c(x_1, x_2) = x_1 + c_0(x_1, x_2)$ into the governing equation for the inhomogeneous model problem (Equation (4.34)):

$$u_1 + u_1\frac{\partial c_0}{\partial x_1} + u_2\frac{\partial c_0}{\partial x_2} = \epsilon^2\frac{\partial^2 c_0}{\partial x_1^2} + \frac{\partial^2 c_0}{\partial x_2^2} + s(x_1), \tag{B.29}$$

where $s(x_1)$ is the IMFM forcing required to enforce $\overline{c'}(x_1) = \overline{c_0}(x_1) = 0$. One can then solve for $c_0(x_1, x_2)$, and obtain the zeroth moment by forming $D^0(x_1) = -\overline{u_1' c_0}(x_1)$. Using Equation (B.29) for $c_0(x_1, x_2)$ rather than the full governing equation for $c(x_1, x_2)$ bypasses the issue of needing to explicitly enforce $\bar{c}$ with periodic boundary conditions.

Similarly, to obtain the first spatial moment of the nonlocal eddy diffusivity, substitute $c(x_1, x_2) = x_1^2/2 + c_0(x_1, x_2)x_1 + c_1(x_1, x_2)$ into the governing equation for the inhomogeneous model problem, and subtract x_1 times Equation (B.29):

$$u_1 c_0 + u_1\frac{\partial c_1}{\partial x_1} + u_2\frac{\partial c_1}{\partial x_2} = \epsilon^2 + 2\epsilon^2\frac{\partial c_0}{\partial x_1} + \epsilon^2\frac{\partial^2 c_1}{\partial x_1^2} + \frac{\partial^2 c_1}{\partial x_2^2} + s(x_1), \tag{B.30}$$

where $s(x_1)$ is the forcing required to enforce $\overline{c_1}(x_1) = 0$. One can then solve for $c_1(x_1, x_2)$, and obtain the first spatial moment by forming $D^{1_s}(x_1) = -\overline{u_1' c_1}(x_1)$. Note Equation (B.30) relies on having $c_0(x_1, x_2)$ from Equation (B.29).

One can obtain the second spatial moment of the nonlocal eddy diffusivity from solving the equation for $c_2(x_1, x_2)$, and so forth. As with IMFM where obtaining the second moment relies on having the zeroth and first moments, the equation for $c_2(x_1, x_2)$ relies on having $c_0(x_1, x_2)$ and $c_1(x_1, x_2)$. However, this decomposition does not raise the cost of obtaining the moments, still requiring one simulation per moment. We leave the extension of this formulation to unsteady and chaotic flows as future work.

B.6.2 Obtaining the full nonlocal eddy diffusivity

This section provides details for obtaining the nonlocal eddy diffusivity for the inhomogeneous problem with periodic boundary conditions in Section 4.4.1. Either the Green's-function-based approach of Hamba (2004) or MFM can be used to obtain the nonlocal eddy diffusivity. However, due to the small number of degrees of freedom in this problem, we obtain the nonlocal eddy diffusivity by directly inverting the discretized advection-diffusion operator and projecting it into the averaged space as detailed in Section 3.3. Due to the periodic boundary conditions, some additional treatment is needed, which is detailed here. In other words, the averaged operator, $\overline{\mathcal{L}}$, can be obtained via Equation (3.16) and can be further written as

$$\overline{\mathcal{L}} = -\frac{\mathrm{d}}{\mathrm{d}x_1}(D + \epsilon^2\mathcal{I})\frac{\mathrm{d}}{\mathrm{d}x_1}, \tag{B.31}$$

where D is the desired nonlocal eddy diffusivity matrix and $\mathcal{I}$ is the identity matrix. However, due to the periodic boundary conditions, $\mathrm{d}/\mathrm{d}x_1$ is uninvertible, and thus one cannot simply solve for D using Equation (B.31).

Rather, the decomposition in Section B.6.1 is applied, and let

$$c' = c_d\frac{\mathrm{d}\bar{c}}{\mathrm{d}x_1}, \tag{B.32}$$

where c' is a discretized vector of the scalar fluctuation ($N_1N_2 \times 1$), c_d is a discretized matrix ($N_1N_2 \times N_1$), and $\mathrm{d}\bar{c}/\mathrm{d}x_1$ is a discretized vector of the mean scalar gradient ($N_1 \times 1$) where N_1 and N_2 are the number of points in the x_1-direction and x_2-direction, respectively. This is equivalent to Equation (B.27) before it is Taylor-series expanded. Then,

$$-\overline{u_1'c'} = -Pu_1'c' = -Pu_1'c_d\frac{\mathrm{d}\bar{c}}{\mathrm{d}x_1} = D\frac{\mathrm{d}\bar{c}}{\mathrm{d}x_1}, \tag{B.33}$$

where P is the projection (i.e., averaging) matrix ($N_1 \times N_1N_2$), and thus the nonlocal eddy diffusivity matrix is

$$D = -Pu_1'c_d. \tag{B.34}$$

To obtain c_d, substitute $c = \bar{c} + c'$ into the governing equation for the inhomogeneous model

problem (Equation (4.34)) with the MFM forcing, $s(x_1)$:

$$u_1\frac{\partial c'}{\partial x_1}+u_2\frac{\partial c'}{\partial x_2}-\epsilon^2\frac{\partial^2 c'}{\partial x_1^2}-\frac{\partial^2 c'}{\partial x_2^2}=-u_1\frac{\partial \overline{c}}{\partial x_1}+\epsilon^2\frac{\partial^2 \overline{c}}{\partial x_1^2}+s(x_1), \tag{B.35}$$

where the role of $s(x_1)$ is to enforce the condition $\overline{c'}(x_1)=0$. In matrix-operator form, Equation (B.35) is written as

$$\mathcal{L}c'=\overline{\mathcal{L}}_1\frac{\partial \overline{c}}{\partial x_1}+s, \tag{B.36}$$

where $\overline{\mathcal{L}}_1=-u_1+\epsilon^2\partial/\partial x_1$. Substituting $s=E\bar{s}$ into Equation (B.36), and forming a matrix system to simultaneously solve for c' and $\bar{s}$ such that $Pc'=0$ leads to:

$$\begin{bmatrix}\mathcal{L} & -E\\ P & 0\end{bmatrix}\begin{bmatrix}c'\\ \bar{s}\end{bmatrix}=\begin{bmatrix}\overline{\mathcal{L}}_1\\ 0\end{bmatrix}\left[\frac{\partial \overline{c}}{\partial x_1}\right]. \tag{B.37}$$

Rearranging,

$$\begin{bmatrix}c'\\ \bar{s}\end{bmatrix}=\begin{bmatrix}\mathcal{L} & -E\\ P & 0\end{bmatrix}^{-1}\begin{bmatrix}\overline{\mathcal{L}}_1\\ 0\end{bmatrix}\left[\frac{\partial \overline{c}}{\partial x_1}\right]=\begin{bmatrix}c_d\\ *\end{bmatrix}\left[\frac{\partial \overline{c}}{\partial x_1}\right], \tag{B.38}$$

allows one to obtain c_d and subsequently the nonlocal eddy diffusivity, D, using Equation (B.34).

B.7 Effect of omitting a_1 for the inhomogeneous problem with periodic boundary conditions

For the inhomogeneous problem with periodic boundary conditions in Section 4.4.1, the coefficient a_1 is smaller than the other coefficients as shown in Figure 4.4a. In this appendix, we show the effect of setting $a_1=0$.

Using the coefficients in Figure 4.4a, i.e., nonzero a_1 when determining the coefficients, but setting $a_1=0$ during model implementation leads to improvement over the Boussinesq model in the mean solution but still slight underprediction of the DNS solution as shown in Figure B.4a. Figure B.4b shows a comparison of the eddy diffusivity kernel at $x_1=1.98$, the location of where a_1 was previously largest in magnitude. With $a_1=0$, the eddy diffusivity kernel also shows slight differences from the shape of the exact kernel.

Alternatively, one can also set $a_1=0$ in the procedure for determining coefficients as well and consider an MMI model of the form:

$$\left[1+a_2(x_1)\frac{\mathrm{d}^2}{\mathrm{d}x_1^2}\right](-\overline{u_1'c'})=a_0(x_1)\frac{\mathrm{d}\overline{c}}{\mathrm{d}x_1}. \tag{B.39}$$

However, there is some ambiguity in determining the coefficients. For example, using the zeroth-

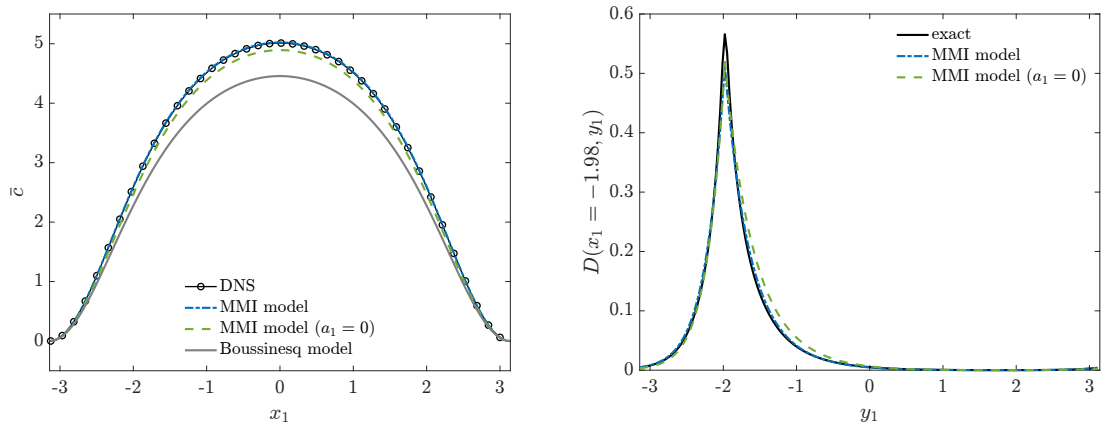

Figure B.4: (a) Model comparison between the MMI model using the coefficients in Figure 4.4a and setting $a_1 = 0$. (b) Comparison of the eddy diffusivity kernel at $x_1 = 1.98$, the location of where a_1 was previously largest in magnitude.

and first-order spatial moment of the eddy diffusivity, i.e., using MFM data for $-\overline{u_1'c'}|_{\bar{c}=x_1}$ and $-\overline{u_1'c'}|_{\bar{c}=x_1^2/2}$ in the procedure described in Section 4.2.5, leads to an ill-posed set equations for the a_0 and a_2 coefficients at $x_1 = 0$. Using MFM data for $-\overline{u_1'c'}|_{\bar{c}=x_1}$ and $-\overline{u_1'c'}|_{\bar{c}=x_1^3/6}$, which contains information about the zeroth-, first-, and second-order spatial moments of the eddy diffusivity as shown in Equation (4.16c), but without a term in the MMI model to match the first-order spatial moment since $a_1 = 0$ also leads to an ill-posed set of equations with singularities in the a_0 and a_2 coefficients. Inclusion of a_1 in the MMI model leads to a more robust procedure for matching the low-order eddy diffusivity moments.

B.8 An alternative MMI formulation

For the inhomogeneous problems in Section 4.4, an alternative to the steady MMI model in Equation (4.37) is

$$\left[1 + a_1(x_1)\frac{\mathrm{d}}{\mathrm{d}x_1} + a_2(x_1)\frac{\mathrm{d}^2}{\mathrm{d}x_1^2}\right]\left(\frac{-\overline{u_1'c'}}{a_0}\right) = \frac{\mathrm{d}\bar{c}}{\mathrm{d}x_1}. \tag{B.40}$$

By choosing $a_0(x_1) = D^0(x_1)$, the MMI formulation in Equation (B.40) matches the zeroth moment of the exact nonlocal eddy diffusivity (i.e., for $\bar{c} = x_1$, the model recovers $-\overline{u_1'c'}|_{\bar{c}=x_1} = D^0$). The remaining coefficients, $a_1(x_1)$ and $a_2(x_1)$, can be determined by matching the other low-order moments via specifying $\bar{c} = x_1^2/2$ and $\bar{c} = x_1^3/6$ as done in Section 4.2. This alternative formulation has one fewer coefficient to solve for than the original MMI formulation, but may have singularity issues if the zeroth moment of the eddy diffusivity goes to zero, for example near a wall.

Figure B.5a shows the coefficients of the alternative MMI formulation for the wall-bounded

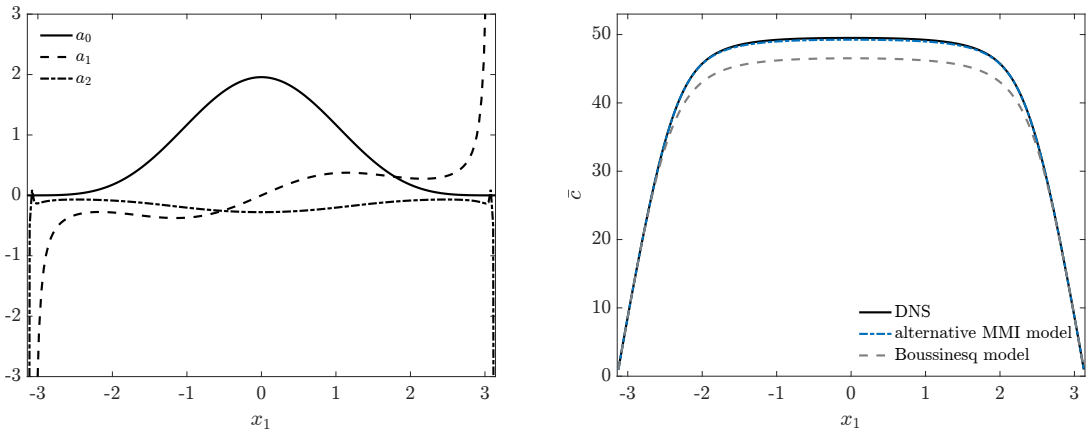

Figure B.5: (a) Coefficients of the alternative MMI formulation in Equation (B.40) for the wall-bounded inhomogeneous problem in Section 4.4.2. (b) Model comparison for the wall-bounded inhomogeneous problem.

inhomogeneous model problem in Section 4.4.2, and Figure B.5b shows the resulting solution, $\bar{c}(x_1)$, of the alternative MMI formulation closely matching the DNS solution. Although the solution of the alternative MMI formulation is very similar to that of the original MMI formulation in Figure 4.15, the coefficients show some differences particularly in $a_1(x_1)$ and the location of the singularities. At the wall, both $\overline{u_1'c'}(x_1)$ and $D^0(x_1)$ go to zero, leading to a zero divided by zero and numerical issues in determining the coefficients at the wall. However, at the wall, molecular effects also dominate and the eddy diffusivity model is unimportant leading to a well-behaved solution.

A coefficient regularization technique similar to the one shown in Section 4.4.2 may be used. A small parameter σ is introduced for determining the MMI coefficients:

$$\left[1 + a_1(x_1)\frac{\mathrm{d}}{\mathrm{d}x_1} + a_2(x_1)\frac{\mathrm{d}^2}{\mathrm{d}x_1^2}\right]\left(\frac{-\overline{u_1'c'} + \sigma\frac{\mathrm{d}\bar{c}}{\mathrm{d}x_1}}{D^0 + \sigma}\right) = \frac{\mathrm{d}\bar{c}}{\mathrm{d}x_1}. \tag{B.41}$$

The σ parameter is added to both the numerator and denominator in order to match the zeroth moment (i.e., for $\bar{c} = x_1$, the model recovers $-\overline{u_1'c'}|_{\bar{c}=x_1} + \sigma = D^0 + \sigma$). Equation (B.41) is used purely for determining the model coefficients; for ease of implementation, the final model is still Equation (B.40) with $a_0(x_1) = D^0(x_1)$. As with the previous coefficient regularization technique in Section 4.4.2, this introduces a small amount of error in matching the first- and second-order moments, but the tradeoff is better-behaved coefficients. Figure B.6a shows the coefficients for the alternative MMI formulation using coefficient regularization with $\sigma = 0.01\epsilon^2$, and Figure B.6b shows a comparison of the model solution with DNS. While the alternative MMI model with coefficient regularization performs slightly better than without coefficient regularization, the choice of σ is not yet systematic.

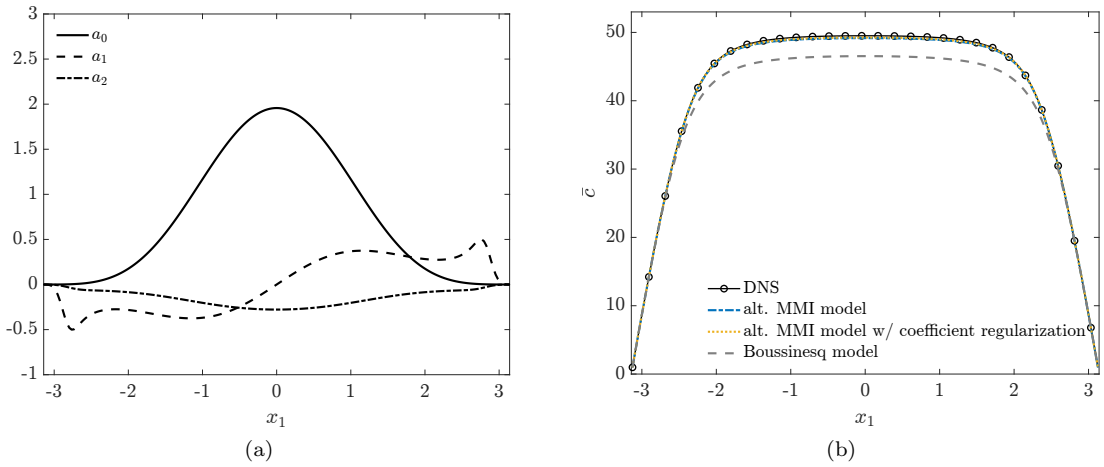

Figure B.6: (a) Coefficients for the alternative MMI formulation with coefficient regularization and $\sigma = 0.01\epsilon^2$. (b) Model comparison for the wall-bounded inhomogeneous problem in Section 4.4.2.

Appendix C

Appendices for Chapter 5

C.1 Row versus column comparison for D_{ij21}

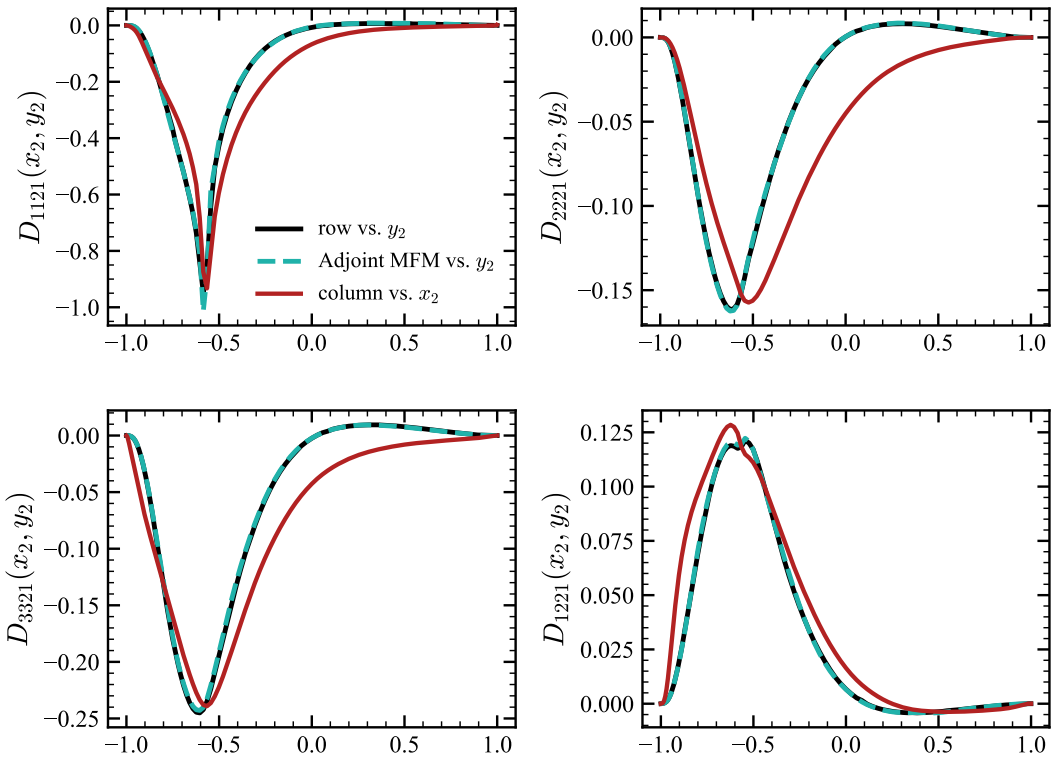

Figure C.1: Comparison of row versus column for D_{ij21} components using data from Park and Mani (2023a). The corresponding row computed using adjoint MFM is also shown.

In general, the rows of the eddy viscosity are not identical to the columns. Figure 3.3 showed the asymmetry in row versus column for D_{2121} at $x_2 = -0.565$. Figure C.1 shows the asymmetry in row versus column for other components of D_{ij21} at $x_2 = -0.565$. Adjoint MFM results from Figure 5.3 are also plotted for comparison.

Appendix D

Appendices for Chapter 6

D.1 Refinement and numerical scheme effects on the 2D non-local eddy viscosity

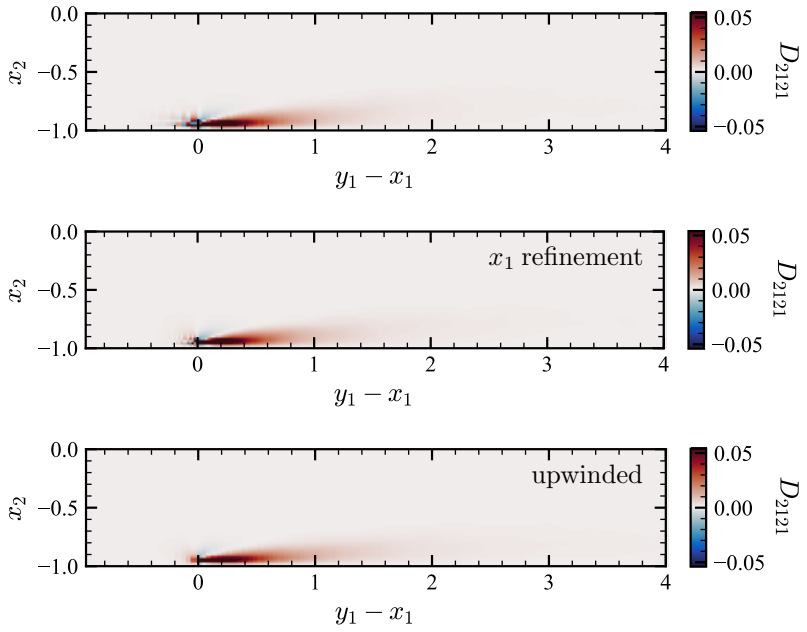

Figure D.1: Comparison of $D(x_2, y_1 - x_1, y_2 = -0.946)$ (column). The top plot shows the original kernel, the middle plot shows the kernel with mesh refinement in x_1, and the bottom plot shows the effect of upwinding the streamwise advection in the GMT equation.

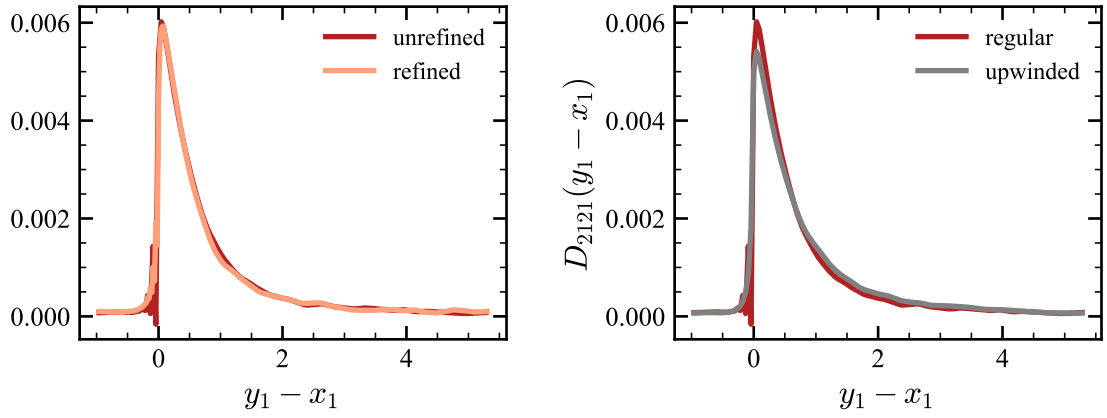

(a) (b)

Figure D.2: Comparison of the effect of (a) mesh refinement in x_1 or (b) an upwind scheme on the streamwise column, computed by integrating the 2D kernels in Figure D.1 over the x_2 direction.

In this appendix, we examine the effect of refinement and an upwinding scheme on the quantified eddy viscosity kernels, particularly on the observed numerical oscillations. For computational ease, we show the results for an eddy viscosity column from a MFM calculation rather than an eddy viscosity row from an adjoint MFM calculation; however, we expect the effects of refinement and numerical scheme to be qualitatively similar between the two cases. Section 6.3.2 discusses differences between 2D eddy viscosity columns and rows.

Figure D.1 shows a column of the eddy viscosity, $D(x_2, y_1 - x_1, y_2)$ at $y_2 = -0.946$, similar to Figure 6.4 but with a box size of $L_1 = 2\pi$ for computational ease. The mesh is uniform in the x_1 direction with $N_1 = 144$ grid points. This is identical to the box size and grid resolution of Park and Mani (2023a) for using MFM to compute the 1D wall-normal eddy viscosity. Figure D.1 also shows the same column of the eddy viscosity under mesh refinement with $N_1 = 288$. While refinement in the x_1 direction reduces the numerical oscillations, it does not get rid of them completely. As was discussed in Section 6.3, the thin region that needs to be resolved due to the Dirac delta function source term is proportional to ν/U_1 and would require a much finer resolution. Figure D.2a shows the eddy viscosity column integrated over the wall-normal direction, where the impact of refinement on the numerical oscillations is more clearly visible. Other than the oscillations, the overall shape of the kernel is unchanged with refinement.

Figure D.1 also shows the same column of the eddy viscosity with an upwind scheme used for the streamwise advection of v_i in the GMT equation in (3.28a). The central differences schemes for all of the other terms in the GMT equations in (3.28a) and (3.28b) and the Navier–Stokes equations in (3.27a) and (3.27b) are unchanged. The upwind scheme removes the oscillations completely; however, the additional numerical diffusion due to the upwind scheme also smooths out the overall

shape of the kernel and reduces the peak. The difference is seen more clearly when the eddy viscosity column is integrated over the wall-normal direction, as shown in Figure D.2b. Hence, we do not use an upwind scheme as it changes the shape of the eddy viscosity kernel.

D.2 Periodic domain effects on the 2D nonlocal eddy viscosity

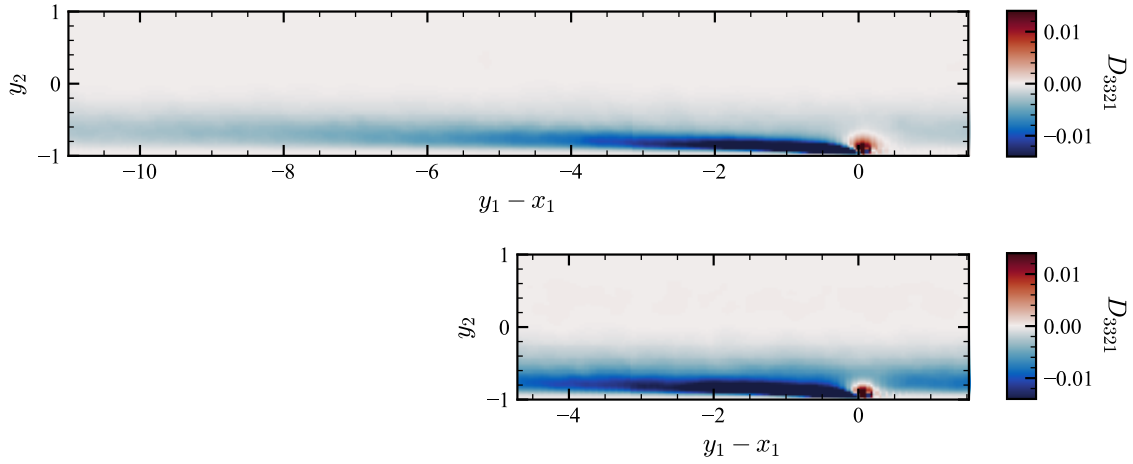

Figure D.3: Comparison of domain size effects on the D_{3321} component of the 2D eddy viscosity, corresponding to $\overline{u_3' u_3'}$, at $x_2 = -0.946$ ($x_2^+ \approx 10$). Top: $L_1 = 4\pi$; bottom: $L_1 = 2\pi$.

In this appendix, we investigate domain size effects on the 2D nonlocal eddy viscosity due to periodic boundary conditions in the x_1 direction. In the limit of an infinite domain, we expect the eddy viscosity kernel to go to zero very far away from the forcing location. The D_{3321} component in Figure D.3, shows slight wraparound of the eddy viscosity due to the periodic boundary conditions. Rather than a longer domain, which is computationally more expensive, we show a comparison with the shorter domain, e.g., used by Park and Mani (2023a) for their 1D wall-normal eddy viscosity calculations, to gain a qualitative understanding of the effect of periodic boundary conditions and a truncated domain.

Figure D.3 shows a comparison between a domain size of $L_1 = 4\pi$, the domain size used for Figure 6.11, and $L_1 = 2\pi$, the domain size used by Park and Mani (2023a). The colorbar for both plots is truncated to the same maximum colorbar values as Figure 6.11. While the qualitative shape of the eddy viscosity is unaffected by the domain size, the eddy viscosity is more negative for the $L_1 = 2\pi$ domain than the $L_1 = 4\pi$ domain due to wraparound from the periodic boundary condition. Figure D.4 shows the eddy viscosity kernels in Figure D.3 integrated over the wall-normal

direction, where the negative shift due to the periodic boundary condition is more apparent. Periodic superposition of the eddy viscosity kernel integrated over the wall-normal direction for the $L_1 = 4\pi$ domain approximately results in the eddy viscosity kernel for the $L_1 = 2\pi$ domain as shown in Figure D.5.

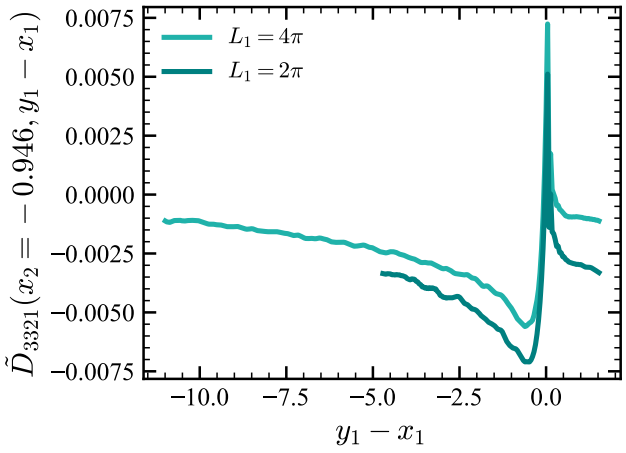

Figure D.4: Comparison of domain size effects on the $\tilde{D}_{3321}$ component of the streamwise eddy viscosity, corresponding to the 2D eddy viscosity kernels in Figure D.3 integrated over the wall-normal direction.

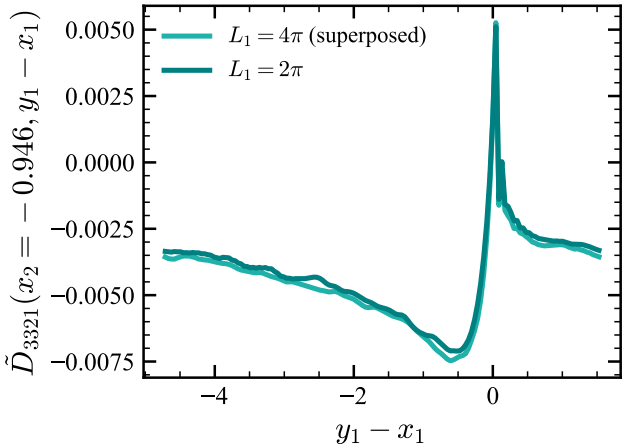

Figure D.5: Periodic superposition of the streamwise eddy viscosity kernel, $\tilde{D}_{3321}$, for the $L_1 = 4\pi$ domain approximately reproduces $\tilde{D}_{3321}$ for $L_1 = 2\pi$. In other words, the region from $-11 \leq y_1 - x_1 \leq -4.7$ for $L_1 = 4\pi$ in Figure D.4 is summed with the region from $-4.7 \leq y_1 - x_1 \leq 1.5$.

Bibliography

Hiroyuki Abe. Reynolds-number dependence of wall-pressure fluctuations in a pressure-induced turbulent separation bubble. *J. Fluid Mech.*, 833:563–598, 2017.

Hiroyuki Abe and Robert A. Antonia. Relationship between the energy dissipation function and the skin friction law in a turbulent channel flow. *J. Fluid Mech.*, 798:140–164, 2016.

Rutherford Aris. On the dispersion of a solute in pulsating flow through a tube. *Proc. R. Soc. A: Math. Phys. Sci.*, 259(1298):370–376, 1960.

George K. Batchelor and Ian Proudman. The large-scale structure of homogenous turbulence. *Philos. Trans. Royal Soc. A*, 248(949):369–405, 1956.

Ruwim Berkowicz and Lars P. Prahm. Generalization of K theory for turbulent diffusion. Part I: Spectral turbulent diffusivity concept. *J. Appl. Meteorol. Climatol.*, 18(3):266–272, 1979.

Ruwim Berkowicz and Lars P. Prahm. On the spectral turbulent diffusivity theory for homogeneous turbulence. *J. Fluid Mech.*, 100(2):433–448, 1980.

Sanjeeb T. Bose, Parviz Moin, and Donghyun You. Grid-independent large-eddy simulation using explicit filtering. *Phys. Fluids*, 22(10):105103, 2010.

Joseph V. Boussinesq. Essai sur la théorie des eaux courantes. In *Mémoires présentés par divers savants a l'Academie des Sciences de l'Institute National de France*, volume XXIII. Impr. Nationale, 1877.

Spencer H. Bryngelson, Florian Schäfer, Jessie Liu, and Ali Mani. Fast macroscopic forcing method. *J. Comput. Phys.*, 499:112721, 2024.

Phares L. Carroll and Guillaume Blanquart. A proposed modification to Lundgren's physical space velocity forcing method for isotropic turbulence. *Phys. Fluids*, 25(10), 2013.

René-Daniel Cécora, Rolf Radespiel, Bernhard Eisfeld, and Axel Probst. Differential Reynolds-stress modeling for aeronautics. *AIAA Journal*, 53(3):739–755, 2015.

Francis H. Champagne, Vascar G. Harris, and Stanley Corrsin. Experiments on nearly homogeneous turbulent shear flow. *J. Fluid Mech.*, 41(1):81–139, 1970.

Xi Chen, Fazle Hussain, and Zhen-Su She. Quantifying wall turbulence via a symmetry approach. part 2. Reynolds stresses. *J. Fluid Mech.*, 850:401–438, 2018.

Kwing-So Choi and John L. Lumley. The return to isotropy of homogeneous turbulence. *J. Fluid Mech.*, 436:59–84, 2001.

Genevieve Comte-Bellot and Stanley Corrsin. Simple Eulerian time correlation of full- and narrow-band velocity signals in grid-generated, 'isotropic' turbulence. *J. Fluid Mech.*, 48(2):273–337, 1971.

Stanley Corrsin. Limitations of gradient transport models in random walks and in turbulence. *Adv. Geophys.*, 18:25–60, 1975.

Bart J. Daly and Francis H. Harlow. Transport equations in turbulence. *Phys. Fluids*, 13(11): 2634–2649, 1970.

F. A. De Souza, V. D. Nguyen, and S. Tavoularis. The structure of highly sheared turbulence. *J. Fluid Mech.*, 303:155–167, 1995.

Chandru Dhandapani, Kyupaeck J. Rah, and Guillaume Blanquart. Effective forcing for direct numerical simulations of the shear layer of turbulent free shear flows. *Phys. Rev. Fluids*, 4:084606, 2019.

Patricio C. Di Leoni, Tamer A. Zaki, George E. Karniadakis, and Charles Meneveau. Two-point stress–strain-rate correlation structure and non-local eddy viscosity in turbulent flows. *J. Fluid Mech.*, 914:A6, 2021.

Paul A. Durbin. Near-wall turbulence closure modeling without "damping functions". *Theor. Comput. Fluid Dyn.*, 3(1):1–13, 1991.

Paul A. Durbin. A Reynolds stress model for near-wall turbulence. *J. Fluid Mech.*, 249:465–498, 1993.

Paul A. Durbin and Bjørn A. Pettersson Reif. *Statistical theory and modeling for turbulent flows*. John Wiley & Sons, 2011.

Bernhard Eisfeld and Christopher L. Rumsey. Length-scale correction for Reynolds-stress modeling. *AIAA Journal*, 58(4):1518–1528, 2020.

Bernhard Eisfeld, Chris Rumsey, and Vamshi Togiti. Verification and validation of a second-moment-closure model. *AIAA Journal*, 54(5):1524–1541, 2016.

Panos G. Georgopoulos and John H. Seinfeld. Nonlocal description of turbulent dispersion. *Chem. Eng. Sci.*, 44(9):1995–2016, 1989.

M. M Gibson and B. E. Launder. Ground effects on pressure fluctuations in the atmospheric boundary layer. *J. Fluid Mech.*, 86(3):491–511, 1978.

Sidney Goldstein. On diffusion by discontinuous movements, and on the telegraph equation. *Q. J. Mech. Appl. Math*, 4(2):129–156, 1951.

Fujihiro Hamba. An analysis of nonlocal scalar transport in the convective boundary layer using the Green's function. *J. Atmos. Sci.*, 52(8):1084–1095, 1995.

Fujihiro Hamba. Nonlocal expression for scalar flux in turbulent shear flow. *Phys. Fluids*, 16(5): 1493–1508, 2004.

Fujihiro Hamba. Nonlocal analysis of the Reynolds stress in turbulent shear flow. *Phys. Fluids*, 17 (11):115102, 2005.

Fujihiro Hamba. Analysis and modelling of non-local eddy diffusivity for turbulent scalar flux. *J. Fluid Mech.*, 950:A38, 2022.

V. G. Harris, J. A. H. Graham, and S. Corrsin. Further experiments in nearly homogeneous turbulent shear flow. *J. Fluid Mech.*, 81(4):657–687, 1977.

Antti Hellsten. New advanced k-ω turbulence model for high-lift aerodynamics. *AIAA journal*, 43 (9):1857–1869, 2005.

Ty Homan, Omkar Shende, Dana L. Lavacot, and Ali Mani. A model form for Reynolds stress decay informed by analysis of anisotropically forced homogeneous turbulence. *Bulletin of the American Physical Society*, 68, 2023.

J. C. R. Hunt and J. M. R. Graham. Free-stream turbulence near plane boundaries. *J. Fluid Mech.*, 84(2):209–235, 1978.

Hussein J. Hussein, Steven P. Capp, and William K. George. Velocity measurements in a high-Reynolds-number, momentum-conserving, axisymmetric, turbulent jet. *J. Fluid Mech.*, 258:31–75, 1994.

Juan C. Isaza and Lance R. Collins. On the asymptotic behaviour of large-scale turbulence in homogeneous shear flow. *J. Fluid Mech.*, 637:213–239, 2009.

Suad Jakirlić and Kemal Hanjalić. A new approach to modelling near-wall turbulence energy and stress dissipation. *J. Fluid Mech.*, 459:139–166, 2002.

Dennis C. Jespersen, Thomas H. Pulliam, and Marissa L. Childs. Overflow turbulence modeling resource validation results. Technical Report ARC-E-DAA-TN35216, 2016.

Javier Jiménez. Near-wall turbulence. *Phys. Fluids*, 25(10), 2013.

John Kim and Parviz Moin. Application of a fractional-step method to incompressible Navier–Stokes equations. *J. Comp. Phys.*, 59(2):308–323, 1985.

John Kim, Parviz Moin, and Robert Moser. Turbulence statistics in fully developed channel flow at low Reynolds number. *J. Fluid Mech.*, 177:133–166, 1987.

Robert H. Kraichnan. Eddy viscosity and diffusivity: Exact formulas and approximations. *Complex Systems*, 1(4-6):805–820, 1987.

Per-Åge Krogstad and Peter A. Davidson. Freely decaying, homogeneous turbulence generated by multi-scale grids. *J. Fluid Mech.*, 680:417–434, 2011.

Doug S. Lacy and Adam M. Clark. Definition of initial landing and takeoff reference configurations for the high lift common research model (crm-hl). In *AIAA Aviation 2020 Forum*, page 2771, 2020.

B. E. Launder, G. Jr. Reece, and W. Rodi. Progress in the development of a Reynolds-stress turbulence closure. *J. Fluid Mech.*, 68(3):537–566, 1975.

Dana Lynn O.-L. Lavacot, Jessie Liu, Hannah Williams, Brandon E. Morgan, and Ali Mani. Non-locality of mean scalar transport in two-dimensional Rayleigh-Taylor instability using the macroscopic forcing method. *arXiv 2307.13911*, 2023.

L. Le Penven, J. N. Gence, and G. Comte-Bellot. On the approach to isotropy of homogeneous turbulence: Effect of the partition of kinetic energy among the velocity components. In *Frontiers in Fluid Mechanics: A Collection of Research Papers Written in Commemoration of the 65th Birthday of Stanley Corrsin*, pages 1–21. Springer, 1985.

Myoungkyu Lee and Robert D. Moser. Direct numerical simulation of turbulent channel flow up to $\mathrm{Re}_\tau \approx 5200$. *J. Fluid Mech.*, 774:395–415, 2015.

Mattias Liefvendahl and Christer Fureby. Grid requirements for LES of ship hydrodynamics in model and full scale. *Ocean Eng.*, 143:259–268, 2017.

Jessie Liu, Hannah H. Williams, and Ali Mani. Systematic approach for modeling a nonlocal eddy diffusivity. *Phys. Rev. Fluids*, 8(12):124501, 2023.

Paolo Luchini. Universality of the turbulent velocity profile. *Phys. Rev. Lett.*, 118:224501, Jun 2017.

Thomas S. Lundgren. Linearly forced isotropic turbulence. *Center for Turbulence Research Annual Research Briefs*, 2003.

Rémi Manceau and Kemal Hanjalić. Elliptic blending model: A new near-wall Reynolds-stress turbulence closure. *Phys. Fluids*, 14(2):744–754, 2002.

Ali Mani and Danah Park. Macroscopic forcing method: A tool for turbulence modeling and analysis of closures. *Phys. Rev. Fluids*, 6(5):054607, 2021.

Mortaza Mani, Deric Babcock, Chad Winkler, and Philippe Spalart. Predictions of a supersonic turbulent flow in a square duct. In *51st AIAA Aerospace Sciences Meeting Including the New Horizons Forum and Aerospace Exposition*, page 860, 2013.

Ivan Marusic, Jason P. Monty, Marcus Hultmark, and Alexander J. Smits. On the logarithmic region in wall turbulence. *J. Fluid Mech.*, 716:R3, 2013.

Beverley J. Mckeon, Jun-de Li, W. Jiang, Jonathan F. Morrison, and Alexander J. Smits. Further observations on the mean velocity distribution in fully developed pipe flow. *J. Fluid Mech.*, 501: 135–147, 2004.

Pavan P. Mehta, Guofei Pang, Fangying Song, and George E. Karniadakis. Discovering a universal variable-order fractional model for turbulent Couette flow using a physics-informed neural network. *Fract. Calc. Appl. Anal.*, 22(6):1675–1688, 2019.

Florian R. Menter. Two-equation eddy-viscosity turbulence models for engineering applications. *AIAA Journal*, 32(8):1598–1605, 1994.

Mohsen S. Mohamed and John C. La Rue. The decay power law in grid-generated turbulence. *J. Fluid Mech.*, 219:195–214, 1990.

Peter A. Monkewitz. Asymptotics of streamwise Reynolds stress in wall turbulence. *J. Fluid Mech.*, 931:A18, 2022.

Yohei Morinishi, Thomas S. Lund, Oleg V. Vasilyev, and Parviz Moin. Fully conservative higher order finite difference schemes for incompressible flow. *J. Comp. Phys.*, 143(1):90–124, 1998.

Laurent Mydlarski and Zellman Warhaft. On the onset of high-reynolds-number grid-generated wind tunnel turbulence. *J. Fluid Mech.*, 320:331–368, 1996.

Y. Na and P. Moin. Direct numerical simulation of a separated turbulent boundary layer. *J. Fluid M.*, 374:379–405, 1998.

Danah Park and Ali Mani. Direct calculation of the eddy viscosity operator in turbulent channel flow at $\mathrm{Re}_\tau = 180$. *arXiv 2108.10898*, 2023a.

Danah Park and Ali Mani. Direct measurement of the eddy viscosity tensor in a turbulent separation bubble with sweep. In *AIAA AVIATION 2023 Forum*, page 3268, 2023b.

Danah Park, Jessie Liu, and Ali Mani. Direct measurement of the eddy viscosity tensor in a canonical separated flow: What is the upper bound of accuracy for local Reynolds stress models? In *AIAA SciTech 2022 Forum*, page 0940, 2022a.

Danah Park, Jessie Liu, and Ali Mani. Non-Boussinesq effects of eddy viscosity in a separated turbulent boundary layer. In *34th Symposium on Naval Hydrodynamics*, 2022b.

R. F. Pawula. Approximation of the linear Boltzmann equation by the Fokker-Planck equation. *Phys. Rev.*, 162(1):186, 1967.

Stephen B. Pope. A more general effective-viscosity hypothesis. *J. Fluid Mech.*, 72(2):331–340, 1975.

Stephen B. Pope. *Turbulent flows*. Cambridge University Press, 2000.

Axel Probst, Rolf Radespiel, Christoph Wolf, Tobias Knopp, and Dieter Schwamborn. A comparison of detached-eddy simulation and Reynolds-stress modeling applied to the flow over a backward-facing step and an airfoil at stall. In *48th AIAA Aerospace Sciences Meeting including the New Horizons Forum and Aerospace Exposition*, page 920, 2010.

Kyupaeck J. Rah, Chandru Dhandapani, and Guillaume Blanquart. Derivation of a realistic forcing term to reproduce the turbulent characteristics of round jets on the centerline. *Phys. Rev. Fluids*, 3:084606, 2018.

Osborne Reynolds. IV. On the dynamical theory of incompressible viscous fluids and the determination of the criterion. *Philos. Trans. Royal Soc. A*, (186):123–164, 1895.

Robert S. Rogallo. *Numerical experiments in homogeneous turbulence*, volume 81315. National Aeronautics and Space Administration, 1981.

Michael M. Rogers and Parviz Moin. The structure of the vorticity field in homogeneous turbulent flows. *J. Fluid Mech.*, 176:33–66, 1987.

Nicolae Romanof. Application of the orthonormal expansion of random functions to turbulent diffusion. In *Proceedings of the seventh conference on probability theory: Aug. 29-Sept. 4, 1982, Braşov, Romania*, page 493. VSP, 1985.

Carlos Rosales and Charles Meneveau. Linear forcing in numerical simulations of isotropic turbulence: Physical space implementations and convergence properties. *Phys. Fluids*, 17(9), 2005.

Julius C. Rotta. Statistische Theorie nichthomogener Turbulenz. *Zeitschrift für Physik*, 129:547–572, 1951.

C. L. Rumsey, J.-R. Carlson, T. H. Pulliam, and P. R. Spalart. Improvements to the quadratic constitutive relation based on NASA juncture flow data. *AIAA Journal*, 58(10):4374–4384, 2020.

Philip G. Saffman. The large-scale structure of homogeneous turbulence. *J. Fluid Mech.*, 27(3): 581–593, 1967.

Sutanu Sarkar and Charles G. Speziale. A simple nonlinear model for the return to isotropy in turbulence. *Phys. Fluids*, 2(1):84–93, 1990.

Jeongmin Seo, Ricardo García-Mayoral, and Ali Mani. Pressure fluctuations and interfacial robustness in turbulent flows over superhydrophobic surfaces. *J. Fluid Mech.*, 783:448–473, 2015.

Michael Sinhuber, Eberhard Bodenschatz, and Gregory P. Bewley. Decay of turbulence at high reynolds numbers. *Phys. Rev. Lett.*, 114:034501, Jan 2015.

Ladislav Skrbek and Steven R. Stalp. On the decay of homogeneous isotropic turbulence. *Phys. Fluids*, 12(8):1997–2019, 2000.

Alexander J. Smits, Marcus Hultmark, Myoungkyu Lee, Sergio Pirozzoli, and Xiaohua Wu. Reynolds stress scaling in the near-wall region of wall-bounded flows. *J. Fluid Mech.*, 926:A31, 2021.

Fangying Song and George E. Karniadakis. A universal fractional model of wall-turbulence, 2018.

Philippe Spalart and Steven Allmaras. A one-equation turbulence model for aerodynamic flows. In *30th aerospace sciences meeting and exhibit*, page 439, 1992.

Philippe R. Spalart. Strategies for turbulence modelling and simulations. *Int. J. Heat Fluid Flow*, 21(3):252–263, 2000.

Philippe R. Spalart and Hiroyuki Abe. Empirical scaling laws for wall-bounded turbulence deduced from direct numerical simulations. *Phys. Rev. Fluids*, 6(4):044604, 2021.

Philippe R. Spalart and Gary N. Coleman. Numerical study of a separation bubble with heat transfer. *Eur. J. Mech. B. Fluids*, 16(2):169–189, 1997.

Charles G. Speziale, Sutanu Sarkar, and Thomas B. Gatski. Modelling the pressure–strain correlation of turbulence: an invariant dynamical systems approach. *J. Fluid Mech.*, 227:245–272, 1991.

Charles G. Speziale, Ridha Abid, and Paul A. Durbin. On the realizability of Reynolds stress turbulence closures. *J. Sci. Comput.*, 9:369–403, 1994.

Stavros Tavoularis and Stanley Corrsin. Experiments in nearly homogenous turbulent shear flow with a uniform mean temperature gradient. part 1. *J. Fluid Mech.*, 104:311–347, 1981.

Geoffrey I. Taylor. Dispersion of soluble matter in solvent flowing slowly through a tube. *Proc. R. Soc. A: Math. Phys. Sci.*, 219(1137):186–203, 1953.

Adrien Thormann and Charles Meneveau. Decay of homogeneous, nearly isotropic turbulence behind active fractal grids. *Phys. Fluids*, 26(2), 2014.

Albert A. Townsend. *The structure of turbulent shear flow*. Cambridge University Press, 1976.

Nicolaas G. Van Kampen. *Stochastic processes in physics and chemistry*, volume 1. Elsevier, 1992.

Theodore von Kármán. Mechanische Ähnlichkeit und Turbulenz. In *Proc. Third Int. Congr. Applied Mechanics*, pages 85–105, 1930.

Stefan Wallin and Arne V. Johansson. An explicit algebraic Reynolds stress model for incompressible and compressible turbulent flows. *J. Fluid Mech.*, 403:89–132, 2000.

Mengze Wang and Tamer A. Zaki. State estimation in turbulent channel flow from limited observations. *J. Fluid Mech.*, 917:A9, 2021.

Mengze Wang, Qi Wang, and Tamer A. Zaki. Discrete adjoint of fractional-step incompressible Navier-Stokes solver in curvilinear coordinates and application to data assimilation. *J. Comp. Phys.*, 396:427–450, 2019a.

Qi Wang, Yosuke Hasegawa, and Tamer A. Zaki. Spatial reconstruction of steady scalar sources from remote measurements in turbulent flow. *J. Fluid Mech.*, 870:316–352, 2019b.

Qi Wang, Mengze Wang, and Tamer A. Zaki. What is observable from wall data in turbulent channel flow? *J. Fluid Mech.*, 941:A48, 2022.

David C. Wilcox. Reassessment of the scale-determining equation for advanced turbulence models. *AIAA journal*, 26(11):1299–1310, 1988.

David C. Wilcox. *Turbulence modeling for CFD*, volume 2. La Canada, CA: DCW industries, 1998.

Wen Wu, Charles Meneveau, and Rajat Mittal. Spatio-temporal dynamics of turbulent separation bubbles. *J. Fluid Mech.*, 883, 2020.

Akira Yoshizawa. Statistical analysis of the anisotropy of scalar diffusion in turbulent shear flows. *Phys. Fluids*, 28(11):3226–3231, 1985.

Tamer A. Zaki and Mengze Wang. From limited observations to the state of turbulence: Fundamental difficulties of flow reconstruction. *Phys. Rev. Fluids*, 6:100501, Oct 2021.